Instability in the Winds of Hot Stars: Theory and Simulation

Edward L. Gomez

A thesis submitted to the
University of Wales,
Cardiff,
for the degree of

Doctor of Philosophy

June 2004

ProQuest LLC
789 East Eisenhower Parkway
P.O. Box 1346
Ann Arbor, MI 48106-1346

Abstract

Radiatively driven winds are a key component in a number of astrophysical settings, most notably the wind of hot massive stars. In this thesis we present the mechanism by which line radiation can drive hot star winds. In order to become familiar with the dynamics of numerical wind solutions in one and two dimensions, we also make calculations for winds driven by perfect gas pressure and continuum radiation pressure. The main emphasis of this work is to approximate the form of the line-driving as given by Owocki, Castor & Rybicki (1986), with an efficient algorithm, in a pure absorption (no scattering) case. We construct an efficient model for the solution to the line-driving problem and use this to investigate the dynamics of perturbations in the wind.

Once we have shown that our method can reproduce the results of previous authors we add more physics to the model. We firstly change the shape of the line-profile function and observe that although this has a stabilizing effect on the flow the response of the wind to perturbations is largely unchanged. As separate refinement we move away from the pure absorption model and include the line drag phenomenon in the radiative driving calculation. This phenomenon also stabilizes the flow but its effect is decreases further from the central star and the downstream flow feels little of its influence.

We use the results from all of our models of hot star winds to create synthetic spectral diagrams. The spectra created from the perturbed models resemble structures which are observed in the spectra of hot star winds called Discrete Absorption Components, the origin of which is unclear. We show that our models can be used to explain astrophysically observed structure and better understand the nature of hot star winds.

Acknowledgments

I have had much support during my time researching, writing and generally living through this work. People in the Department of Physics & Astronomy I would like to thank are; John Inglesfield for support all throughout my undergraduate and postgraduate career, Paul Jones for computing and distraction one way or another, Robin Williams for stepping into the breach, pulling a project out of the hat with 24 hours notice, and much support and advice over the past 4 years, Ashley James for keeping me sane for the past 4 years and acquainting me with vocabulary which will bewilder for the rest of my life. I would like to thank Mark Runacres, without whose intervention I would have moved to Chicago.

Outside of astronomy many people have been invaluable. Paul Buckle should be named first in large friendly letters for taking my mind off astronomy as often as possible and enforcing the general life philosophies of Victoria Wood. The entire Cardiff University Church Choir Graduate Association, as a wonderfully warm and caring group that I consider with more affection than members of my own family (distant ones). Who, when all else failed, were able give me consolation through the beauty and splendour of the English choral repertoire. There are a few exceptional individuals whose name must stand in stone for ever; Sue "Awright" Moss, Gareth "Gin o'clock" Thomas, along with the less notorious William Byrd and Henry Purcell. Added to these friends must be Nik Tabbener who has seen-in probably most of the more significant moments of my life, and has been wonderfully unabashed in telling people exactly what she thinks. The world needs more people like her, but not too many.

Now to the loose grouping of vagrants I think of as my family. To Nanny and Grandad who were both wonderful in their own slightly terrifying way and will forever be immortal in the ones who loved them. To Aunt Kit, a lady who lives close to the letter from the Queen, but has a mind so sharp she can still do the Times Crossword and Countdown Conundrum, who I am completely dotty about. My parents and sister deserve a gargantuan portion of praise for putting up with me for the past 27 years (and my sister for 14 of those). Even though I may not have always shown it, I am grateful for everything that they have done. There are so many ways that they have helped it is impossible for words to describe how proud I am of the 3 of them.

Lastly I would like to thank from a place deep within my soul, Haley Morgan without whose strength and love my life would be pallid and cold. Meeting her has been the single most important moment in my life, and is the reason that all that comes after was worthwhile.

To all of you, I dedicate this work.

June 2004

"But though even words like joojooflop, swut and turlingdrome are now perfectly acceptable in common usage there is one word that is still beyond the pale. The concept it embodies is so revolting that the publication or broadcast of the word is utterly forbidden in all parts of the Galaxy except one where they don't know what it means. The word is 'belgium' and it is only ever used by loose tongued people in situaions of dire provocation."

- *Hitchhiker's guide to the Galaxy, Fit the 10th,*
Douglas Adams

Contents

List of Figures

List of Tables

Chapter 1

Introduction

As part of this work we develop computational models of winds from astrophysical objects. The main thrust of the work presented here is in modelling the winds from OB stars. To put these winds in context we discuss models of coronal winds (e.g. the Solar wind) and winds from Red Super Giants (RSGs), Asymptotic Giant Branch (AGBs) and from close to Active Galactic Nuclei (AGN). The study of the winds from stars began with subject of interest being our nearest star, the Sun. The solar wind has a great many effects on the atmospheric conditions on the Earth, from the Aurorae Borealis and Australis to electromagnetic interference strong enough to induce power cuts to cities. The stars which we consider in this work are quite different in nature from the Sun. For example the rate at which gas is expelled from the Sun is $\sim 10^{-14}\mathrm{M}_{\odot}\,\mathrm{yr}^{-1}$ whilst that of a typical O star is $\sim 10^{-6}\mathrm{M}_{\odot}\,\mathrm{yr}^{-1}$.

The effect of the Sun on the solar system is quite striking and such effects as the Solar Sun spot cycle have been documented since the 17^{th} century. The effect of hot, young stars on their environment is even more striking since generally the velocities of such winds are higher than the Solar wind and the neighbourhood of a young star is also quite different from the neighbourhood of the Sun. Perhaps the largest effect that these stellar winds have on their environment is shown in observations of stellar wind bubbles (SWBs) such as NGC 7635 (cf. Fig. 1.1, Walter 2000). These objects show the outer edge

Figure 1.1: NGC 7635, stellar wind bubble. The stellar wind from a massive star (BD-602522) pushes out region of the local interstellar medium forming the dense shell, or bubble seen here.

of a wind ploughing into the surrounding neutral gas and shock heating it. This process has serious implications for local star formation since any lower mass stars which were beginning to form in the neighbourhood of such a hot star will be affected. The nature of the effect is still a matter of some controversy. One argument is that a forming pre-stellar core is left with a reduced gas cloud from which to grow, thus leading to a change in the stellar population formed. Alternatively, the fast shock front of the expanding SWB can 'freeze-in' and exacerbate any perturbations and trigger star formation, therefore having the opposite effect of the former argument.

In this chapter we discuss the observational evidence for winds around astrophysical objects. The understanding of the observations is the chief reason and motivation for our theoretical study. There is still much which is unknown or at least only partly understood about the physical cause of the observed properties of stellar winds. At present theoretical models of winds are incomplete and are viewed very much by those working in the field as a work-in-progress. This is not to say that the models are simplistic, as we will show that the models are indeed highly detailed in accounting for many physical effects. However as with any mathematical or numerical model, compromises must be made in order to make the model practicable. In this thesis we examine perturbed wind models with the aim of understanding the behaviour of the flow and the interaction of the hydrodynamics and the driving mechanism. We will discuss the form of our models further in later chapters.

1.1 Observational evidence for a Solar wind

There is evidence for winds from astrophysical objects in every wave-band, however some evidence is more clearly attributable to the wind phenomena than others. The first observational evidence for a wind emanating from the Sun was in the study of cometary dynamics. A source of 'corpuscular radiation' (korpuskularstrahlung) from the Sun was proposed by Biermann (1951) to explain the dynamics of cometary ion tails. By the end of the decade Parker (1958) calculated that a fast outflow or *wind* could be driven by gas pressure. The driving in this case is only effective because of the high coronal temperature of the Sun. A much cooler corona will push the sonic radius of the wind much further from the star, making the mass loss rate and terminal velocity of the wind very low (in this case the outflow will be more dominated by effects such as rotation of the star and magnetic field).

This simple model gave results qualitatively similar to the observations available of the wind at the time, however once more detailed observations were made, it was realized that the Solar wind was much more complicated (e.g. Habbal et al. 1997). The complicated wind structure was observed by the space-crafts *Pioneer 10* and *11*, where abrupt changes in the speed of the wind were found at a distance of between 1 and 5 AU from the Sun (Hundhausen & Gosling 1976, Smith & Wolfe 1976). These fluctuations had a periodic 'saw-tooth' shape implying that they were persistently generated structures. A large number of these regions were found to have accompanying forward, reverse or forward/reverse shock pairs. This shows that there are two velocity components to the solar wind and these observations support the theoretical prediction that the two components interact. These, so called, Co-rotating Interaction Regions (CIRs) are formed by the interaction of high velocity ($> 500\mathrm{km\,s^{-1}}$) and low velocity ($\approx 100\mathrm{km\,s^{-1}}$) radial streams of gas. The base point of each radial stream changes because of the rotation of the Sun. The gas in a slow stream is hit by gas from a neighbouring fast stream which left the stellar surface later forming a shock front at the interface. These features are proposed

to explain observable features in the spectra of line driven winds which will be discussed further in § 1.4 and Chapter 6.

1.2 Studies of radiation driven winds

In this thesis we model winds driven by radiation pressure from both continuum and line radiation. In this section we discuss different models of radiation driven winds.

The phrases continuum and line driving refers to the form of opacity which dominates in the wind gas. Winds in both these cases are accelerated by the exchange of momentum between the continuum radiation from the central star (or a galactic nucleus in the case of AGN) and the gas in the photosphere (the theory behind this is discussed more in Chapter 2). For a continuum driven wind, the gas, or in the case of RSG and AGB stellar winds dust, absorbs radiation across the continuum of wavelengths present in the incident radiation field. Dust can be thought of as a macroscopic sphere which can absorb (and scatter) radiation at a wide range of wavelengths. However it is more effective at absorbing short wavelengths than long.

The metal ions present in the winds of OB stars can absorb photons which correspond to electronic line transitions within the ion. There are 3 factors which affect the magnitude of the line driving force. Firstly, the metal ions in the wind feel a strong force from line photons (momentum gained by an ion from absorbing a photon which pushes an electron into an excited state). The maximum force on a bound electron is a factor of 10^7 stronger than the force experienced by a free electron, because the bound transition is a resonance process. The number density of bound electrons in the ground state is a factor of 10^{-5} less than the number density of free electrons, making the resultant force on metal ions from line absorption a maximum of 100 times greater than the force from electron scattering (Gayley 1995). Secondly, this force on the metal ions is reduced by Self-Shadowing. An ion in the flow that lies in the shadow of another identical ion is shielded from the

Parameter	ζ Pup	P Cyg	WR1	RSG	AGB
Type	O4 f	B0 Ia	WN5	M	M or C
$L_\star/L_\odot$	7.9×10^5	7.2×10^5	1.0×10^5	$5 \times 10^4 - 5 \times 10^5$	$1 \times 10^3 - 5 \times 10^4$
$T_{\rm eff}$(K)	42,400	19,300	40,000	4000	3000
$R_\star/R_\odot$	17	76	2.2	$10^2 - 10^4$	$50 - 10^3$
$M_\star/M_\odot$	59	30	9	8-50	0.8 - 8
$\dot{M}(\mathrm{M_\odot yr^{-1}})$	2.4×10^{-6}	1.5×10^{-5}	6×10^{-5}	$10^{-6} - 10^{-3}$	$10^{-8} - 10^{-4}$
v_∞ (km s^{-1})	2200	210	2000	20-50	5-25

Table 1.1: Stellar characteristics for specific OB stars and typical values for RSG and AGB stars.

incident radiation and is driven less forcefully. The occurrence of this process across the wind leads to a net reduction in the acceleration of the metal ions. Hot stars are close to the Eddington limit[1], and the presence of resonance scattering without self-shadowing would push the atmosphere beyond this limit and it would be completely blown away. Self-shadowing is highly important to the stability of the wind. Thirdly, the velocity of the metal ions in the wind allows the incident stellar continuum radiation to be Doppler shifted to the correct resonance frequency for ions throughout the wind. In a monotonic flow a photon has a unique location in the wind where it falls inside the interaction region of a metal ion because of the Doppler shift. In a real wind gradient allows a single line to absorb photons over a much wider range than its thermal width, $\approx \nu_0 v_{th}/c$, where ν_0 is the line centre frequency in the stationary frame.

In Table 1.1 we show the physical characteristics for the various astrophysical objects which are subject to these driving mechanisms and Fig. 1.2 shows a labelled HR diagram indicating where the various types of star are located. Below we discuss the physical motivation for each of these driving mechanisms.

[1]The Eddington limit is the point where the force from electron scattering will exceed gravity and all of the stellar atmosphere will be blown away. For a star to be stable $\sigma_e L_\star/(4\pi c G M_\star) = \Gamma_e < 1$, where σ_e is the opacity coefficient for electron scattering (Lamers & Cassinelli 1999)

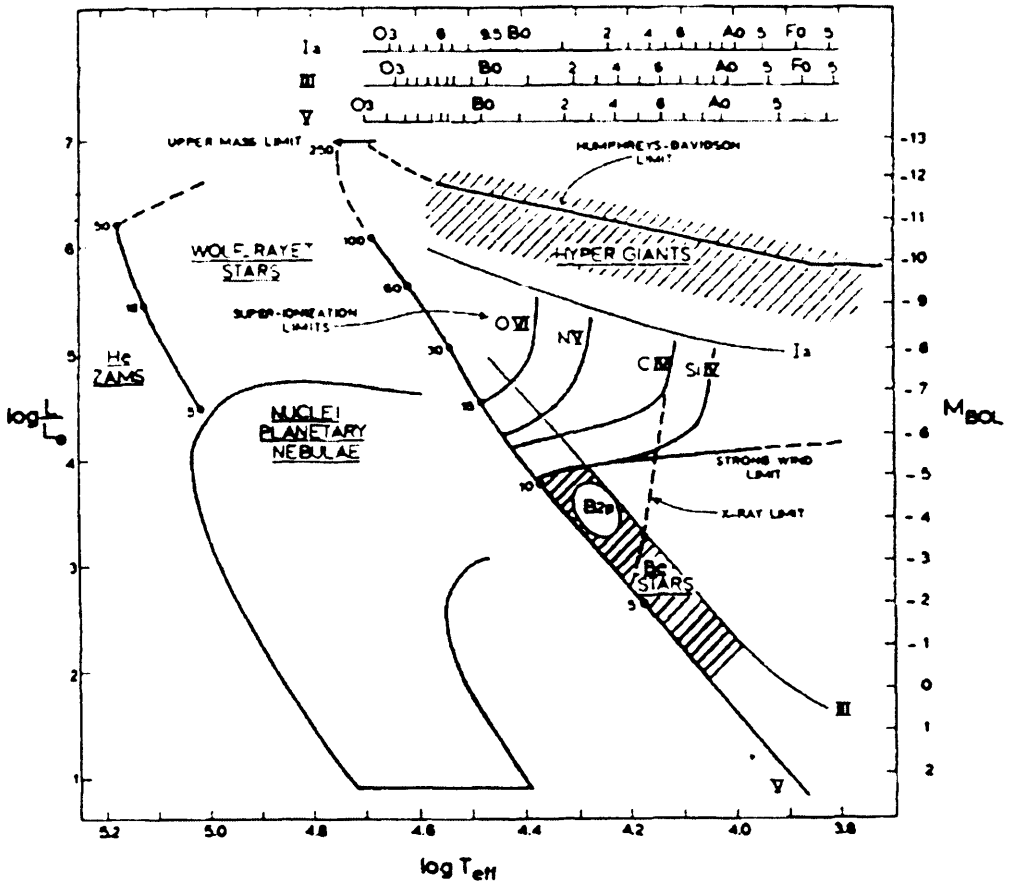

Figure 1.2: A Hertzsprung-Russell diagram (Cassinelli & Lamers 1987) displaying the limits of different regimes of stars with different spectral classifications. It labels the superionisation limits which indicates the range of effective temperatures of stars which show these high ionisation states.

1.2.1 Continuum driven winds

We can apply the term "continuum driven" to the winds from two vastly different astrophysical scenarios since they both have similar physical origin; the winds from close to the nucleus of a certain type of radio quiet AGN and the winds from Red Super Giant (RSG) and Asymptotic Giant Branch (AGB) stars.

The dynamics of the cool gas in and around AGN may be seen in the broad absorption-lines (BALs) of the spectrum of some radio-quiet AGN (Foltz et al. 1987; Turnshek et al. 1988). The variation in the BALs is attributable to high velocity clumpy structure, such as narrow Lyα emission. There are also, within the absorption troughs of various lines, regularly spaced components implying periodic wind structure, some of the observed features even appear to be travelling as fast as $\approx 0.2c$. This is a phenomenon which affects a small number of BALs so how much they represent the dynamics of gas around all AGN is uncertain.

The driving mechanism for AGN winds has been explored by many authors. The formalism of Falle et al. (1981) concentrates on a region of gas which has been swept up and shock heated by an expanding AGN wind bubble. This gas while at a high temperature is optically thin to the radiation field. However once the shock has passed, the shell begins to cool. As the shock front continues to propagate outward the expansion velocity decreases, decreasing the maximum temperature of the shock heating. As this region cools its opacity increases and the radiation field can couple to the gas with increasing effectiveness; the cooled gas behind the outer shock front is driven by the continuum radiation field. Falle et al. (1981) make various assumptions in their treatment in order to simplify the form of the driving to being proportional to the density ($g_{\rm cont}(r) \propto \rho(r)$; Röser 1979). The results of Röser (1979) support the use of a constant K since it is relatively insensitive to the ionisation state of the gas.

The interaction of the matter and radiation field in the AGN wind model is essentially an n^2 process, since the driving force is dependent on the recombination process. Although

the energy of the photon captured is important, the driving force is dependent on the number of recombination events because the gas is highly ionized.

An alternative astrophysical application of continuum driving is dust driven winds in AGB and RSG stars. These are stars close to the end of their lives. Their characteristics are very different from those of OB stars, having typical radii of $R \approx 150 - 1000 R_{\odot}$, terminal wind velocity $v_{\infty} \approx 30 \mathrm{km\,s^{-1}}$, and mass loss rates of $\dot{M} = 10^{-8} - 10^{-3} M_{\odot} \mathrm{yr}^{-1}$. The inflated stellar radius means that the photospheric temperatures of these stars decrease to $T \approx 2000 - 4000\mathrm{K}$. The low temperature and outflow velocity facilitate the formation of dust in the envelopes of such stars (Gail et al. 1984), but in addition to these there must also be high density regions which can arise from such events as large mass ejection. Yet the exact formation process of dust and how much is formed in stellar photospheres is still a matter of some controversy. The absorption of continuum photons by the dust grains, irrespective of their frequency, is the process by which the wind is driven in this scenario, thus the outflow is highly dependent on the number density of the dust grains.

We can model the dust driving force as being proportional to the density, $g_{dust} = K(T, \rho)$, but in doing so we must make many assumptions. The previous statement assumes that the gas/dust ratio is constant, which is certainly not the case, however the variation in the ratio is highly uncertain. The gas/dust ratio is affected primarily by the temperature (which is highly variable throughout the flow) and local hydrodynamical stability of the wind. This can be taken into account by making the proportionality constant a function of the state of the gas. Once dust is formed it is rapidly accelerated through the sonic point because of the increased opacity and therefore we assume that the dust generation is frozen at this point and the gas/dust ratio is constant. Other authors have modelled the evolution of dust driven winds in similar ways (cf. Feuchtinger et al. 1993).

In the rest of this work we will only use the AGN wind force model for calculations and comparisons with line-driving models.

1.3 Observational evidence for hot star winds

UV spectra

A prominent signature of line driven winds is the P-Cygni profile in the UV part of their spectra, named after the star which has a large number of these features. These profiles are formed around the scattering lines of metal ions present in the wind. Their structure is derived from the scattering of photons from the central star by the ions in the wind.

P-Cygni profiles

An understanding of the shape of P-Cygni profiles comes from an understanding of the radiative transfer mechanisms present in the atmospheres of hot stars that lead to their formation. Scattering is the important process in driving winds which appears in P-Cygni profiles as absorption of the stellar continuum radiation along the line of sight in front of the star and emission of photons scattered into the line of sight by ions from the wind halo (photons which were originally emitted by the star not along the line of sight).

If we were to look at the absorption and emission from one metal ion species only (e.g. C^{3+}, N^{4+}), we would observe the emission peak to be symmetrical, centred on the rest frequency of the resonant line and the absorption trough to be asymmetrical. The absorption extends from the line rest frequency, and since the part of the wind that generates this feature is directed toward the observer, the absorption from ions further out in the wind is Doppler blue shifted. In observed spectra there is a sharp cut off in the absorption trough at a particular velocity, beyond which there is very little absorption, even around strong lines, called the blue absorption edge. The maximum or *terminal* velocity for the gas in the wind occurs when the force of the driving has become negligible and the wind is carried by its own inertia. The emission peak is symmetrical about the line rest frequency, with emission that extends to the terminal velocity in both red

(receding) and blue (approaching) directions although the largest contribution is around the line centre or rest frequency (Lamers & Cassinelli 1999).

Consider a stellar atmosphere which has a species of ion X, which can undergo a bound transition with frequency ν_0 associated with it (in the rest frame of the ion). In a static atmosphere the absorption and emission of a line is symmetrical about ν_0. The line is broadened by many different effects but the predominant effect is the thermal motion of the gas which is modelled by a Maxwellian distribution. The emission peak and absorption trough are both broadened into a Gaussian shape with the standard deviation given by $\nu_0 v_{\rm th}/c$.

For ions in the atmosphere which are moving in respect of the stellar rest frame the Doppler effect becomes important as the component of the outflow velocity along the line of sight to a distant observer is Doppler shifted. The majority of emission comes from the area not along the line of sight to the star. This is illustrated in Fig. 1.3 by particles labelled 'b', 'c' and 'd'. The emission peak extends from $\nu_0(1 - v_\infty/c)$ to close to $\nu_0(1 + v_\infty/c)$ (gas travelling close to the terminal velocity away from the observer is obscured by the star) where v_∞ represents the asymptotic maximum value of the radial outflow velocity.

The absorption trough comes from ions which occult the stellar disc (i.e. particle labelled 'a') since the majority of these ions scatter photons out of the line of sight. This feature extends from ν_0 to $\nu_0(1 - v_\infty/c)$ since only out-flowing ions contribute to it. Generally speaking the strongest absorption comes from gas close to the star, which has the lowest radial velocity and highest density (if we assume that the wind is smooth and monotonic).

The P-Cygni profile is formed from the addition of these two components (strictly there is also a reduction in the red-shifted emission as some of the photons are scattered back to the stellar surface; cf. Fullerton 1997). The depth of the absorption trough and the emission peak are both affected by the strength of the line, due to the conservation

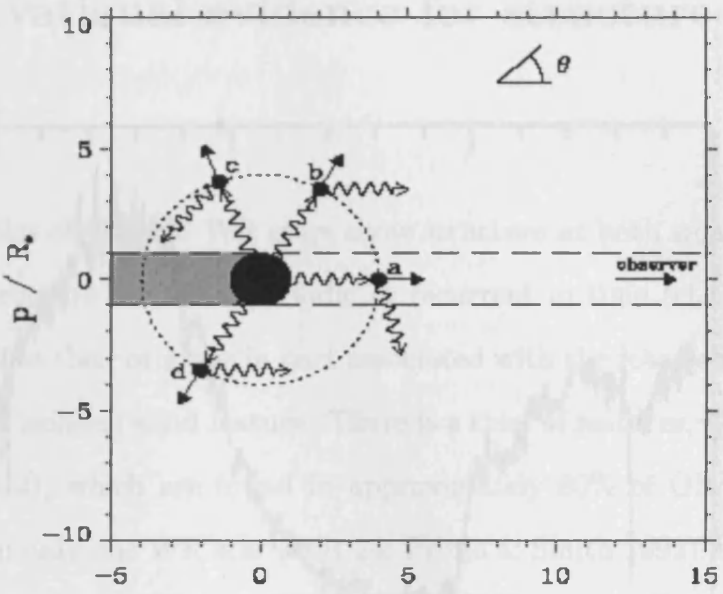

Figure 1.3: This schematic diagram shows 4 particles, labelled a, b, c and d which are at the same radial distance from the central star and radial velocity. Each of them has a different line of sight velocity in the observers frame. Particle a illustrates absorption along the line of sight, since it scatters light away from the observer. Particles b and d scatter light towards the observer which is seen as emission that is blue-shifted and red-shifted respectively. Particle c is not observed since it scatters light away from the observer. This is taken from Fullerton (1997).

of energy.

There are other indicators of the presence of winds and circumstellar material but we will discuss them more in the context of identifying structure in hot star winds in the following section.

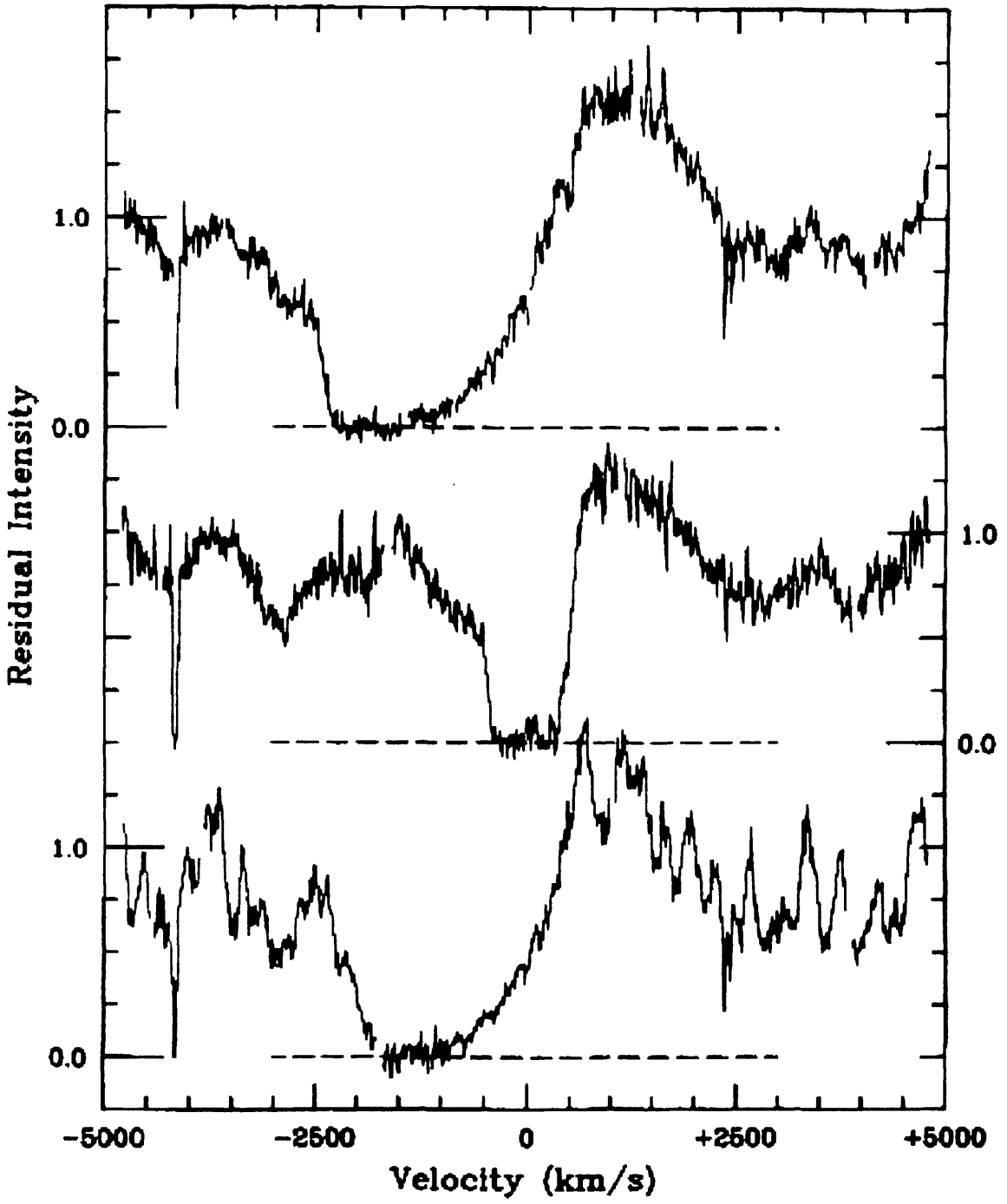

Figure 1.4: Examples of the P-Cygni profiles around the CIV resonance line doublet of three stars (top to bottom): ξ Per, HD 93521, μ Nor. This Figure was taken from Prinja & Howarth (1986).

1.4 Observational evidence for structure in hot star winds

The P-Cygni profiles of OB and WR stars show structure at both small and large scales. The large-scale structure are often periodic or recurrent in time (cf. Prinja & Howarth 1986) suggesting that their origin is in part associated with the rotation of the central star and not an entirely isolated wind feature. There is a class of features, Discrete Absorption Components (DACs), which are found in approximately 80% of OB stars (Howarth & Prinja 1989) but in only one WR star (WR 24; Prinja & Smith 1992), and slowly migrate across the UV spectra. An example of such structure is given in Fig. 6.8 where the DAC structure in ζ Pup can be seen to appear with strong regularity. From models of DACs the general behaviour is known to start as a relatively wide, low velocity absorption feature ($\Delta v \leq 0.5 v_\infty$, $0.2-0.4 v_\infty$) which gets narrower as it accelerates up to the terminal velocity. These models show that a DAC reaches a maximum column density (corresponding to a density enhancement of about a factor of 2 above the unperturbed wind solution) at $v \sim 0.75 v_\infty$. The column density gradually decreases as the feature approaches the blue edge of the profile (i.e. the terminal velocity). This slow advancement is frequently accompanied by variability in the blue absorption edge of the spectral feature. It is difficult to fully investigate the nature of the variations in the blue edge by observational means, since such strong variability can only be observed in strongly saturated lines whereas the DAC structure is best observed in weaker absorption lines.

In Fig. 1.4 the CIV profiles in ξ Per and μ Nor are shown (Prinja & Howarth 1986). Both show extended saturated regions (called a 'Black troughs') and blue edges which are 'softened' by a turbulent velocity dispersion about the terminal velocity.

In the spectra of hot stars there is also evidence for small scale structure. This is however not easily distinguishable from noise in the spectra and must be treated with caution. In high S/N observations of WR stars with good spectral resolution, Lépine &

Moffat (1999) suggest that small-scale, over dense wind structures are responsible for the numerous sub-peaks seen in the emission. Observations of 9 WR stars corroborated this hypothesis, but as yet only one O star has shown similar behaviour (Eversberg 1998). This was seen in He II λ4686 emission profile and the probable reason for this sparsity of data is that weak lines are difficult to observe. This matter is still controversial since the He II λ4686 is formed in the early part of the wind, $r \leq 1.5R_\star$, where the diffuse radiation field is most effective at damping oscillations in the flow (cf. §5.3 and Owocki & Rybicki 1985).

Photometry

There is extensive photometric evidence that the winds of single OB and WR stars contain dense clumps. Transient phenomena (with time scales of days-to-months) appear as variability in the polarization and are thought to originate from photospheric inhomogeneities. There is more variability in OB giants than in main-sequence OB stars. This variability is attributed to electron scattering from the surface of the dense clumps within the winds. Similar variability is also observed in $\sim 80\%$ of WR stars (Robert et al. 1989). Brown (1994) stipulates that these clumps emanate directly from the inhomogeneities in the photospheric flow unless they are optically thick or they can collapse from a more diffuse state on a wind flow time. We will discuss the behaviour of such clumps or perturbations to the flow in more detail in later chapters in both one and two dimensional flows (e.g. §3.5.1, 3.6, 4.6). At present the observations lack spatial resolution and we aim to expand the understanding of their physical behaviour through numerical simulations.

Radio and IR excess emission

Another fingerprint of circumstellar material (whether in a wind or static) is found in 'excess' radiation. This arises from free-free and free-bound interactions and is present in both the IR and radio bands. This is called an 'excess' because the radiation is in addition to that purely from the outer atmosphere (e.g. Lamers & Cassinelli 1999). Once the flux of excess emission is known, the mass loss rate can be calculated from it, provided that

the various parameters about the star and the stellar wind are also known (e.g. distance to the star and terminal velocity) and a model for the stellar wind can be constructed.

By comparing observations of infrared and radio fluxes it has suggested that there is structure in the inner wind of O stars. Runacres & Blomme (1996) compare time-independent stellar atmosphere models with observations in the radio and infrared. In their sample of 18 stars there is good agreement between theory and observations except in 4 cases. In these stars there is a higher than predicted flux in the far-infrared and sub-mm, while the radio observations remain as predicted. The optical depth of the free-free and free-bound emission is dependent on the frequency squared, so radio emission corresponds to a position further out from the star than IR emission. The emission is also proportional to the density squared, and so the emission is higher where is the wind is clumped. The results of Runacres & Blomme suggest that there is clumped structure in the inner part of the wind, while the outer part of the wind is smoother. These findings are supported by further work by Blomme et al. (2003) where they infer that structure persists in the wind out to $\approx 70R_{\star}$.

Thermal and non-thermal emission

Hot star winds have been observed to have both thermal and non-thermal radio emission, the latter attributable to Synchrotron emission from electrons accelerated to relativistic speeds in shocks. Thermal radio emission is generated from shocks between clumps in the wind. There is controversy surrounding the nature of shock generated radio emission. The presence and analysis of observations of radio requires detailed study of each individual case. It is uncertain as to whether the emission is primarily from instability driven shocks in the winds of single stars or from colliding wind binaries (cf. Dougherty & Williams 2000). There is clear evidence that non-thermal radio emission is found in various binary WR stars (e.g. Williams & et al. 1994, Setia Gunawan et al. 2000), although this, by no means, discounts the single star models.

X-ray emission

The *Copernicus* satellite made extensive observations of the winds around hot stars, such as τ Scorpii and ζ Puppis, to very high resolution ($\lambda/\Delta\lambda = 10^4$) over the range 1000 to 1450 Å. These observations made the controversial discovery that unexpectedly high ionisation stages are present in these winds. The entire range of observed O stars contains the OVI doublet (around 1040 Å) and the NV doublet (around 1240 Å). The presence of these ions in the winds of hot stars was from an effect dubbed 'superionisation' as discussed in Cassinelli (2002). The controversy of this discovery was that these ions were not expected because the photospheric emission was not thought to be hot enough to produce these high ionisation states. Various different theories were proposed to explain these surprising results (e.g. Lamers & Morton 1976 proposed a 'warm wind' model which requires a photospheric temperature $> 10^5$K). However, there was a problem when the observations did not match the theory. Nesting a cool wind on top of a hot corona should cause the x-ray emission to be strongly attenuated in the wind, but the presence of superionised states continued to be observed throughout the wind. Cassinelli, Castor & Lamers (1978) proposed a "corona plus cool wind" model. This proposes a thin corona similar to that proposed by Hearn (1975) with a temperature of a few 10^6K and a photosphere of ~60,000K. Due to the hot corona, this model allows the production of x-rays from the coronal gas which can be used to ionize the gas to some of the states observed. This idea was further developed by Cassinelli & Olson (1979) who argued that the superionisation effect is produced by the Auger effect, where an absorbed x-ray will cause certain ions to emit two electrons. This model also led to the prediction that OB stars would be significant thermal x-ray emitters.

The "cold wind plus corona" model only considers x-rays emitting from the corona, and not throughout the flow. The *Einstein* satellite and ROSAT showed that x-ray spectra significantly deviated from this model, which prompted Lucy & White (1980) to propose that shock structures in the winds were responsible for the additional x-ray spectral features. Further work by Kramer et al. (2003) suggests that instability generated shocks are

the origin of such x-ray emission. The shock heated gas can reach temperatures of 10^8K which is hotter than the maximum coronal temperatures and could explain the presence of high ionisation states throughout the wind, matching the observations. This x-ray emission from early type stars shows a flux which is almost constant with time. Cassinelli & Swank (1983) proposed that a roughly constant number of x-ray producing shell fragments is dispersed about the accelerating wind. More recently Feldmeier, Oskinova & Hamann (2003) have considered a 3D distribution of shock fragments. Their results are preliminary, but they indicate that as the optical depth of the shell fragments decreases, the x-ray profile tends towards that of a homogeneous wind.

Soft x-ray emission is good evidence for highly structured winds. Shock structure, which appears from collisions between dense clumps (Feldmeier, Puls & Pauldrach 1997) has been suggested as a source of these x-rays.

From all of these observations it is clear that OB and WR stars have highly structured winds. The origin of the structure is uncertain but in modelling the winds of such stars we will show the effect of physical perturbations, and how they respond to the driving mechanism. There is a wealth of information contained in observations of the winds of hot stars, which has fast become a many parameter problem to fit. Hydrodynamical simulations have an important part to play in the solution of the issues raised above as we will show in later sections. In the Chapters 2 and 5 we show the developments in the theory which allow us to model the behaviour of stellar outflows.

1.5 Thesis outline

The thesis is laid out as follows. In this introduction we have briefly discussed the major developments in stellar wind theory, the assumptions that are used in these models and the observations which are the motivation for such detailed models. Chapter 2 is concerned

with expanding on the theoretical development of stellar winds with particular attention to the formulation and evolution of the line-driving mechanism. We also give details of our approach to the calculation of the line driving force. Using this theoretical background, one dimensional calculations are performed which introduce the effect of the different driving mechanisms and allow comparison with the work of other authors is presented in Chapter 3. We move these models into two dimensions in Chapter 4, still using a plane parallel approach, to investigate further the stability of the wind to perturbations and the large scale effects these produce. In Chapter 5 we further develop our model of line driven winds by changing the line-profile function in the pure-absorption case and adding a line drag driving term to the pure-absorption case in an approximate way. We also apply a finite disc correction factor to model a wind with a subsonic inner boundary, which we use as the basis for a full SSF approach. In Chapter 6 we use the results from the two dimensional line-driving models to build synthetic P-Cygni profiles. From these we identify the various physical features which were observed in the density plots of Chapters 4 and 5.

Chapter 2

A theoretical background to stellar wind stability

2.1 Parker wind

Perhaps the simplest model for the structure of a stellar wind is that put foward by Parker (1958), who analytically calculated solutions for the isothermal coronal wind of the Sun. This achievement is significant since it shows that without any driving force other than ideal gas pressure, stellar mass loss can occur. As is shown below, the solar mass loss rate and terminal velocity of the wind produced are low, in comparison to young hot stars. However the fact that an average star in the middle of the main sequence of the HR diagram has a wind that expels $\approx 10^{-14} M_{\odot} \mathrm{yr}^{-1}$ is quite remarkable. At that rate the Sun jettisons the mass of an ocean going oil tanker every second!

This theory is analytically soluble and so provides an excellent place from which to begin a journey into different wind driving mechanisms. The Parker wind assumes the gas to be isothermal. This assumption is only sustainable in the early part of the wind, close to the star where heating and cooling have short time scales; as the wind material becomes more diffuse, the total contribution of all transport mechanisms becomes less

important and isothermality is no longer maintained. The outer wind requires a more advanced model to accurately simulate the physical situation. We do not include results far from the Sun and so use an approximate isothermal solution.

2.1.1 A stationary isothermal model

The Eulerian equations of hydrodynamics as shown by equations (A.1)-(A.3) can be written in the steady state, scalar form,

$$\rho v \frac{dv}{dr} = -\frac{dP}{dr} - \frac{GM_\odot}{r^2}\rho \tag{2.1}$$

Since the model is isothermal the energy equation can be expressed as

$$T(r,t) = \text{const}, \tag{2.2}$$

assuming that the temperature structure is maintained by detailed balance. The continuity equation in differential form is written (cf. equation(A.1)) as,

$$\frac{d}{dr}(\rho v r^2) = 0, \tag{2.3}$$

whose solution can be expressed in the following form,

$$\dot{M} = 4\pi\rho v r^2. \tag{2.4}$$

which defines the constant $\dot{M}$, the mass loss rate of the wind. In order to solve the above hydrodynamical equations we must impose an equation of state which relates the variation in gas pressure to that of the density. In this case and throughout this work we use the ideal gas law,

$$P = \frac{\mathcal{R}T}{\mu}\rho, \tag{2.5}$$

where $\mathcal{R}$ is the molar gas constant, μ is the molar mass of the gas (for the present case it can be taken to be the value for solar composition, $\mu = 0.602$, assuming complete ionisation) and T corresponds to the temperature of the gas.

The coronal temperature of the solar wind ($\approx 2 \times 10^6$K) is high in comparison to the winds of OB stars ($\approx 4 \times 10^4$K), which gives the solar wind a large isothermal sound speed,

$$a_0 = \left(\frac{\mathcal{R}T}{\mu}\right)^{1/2} = 525\,\mathrm{km\,s^{-1}}. \tag{2.6}$$

Using the isothermal equation of state, equation (2.5), we can write,

$$\frac{1}{\rho}\frac{dP}{dr} = \mathcal{R}\mu\frac{dT}{dr} + \frac{\mathcal{R}T}{\mu\rho}\frac{d\rho}{dr} = \left(\frac{\mathcal{R}T}{\mu}\right)\frac{1}{\rho}\frac{d\rho}{dr} \tag{2.7}$$

which can be used to remove the dependence of equation (2.1) on gas pressure. The dependence on density can also be removed using the continuity equation. The continuity equation, from equation (A.1) can be written,

$$\frac{1}{\rho}\frac{d\rho}{dr} + \frac{1}{v}\frac{dv}{dr} + \frac{2}{r} = 0 \tag{2.8}$$

which can then be used with the momentum equation (2.1) to give, after rearranging, the final equation describing the Parker wind in differential form and as shown by many authors (e.g. Lamers & Cassinelli 1999),

$$\frac{1}{v}\frac{dv}{dr} = \left(\frac{2a_0^2}{r} - \frac{GM_\odot}{r^2}\right) \Big/ \left(v^2 - a_0^2\right). \tag{2.9}$$

The solution of this can be obtained in closed form,

$$v^2 - 2a_0^2 \ln v = 4a_0^2 \ln r + 2\frac{GM_\odot}{r} + \text{const.} \tag{2.10}$$

From inspecting equation (2.9) it can be seen that there is a singularity when $v^2 = a_0^2$,

as the denominator reaches zero. This singularity is regularised when the numerator of the RHS also becomes zero.

Using the above model we introduce the concept of a critical point in the wind. In this case it is found at the isothermal sonic point, the point at which a wind moves from the *sub*-sonic to the *super*-sonic regime. The isothermal sonic radius is defined, from equation (2.9) by,

$$r_s = \frac{GM_\odot}{2a_0^2} \tag{2.11}$$

as the radius at which the velocity is equal to the isothermal sound speed a_0 as indicated above, thus both the numerator and denominator tend to zero at the same point.

The solution which passes through this critical point, the critical solution, is unique since it is the only physical solution which is subsonic close to the star and supersonic far from the star. Aside from this *trans*-sonic solution there is only one family of solutions which are also physical. These solutions begin subsonic, rise to a subsonic maximum at the sonic radius and decrease again further downstream. They have been termed Chamberlain breeze solutions (Chamberlain 1965) and their physical existence was the subject of some debate during the 1960's. The resolution came when it was discovered that the Sun had a two component wind with fast and slow regions. The fast wind, emanating primarily around the poles was believed to be driven according to the Parker model, while the slow wind, extending from the equatorial regions, lent credence to the Chamberlain breeze solutions (in reality the solutions are further complicated by surface features of the Sun and its magnetic field). Current theories propose that the fast wind emanates from the magnetic flux tubes.

The complete set of solutions to the Parker model are graphically represented in Fig.2.1. This type of solution topology is called 'x-type'. The trans-sonic critical solution is marked I and the breeze solution regime is marked with II. The remaining regions III, IV, and V are non-physical since they are either degenerate at some radius, require the wind to be at a very high velocity at the stellar surface, or both.

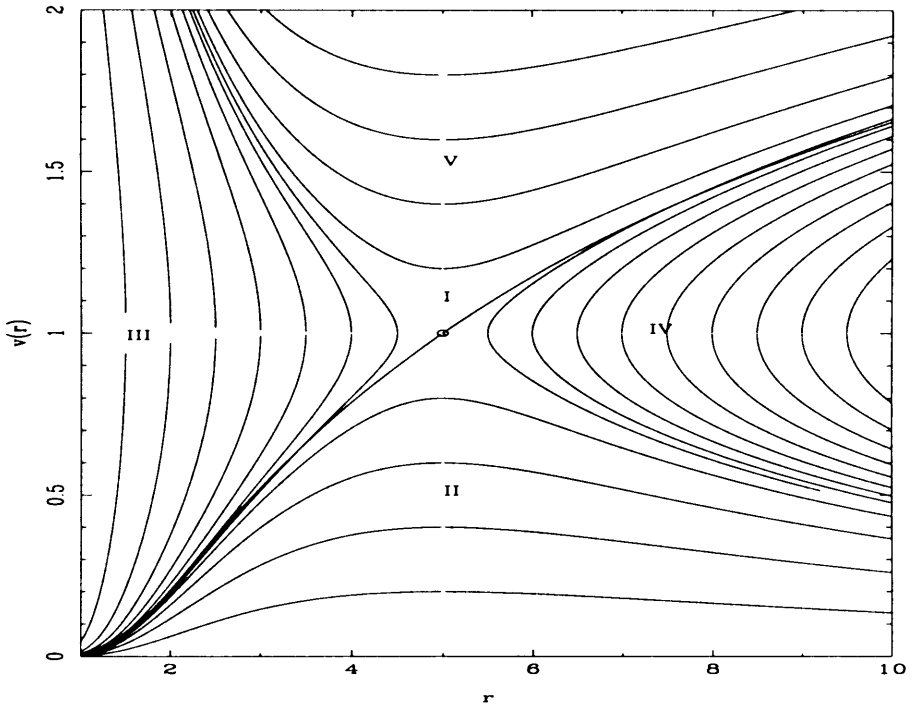

Figure 2.1: A plot of the velocity solutions for the Parker wind made using equation (2.9). The sonic point is located at $v = 1$, $r = 5$. Solar units are not used, since this plot is an illustration of the solution behaviour. The trans-sonic solution is labelled I and the Breeze solutions are in the region labelled II. The remaining non-physical solutions are labelled III, IV and V. Strictly there is another trans-sonic solution, where a branch from V joins a branch of IV at the critical point, which is the solution for an accretion flow onto the star.

The driving mechanism of this outflow from the Sun (Solar wind) is only gas pressure. The reason for this extreme effect is the high temperature of the wind gas. For an OB star with $T_{\rm eff} = 4 \times 10^4 K$ and $M_* = 50 M_\odot$, the sonic radius is $\approx 140 R_* = 2800 R_\odot$, whereas in the case of the Sun it is close to the surface, at $\approx 1.3 R_\odot$. The steep critical solution has a very short distance to pass through the sonic point in the Sun. If OB stars relied on gas pressure alone to accelerate them, their terminal velocities and mass loss rates would be very low.

2.1.2 Asymptotic Parker wind and the energy equation

In equation (2.10) we have given a solution for the Parker wind velocity law. As Fig. 2.1 shows there is degeneracy in the solution space and for that reason we have until now only considered the derivative form. To understand the asymptotic velocity solution better we return to equation (2.10).

The value of the constant in equation (2.10) can easily be determined from the critical point values $v_{\rm c} = a_0$, $r_{\rm c} = GM_\odot/(2a_0^2)$. Lamers & Cassinelli (1999) describe a solution that can be approximated to the asymptotic result,

$$v(r) \approx 2a_0\sqrt{r/r_0}, \tag{2.12}$$

for $r \rightarrow \infty$ and r_0 is the radius at the inner boundary (the position of the photosphere). This shows that the velocity can continue getting infinitely large further away from the central star, as $r \rightarrow \infty$, $v \rightarrow \infty$.

We can look at how much energy this solution requires to sustain such an expansion. The total energy for outflowing material (per unit mass) for an isothermal wind is given by,

$$e(r) = \frac{v^2}{2} - \frac{GM_\odot}{r} + \frac{5\mathcal{R}T}{2\mu}. \tag{2.13}$$

The first term is the kinetic energy, the second term is the gravitational potential energy

and the last is the enthalpy (total thermal energy, sum of the internal energy and the potential work done by adiabatic expansion). When $r \rightarrow \infty$ the gravity term vanishes, but the energy does not tend to a thermal equilibrium value, because of the kinetic energy term. From the asymptotic velocity, given in equation (2.12), we can see that in order to maintain the isothermal assumption the energy must increase to infinity.

Clearly, isothermality cannot be maintained out to infinity but in the region where all three terms in $e(r)$ are of the same order the approximation has some validity. This is satisfied in the inner portion of the wind where the effects of radiative heating and cooling do approximate to an isothermal balance.

2.2 Continuum driving

The astrophysical applications of continuum driving have two distinct but important branches, in modelling the acceleration of the winds from of AGB and RSG stars and Broad Absorption Line Quasars (BALQSOs). The force experienced by the winds of AGB stars is weak since the photon-absorbing dust experiences relatively low energy interactions with the radiation field of the star. However there is a plentiful supply of photons from the star, so what is lacking in the energy exchange in each photon capture event is in part made up for by the large number of such events. Dust is accelerated by the photons from the star and conveys this energy to the ionic component of the wind through collisions. The large cross section of dust grains makes this practicable.

Continuum driving is also applicable in a small region of the outflow from an AGN wind, where the wind ploughs into the ambient medium surrounding the AGN, shock heating the gas. The ionisation state of the shocked wind is too high for the radiation field to couple to the gas, but as the evolution continues the swept up gas radiatively cools and becomes optically thicker. It then has the ability to absorb radiative momentum and be accelerated. This region can now contribute to the absorption spectra, which is the observational motivation that Williams (2000) takes for studying structure formation in

this region from a perturbation.

The force per unit volume from this exchange of momentum from the continuum photons in BALQSOs is of the form $\rho g_{\rm rad} = K\rho^2$. The gas which is accelerated into a wind by the incident radiation from an AGN, is highly ionised. This produces a bottle neck in the wind acceleration process, since the ions must undergo recombination before any large scale driving can occur. A detail derivation of the continuum radiation force law can be found in Röser (1979). We present a simple treatment, by way of a plausibility argument.

From the ionisation balance equation for bound-free transitions,

$$\frac{F_{\rm cont}\sigma_{\rm cont}}{h\nu_{\rm cont}} n_{\rm H^0} = \alpha(T) n_{\rm e} n_{\rm p} \tag{2.14}$$

which says that the number of ionisation events is equal to the number of recombination events, per unit time (where the gas is completely ionized). The numerator of the LHS gives the rate at which energy is emitted from ionising H^0, where $F_{\rm cont}$ is the flux of continuum radiation, $\sigma_{\rm cont}$ is the average cross-section to continuum radiation of H^0 and $n_{\rm H^0}$ is the number density of H^0. From this we can express the force per unit mass for average continuum photons as,

$$g_{\rm cont} = \alpha(T)\frac{h\nu_{\rm cont}}{c}\frac{n_{\rm e} n_{\rm p}}{\rho} \tag{2.15}$$

$$= \alpha(T)\frac{h\nu_{\rm cont}}{c}\frac{1}{m_{\rm e} m_{\rm p}}\rho, \tag{2.16}$$

assuming the continuum photons to have an average momentum of $h\nu_{\rm cont}/c$. This assumes complete ionization which although not strictly the case in these AGN winds, is a useful approximation for this illustration.

The static momentum equation for this case is the same as the Parker model (cf. equation (2.9)) with the extra source term $g_{\rm rad} = K\rho$, which allows equation (2.9) to be

re-expressed as

$$\begin{aligned} \rho v \frac{dv}{dr} &= -a_0^2 \frac{d\rho}{dr} - \rho(g_{\rm grav} - g_{\rm rad}) \\ &= -a_0^2 \frac{d\rho}{dr} - \rho \frac{GM_*}{r^2} + K\rho^2. \end{aligned} \tag{2.17}$$

The value of the proportionality constant K is dependent on the ionisation state of the gas in the wind, the composition and the spectrum of the incident radiation. The value, $K = 10^{14}\mathrm{cm}^4\mathrm{s}^{-2}\mathrm{g}^{-1}$, is a typical value for a solar composition BALQSO (Kippenhahn, Perry & Röser 1974).

2.2.1 Critical point in radiation driving

In the case of the isothermal Parker wind model there is a critical point in the velocity solution which is aligned with the sonic point. We can investigate the effect of radiation driving on the topology of the wind using the continuum driving form of the driving force. The form of the radiation driving has been given above and the form of the momentum conservation equation for static solutions with a continuum driving source term is given by equation (2.17). We can re-write this equation, substituting for the density gradient using the continuity equation, in a similar manner to that of the Parker wind model (cf. §2.1.1 above), as follows

$$\frac{1}{v}\frac{dv}{dr} = \left(\frac{2a_0^2}{r} - \frac{GM_\odot}{r^2} + \frac{K\dot{M}}{4\pi v r^2}\right) \Big/ \left(v^2 - a_0^2\right). \tag{2.18}$$

From this equation we can see that the critical point appears where the numerator and the denominator of the RHS equal zero. Therefore this point can be written as,

$$r_{\rm c} = \left(GM_* - \frac{K\dot{M}}{4\pi a_0}\right) \Big/ 2a_0^2, \tag{2.19}$$

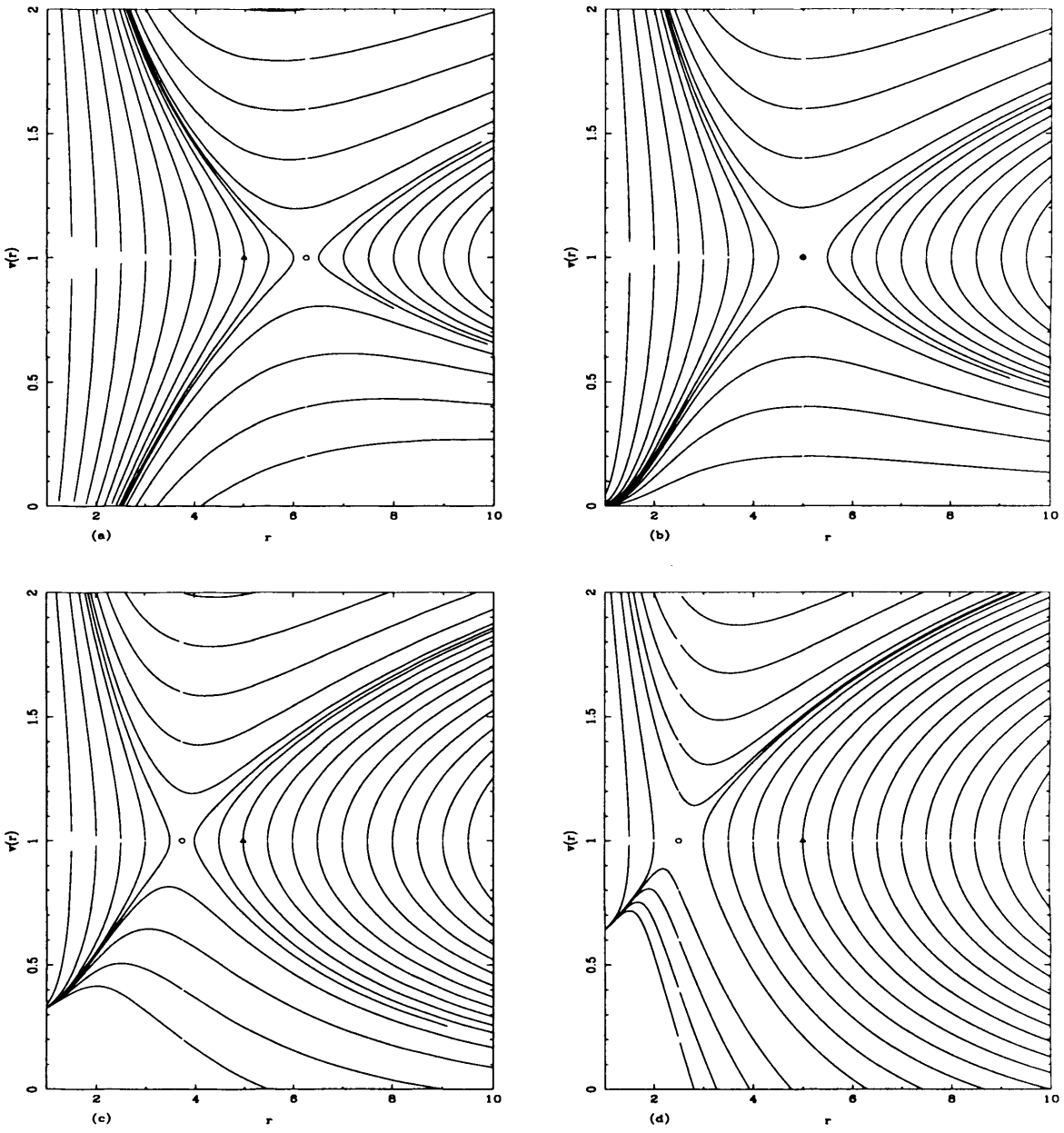

Figure 2.2: The effect of the value of driving constant K is illustrated in these graphs made by solving equation (4.1): (a) $\dot{M}$ is negative $K = 10^{14}\mathrm{cm}^4\mathrm{s}^{-2}\mathrm{g}^{-1}$, accretion flow, (b) $K = 0$, the Parker wind case, (c) $K = 10^{14}\mathrm{cm}^4\mathrm{s}^{-2}\mathrm{g}^{-1}$, continuum driven and (d) $K = 2 \times 10^{14}\mathrm{cm}^4\mathrm{s}^{-2}\mathrm{g}^{-1}$, strongly driven wind. In the cases which contain radiation driving, (c) and (d), the position of the critical point (denoted by a circle) retreats inward away from the isothermal sonic point at $r = 5$, $v(r) = 1$, (denoted by a triangle).

where $\dot{M}$ is the mass loss 4rate of the wind (which we approximate to a constant for the purposes of this illustration).

From equation (4.1) we generate the solution space shown in Fig. 2.2, substituting different values of K to reflect different regimes of interest. In Fig. 2.2(a) we show an accretion flow where a negative value for the mass loss rate.

The case where $K = 0$ is the Parker wind case, Fig. 2.2 (b), and its behaviour has been discussed above. The region where K is positive corresponds to continuum driven wind solutions. Figs. 2.2 (c)-(d) show that the effect of increasing the K parameter is to move the critical point closer to the stellar surface. Here, only the steeper solutions extend towards infinity and the shallower breeze solutions decelerate to zero velocity at a finite radius. In Fig. 2.2(d) the value of K is twice that of (c) and the increased driving force shows that the only physical solution which survives into the outer wind is the critical solution. The Breeze-like solutions in this case have sufficient momentum to be carried only a short distance from the star before reaching a maximum velocity (lower than the sound speed) then decreasing to zero.

In Fig. 2.2 the Parker critical point and the location of the radiative critical point are marked with a triangle and a circle, respectively. We assume that the mass, M_*, and the mass loss rate, $\dot{M}$, remain constant (except in Fig. 2.2(a) where we assume that the mass loss rate is negative). As the driving force (i.e. the value of K) increases the location of the critical point retreats towards the stellar surface. This forces the velocity at the stellar surface to a higher value and causes the Breeze-like solutions to have a shorter physical extent.

2.2.2 Stability of Continuum driving

Williams (2000) introduced a perturbing wave of the form $\exp(-i\omega t + i\mathbf{k}\cdot\mathbf{r})$ to the equillibrium wind solution. The form of the dispersion relation is,

$$\omega^2 = a_0^2 k^2 + ik_z/K\rho_0, \tag{2.20}$$

where $k^2 = \mathbf{k}\cdot\mathbf{k}$ and ρ_0 is the equillibrium density. Williams uses this to show that waves directed away from the source of the radiation (parallel to the photon path) have unstable growth rates with short wavelength modes being the most unstable. The unstable growth of the modes can be limited by the viscosity of the flow so that when shocks form the growth of the mode is halted.

2.3 Radiative line driving

Here we introduce the form of driving which will be the subject of the majority of this work, driving from scattering of line radiation. The scattering of radiation is the dominant process which drives hot star winds. OB and Wolf-Rayet stars can sustain fast, high mass loss rate winds because of their high luminosities, but also because of the strong coupling between the radiation field and the photospheric gas. This comes from the presence, in the photosphere, of metal ions with large cross-sections which can more readily absorb radiation from the star than the surrounding H and He ions. The mechanism which is responsible for all radiation driving is the exchange of momentum between the photons from the stellar radiation field and the material of the photosphere (in this case we assume the material to be gas of solar composition with no dust component). The highest amount of momentum absorbed by the ions is from a resonance line interaction since this effectively presents an increased ion cross-section to the incident radiation. The ions can absorb much more momentum from this interaction than from many free-free interactions. The frequency band of such an interaction is Doppler shifted by the

ion velocity. The strong resonance line self-shadows in frequency, saturating and hence reducing the effec of absorption. The velocity gradient shifts the ion in frequency out of the shadow of underlying similar ions, allowing much greater driving. OB stars are close to the Eddington limit ($\Gamma_e \approx 0.5$), if it were not for a third effect, Self-Shadowing, the stellar atmosphere would be completely blown away. Self-shadowing occurs when the radiation field incident on an ion is blocked by an identical ion in the upstream flow which decrease the global effect of the driving.

The radiation force is provided by the absorption of photon momentum ($h\nu/c$) within the resonant interaction region of an absorbing ion. An important factor in the absorption of radiation is the opacity defined as,

$$\chi(\nu, r) = \rho(r)\kappa_\nu, \tag{2.21}$$

which is dependent on the density ρ, and frequency dependent opacity coefficient κ_ν which is in turn dependent on the cross section of the absorbing species. The acceleration due to the absorption of radiation is a function of the optical depth τ_ν, which is the integral of the opacity along the line of sight,

$$\tau_\nu(r) = \int_{R_*}^{r} dr' \chi(\nu, r') = \int_{R_*}^{r} dr' \rho(r')\kappa_\nu. \tag{2.22}$$

The shape of the interaction region in frequency space ϕ_ν, for a particular line, can be factored out of the opacity coefficient as follows

$$\kappa_\nu = \phi_\nu \int_0^\infty \kappa_\nu d\nu = \kappa_l \Delta\nu_D \phi_\nu \tag{2.23}$$

where $\kappa_l \Delta\nu_D$ is the value of the total opacity averaged over the width of the line, $\Delta\nu_D = \nu_0 v_{th}/c$ is the thermal width of the line. The total opacity $\kappa_l \Delta\nu_D$ is not a function of v_{th} and therefore we expect that the opacity coefficient to be accompanied by v_{th}.

This is the case for a static atmosphere, since the atmospheres we consider here are winds we must include a Doppler shift term in the profile function. We change to a dimensionless frequency variable x, defined as

$$x = \frac{\nu - \nu_0}{\Delta\nu_D} \tag{2.24}$$

where ν_0 is the line centre frequency. Using this we can express the optical depth for a single line at a point z and dimensionless frequency in a non-static atmosphere as,

$$\tau_l = \kappa_l \int_{R_*}^{z} dz' \rho(z') \phi(x - v(z')/v_{th}) \tag{2.25}$$

where we have used $v(z')$ as the velocity at each point in the flow. The normalisation of the profile function is such that regardless of its form $\int \phi_\nu d\nu = \int \phi_x dx = 1$.

The acceleration from a single line can be expressed as the amount of momentum absorbed from the central star per unit mass,

$$\begin{aligned} g_l &= \frac{1}{c} \int_0^\infty \kappa_\nu I_\nu d\nu & (2.26)\\ &= \frac{\kappa_l \Delta\nu_D}{c} \int_0^\infty \phi_\nu F_{\nu_0} e^{-\tau(\nu)} d\nu & (2.27)\\ &= \frac{\kappa_l v_{th}}{c^2} \nu_0 F_{\nu_0} \int_{-\infty}^\infty \phi(x - v(z)/v_{th}) e^{-\tau(x)} dx, & (2.28) \end{aligned}$$

where we have replaced the frequency specific intensity with $I_\nu = F_{\nu_0} e^{-\tau(\nu)}$, expressing the attenuation of the flux of stellar radiation F_{ν_0} at frequency ν_0. For a particular line we can express variables in terms of the line centre frequency, however when we later derive more complete expressions we replace $\nu_0 \rightarrow \nu$ to emphasise that the relevent quantity is continuous in frequency.

2.3.1 Radiation driving of metal ions

Lucy & Solomon (1970) made detailed calculations of the contribution to the acceleration of a stellar wind from a single line transition. Their seminal work expresses how the potent force of the radiation driving is incompatible with a static atmosphere model, because it sets up a continuous mass outflow or wind. They show that for various different metal ions, the acceleration produced by the absorption of line radiation is large enough to accelerate the wind to a terminal velocity of $v_\infty \sim 3000\mathrm{km\,s^{-1}}$.

The mechanism which transfers the velocity of the accelerated ions to the bulk plasma (H^+, He^{2+} and e^-) is known as Coulomb coupling. This is an electro-static repulsion (or attraction in the case of e^-) between the metal ions and the other less massive, charged species in the wind. This phenomenon, first discussed by Lucy & Solomon (1970) and further developed by Lamers & Morton (1976) is responsible for dragging the bulk of the wind along with the driven ions. Recently studies have been done of low density stellar winds (for main sequence B stars) where the ion drift speed is higher than the thermal speed of the bulk plasma (Krticka & Kubát 2000, Owocki & Puls 2002). They observe the somewhat surprising result that there is not a separation of the ions and the bulk plasma as the ion velocity increases, but the acceleration of the wind as a whole moves onto a lower velocity solution.

Using the theory of Lucy & Solomon (1970), the first calculations of the mass loss rates and terminal velocities of hot star winds were made using a look-up table approach for the line opacities. The total line force from all contributing lines is calculated by solving the radiative transfer problem for each atomic transition and summing the contributions. This process is tedious but once the ionisation state of the metal ions in the wind is known the line opacity can be looked up from a table of calculated values. This requires knowledge of the species density in the wind as well as the ionisation state of the ions. Although the problem of calculating the exact state of the gas in the wind is highly complicated, Lucy & Solomon (1970) show that a few strong resonance lines alone can drive the wind to a

large terminal velocity but with a mass loss rate which was too small when compared to observational values.

2.3.2 The CAK power law approach and Sobolev approximation

In their work Castor Abbott & Klein (1975 - hereafter CAK) evaluate the line force multiplier (the relation between optical depth and line force) for the lines of C^{2+} (the resonance line and other weaker lines) for different temperatures. They find two important results: firstly that the contribution of only the resonance line to the force is a factor of approximately 100 times smaller than the sum of all the C^{2+} lines, and secondly the contribution of all the lines can be modelled by a power law of the optical depth. The force is not strictly modelled by a power law but CAK quote an accuracy of 1% for $T = 4 \times 10^4$K but the error increases away from this wind temperature.

Lamers & Cassinelli (1999) quote values for the three 'force multiplier' parameters, α, δ and k which produce velocity solutions that fit observed P-Cygni profiles cited in their work. For example, Lamers (1986) models the wind from P-Cygni using this line ensemble formalism taking values of $\alpha = 0.611$, $\delta = 0.046$ and $k = 0.114$. He uses these values as constants and successfully fits the observed wind parameters with variable opacity and wind temperature. For the purposes of our investigation the most important of these parameters is α which is the index of power law in optical depth from which the radiation force is calculated. The other parameters are related to the maximum opacity of the gas in the wind, in the case of k and to the geometric dilution factor (cf. Lamers & Cassinelli 1999), in the case of δ.

The expense of using the CAK model is that it assumes the flow velocity to be monotonic and the calculation of the line force to be entirely local (derived from the state of the gas at a specific radius). It relies on the Sobolev approximation of large velocity gradients to perform the above calculation of the line optical depth analytically. The Sobolev assumption simplifies this calculation by assuming that the line interaction region

is infinitely thin, $\phi(\nu) \rightarrow \delta(\nu)$. The optical depth for a single line then becomes,

$$\tau_s \approx \frac{\kappa_l v_{th} \rho}{|dv/dr|}. \tag{2.29}$$

The optical depth is independent of frequency since photons are absorbed at the (Doppler shifted) line centre frequency.

Using the Sobolev approximation the solution of equation (2.28) can be written as,

$$g_{sob} = \frac{\kappa_l v_{th}}{c^2} \nu F_\nu \left(\frac{1 - e^{-\tau_s}}{\tau_s} \right), \tag{2.30}$$

which reduces to

$$g_{sob} = \left(\frac{\nu F_\nu v_{th}}{c^2 \rho} \right) \left| \frac{dv}{dr} \right|, \tag{2.31}$$

in the optically thick limit (i.e. $\tau_s \gg 1$). In this limit the force is independent of the cross-section of the ions. This assumes that the stellar radiation is strongly absorbed by the wind, the bulk wind properties dominate over the microscopic state, such as gas particle size.

In the optically thin limit ($\tau_s \ll 1$) the acceleration can be expressed with

$$g_{sob} = \frac{\nu F_\nu \kappa_l v_{th}}{c^2} = g_{thin,0}. \tag{2.32}$$

In this limit every ion is susceptible to the full flux of the stellar radiation field, and therefore the driving depends on the ability of each ion to absorb photons, i.e. the line opacity coefficient.

The ratio of the thermal velocity to the velocity gradient, $\ell_s = v_{th}/(dv/dr)$, is called the Sobolev length. This is the length scale over which the flow velocity increases by a thermal velocity, and therefore the typical size of a region where the wind properties would change significantly. Where ℓ_s is small the velocity increases rapidly with radius (velocity gradient is large), which makes the line profiles appear narrow to the gas in the

flow. The Sobolev approximation is invalid when velocity gradients are small and should not be used to study the dynamics of processes with wavelengths smaller than the Sobolev length.

CAK extended the Sobolev approach by calculating the radiation force for an ensemble of lines, represented by a power law in optical depth. The total force from all the lines present in the wind of a star can be written in a form which is consistent with the rest of our notation,

$$\begin{aligned} g_{\rm CAK} &= \frac{\kappa_0 v_{\rm th}}{c}\frac{F}{c}\frac{\Gamma(\alpha)}{(1-\alpha)}\left(\frac{1}{\kappa_0 \rho v_{\rm th}}\left|\frac{dv}{dr}\right|\right)^{\alpha}, \\ g_{\rm CAK} &= g_{\rm thin}\frac{\Gamma(\alpha)}{(1-\alpha)}\left(\frac{1}{\kappa_0 \rho v_{\rm th}}\left|\frac{dv}{dr}\right|\right)^{\alpha} \end{aligned} \tag{2.33}$$

where F is the frequency integrated stellar flux, and the third term on the RHS is normalisation factor, related to the number distribution of lines. We have introduced an opacity term κ_0 which we will discuss in more detail later, but is related to the maximum line strength of an optically thick line in the wind. This term appears because we are no longer considering the force from a particular line but rather the force from an ensemble of lines, the distribution of which we will introduce later (cf. equation (2.38)).

In CAK, the term $g_{\rm thin}$ is the maximum amount of acceleration from the incident radiation field and is defined as

$$g_{\rm thin} = \frac{\kappa_0 F v_{\rm th}}{c^2}. \tag{2.34}$$

The index of the line distribution was in CAK an observationally fitted parameter, and reflects the contribution of optically thick lines to the line force.

The steady state equation for momentum conservation including the CAK force has the following form

$$\rho v\frac{dv}{dr} = -a_0^2\frac{d\rho}{dr} - \rho\frac{GM_*}{r^2}(1-\Gamma_{\rm e}) + \rho g_{\rm thin}\frac{\Gamma(\alpha)}{(1-\alpha)}\left(\frac{1}{\kappa_0 \rho v_{\rm th}}\left|\frac{dv}{dr}\right|\right)^{\alpha} \tag{2.35}$$

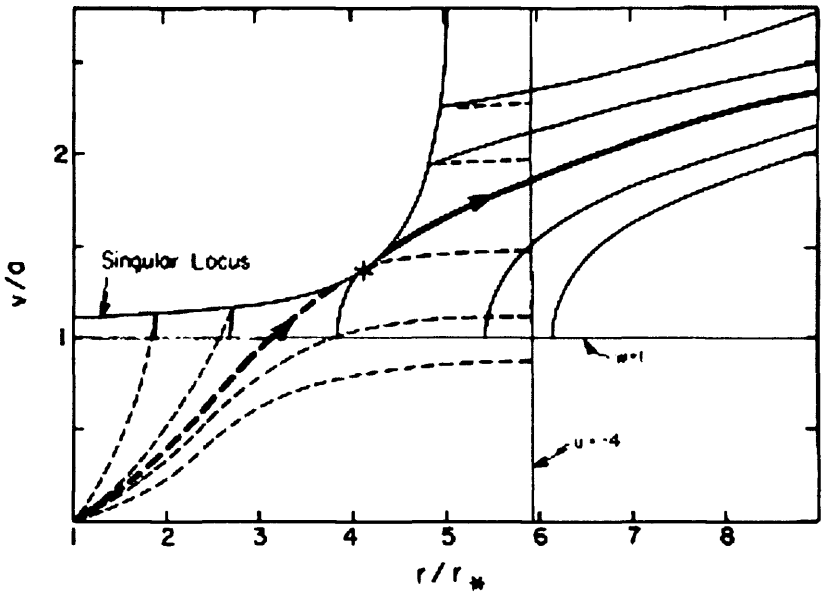

Figure 2.3: This is a reproduction of the CAK wind solutions using the physical parameters of Abbott (1980). The bold dashed line and the bold solid line demonstrate how these two solutions are married together to make the continuous trans-sonic solution at the singular point, marked +. Also displayed are other possible solutions, alternatives to the unique smoothly trans-sonic solution. In our numerical method we are not concerned with the unique trans-sonic solution but choose any super-sonic solution as the subject of our research, since the family of super-sonic solutions (represented by the solid curves) all have the same response to the line driving (we relax this assumption in Chapter 5).

which breeds a family of solutions, of which the critical solution is a composite of two solutions, as can be seen in Fig. 2.3. The trans-sonic solution can be altered from the true critical solution if these conditions are not met and the sub-sonic solution can pass on to a neighbouring super-sonic solution at the critical point. This becomes a problem if the super-critical solution taken falls in the forbidden region (a range of nonphysical solutions, analogous to the Parker wind solutions marked III and V in Fig. 2.1). A lump of gas that follows a forbidden solution will find that in the forbidden region it decelerates, colliding with material upstream of it, which shocks the gas onto a different solution branch. This behaviour does not necessarily shock the gas onto the trans-sonic solution, and the process may repeat many times before the critical solution is found.

By using equation (2.35) for the momentum equation, the regularity and singularity conditions give a simple relation for the velocity gradient at the critical point, viz.,

$$v'_{\rm c} = \frac{v_{\rm c}}{r_{\rm c}}, \tag{2.36}$$

which can be used to derive an expression for the value of the velocity at the critical radius,

$$v_{\rm c}^2 = a_0^2 + \left(\frac{1}{1-\alpha}\right)\left[\frac{GM_*(1-\Gamma_{\rm e})}{r_{\rm c}} - 2a_0^2\right], \tag{2.37}$$

where a_0 is the sound speed, showing that for $\frac{GM_*(1-\Gamma_{\rm e})}{r_{\rm c}} \neq 2a_0^2$, the critical point is supersonic and not aligned with the sonic point.

2.3.3 Pure absorption non-Sobolev approaches

A further development in the model and understanding of the theory of line driving in winds came from the development of a non-Sobolev approach by Owocki & Rybicki (1984, 1986) and pure absorption theory in Owocki, Castor & Rybicki (1988; hereafter OCR). This approach considers the pure absorption case of the radiation/metal-ion coupling (as does the CAK formulation) but uses a line-profile function that more accurately represents

its shape of the function with a Gaussian function. As a consequence of this move away from the Sobolev approximation the full integral form of the optical depth must be used in the calculation of the radiation force and the force is no longer a calculation from local variables. Their approach still considers the distribution for the participating lines as a power law of the opacity of each line, and thus making the driving acceleration a power law of the optical depth in the flow.

The line-profile function is particularly shaped by two physical effects; the thermal motion of the gas and the uncertainty in the energy of the particles. The thermal state of the gas is assumed to be modelled by a Maxwellian distribution, which is a Gaussian function of frequency, in the ion rest frame (called Doppler broadening of the line profile). The de-excitation energy from a particular level can be thought of as a damped harmonic oscillator where the energy is distributed as a Lorentz profile (called Natural broadening) with much smaller width than the Gaussian profile, for a high temperature plasma like a stellar atmosphere. The correct form of the line profile function is therefore a convolution of a Doppler and a Lorentz profile, which is referred to as a Voigt profile. Owocki & Rybicki (1984) discuss the use of a Voigt profile and note that although it more correctly calculates the radiation absorption in the Lorentz wings of the frequency distribution (the blue absorption edge), the Gaussian profile fits the majority of the frequencies that are affected. There are other mechanisms which can affect the shape of the profile function, such as collisional broadening or non-thermal motion (e.g. turbulence).

The CAK treatment of the line force is very useful since it provides a system of ODEs which can be integrated to find static velocity-solutions or used in conjunction with a full hydrodynamical code to investigate the time varying behaviour. The notion of calculating the optical depth of the gas from local conditions does have its limitations. The wind is assumed to be optically thin and the flow wvariables to be constant on scales smaller than the Sobolev length, thus making such small scale disturbances unstable. In the CAK model the wind experiences growth rate instabilities on scales larger than the Sobolev

length, which does not lead to the highly structured winds that are seen in non-Sobolev models.In this section we outline an approach to the calculation of the acceleration due to line radiation which is not dependent on the Sobolev approximation, but calculates the optical depth from the global state of the wind.

OCR found an approximation to the radiation driving provided by all lines by assuming that the line opacity distribution could be written in terms of the opacity coefficient only by integrating it over frequenc

$$N(\kappa) \equiv \int_0^\infty d\nu \left(\frac{\nu F_\nu}{F}\right) N(\nu,\kappa)$$

$$N(\kappa N(\kappa) = \frac{1}{\kappa_0}\left(\frac{\kappa}{\kappa_0}\right)^{\alpha-2} \exp(-\kappa/\kappa_{\max}), \quad (2.38)$$

$$N(\kappa) = \frac{1}{\kappa_0}\left(\frac{\kappa}{\kappa_0}\right)^{\alpha-2} \exp(-\kappa/\kappa_{\max}), \quad (2.39)$$

including an exponential cut-off ($\exp(-\kappa/\kappa_{\max})$) at the high opacity end of the number distribution. This limits the maximum strength of the line force, which is necessary because the number distribution becomes invalid at the low number density end. The value of $\kappa_{\max}$ should be close to the maximum line strength κ_0 but in numerical calculations it is typically set to a much lower value (Runacres & Owocki, submitted 2004, addresses the issue of using the higher, more realistic value of $\kappa_{\max}$).

The total line force from all contributing lines can be found by using this number distribution with equation (2.28),

$$g_{\rm rad} = \int_0^\infty d\kappa \int_0^\infty d\nu N(\kappa,\nu) g_{\rm thin,0} \phi_\nu e^{-\tau(\nu)}, \quad (2.40)$$

$$= \int_{-\infty}^\infty dx \int_0^\infty d\kappa N(\kappa) \frac{\kappa v_{\rm th}}{c^2} F \phi_x e^{-\tau(x)}$$

$$= \frac{\kappa_0 v_{\rm th}}{c^2} F \Gamma(\alpha) \int_{-\infty}^\infty dx \frac{\phi(x - v(z)/v_{\rm th})}{[\kappa_0/\kappa_{\max} + \tau(x,r)]^\alpha}, \quad (2.41)$$

where $\Gamma(\alpha)$ is the complete gamma function. This is essentially a re-expression of the CAK force except with a factor $\kappa_0/\kappa_{\max}$. Previously we considered only 1 line with opacity $\kappa_1\rho$,

we now use the opacity coefficient as a variable and replace the term κ_l with κ. The number of lines with opacity coefficient κ, which contribute to the force is given by the number distribution $N(\kappa)$.

Assuming that the underlying continuum radiation is approximately constant over the line absorption band, the radiation acceleration is given by

$$g_{\rm rad}(r) = g_{\rm thin}\frac{\Gamma(\alpha)}{\kappa_0^\alpha}\int_{-\infty}^{\infty} dx \frac{\phi(x - v(r)/v_{th})}{(\eta(x,r) + 1/\kappa_{max} + \phi(x)/\sigma_e)^\alpha}\ , \tag{2.42}$$

where x is the frequency displacement from line centre for gas at rest with respect to the star, in units of the line width, $\Delta\nu_{\rm D}$ and $\sigma_{\rm e}$ is the Thompson electron-scattering coefficient. The lines are Doppler shifted by the local velocity, $v(r)$ of the stellar wind. We have also included a reversing layer term in the above expression, which represents the shape of the photosphere $F(r)e^{\phi(x)/\sigma_c}$.

As mentioned previously α is measure of the contribution of the optically thick line to the total force. For example, if $\alpha = 0$ the contribution to the line force is entirely from optically thin lines ($g_{\rm rad} = g_{\rm thin}$), whereas for $\alpha = 1$ the contribution to the line force from optically thick lines dominates over that from optically thin lines. Non LTE calculations of the contribution of different optical depth lines favour a value of $\alpha = 0.65$ (Pauldrach, Puls & Kudritzki 1986) and we use a value of $\alpha = 0.7$, used in many hydrodynamical calculations (e.g. OCR, Feldmeier et al. 1997).

The function $\eta(x,r)$ is the ratio of the optical depth at x to the opacity coefficient,

$$\eta(x,r) = \frac{\tau(x,r)}{\kappa} = \int_{R_*}^{r} dr'\rho(r')\phi\left(x - \frac{v(r')}{v_{th}}\right). \tag{2.43}$$

and can be thought of as a profile weighted column density from the photosphere to a point r in the wind.

This formulation of the radiative force is similar to the CAK expression of the line force except no assumptions are made about the line interaction region, leaving the form

of the profile function undefined. If we replace the general profile function with a delta function equation (2.43) becomes,

$$\eta(x,r) = \int_{R_*}^{r} dr' \rho(r') \delta \left(x - \frac{v(r')}{v_{th}} \right), \tag{2.44}$$

which can be solved by changing the integration variable, $u(r) = v(r)/v_{\rm th}$,

$$\eta(x,r) = \int_{u(R_*)}^{u(r)} du \, \frac{\rho(u)}{du/dr'} \delta(x-u). \tag{2.45}$$

$$\left(= \sum_{r'<r:u(r')=x} \rho(r') \frac{v_{\rm th}}{|dv(r')/dr'|} \right) \tag{2.46}$$

In some circumstances usefully expressed as the above.

This is an expression of the profile weighted column density and when multiplied by the opacity coefficient, κ_0, is the Sobolev optical depth. This reinforces the fact that the Sobolev optical depth is constructed about the assumption of an infinitely thin line interaction region. This can then be used in equation (2.42) to find the CAK formulation of the line force. Replacing the general profile function of equation (2.42) with a delta function and using the form of η derived above we can show,

$$\begin{aligned} g_{\rm rad}(r) &= g_{\rm thin} \frac{\Gamma(\alpha)}{\kappa_0^\alpha} \int_{-\infty}^{\infty} dx \frac{\delta(x-u(r))}{[\eta(x,r)+1/\kappa_{\rm max}]^\alpha}, \\ &= \frac{g_{\rm thin}}{(1-\alpha)} \frac{\Gamma(\alpha)}{\kappa_0^\alpha} \frac{1}{\eta(x,r)^\alpha}, \\ &= \frac{g_{\rm thin}}{(1-\alpha)} \Gamma(\alpha) \left(\frac{1}{\kappa_0 \rho v_{\rm th}} \left| \frac{dv}{dr} \right| \right)^\alpha, \end{aligned} \tag{2.47}$$

where we assert that there is no limit on the maximum number of optically thick lines, and set $1/\kappa_{\rm max} = 0$ as do CAK. We assume the that the flow is smooth so that the opacity at each point in the flow is unique. The CAK formulation allows the wind to be strongly accelerated as the gas gets optically thinner until $\tau \to 0$ and $g_{\rm CAK} \to \infty$.

Following OCR we write the force per unit mass in terms of the radiation pressure,

which in plane parallel geometry is given by

$$\rho g_{rad} = -\frac{d(P_{rad})}{dz} \tag{2.48}$$

$$P_{rad} = -\frac{g_{\rm thin}}{(1-\alpha)}\frac{\Gamma(\alpha)}{\kappa_0^\alpha} \times \int_{-\infty}^{\infty} dx \left[\eta(x,r) + \frac{1}{\kappa_{max}} + \frac{\phi(x)}{\sigma_c}\right]^{1-\alpha} . \tag{2.49}$$

The above neglects the effects of re-emitted or scattered radiation which is assumed to be globally isotropic. One important effect is the 'line-drag' phenomenon, described by Lucy (1984). This reduces the growth of small-scale velocity perturbations and is particularly important in the inner wind. This is revisited in Chapter 5 in more detail.

2.3.4 Stability of the non-Sobolev driving

A feature of line-driving which is of extreme importance is instability. The Line De-shadowing Instability (LDI, Feldmeier 1995), first hinted at by Milne (1926), is particular to the non-local nature of the driving, and is an affect of a real flow being non-monotonic. A clump of gas in the downstream flow is shaded from the stellar radiation field at a particular frequency by an upstream clump. The clump decelerates relative to its upstream counterpart, moving out of the shadow, and receives unattenuated stellar flux. The acceleration that the clump feels is due to the 'de-shadowing' instability.

Initial studies of the instability appeared to have conflicting findings due the fact that they were looking at two different regimes (e.g. Carlberg 1980, Abbott 1980, Owocki & Rybicki 1984). We now understand that the driving force is unstable to small wavelength optically thin perturbations.

A detailed study of the stability of this formulation was performed by Owocki & Rybicki (1984; hereafter OR84). The controversy surrounding this subject was resolved by Owocki & Rybicki when they showed that the wind solutions were both stable and

unstable, in different regimes. They expand the line acceleration

$$g_{\rm rad}(z) = g_{\rm thin} \int_{-\infty}^{\infty} dx \phi(x - u(r)) e^{-\tau(x,r)} \tag{2.50}$$

at an arbitrary mean flow point (denoted by a subscript, 0) the optical depth and velocity are perturbed, $\tau(x,r) = \tau_0 \Phi(x) + \delta t$, where $\Phi(x) = \int_x^{\infty} dx' \phi(x')$ and $v = v_0 + \delta v$. Using a form for the velocity perturbation that is a sinusoidally varying function of height, $\delta v(z) \sim e^{ikz}$, OR84 obtain the following relation,

$$\begin{aligned} \frac{\delta g}{\delta v} &= iK\omega_0\tau_0 \int_{-\infty}^{\infty} dx \phi(x) \exp[-\tau_0 \Phi(x)] \\ &\times \int_x^{\infty} dx' \phi(x') \exp[-iK(x' - x)], \end{aligned} \tag{2.51}$$

where $K = k\ell_{\rm s}$ is the perturbation wavenumber in units of the Sobolev length, $\omega_0 = g_{\rm thin}/v_{\rm th}$ is the amplification rate. We cite this with little justification to display the form that the ratio of the perturbed acceleration to the perturbed velocity takes. An important point is that this quantity (and the stability of the wind) depends on the form of the profile function as well as on perturbation wavenumber and line optical depth. However when considering an optically thick line an analytical approximation can be obtained. After some manipulation OR84 derive the form,

$$\frac{\delta g}{\delta v} \approx \omega_{\rm b} \frac{ik}{\chi_{\rm b} + ik} \quad (\tau_0 \gg 1), \tag{2.52}$$

where the line strength (opacity defined at the blue edge of a line) is $\chi_{\rm b} = \kappa_0 \rho_0 \phi(x_{\rm b})$ and the amplification rate is $\omega_{\rm b} = \omega_0 \phi(x_{\rm b})$ and $x_{\rm b}$ is the location of blue edge of the profile function in frequency in space.

This is a useful asymptotic analytical result which shows [OR84, Fig.1a] that in this optically thick limit, high wave-numbers are highly unstable (Carlberg 1980) and low wave-numbers are more stable (Abbott 1980). We can further explore the stability of the

wind by replacing the general profile function with a specific function. A natural first approximate form for this is a top-hat or box profile function which OR84 define as,

$$\phi(x) = \begin{cases} 1, & |x| < 1/2 \\ 0, & |x| > 1/2 \end{cases} \tag{2.53}$$

From this they show that the optically thin limit is,

$$\frac{\delta g}{\delta v} \sim \tau_0 \quad (\tau_0 \ll 1) \tag{2.54}$$

which means that the perturbed force produced from a velocity perturbation tends to zero; the slight Doppler shift produced by a shift of δv away from the mean flow velocity does not change the acceleration from optically thin lines. In the limit of optically thick lines, OR84 derive,

$$\frac{\delta g}{\delta v} \approx \omega_0 \frac{ik}{\chi_0 + ik} \quad (\tau_0 \gg 1), \tag{2.55}$$

which is the same as the form for a general profile function, except that the amplification rate and the line strength take the mean flow values; the value of the profile function at the blue absorption edge is the same as at the profile centre. The top-hat form of the profile function overestimates the line force and consequently is more unstable than a Gaussian profile function at this point. However the two profile functions have comparible values around the line centre (both the functions have reached a maximum).

These results show that in the optically thin limit the force is stable since the perturbed acceleration tends to zero. In the optically thick limit, the wavenumber dependence makes it unclear as to whether there is stability or not. Considering short wavelength perturbations, $k \gg 1$, equation (2.55) reduces to $\delta g/\delta v \sim \omega_0$, which shows that in this limit the perturbed force is unstable and grows in direct proportion to the amplification

rate. For a long wavelength, $k \ll 1$, optically thin line equation (2.55) reduces to,

$$\begin{aligned} \frac{\delta g}{\delta v} &\sim ik\frac{\omega_0}{\chi_0} \\ \delta g &\sim \delta v'. \end{aligned} \tag{2.56}$$

This demonstrates that the stability of a perturbation is highly dependent on its wavenumber and its optical thickness.

2.3.5 The diffuse radiation field

This pure absorption approach is further improved upon by the treatment of a scattered or diffuse radiation field. The scattered radiation produces a force which is not isotropic over a small distance, called Line Drag (Lucy 1984). Lucy describes this force as being "due to emission from scattering ions throughout the flow. Because these ions are everywhere receding from an observer moving with the unperturbed flow, the diffuse component to the radiation field is seen by this observer to start abruptly (in the narrow-line limit) at the line rest frequency and to extend to lower frequencies. Consequently, ions in an optically thin blob which moves relative to the adjacent unperturbed flow find themselves radiatively coupled to some ions ahead of the blob but not to any of those in its wake. Thus the blob sees a negative flux of line photons and experiences a radiative drag" (Lucy 1984).

Owocki (1991) introduces a hydrodynamical approach to the line drag, thus improving on the pure absorption approach of OCR and subsequent work. His treatment makes the simplifying assumption that the radiation field source function is smooth, in the sense that there is no detailed feedback between it and the diffuse field. As in the case of the pure absorption approach (OCR) the flow is dominated by reverse shocks (where a high speed, low density gas decelerates into slow, dense downstream gas forming a shock), but the stability of the wind solution is generally increased.

The Smooth Source Function (hereafter SSF) method, developed by Owocki (1991), consolidates the pure absorption formulation of OCR and introduces the line drag force. The OCR method calculates the line driving force in a more hydrodynamically consistent fashion than the CAK approach, but it produces a velocity solution which has a greater slope than would be obtained by using the CAK approach. This is a limitation since for a steady flow, the CAK method reproduces observations well. The SSF approach, although it has at its heart a detailed calculation of the optical depth (similar to OCR), produces time averaged solutions which more closely reproduce the results of CAK. This approach is later improved upon to take a more detailed account of second-order effects in the diffuse radiation field. Owocki & Puls (1996) develop an Escape Integral Source Function (EISF) approach which replaces the assumption that the source function is smooth with a description of the source function that reflects the variation in the local state of the photospheric gas. This model more realistically describes the physical processes in the wind and produces time averaged results which a closer to those of CAK, than the results of the OCR and SSF methods. We will discuss SSF more in Chapter 5.

2.3.6 An alternative approach to optical depth calculation

A major problem when using a numerical method to solve this form of the radiation driving is the double integral required to evaluate equation (2.49). This is computationally demanding to calculate directly. However, at any position the transmitted spectrum will only change over a small range of offsets x around the value for the local mean flow, and the radiation driving can be obtained from the momentum of just these absorbed photons. The force calculation can therefore be speeded up considerably by storing the local scaled optical depth $\eta(x)$, and advancing it by a method of short-characteristics.

The form of the profile function has little effect on the radiation driving force on scales larger than the Sobolev length, since at these scales the profile appears to be a delta function. As we find (and as has been seen in previous work, e.g. OCR, Feldmeier

1995, Runacres & Owocki 2002), the growth of instabilities soon leads to smooth flow regions which are separated by strong shocks and high-gradient rarefactions in which the Sobolev length will not be resolved by the numerical grid. In these latter regions, discretisation errors in the hydrodynamical scheme will probably be at least as important as errors due to our approximation to the line profile function, and so it seems reasonable to use a top-hat profile function in this first treatment.

This may be generalised by approximating a Gaussian profile by multiple top hat functions, or by higher order approximations such as triangular functions. While a top-hat profile function is adequate for use in an initial calculation, the effect of other, more physical profile shapes is further investigated in Chapter 5. The formulation presented here remains independent of function shape, to maintain generality.

At each point in the flow, the reduction in the radiation field due to the optical depth must be determined in order to calculate the radiation force, from equation (2.48) and equation (2.49). However we start by considering the radiation field at just one cell of interest. The calculation of equation (2.49) for a particular cell reduces to differencing the values of the radiation pressure at the interfaces of the cell,

$$P^i_{\rm rad} \propto \int_{x2}^{x_1} dx \left[\eta(x,z) + \frac{1}{\kappa_{\rm max}} + \frac{\phi(x)}{\sigma_c}\right]^{1-\alpha}, \tag{2.57}$$

where $\eta(x,z)$ is the profile weighted column density which is the amount of radiation absorbed by the wind up to the point z.

Numerically a bottle-neck is caused by the calculation of the profile weighted column density, $\eta(x,z)$. We present here a method for solving this which does not require a complete integral over the independent distance variable to be performed at each grid cell and also retains spectral information. A local approach can be taken. Only the value of η from the previous spectral step, η_{i-1}, and the increase across the current cell $\Delta\eta_i$ are

necessary to calculate the driving force in cell i,

$$\left.\frac{dP_{\rm rad}}{dz}\right|_i \propto \sum_{n=x_1}^{x_2} [(\eta^\star_{n,i})^{1-\alpha} - (\eta^\star_{n,i-1})^{1-\alpha}] \frac{\Delta x}{\Delta z}, \tag{2.58}$$

where Δx is the separation of the cells in frequency space , Δz is the spacing of the spatial grid, and the summation is over all frequencies Doppler shifted into the velocity range of the grid cell $x_1; x_2$.

Using the quantity

$$\eta^\star(x,z) = \eta(x,z) + \frac{1}{\kappa_{\rm max}} + \frac{\phi(x)}{\sigma_c}, \tag{2.59}$$

in our numerical calculations allows the photospheric profile and opacity limit to be absorbed into the initial conditions.

We can think of the calculation of $\eta(x,z)$ as a convolution in velocity space if we write equation (2.43) as,

$$\eta(x,z) = \int_{v(R_\star)}^{v(z)} \rho(v)\phi(x - v/v_{\rm th})\frac{dv}{v'}. \tag{2.60}$$

If we shrink the domain that this convolution is performed over to one spatial grid cell, i, of width Δz, the amount that the absorption has been increased across this cell can be written as,

$$\Delta\eta_i = \int_{v_{i-1}}^{v_i} h_i(v)\phi(x - v/v_{\rm th})dv. \tag{2.61}$$

We assume that the density and velocity gradient are constant across the grid cell and re-express them as $h_i = \rho_i/v_i'$, using v_i' as the velocity gradient across the cell i. Using this relation we can write the increase in the absorption from all frequencies Doppler shifted into cell i as,

$$\Delta\eta_i = \phi_i \otimes h_i \ . \tag{2.62}$$

While this is different from the internal profile assumed in the hydrodynamical solution, we are free to assume a different profile as a result of the operator splitting. As we shall see, the results are sensitive to the way in which the assumed gradients depend on

cell values, so it is of paramount importance to use a physically consistent model in the evaluation of these terms.

Assuming that the velocity gradient and density are constant between adjacent grid cells, h_i will be a top-hat function and with the additional assumption that ϕ_i is also a top-hat function, the analytical form of $\Delta\eta_i$, the change in absorption of the radiation field at a particular velocity, can be determined analytically. In this case the convolution of two top-hat profiles can be performed analytically outside the numerical routine. At run-time the functional form of the convolution can be accessed in the code and scaled depending on the values of the velocity gradient and density.

2.4 Assumptions made in the wind solutions

In this section we present the important assumptions specific to our implementation, including the assumptions which relate to the line driving and the state of the gas and those which relate to the numerical implementation of the hydrodynamics.

The important assumptions which relate to the nature of the photospheric gas and the interaction with the radiation field are: Coulomb coupling, zero effect of the net scattering radiation field, absorption lines not overlapping in the spectrum, an isothermal equation of state and no heating or cooling of the gas.

Isothermality and thermal equilibrium A perfect gas equation of state is used given by the thermal energy density of the gas, $e = nkT/(\gamma-1)$, where the number density $n = \rho/\overline{m}$, $\overline{m}$ is the mean gas-particle mass, and γ is the ratio of specific heats.

We have assumed that the gas in the wind behaves isothermally. This means that the cooling and heating zones are infinitely thin. Due to the photoionisation of hydrogen in the wind the ambient temperature is approximately 10^4K (Field, Goldsmith & Habing 1976, Drew 1989). Hotter gas tends to cool because of collisionally excited emission.

Although isothermality is not generally applicable it is not wildly incorrect in the mean flow.

Heating and cooling The photospheric gas can become very diffuse in the rarefactions associated with the shock structure. In these regions the gas is susceptible to extended cooling zones which should be treated in detail by the numerical routine. However, as has been found by previous authors (Cooper & Owocki 1992, Runacres & Owocki 2002), when including heating and cooling, the cooling zone collapses making the shocks remain isothermal. The reasons for this are not fully resolved.

Heating and cooling can be tricky mechanisms to employ in a numerical code. An explicit scheme is relatively simple to implement but can result in spurious results if cooling zones are under-resolved. Implicit schemes are more difficult to implement but give results that are more reliable. We do not include either of these methods but recognise that it would be important to update our numerical simulations to include these at a later stage.

Coulomb coupling: This process is described above and we re-iterate that we assume that the drift timescale is much larger than the time scale over which the ions slow down. Lamers & Cassinelli (1999) quote the useful condition,

$$\frac{L_\star}{[L_\odot]}\frac{[M_\odot \mathrm{yr}^{-1}]}{\dot{M}}\frac{v}{[\mathrm{km\,s}^{-1}]} < 5.9 \times 10^{16} \tag{2.63}$$

expressing the requirement for Coulomb coupling in terms of the stellar luminosity $L_\star$, velocity of the wind v, and the mass loss rate of the flow $\dot{M}$. For a typical hot star with $\dot{M} > 10^{-7} M_\odot \mathrm{yr}^{-1}$, $L_\star = 10^6 L_\odot$ and $v = 1000 \mathrm{km\,s}^{-1}$ this condition is satisfied.

Scattered radiation: All of the absorption events in a stellar wind are accompanied by re-emission events which are called scatterings. The scattered photon field is

considered to be globally isotropic. We will discuss local anisotropy in Chapter 5 during the inclusion of the diffuse radiation field. For the remainder of this work we consider the stellar photons to have a maximum of one scattering event before escaping the wind.

Overlapping lines Two emission lines can overlap spectrally if they have even a moderate optical depth. This changes their contribution to the line force, but the calculation of this effect requires a more detailed approach than the ensemble method of CAK. We therefore follow CAK (and subsequent authors) in assuming that none of the lines that contribute to the line driving overlap.

The major approximations which we impose on our models for computational ease are: plane parallel geometry, super-sonic boundary condition, single photon ray approach, negligible finite disc effects, fixed hydrodynamical computational grid using the Piecewise Parabolic Method (PPM), variable CFL time step.

Plane parallel: Throughout this work we will use a plane parallel approach. We only consider a single ray in the calculation of the radiation force (see the next item). We assume the physical domain of the models in the work are sufficiently downstream of the stellar surface so as to consider the rays incident on the inner boundary to be parallel.

Supersonic boundary: Linked to the plane parallel geometry assumption is our assumption of supersonic inner boundary, since both of these follow from the downstream flow assumption (used in the plane parallel description of the flow). This is justified because any features present in the supersonic flow cannot propagate towards the stellar surface, interior to the sonic point. Structure which appears in the sub-sonic flow and is directed towards the stellar surface cannot affect the outer wind. Mass loading can occur in the wind where a feedback process in the sub-sonic wind locally increases the mass-loss rate, forcing the sub-sonic solution

onto a different solution branch at the stellar surface. This effect can communicate with the supersonic flow but produces a dynamical disturbance which could have its origin in the subsonic flow. This assumption will be relaxed in Chapter 5.

Single ray: A detailed treatment of a two dimensional spherically symmetric geometry should calculate the driving force using non-radial photon rays, however this is highly computationally expensive, even with a short characteristic method. A preliminary case was constructed by Owocki (1998), consisting of a single radial ray and two non-radial rays, each making the same angle with the normal on the left and right sides. He found significant differences between Sobolev and SSF approaches, such that the structure in this preliminary SSF approach disperses much of the imposed structure in the wind. To ensure that all of the rays intersect at the cell boundaries Owocki increases the radial length of grid cells with distance from the central star. This practice is acceptable in one dimension but has disadvantages in two dimensions because of asymmetrical hydrodynamical effects. We therefore recognise that non-radial rays are important but at present they are not used in the calculation of the line driving.

Finite disc effect: Close to the surface of the star the solid angle which the stellar photosphere subtends is large thus affecting the calculation of the line force. The calculation of the force from each line includes an integral average over the cone subtended by the stellar disc, weighted by the intensity of the incident radiation. However, further out in the wind, the stellar disc has a negligible effect on the evaluation of the line acceleration. At this point and beyond, the radiation can be considered as radially emitted (radial streaming approximation; Pauldrach, Puls & Kudritzki 1986).

This effect does not alter the nature of the line driving, only scales the magnitude of the force. Pauldrach, Puls & Kudritzki (1986) show that the radial streaming

approximation is unrealistic. Their primary interest is not the dynamics of the wind solutions but rather the generation of physically consistent mass loss rates and terminal velocities. We ignore the effect of the finite stellar disc since we consider a flow which is supersonic and therefore an appreciable distance downstream of the stellar photosphere. Having said that, a finite disc treatment will be employed in the Chapter 5, in calculations which extend towards the stellar photosphere and subsonic domain, where the finite disc becomes highly important.

Rotation: We make the assumption that there is zero rotation in the wind. This is certainly incorrect in a real wind as the observations of rotational broadening of lines suggest. However we are concerned with investigating the wind properties arising from the interaction of the driving and hydrodynamics, any further complications would serve only to blur these effects. We assume that the rotational velocity is substantially lower than the radial wind velocity.

Fixed grid PPM: Our concern with the time dependent behaviour of stellar winds is tied to the solution of the Eulerian equations of hydrodynamics, equations (A.1)-(A.3) with different forms of the source function in equation (A.2). In this work we use the VH-1 hydrodynamical code which uses a Godunov method (1959) of solving the Euler equation called the Piecewise Parabolic Method (PPM). The general philosophy of Godunov methods is to form an exact solution to the Euler equations for a small local zone. This reduces the complexity calculation by removing the need for a complete description of the flow. The hydrodynamics are solved for each small zone and they are then *piece*-d together. The piecing together can cause numerical anomalies since an analytically smooth distribution can only be represented as a sequence of discrete steps in a numerical scheme. The approach of Collela & Woodward (1984; PPM) is to construct a parabola within each zone from which the full description of the state variables can be pieced together. The PPM method actually solves the Lagrangian hydrodynamical equations, remapping the solution

onto an Eulerian grid.

This method is not as fast as implicit finite difference methods, however it does prevent spurious hydrodynamical behaviour which usually has to be damped by such means as artificial viscosity. Shock structure can be spuriously created at the interface of zones in coarse representations of continuous functions. We discuss this further in Appendix A.

Variable CFL limited time step: This condition (Courant, Friedrichs & Lewy 1928; CFL) is required in an explicit numerical scheme for hydrodynamics to be stable. In essence, it is a causal constraint, requiring that the computational time-step must be short enough that the physical characteristics will remain inside the template of the numerical scheme. This time step is defined as

$$\Delta t = \frac{\Delta x}{v_c} \tag{2.64}$$

where v_c is the characteristic speed (maximum of isothermal sound speed, a_0 and flow velocity, v) and Δx is the spacing of the cells, which is fixed in this implementation. Some authors have noted that the variation in this time step is the root of structure which appears in the wind solutions. In order to study the flow these authors seed the subsonic region of the flow with small amplitude periodic perturbations and use a constant time step that satisfies the condition $\Delta t = \Delta x/a_0$. We allow the time step to vary with the dynamics and use the noise structure that this generates to study the wind. There is a degree of control over the timestep, built into most hydrodynamical codes in the form of the Courant number, C, which lies $0 < C < 1$. The expression for the CFL timestep becomes $\Delta t = C\Delta x/a_0$. The CFL timestep is the limit at which the system will not allow information to propagate faster than the sound speed but setting the Courant number to $C < 1$ allows the user to add additional safety to the stability of the calculations; the particular

nature of the calculations performed can make the value of this 'safety factor' an important consideration to ensure stability in the numerical routine.

Summary

In this chapter we have discussed the theory of driving mechanisms for astrophysical winds and investigating their stability in analytically tractable ways. The winds which have been discussed are:

- The isothermal Parker wind. A wind emitted from stars with intermediate mass ($\approx 1 M_{\odot}$) and hot corona ($\approx 10^6 K$), driven entirely by ideal gas pressure. The wind has a unique trans-sonic solution but the theory also allows for shallow solutions, Chamberlain Breeze solutions, which remain subsonic at large distances from the central star.

- The continuum wind. A wind which is driven by interactions between free electrons and the incident radiation field. These type of winds can occur around Broad Absorption Line QSOs (BALQSOs) and stars with a dust component to the wind (e.g. RSG and AGB stars). Their driving mechanisms differ and we only model that of the former.

- The line driven wind. A wind which arises from the interaction between the incident radiation field and metal ions in the stellar atmosphere. This interaction is prevalent in hot stars such as OB and WR stars, and is highly potent, resulting in high terminal velocities and large mass loss rates. The driving force can be modelled using a power law of the opacity, with results that are in good agreement with observations. A stability analysis of the driving force shows that the wind is most unstable to small optically thin perturbations.

- We have given details of a convolution approach to the calculation of the driving

force, without invoking the Sobolev approximation, in a pure absorption model.

In the following chapter we demonstrate the stability of the continuum and line driven models using numerical simulations and compare our convolution method to the results of other authors.

Chapter 3

1D time-dependent numerical results

3.1 Introduction

In the previous chapter we have only considered static solutions for different driving mechanisms. This approach is useful to develop an understanding of stationary properties and for estimating such observable quantities as mass loss rates and terminal velocities for specific stellar parameters. However as is indicated by observational evidence, the winds of stars (and especially hot stars) strongly deviate from a static solution. Therefore a time dependent hydrodynamical simulation is embarked upon. Ideally a code could be constructed with the specific physical situation in mind, however, there are many freely available hydrodynamical codes which have been professionally written and fully tested in many different physical scenarios.

We chose to use the hydrodynamical code VH-1 (Blondin 1994), in its isothermal implementation, which employs the Piecewise Parabolic Method (PPM) for solving hydrodynamical equations. The code makes efficient use of an Eulerian remap method, where the Lagrangian (mass as the independent variable) form of the Riemann problem is solved and then mapped on to an Eulerian (distance as the independent variable) grid. The Riemann problem contains the essentials of the hydrodynamics, in the form of non-linear interaction of two constant states of the fluid (Woodward 1982). This scenario is

essentially a shock tube and its exact solution is well known. The starting conditions also are stored in terms of Eulerian parameters, therefore there is also a mapping of these to the Lagrangian grid for the solution of the Riemann problem. The creators of VH-1 quote that the reason for this "is to avoid the subtleties associated with constructing the correct input states for the Riemann problem" (VH-1 Users Guide, Blondin 1994).

The solution of the Riemann problem is simpler when it is expressed in the Lagrangian form, rather than the Eulerian form. Once the Riemann problem has been solved in each Lagrangian zone VH-1 interpolates between them using parabolae, obtaining a continuous function from which the values on the Eulerian grid can be calculated. Parameter values are stored as cell averages.

In the results presented here we use a toy model for the wind[1]. The hydrodynamical and radiation driving equations are scaled in a simple manner which equates to the scaling of OCR corresponding to an idealised stellar wind and not that of a particular star. Relevant values used for the OB star model are given in Table 3.1. This model is useful for understanding flow behaviour but clearly will not be acceptable when comparing such a model to observational evidence. The ratio of the ion thermal velocity to the isothermal sound speed is artificially high ($v_{\rm th}/a_0 = 0.5$, a realistic value is closer to 0.3) so as to retain a stable flow. This was explored by Poe, Owocki & Castor (1990), where they notice that for a large value the wind is stable with decreasing stability as the value gets smaller. The reason for this can be understood in terms of the width of the profile function. Increasing this ratio widens the profile function so that in a numerical scheme the overlap between grid cells in frequency space is larger and the total absorption is therefore smoother.

The value of the wind temperature was set to an unphysically high value by OCR. because of a need to conserve computing time. Although this is not so much of an issue when running our code because of advances in computing since 1988, we use a value of

[1]Sections from this chapter have been published in Gomez & Williams (2003)

Physical Parameter		Value
Stellar mass	$M_\star$	$50M_\odot$
Stellar radius	$R_\star$	$20R_\odot$
Isothermal sound speed	a_0	$70\mathrm{km\,s^{-1}}$
	v_{th}/a_0	0.5
CAK index	α	0.7
Wind temperature	T	3.7×10^5 K
Stellar Luminosity	$L_\star$	$6.8 \times 10^5 L_\odot$
Opacity constant	$\kappa_0 v_{\mathrm{th}}/c$	$2270\ \mathrm{cm^2 g^{-1}}$
Optically thick line limit	κ_{max}	$10^{-3}\kappa_0$
Inner Boundard Condition	**Parameter**	**Value**
Density	ρ_0	$2.5 \times 10^{-12}\mathrm{g\,cm^{-3}}$
Velocity	d^2v/dz^2	0

Table 3.1: Code and physical parameter values.

the temperature which is similar to that used in OCR, for the purposes of comparison. At the end of this chapter we compare this model with one that uses the parameters of a real star, ζ Puppis.

An equilibrium, but structured, flow is established and used as the background upon which perturbations are subsequently added. Therefore all starting flow states are either smooth flow equilibrium states, or if this is not available (i.e. in the non-Sobolev case), a representative data set is used (which contains structure from line de-shadowing instabilities) .

In the following sections we will discuss the results of time dependent numerical simulations. We show particular interest in the stability of the driving since this is where there lies the potential of detailed and interesting wind structure.

3.2 Flow characteristics of stellar winds

Before embarking upon a discussion of results from these driving forces, it is of use to introduce some characteristic flow structures which will appear. Flows can become highly complicated, as structures wax and wane.

3.2.1 Basic wind structure

Shocks, rarefactions and mean flow are the basic structure elements of a wind. Generally speaking, when a region of gas is accelerated it leaves behind it a rarefied region. In this region, or depression in the velocity field, the optical depth drops and the flow will remain close to an equilibrium solution. The accelerated downstream edge of the region will carry on being accelerated until it is inhibited in a number of possible ways. Where this edge meets slower moving gas, the accelerated gas is braked and a reverse shock is formed. This shocked gas is fed into a dense shell which forms immediately downstream of the shock front. A reverse shock is where fast moving gas collides with slower moving gas. In the collision the faster moving gas is decelerated. Also in this interaction the velocity and density are out of phase with each other, the high density preshock shell leading the high velocity shock. There can occur *forward* shock structure in winds, where the density and velocity are correlated, however they appear to be weaker in line-driven winds than reverse shocks (Feldmeier 1995). Forward shocks are of great importance in such astrophysical events as supernovae where the force of the shock front is orders of magnitude larger than this case, accelerating the shocked gas and not decelerating it.

In non-Sobolev line driven wind models, radiation shadowing has a profound effect on the structure of the wind. Shadowing occurs when an upstream clump (u) of gas blocks a region of the stellar radiation field that had been accelerating a clump of downstream gas (d). Clump (d) will therefore receive less driving and decelerates. De-shadowing is the reverse process, when a region of shadowed gas receives driving as the upstream structure changes to reveal the necessary region of the spectrum.

All other flow properties will be discussed as they appear in the results. These are the main flow characteristics which produce interesting structure. We must be mindful that all structure is likely to be born from more than one of these processes, therefore making the structure tricky to interpret fully.

In all of the plots, either graphs or two dimensional greyscale density maps of Chapter

4, the rather vague coordinates, 'upstream' and 'downstream' are used extensively. In all cases these refer to, in the case of upstream, gas or structures which are closer to the star (that is to say, to the left of) a particular flow feature, and *vice versa.* When an 'upstream edge' is discussed, this can be taken as referring to the left most part of the disturbance of concern. The opposite applies to a 'downstream edge'.

Perturbations are added to the equilibrium flow and with fixed density and/or velocity, expressed in terms of the ratio of the perturbed density to the equilibrium ($\rho_c/\rho_0 = R_\rho$) and the ratio of the perturbation to the mean flow velocity (M) at the position of the upstream edge perturbation. Therefore in our notation, a value of M means that the perturbation has an initial velocity which is much greater than the unperturbed background at this location.

In one dimension each perturbation has a width of 20 grid cells, $\Delta z = 0.075 R_\star$ in code units, unless otherwise stated.

3.2.2 Flow stability

In general terms a flow can be called unstable if a perturbation disturbs the 'equilibrium of the external forces, inertia and viscous stress of the fluid' (Drazin & Reid 1981). The evolution of the disturbance with time (and also with position in the flow) further defines what is meant by *stability* and *instability.* It is common to define a perturbation which dies back to the equilibrium as *stable*, one which persists at a similar magnitude as *neutrally stable* and one which grows so that it grossly affects the flow as *unstable.*

In the multivariate flows that we are concerned with, there is the probability that a disturbance in one of the flow variables will induce a disturbance in others, with growth rates that are related but not necessarily dependent. Such an induced, sympathetic disturbance may introduce further instabilities of its own, further complicating the flow. Each disturbance is, with a high level of probability, composed of different modes of oscillation. When the perturbation begins its evolution it may be dominated by the

growth rate of one mode. However as the evolution continues, the less dominant modes may grow and become more distinct causing the smooth evolution to break.

In later sections we will discuss more specific instabilities inherent in purely hydrodynamical flows and ones more specific to radiatively driven winds.

3.3 Statistical descriptors of the flow

As suggested by Runacres & Owocki (2002), the flow of the wind can be usefully described by three statistical parameters; the clumping factor ($f_{\rm cl}$), velocity dispersion ($v_{\rm disp}$) and correlation function (C). The clumping factor is a measure of how the mass in the wind is distributed, where a small value indicates that there is little clumping. The velocity dispersion is nothing more than the standard deviation away from the mean flow velocity at each point in the flow. The importance of this is that it shows regions that have persistent velocity features. The correlation function indicates if the velocity and density are in (out) of phase, corresponding to a dominance of forward (reverse) shocks in the flow, strong (anti) correlation is shown when $C \rightarrow (-)1$.

The clumping factor, velocity dispersion and correlation coefficient are given by,

$$f_{cl,i} = \frac{\langle \rho_i^2 \rangle}{\langle \rho_i \rangle^2}, \tag{3.1}$$

$$v_{\rm disp,i} = \sqrt{\langle v_i^2 \rangle - \langle v_i \rangle^2}, \tag{3.2}$$

$$C_{v \log \rho, i} = \frac{\langle v_i \log \rho_i \rangle - \langle v_i \rangle \langle \log \rho_i \rangle}{v_{\rm disp} \sqrt{\langle (\log \rho_i)^2 \rangle - \langle \log \rho_i \rangle^2}}, \tag{3.3}$$

respectively, where the angle brackets refer to a time average of flow quantities in cell i: the parameters are functions of the position at which the time average is calculated.

3.4 Numerical continuum driving

We discuss the stability of continuum driving in this section with support from numerical results. The wind solution is assumed to be one of the family of supersonic solutions. Although in § 2.2 it was stated that these solutions were unphysical, that was in advocacy of the solution as a whole. Past a certain point in the flow (i.e. the critical point) the solution is quite plausible. This family is similar in nature to the family of supercritical solutions in the CAK formulation. The CAK solution uses an extra condition to ensure that the critical solution joins continuously to an appropriate member of the super-critical solution family. It is a solution of a similar family which is considered with continuum driven winds (cf. Fig. 2.2).

The parameters of this model are the critical velocity, v_c, the continuum driving constant, K, and the proportionality constant of the gravity of the system, $GM_\star$. The mass loss rate is not fixed in advance because at every point in the flow the value will be subject to the local conditions (cf. equation (2.4)).

3.4.1 Thin Density-perturbation

To investigate further the stability of the continuum driving case we add a density perturbation to the background flow. The perturbation has the characteristics $R_\rho = 2.5$, $M = 1$ (unperturbed in velocity). From this evolves the structure seen in Figs. 3.1, 3.2. As predicted in §2.2.2 the flow is unstable to this density perturbation (which grows in a direction parallel to the radiation field only). The enhanced density region locally increases the driving from continuum radiation. This region is optically thicker than the surroundings, increasing the amount of radiation it absorbs and increasing the acceleration by $K\delta\rho$.

There are different processes at work on the perturbation giving rise to the observed evolution. The smoothly varying background velocity field causes the velocity across the perturbation to increase with radius, and although the radiation driving across it is

constant the dynamics of the perturbation is not. If the perturbation had been added to a uniform density the evolution would have been similar to 2 Sod shock tubes back to back (Sod 1978; more details of Sod Shock tubes and the evolution of such a pair in this scenario are given in § A.4). However this is not the case and the background is more dense upstream of the perturbation than it is downstream of it. The most significant difference between this and the Sod case is that the external driving force is directed outwards and dependent on the density. The background velocity is not constant, which influences the initial dynamics of the perturbation.

This effect is quite obvious in Fig. 3.2(a), where the upstream and downstream edges have become completely separate. The density at the downstream edge is further enhanced from swept up material and from accelerated material ballistically impacting from behind, which further accelerates it. This high density and high velocity edge steepens into a forward shock front (cf. Fig. 3.1(c) and Fig. 3.2(c)), where the swept up material is accelerated by the shock. The amplitude of the shock front increases as the material behind it increases in density and is accelerated more strongly by the radiation field. The velocity difference across the shock thus becomes greater and the shock becomes stronger.

3.4.2 Thin velocity-perturbation

Positive velocity perturbation

The behaviour of a thin velocity perturbation with $M = 2$, $R_\rho = 1$ is similar to the structure produced by a density perturbation, as can be seen by comparing Fig. 3.3 and 3.4. The results in these figures and those of the previous section both show that either an over-dense or high velocity perturbation will form a shock at its downstream edge whilst the disturbed flow upstream of it, having insufficient density or velocity to form any detailed structure, will gradually be smoothed out to match the mean flow solution. Therefore high density or velocity perturbations will generate dense shells, which will receive stronger driving and further steepen the shock front. This form of unstable flow

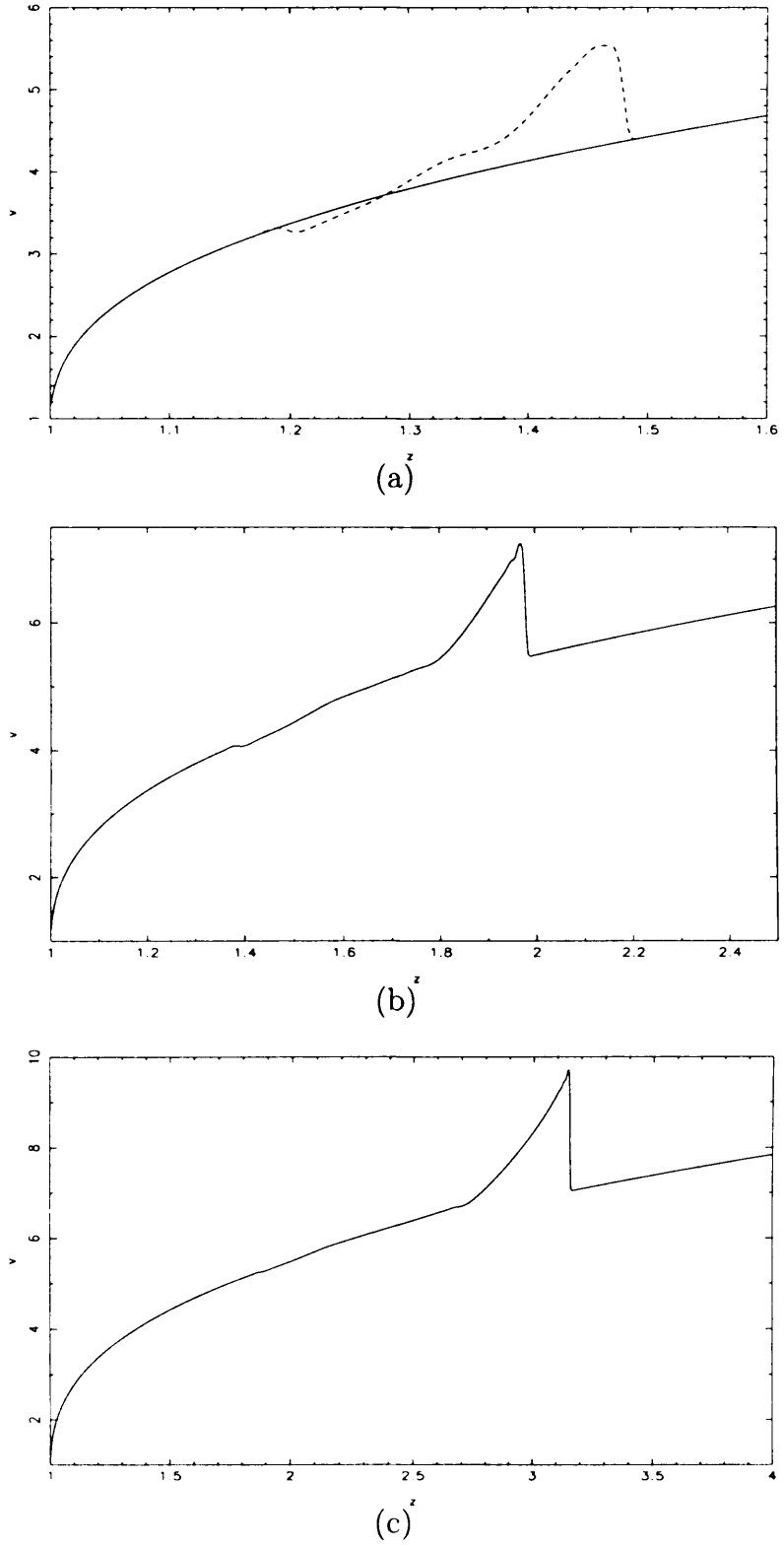

Figure 3.1: Density perturbed flow, velocity plots. The solid line in (a) is the background mean flow, and the dotted line shows the perturbation at $t = 0.0345$. Plot (b) shows the perturbation at $t = 0.069$ and plot (c) shows the perturbation at $t = 0.138$. These plots show the evolution of an over-dense region as it accelerates in an unstable fashion due to the incident continuum radiation.

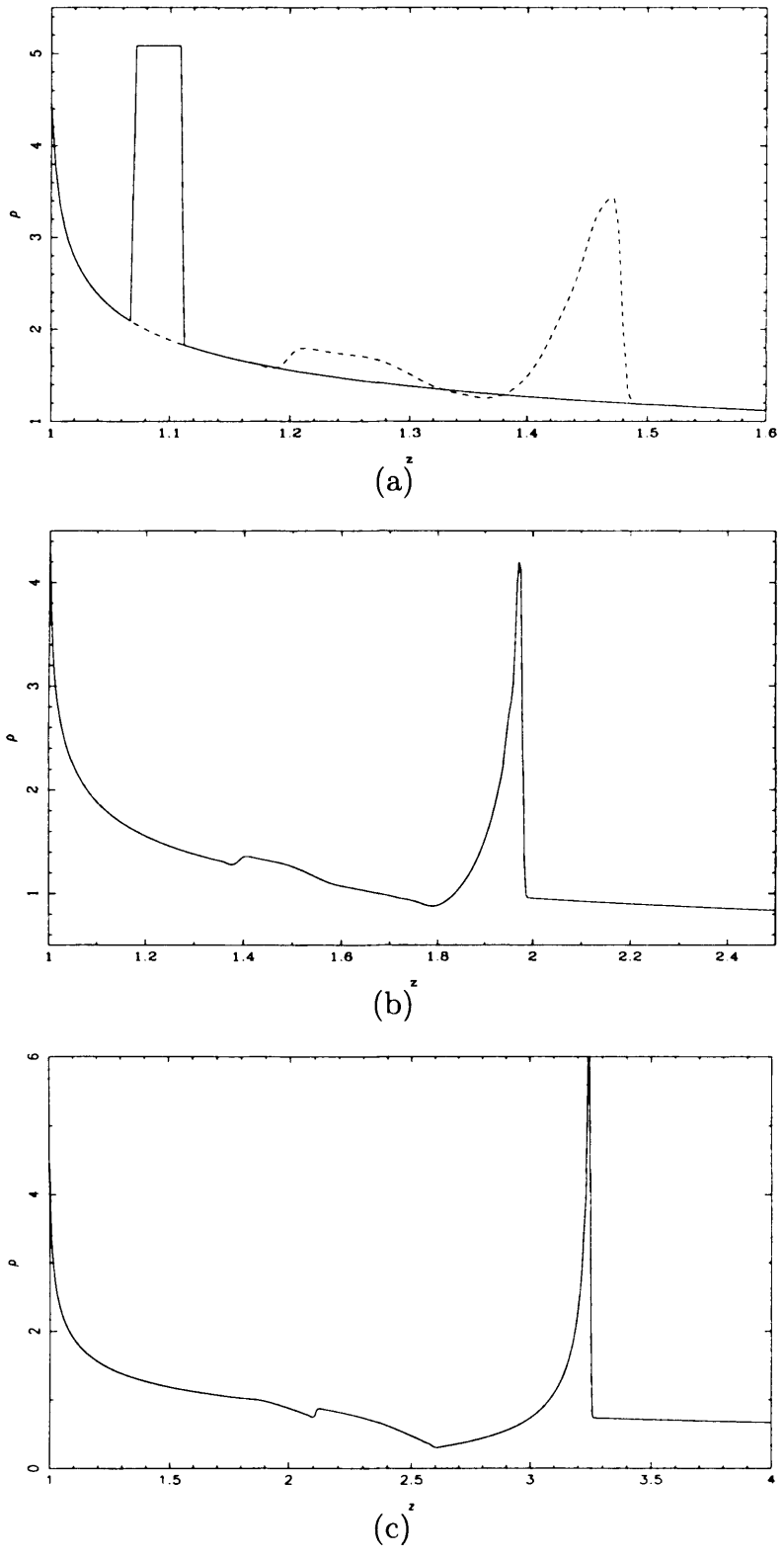

Figure 3.2: Density perturbed flow, density plots. The solid line in (a) is the background mean flow with the initial perturbation, and the dotted line shows the perturbation at $t = 0.0345$. Plot (b) shows the perturbation at $t = 0.069$ and plot (c) shows the perturbation at $t = 0.138$. These plots are the counterparts to Fig. 3.1 and show clearly the high density perturbation evolve into a steep shock, whilst the lower density part shrinks back to the level of the mean flow. Units of z are R_* in all plots.

could lead to observable features, if the non-thermal emission from the shock fronts is detected.

Negative velocity perturbation

Previously we have only considered an *increase* in the local conditions of the flow. Here we seed a depression in the mean flow velocity with $M = 1/2$. As one might expect, the evolution of an optically thin velocity depression (or negative velocity perturbation) is stable to the continuum driving. As the perturbation is optically thin and is not driven thermal expansion makes it more diffuse and less subject the radiation driving. Figs. 3.5, 3.6 show this behaviour neatly. The hydrodynamics cause more complicated interactions between the mean flow and the perturbation, which clouds the effect. In the central portion of the perturbation the density decreases toward the mean flow, whilst the velocity is accelerated to a level close to that of the mean flow, as shown by Fig. 3.5 (b). In this portion and at the upstream edge, the driving assists the structure to approach the level of the mean flow. In contrast the upstream edge evolves in a fashion that is unaffected by the driving. The low density and low velocity of the upstream portion means that the strength of the driving is small, which keeps this portion of the structure unchanged in the flow. Meanwhile the high density edge becomes unstable and steepens into a shock.

The results in this section show that perturbing a continuum driven wind always produces an unstable flow feature. However the driving mechanism is not strongly unstable so that once a perturbation has passed, the flow settles down to a smooth background flow. The instability in this case is advective. When the perturbation is removed the flow settles back down, since the information that propagates inwards is stable. We we will see below how other driving mechanisms respond to perturbations in the flow and the consequences for the end state of the wind.

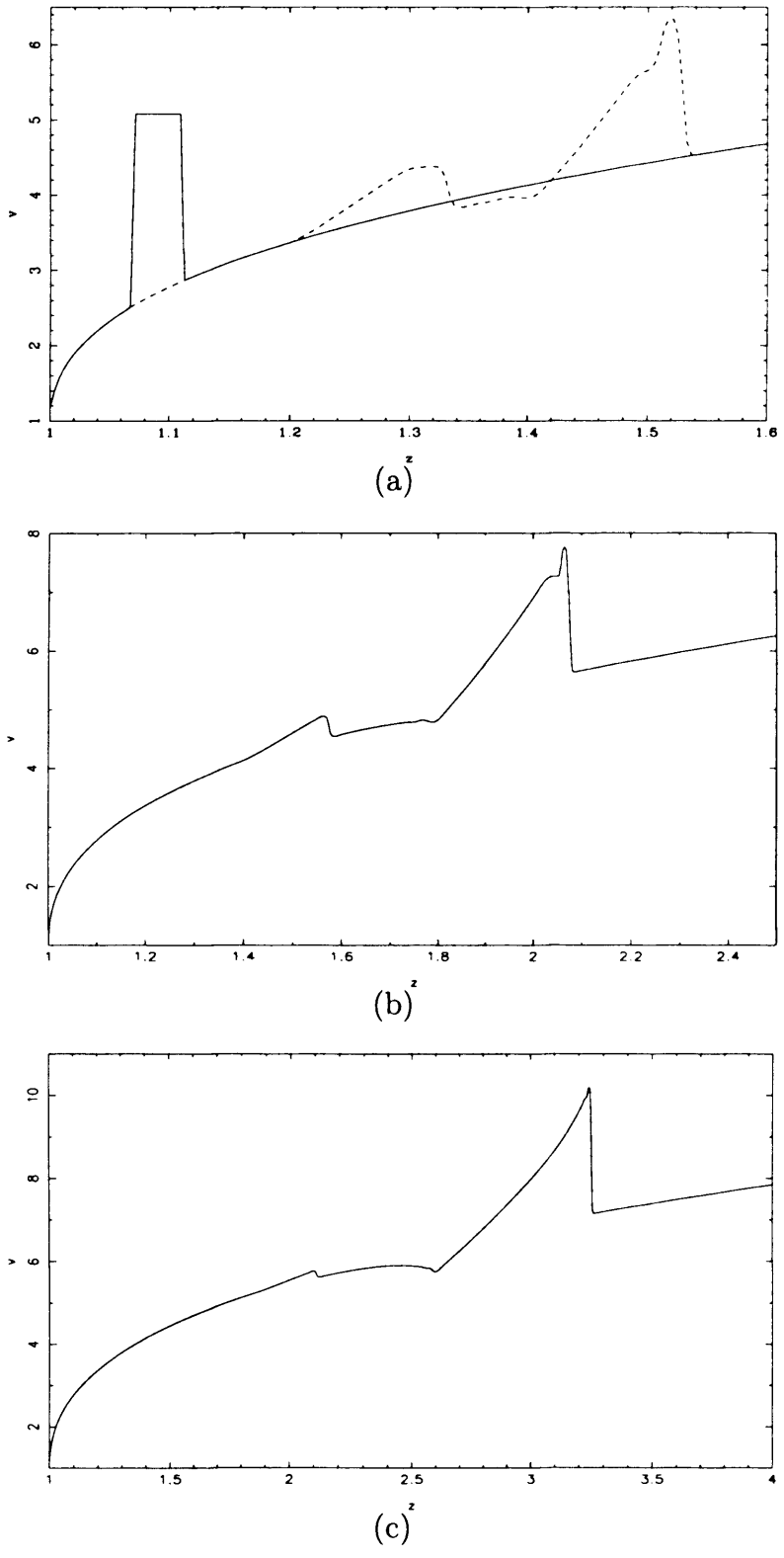

Figure 3.3: Positive velocity perturbed flow, velocity plots. The solid line in (a) is the background mean flow with the initial perturbation, and the dotted line shows the perturbation at $t = 0.0345$. Plot (b) shows the perturbation at $t = 0.069$ and plot (c) shows the perturbation at $t = 0.138$. These plots show the evolution of a high velocity region as it accelerates in an unstable fashion due to the incident continuum radiation.

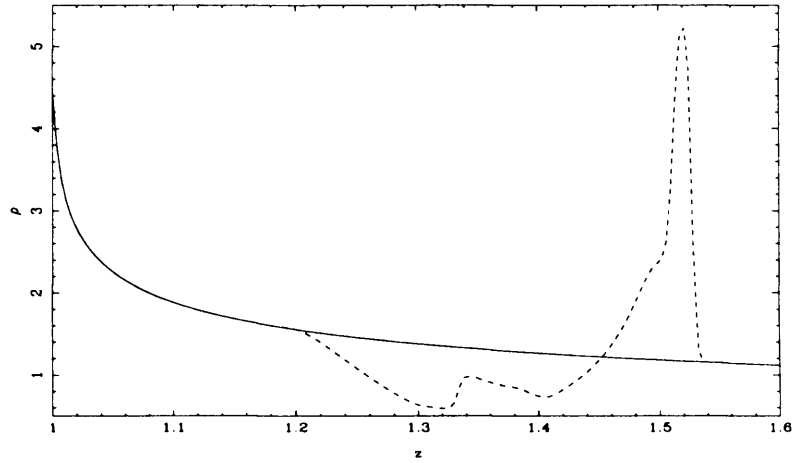

(a)

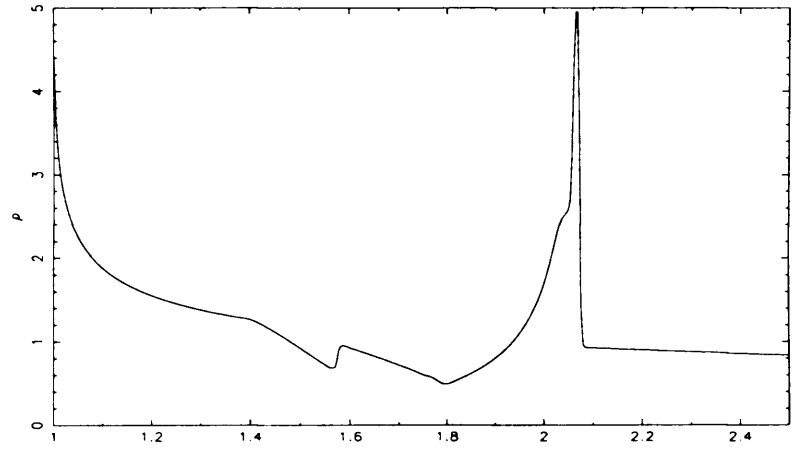

(b)

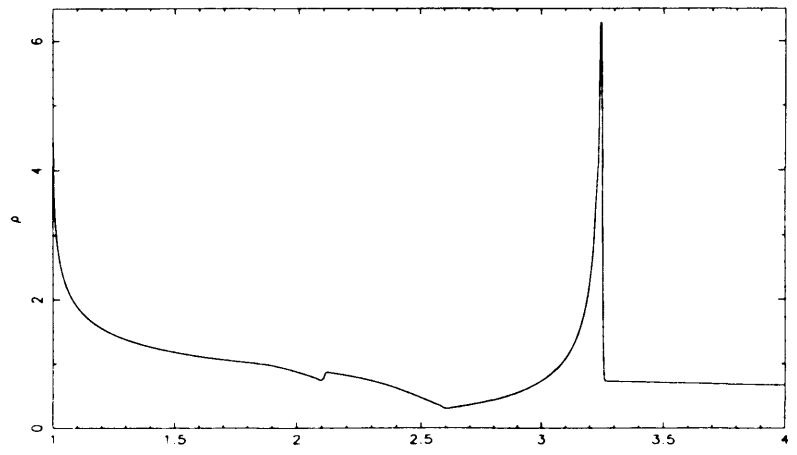

(c)

Figure 3.4: Positive velocity perturbed flow, density plots. The solid line in (a) is the background mean flow, and the dotted line shows the perturbation at $t = 0.0345$. Plot (b) shows the perturbation at $t = 0.069$ and plot (c) shows the perturbation at $t = 0.138$. These plots are the counterparts to Fig. 3.1 and show clearly the high density perturbation evolve into a steep shock, whilst the lower density part increases back to the level of the mean flow.

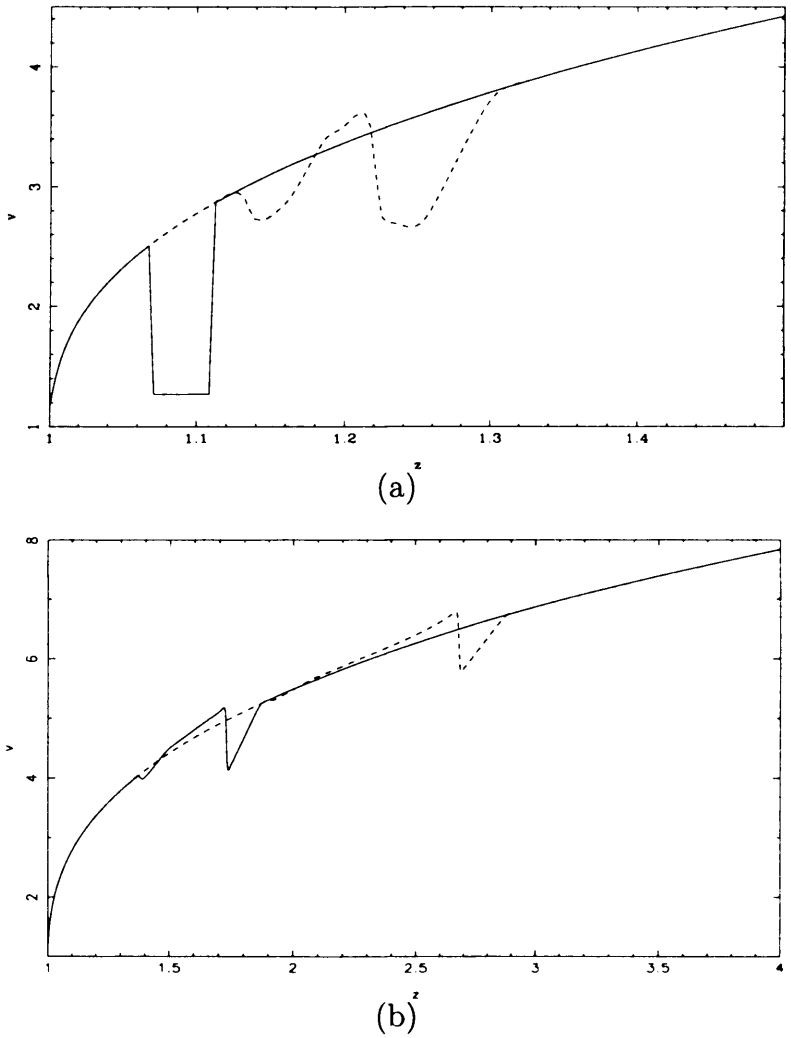

Figure 3.5: Negative velocity perturbation, velocity plot. The solid curve in (a) shows the perturbation at $t = 0$. The dotted curve shows it at $t = 0.0435$ displaying the acceleration of the central portion of the perturbation. In plot (b) the solid curve shows the perturbation at $t = 0.145$ and the dotted curve is at $t = 0.29$. Here the upstream edge of the perturbation has returned to a value close to the mean flow whilst the upstream edge is advected, stably through the flow.

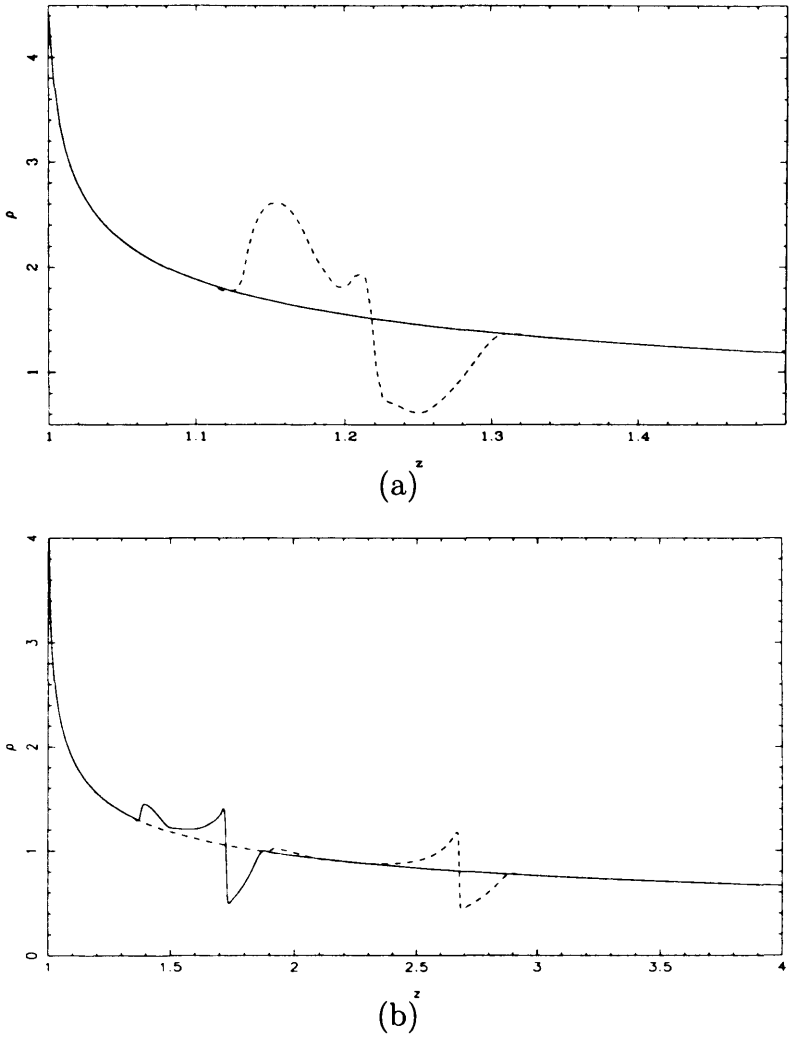

Figure 3.6: Negative velocity perturbed flow, density plot.The solid curve in (a) shows the perturbation at $t = 0$ and The dotted curve shows it at $t = 0.0435$. The difference in the background density across this velocity perturbation produces the dotted structure. In plot (b) the solid curve shows the perturbation at $t = 0.145$ and the dotted curve is at $t = 0.29$. The density in the upstream part returns to the mean flow level whilst the rest of the structure evolves slowly as it is advected through the flow.

3.5 Numerical Sobolev line driving

As we have discussed previously, a driving force law which uses the Sobolev approximation provides results which are in good agreement to observable mass loss rates and terminal velocities. In this section we present the results of numerical simulations which use the CAK power law formulation of the line driving force.

We use fixed values of the velocity and density at the inner boundary which can lead to over specification of a wind solution. The consequence of this is that it can trap a shock at the inner boundary which periodically tries to force the inner wind on to a different solution to that which the outer wind relaxes to. The results for our models do not appear to be affected by this phenomenon, suggesting that the values chosen for the boundary conditions closely match the hydrodynamical solution.

3.5.1 Numerical stability in the CAK wind

The numerical calculation of the CAK force using equation (2.33) requires a numerical velocity gradient to be calculated, involving both velocity and spatial differencing. A consideration when differencing flow variables is the direction in which the differencing is performed since this affects the direction of information propagation. Comparing upstream and downstream differencing methods lead us to some interesting conclusions. which must affect all calculations of this nature.

In a simple method of gradient calculation, we consider 3 possible arrangements of gradients calculated from f_i, f_{i-1} and f_{i+1}, where f is a flow variable and i is an arbitrary grid cell. We define the 3 combinations of these variables as,

$$\text{downstream} \left\{ \frac{\Delta f_{\rm d}}{\Delta x} = \frac{f_{i+1} - f_i}{\Delta x}, \right. \tag{3.4}$$

$$\text{upstream} \left\{ \frac{\Delta f_{\rm u}}{\Delta x} = \frac{f_i - f_{i-1}}{\Delta x}, \right. \tag{3.5}$$

$$\text{midpoint} \left\{ \frac{\Delta f_{\rm m}}{\Delta x} = \frac{f_{i+1} - f_{i-1}}{2\Delta x} \right. \tag{3.6}$$

In all calculations we assume a constant grid spacing $x_{i+1} - x_i = x_i - x_{i-1} = (x_{i+1} - x_{i-1})/2 = \Delta x$.

On inspection of the above forms we can expect that the downstream method will allow information to propagate *from* downstream in an upstream direction. The upstream method only uses information along the characteristic from the star, propagating information in the same direction as the radiation field. The midpoint method takes the average of values at its neighbouring cells. By this reckoning the upstream method is the most physically consistent of the 3 methods, since it derives a gradient only from the state of the gas which it is causally (not dynamically) in contact with. The gas in cell i can 'see' only the gas that is upstream of it, which implies that information is propagating outwards from the interior of the wind. In the downstream method, the wind flow and the photon propagation is from upstream to downstream, as with all the methods, while the information propagates in the reverse direction due to the differencing scheme.

We calculate the force using all three methods and the resulting velocity plot can be seen in Fig. 3.7. The stability of the model is dramatically improved by using the downstream or midpoint methods. This difference in the calculation direction for the velocity gradient will be used in the calculation of an approximate line drag force in Chapter 5.

3.5.2 Abbott Waves

This behaviour may be understood in terms of the propagation of 'Abbott waves'. Abbott (1980) treated the propagation of flow perturbations in the Sobolev limit. In one dimension, he found 2 radiative-acoustic wave modes moving at speeds

$$v_- = v - \frac{1}{2}g'_{\rm rad} - \sqrt{\left(\frac{1}{2}g'_{\rm rad}\right)^2 + a_0^2} \tag{3.7}$$

$$v_+ = v - \frac{1}{2}g'_{\rm rad} + \sqrt{\left(\frac{1}{2}g'_{\rm rad}\right)^2 + a_0^2}, \tag{3.8}$$

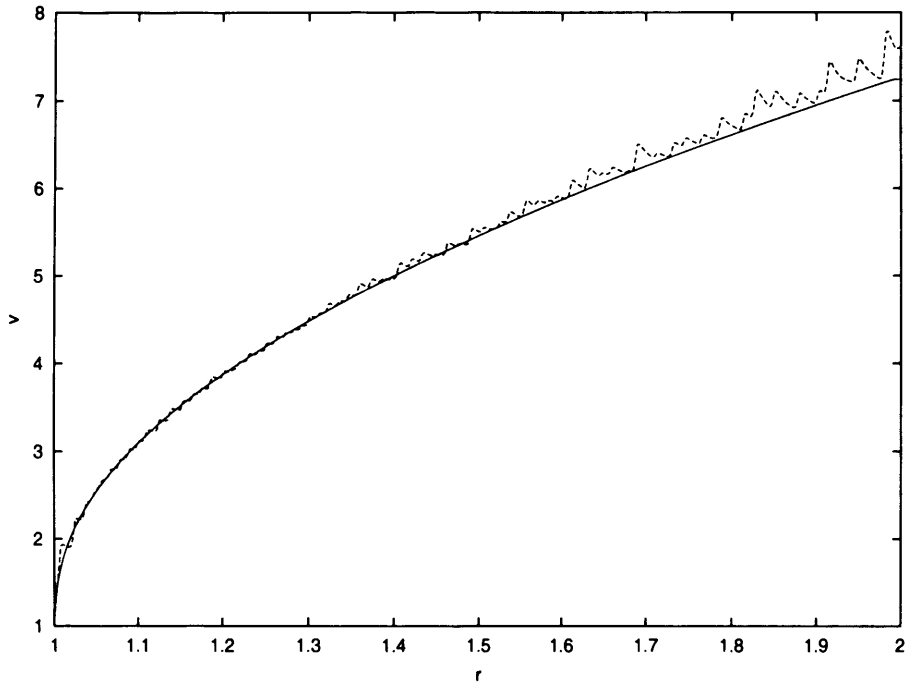

Figure 3.7: Instability in the wind produced by changing the direction of velocity calculation. Dashed curve shows upstream gradient results and solid shows downstream and midpoint gradient results. All curves use the CAK radiation driving force law. As is shown the downstream and midpoint methods are stable while the upstream method is highly unstable.

where $g'_{\rm rad}$ is the derivative of the radiation acceleration with respect to the velocity gradient. The critical points in the steady-state CAK equation occur where one or other of these mode velocities is zero.

The first of these radiative-acoustic modes is, however, somewhat mysterious, as it moves *upstream* through the flow at a speed faster than the sound speed in the gas. Owocki et al. (1986) demonstrated that Abbott's approach is justified only for purely wave-like modes. The implication of this research is that the upstream propagation of the information is a mathematical illusion. The authors find the subtle result that when a small part of a perturbation function is added to the flow (i.e. a part of the asymptotic tail of a Gaussian) the entire perturbation function is generated by the driving. This is not a result of information propagating upstream, only that the function already exists in the flow and the time dependence of the phase makes the structure appear. While information cannot propagate upstream in this pure absorption model because of the purely downstream direction of photon propagation, that does not prevent the phase and group velocities of wave-like perturbations being directed upstream in an unstable flow.

This is of relevance in explaining the stability analysis in §3.5.1 and later in §3.6.1 where, in the former case, there is a choice as to which direction the velocity gradient calculation is performed. In the latter case, there is effectively a choice of direction in which the radiation pressure gradient is calculated. Using the downstream velocity gradient in the calculation of the Sobolev line force allows information to travel upstream through the grid, and as a result genuine modes with the properties of Abbott waves arise in our numerical simulation. The midpoint method also allows for the propagation of information upstream and hence this method too is stable.

The speed of information propagation in these artificial grid waves is limited to $|v| < \Delta x/\Delta t$, however since all of our calculations use the CFL timestep this is a fixed quantity and these grid waves will always travel faster than the sound speed (Mark Runacres 2003, Priv. Comm.). The upstream velocity of these modes no longer *requires* the flow

to be unstable, and in the outcome it is not. This can be illustrated, for example, b observing that the Abbott-like modes can allow the solution at the photosphere to adju to satisfy the conditions at the CAK critical point, and hence the flow overall to relax t the steady-state CAK solution.

This stabilising feature of Abbott waves should, however, not be dismissed out of han as a numerical artifact, as scattered radiation can lead to *some* upstream propagation o information. The line-drag effect may be thought of as the result of just such a stabi ising influence, although at a different level to that implicit in fully downstream gradien evaluation.

3.5.3 Thin velocity-perturbation

We added a thin velocity perturbation with $M = 2$, $R_\rho = 1$ to the mean flow solutio of the CAK formulation with the purpose of investigating the evolution of optically thi disturbances to the flow. Due to the higher velocity, the smooth background densit becomes more diffuse as it is pushed downstream faster than the unperturbed flow. Th accelerated gas forms a dense shell at the downstream edge of the diffuse patch where encounters the unperturbed higher density, lower velocity gas.

Fig. 3.8(a) shows the initial velocity distribution of the flow and the state of th perturbed region after $t = 0.027$. Fig. 3.9(a) shows the equivalent information in densit space. We observe that after this short time the increased velocity has swept the ga in the perturbed region into a dense shell which leaves a diffuse region behind it. Th shape of the perturbation, in velocity space, begins to deviate from the symmetrical initi condition, reflecting the density evolution.

After $t = 0.069$ the perturbation has swept up an optically thick clump and lookin at Fig. 3.8(b), it seems that the velocity of the perturbation has a dip part of the wa across it. We might expect the density to reflect this trend, however Fig. 3.9(b) displa quite different structure. The high velocity perturbation causes a local discontinuity in th

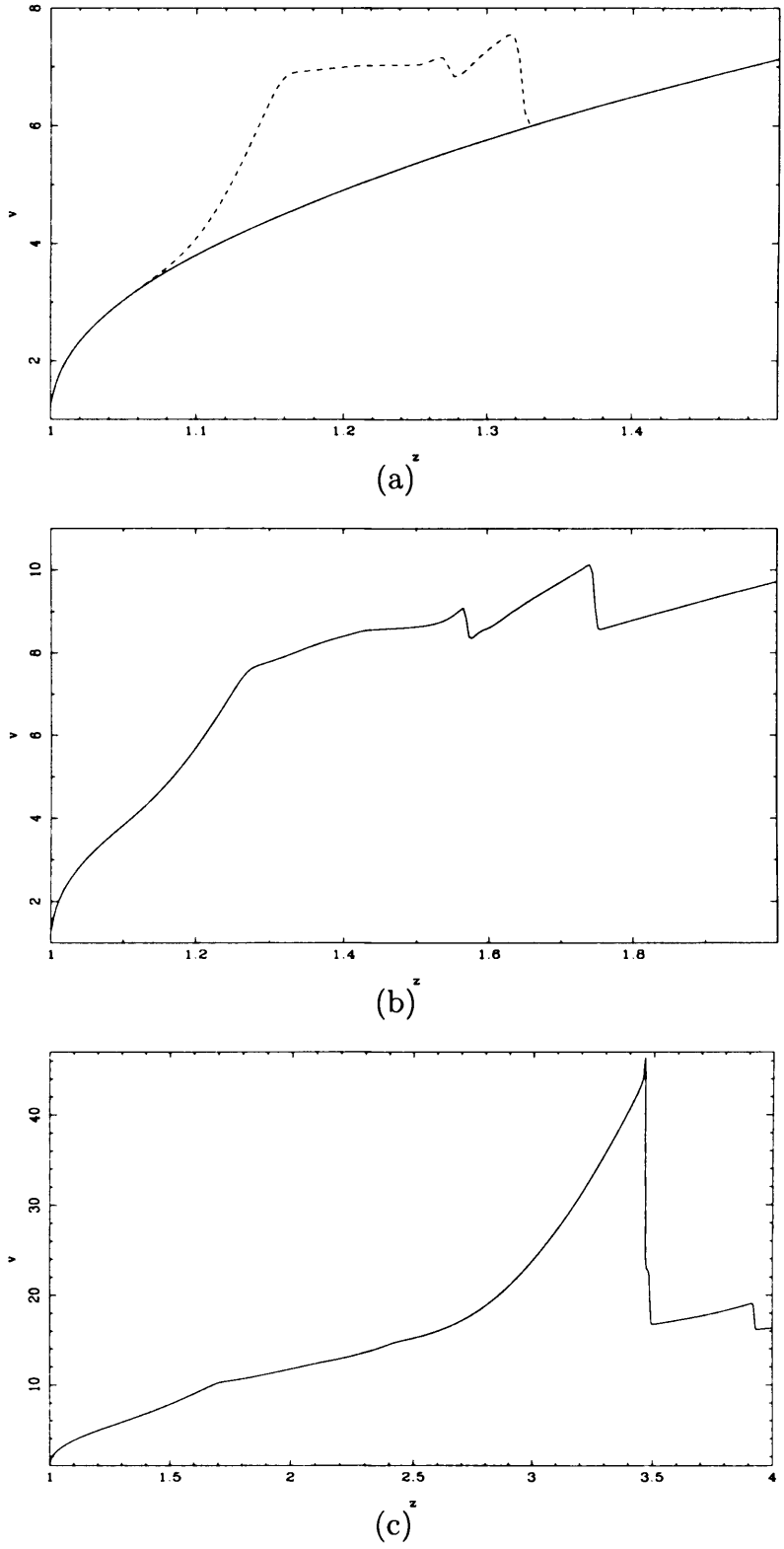

Figure 3.8: Velocity plots for a velocity perturbed CAK flow, with an initial perturbation of $M = 2$, $R_\rho = 1$. The plots correspond to times, (a) $t = 0.000$ (solid) which includes the initial perturbation, $t = 0.028$ (dashed), (b) $t = 0.069$, (c) $t = 0.276$. The downstream edge of the perturbation steepens into a strong reverse shock at $t = 0.1656$ (not shown). The shock continues to grow stronger from the line driving force.

density, as discussed above, thus changing the form of the mass conservation equation. For mean flow this can be written as, $\frac{\partial(\rho v)}{\partial z} = 0$, since there is no appreciable time variance. However when such a dramatic perturbation is introduced, altering the smoothness of the flow, the time derivative of density is needed to balance the increase in density at the current cell and mass conservation once again returns to the form shown in equation (A.1). This behaviour is hydrodynamical, although it is initiated by the line-driving interaction with the perturbation.

It is not until Figs. 3.8(c), 3.9(c) at $t = 0.276$ that the unstable nature of the wind is realised. In Figs. 3.8(b), 3.9(b) the behaviour is hydrodynamical, but now the driving has steepened the discontinuity between the diffuse and dense regions into a reverse shock front. In the wake of this front the main dense shell begins to fragment into a smaller shell, which if followed further downstream could lead to more detailed flow structure. The acceleration of the diffuse region is symptomatic of an unstable flow, since in a short distance the evolution has gone from slow hydrodynamical expansion to rapid shock formation.

3.6 Numerical non-Sobolev line driving

The behaviour of an unperturbed non-Sobolev model has been studied by many different authors (e.g. OCR, Runacres & Owocki 2002) so the discussion of free flow is not included here; the discussion concentrates on the similarities between this model and previous models. The basic structures of line driven flows are rarefactions, steep reverse shocks as fast upstream material runs into slow downstream material and de-shadowing of downstream gas. These effects are seen but the matter of interest is how they all affect the evolution of the flow and specifically a perturbation to the flow.

Initially the mean flow of the wind in one dimension was simulated from the above model. Although the model as described, is physically incomplete it is useful to explore the most simple case of a line-driven wind, i.e. unperturbed flow. Unperturbed here

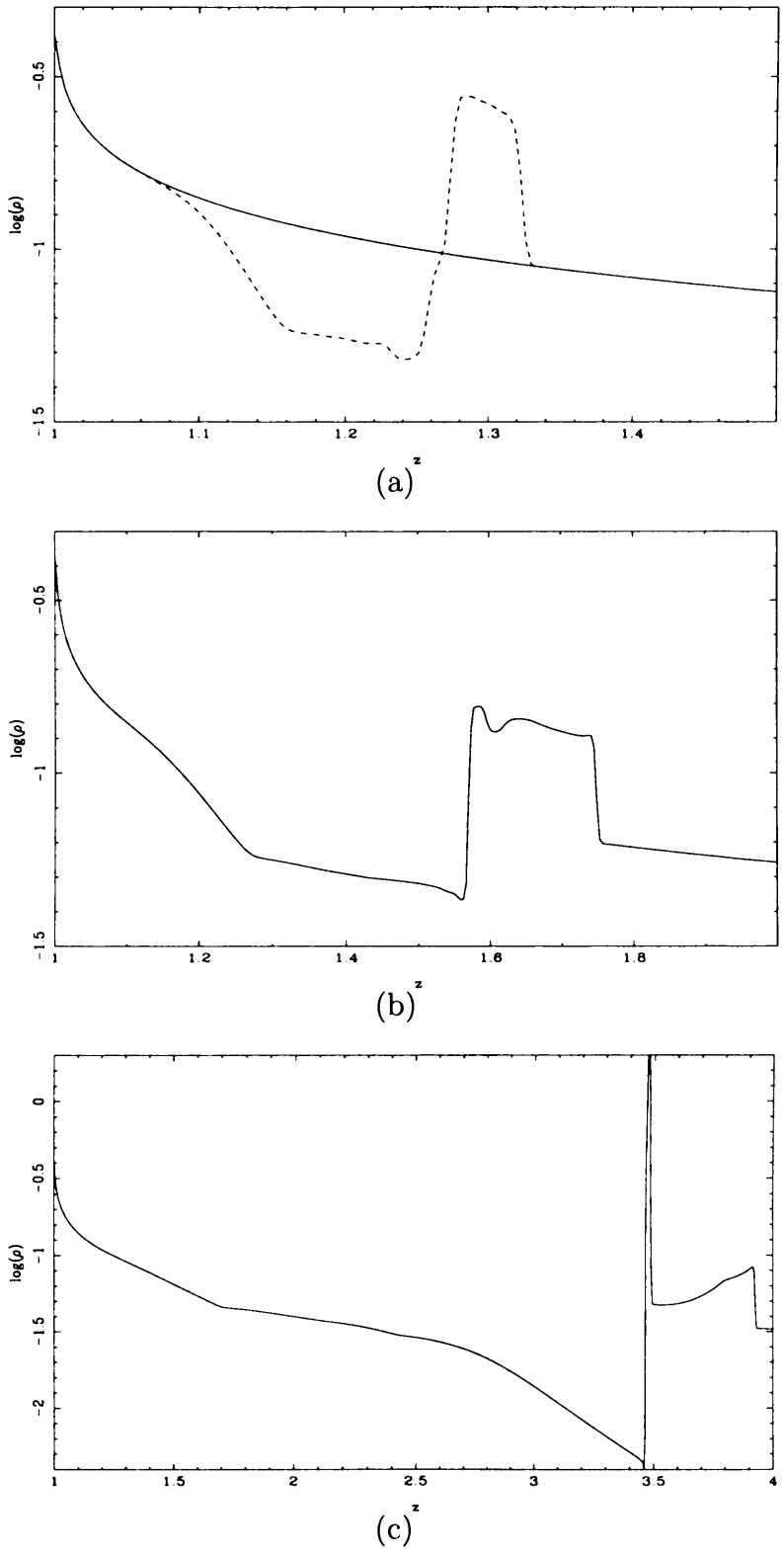

Figure 3.9: Plots for a velocity perturbed CAK flow, with an initial perturbation of $M = 2$, $R_\rho = 1$, showing the counterpart density results to Fig. 3.9. The plots correspond to times, (a) $t = 0.000$ (solid), $t = 0.028$ (dashed), (b) $t = 0.069$, (c) $t = 0.276$. The strength of the shock formed by the perturbation is shown in (c) as having a height of ≈ 2.5 orders of magnitude.

means that there is no extra perturbation inserted by hand, however the flow does contain features that arise from its unstable nature in the optically thin limit. This means that such a pure absorption model is especially susceptible in the early wind to instabilities.

3.6.1 Numerical stability in the non-Sobolev wind

As was shown previously for the CAK force, the choice of the direction of velocity gradient calculation can affect the stability of the flow. VH-1 stores variables as cell averages which we convert into values at the interface between each cell. The method that we use to calculate the line driving force requires the differencing of the radiation pressure at the interface between adajent grid cells (cf. §2.3.6). During the calculation of the force we need the velocity range for the current grid cell (difference between the velocity at the interface between the grid cell and its neighbours in the radial direction).

Two methods were used to calculate the interface values of the velocity; a mixture of interpolation and extrapolation from upstream information, and interpolation using downstream and upstream information,

$$\text{mixture} \begin{cases} v_{\rm u} &= \frac{1}{2}(v_n + v_{n-1}) \\ v_{\rm d} &= \frac{3}{2}|v_n - \frac{1}{2}v_{n-1}| \end{cases}$$

$$\text{interpolation} \begin{cases} v_{\rm u} &= \frac{1}{2}(v_n + v_{n-1}) \\ v_{\rm d} &= \frac{1}{2}(v_n + v_{n+1}) \end{cases}$$

respectively. The subscripts refer to upstream (u) and downstream (d) values. The mixture method is the most physically consistent since it will not allow information to propagate upstream as a result of the numerical method. The interpolation method, since it uses both upstream and downstream grid cells, does permit information propagation upstream. It may seem clear which method should be employed, however as with the CAK calculation the more physically consistent method is also the more unstable, as is

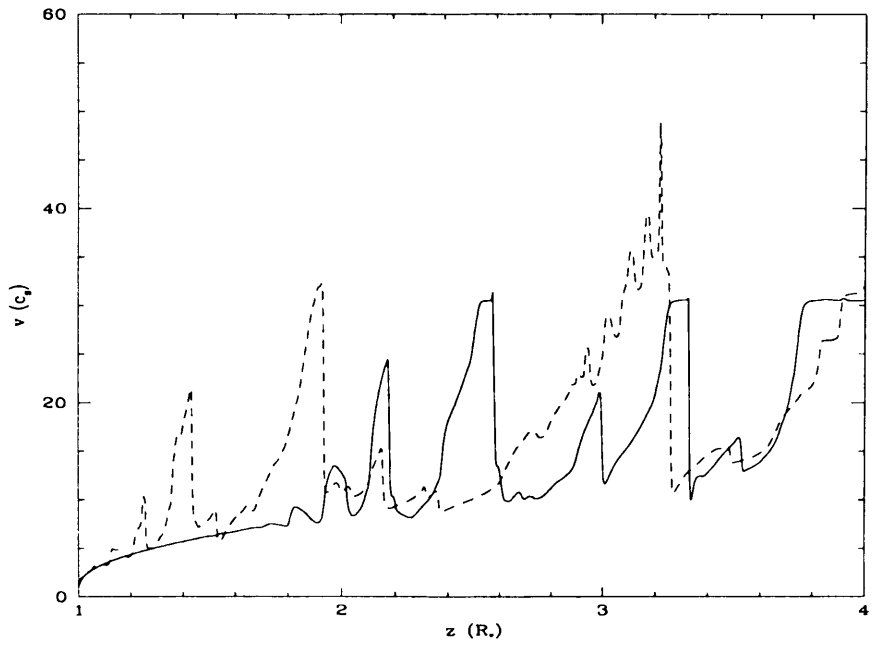

Figure 3.10: A plot showing two different models for the calculation of the cell interface velocities (which are required in the calculation of the line driving). Solid curve shows the evolution of the flow using the interpolation method and the dashed curve the evolution using the mixture method. The instabilities in the dashed curve appear earlier in the flow compared with the interpolation method.

shown by Fig. 3.10. In this case the instability is an inherent effect of the radiation driving which is exacerbated by the mixture method.

The interpolation method will therefore be consistently used in the remainder of this work. This has the additional benefit that the development of finite perturbations may be studied in the relatively smooth region $z = 1 - 2R_\star$ without being confused by the effects of rapidly-growing small-scale instabilities.

3.6.2 Optically thin perturbation

A perturbation is applied to the base of the wind with $M = 10$, $R_\rho = 1/10$. The evolution of such a perturbation, that would not occur as a natural fluctuation, was investigated with the express purpose of analysing the optically thin nature of the wind. This was

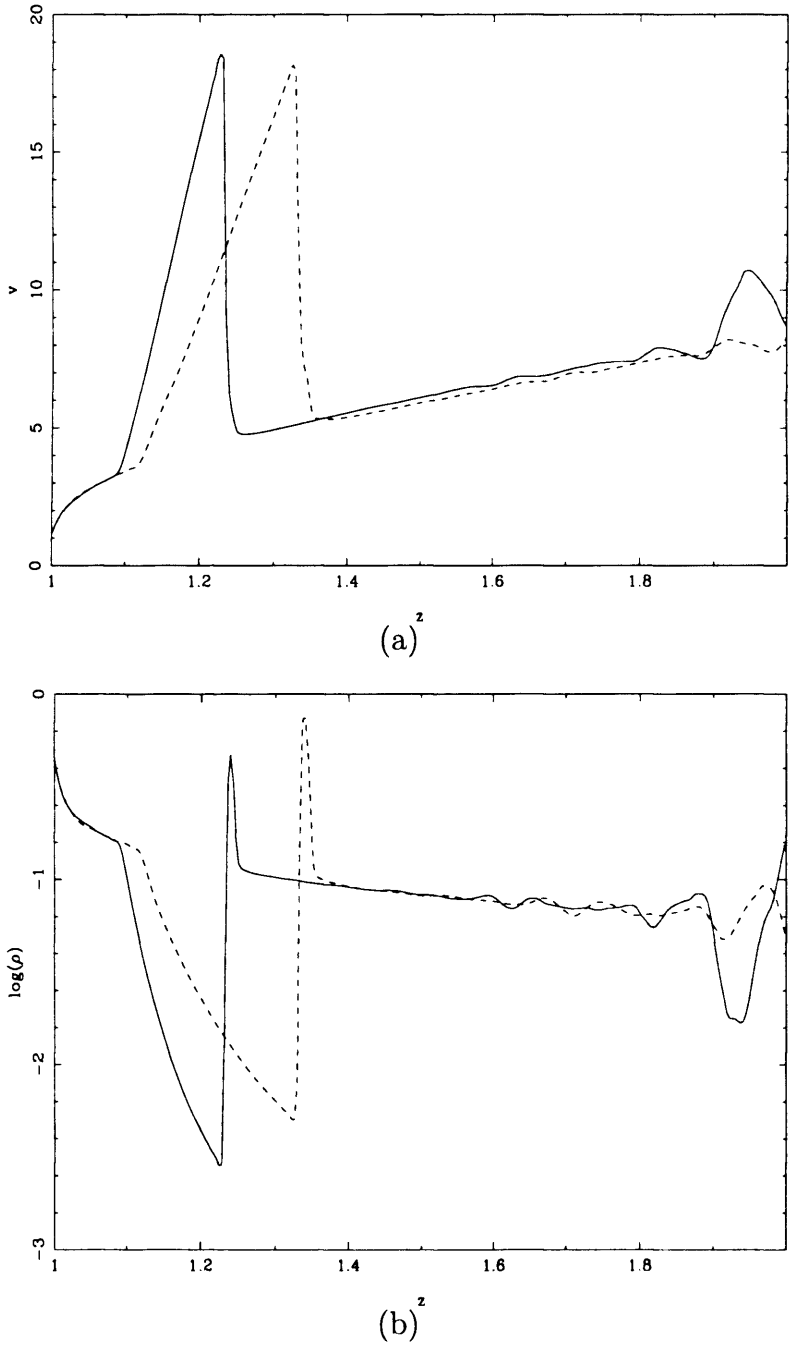

Figure 3.11: Velocity (a) and density (b) plots: Data from two different times have been overlaid; $t = 0.005$ (solid), 0.01 (dashed). The prominent features of the plots are the advection of the optically thin perturbation in the upstream portion of the wind.

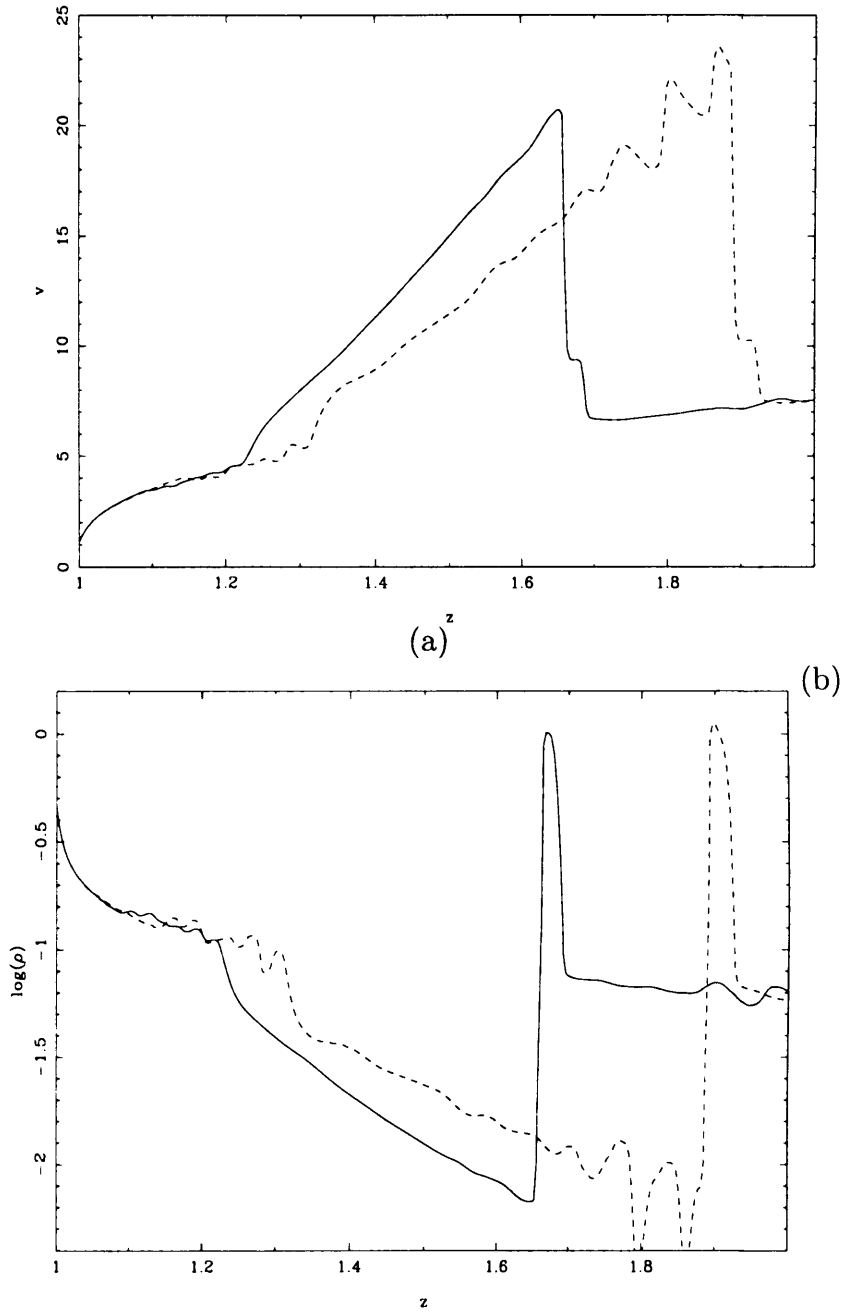

Figure 3.12: Velocity (a) and density (b) plots: Data from two different times have been overlaid; $t = 0.016$ (solid), 0.021 (dashed). The advected material now becomes unstable and begins to break into dense shells.

done with the aim of comparing it to the analytical work from Owocki & Rybicki (1984). presented above.

In this limit the evolution of the perturbation should follow equation (2.54). At this position in the flow the perturbation experiences a constant force, $\sim \tau_0 \delta v$. In Fig. 3.11 the behaviour of the perturbation appears to be stable, as the structure advects slowly across the grid. It is interesting to note that because of the low density and high velocity gradient here the force term approximates to constant acceleration. The shape is characteristic of a non-driven rarefaction. The acceleration it feels is a slowly changing function of position initially because both the background flow optical depth and the velocity are slowly varying also. It seems that the behaviour is stable, however this is just because the dynamical timescales in this part of the flow dominate over the evolutionary timescale of the instability; the stable patch is short lived and the evolution of the perturbation becomes more unstable. The effect of the perturbation on the radiation field can be observed by the difference between the solid and dashed curves in Fig. 3.11. The structure downstream of the perturbation continues to evolve but the flow immediately downstream of it remains smooth. This is a result of line shadowing from the perturbation. The downstream structure, because of its higher velocity, is affected by an unshadowed region of the spectrum. As the perturbation grows, so does the extent of the smooth region in front of it, as a wider region falls into the shadow.

Eventually the perturbation begins to break up. As is shown by Fig. 3.12 the smoothly varying rarefaction behind the perturbation becomes disturbed by noise waves. These arise from small amplitude fluctuations in the wake of the perturbation and have been amplified by the driving instability to a macroscopic size. They disrupt the reverse shock associated with the perturbation and accrete on to the shell in front of the shock. The disturbance at the upstream end of the rarefaction arises from the driving instability also but is seeded by larger fluctuations than those which appear at the downstream end of the perturbation. At longer times, these fluctuations will come to dominate the flow in

the rarefied region, removing the original perturbation as a distinct object. In 2D these structures are present but are complicated by the presence of hydrodynamical instabilities (e.g. Rayleigh-Taylor, Kelvin-Helmholtz), and not quite as visible.

The dense shell is not subject to the formation of instabilities and is gently advected across the grid. This supports the asymptotic form, equation (2.55) which implies that this feature is stable for small wavelength perturbations; any change in the radiation force will only affect the phase of the perturbation, or the derivative of the velocity. The coupling of the radiation field with the dense shell is very weak which is evident in its unchanging amplitude, indicating that it is largely unaided by the driving force.

Shock structure begins to develop in the flow as an optically thin flow encounters a dense shell. A good example of a reverse shock can be seen in Fig. 3.13, a dense shell with a smoothly rarefied region preceding it. This figure also shows other shocks forming and interacting with the surrounding dense regions.

3.6.3 One dimensional statistical information

The variation of the statistical information within the flow, for the above model, provided by equation (3.1) is graphically presented in Fig. 3.14(a)-(c). The noise in the system only becomes dominant at larger radii, in the clumping factor but it remains small in both the velocity dispersion and correlation coefficient.

As one might expect, the velocity dispersion, $v_{\rm disp}$, is close to zero at the base of the wind and the clumping factor, $f_{\rm cl}$, is approximately unity. In this region there is little contribution to the flow structure from the noise excited waves, so the wind is smooth and has an almost constant velocity.

A minor peak in $f_{\rm cl}$ is reached at $z = 2R_*$, the radius where the noise waves begin to dominate the flow. Upstream of this point there are no dense shells but in the downstream flow the dense shells steepen into shocks. The flow contains many dense shells but it is dominated by the accompanying rarefactions. The noise in $f_{\rm cl}$ beyond $z \approx 3R_*$ results

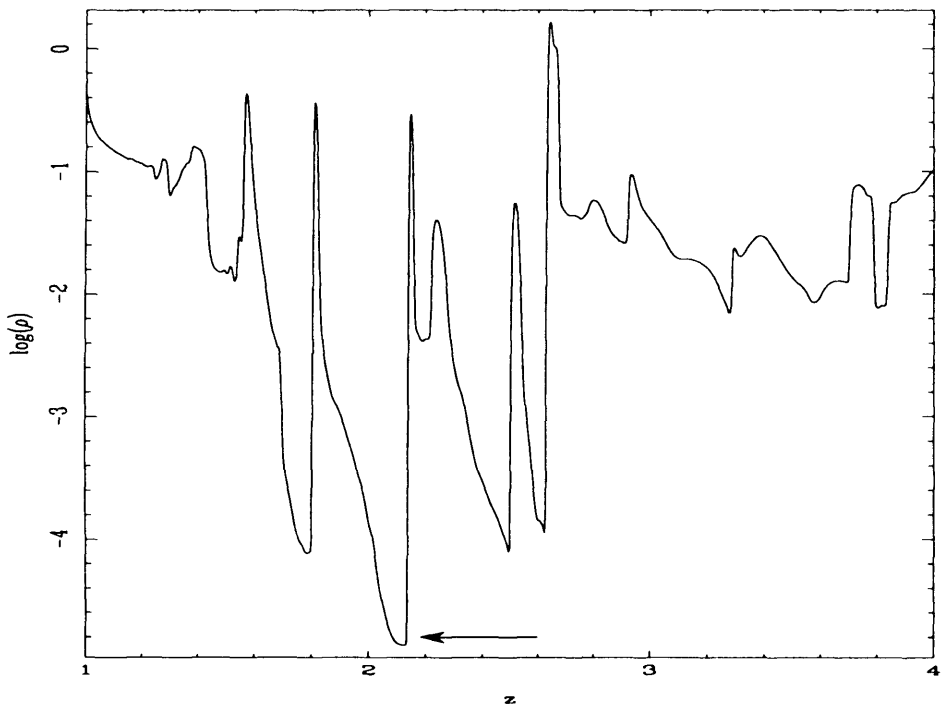

Figure 3.13: A plot of non-Sobolev driven model given in Fig. 3.11 at $t = 0.028$, where reverse shock structure can be observed forming in the unstable wake of the initial perturbation (indicated by the arrow).

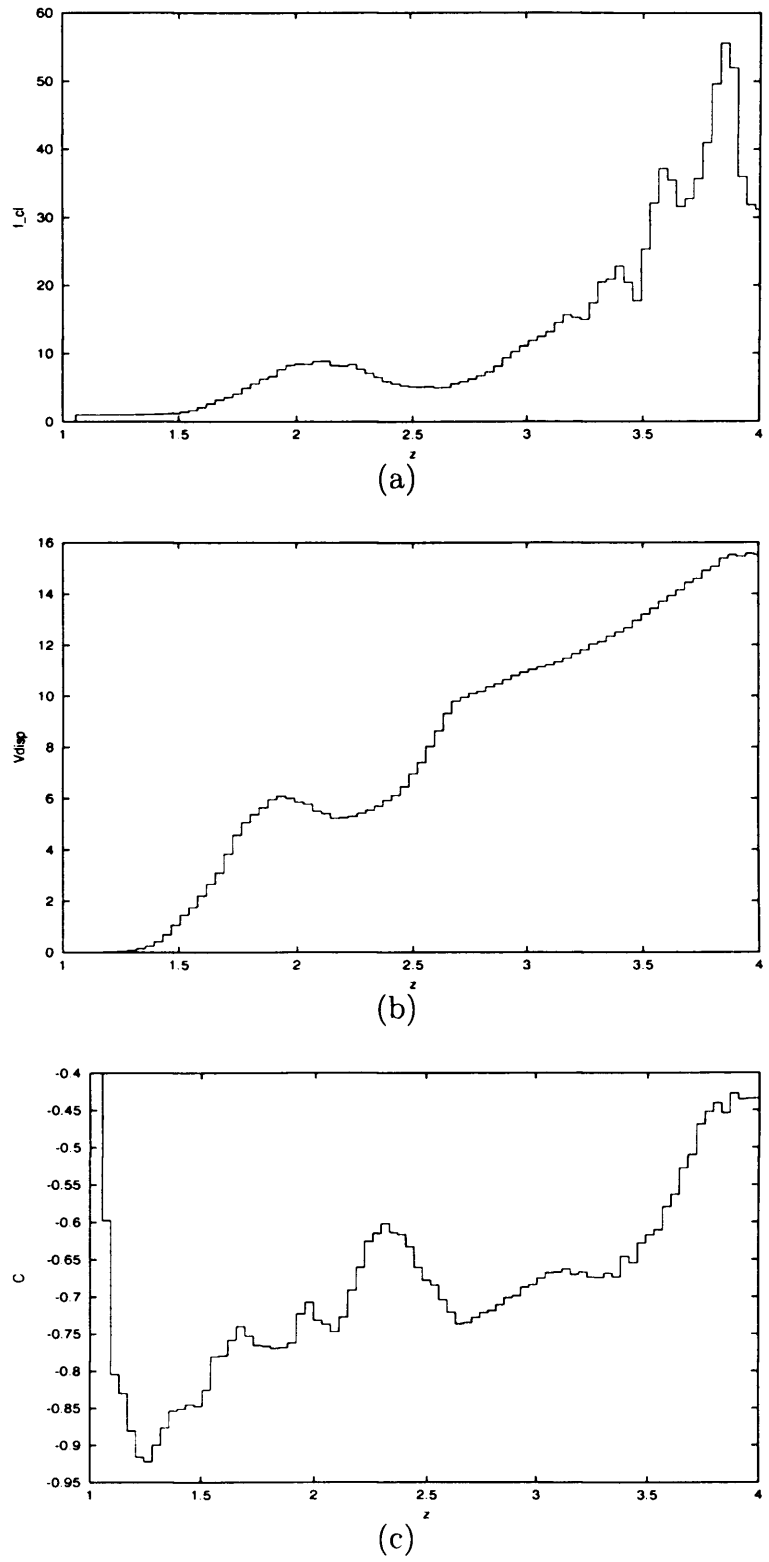

Figure 3.14: The above graphs show the variation of each of the statistical descriptors from equation (3.1) with radial distance. The noise in the clumping factor, $f_{\rm cl}$, is most evident, while the other parameters are tightly constrained. The data has been binned from 800 grid cells to 80 bins of equal size, to reduce the scatter in the plots. This scatter does not represent noise in the data but that the flow features move quickly across the grid and are under resolved in the time average.

from the extreme variability of the flow in this regime, so an average over 100 time sets has still not adequately sampled the behaviour of the flow in this region. Nevertheless, it is clear that the amount of clumping and velocity variation is increasing rapidly in the region.

Examination of $v_{\rm disp}$ in Fig. 3.14(b) shows that it too reaches a minor peak at $z = 2R_\star$. Because this marks the point where the diffuse clumps form into dense shells bounded by forward and reverse shocks, $v_{\rm disp}$ decreases as the smooth rarefied region begins to dominate. This downturn is short lived as the rarefied regions broaden and the shocked gas moves downstream.

The behaviour of C is a little surprising but not totally unexpected. A flow dominated by reverse shocks will have $C \approx -1$, since the velocity and density are anti-correlated. Fig. 3.14(c) shows this to be the case for the majority of the wind studied here. The initial portion of the wind moves sharply from correlated at the inner boundary to anti-correlated after a short distance, reaching a minimum at $z = 1.2$. This implies that reverse shocks are the dominant structures, but it is unwise to ignore the forward shocks. Indeed, in the later stages of the flow each dense shell is bounded by both an upstream reverse shock and a downstream forward shock. These forward shocks, although small in amplitude, could begin to dominate the flow further downstream.

Comparing these results with Runacres & Owocki (2002), shows good agreement in all of the parameters except C. They observe a downstream value of $C \approx 0$ indicating that both forward and reverse shocks are equally prevalent. In the model here the reverse shocks control the flow to a greater extent than the forward shocks, borne out by the the slow rise, away from $C = -1$ to $C = -0.5$ at the edge of the grid.

3.6.4 Spectral information

An indication of the absorbed radiation flux can be gained from displaying $\eta(x) = \eta(x, R_{\rm max})$ graphically, where $R_{\rm max}(= 4R_\star)$ is the maximum radius in the numerical do-

main. It is useful to view a time average of this quantity, Fig 3.15, since the higher frequencies are affected by the movement of the structure across the grid; the high frequency end is affected by high velocity material. From this quantity a P-Cygni profile for the time-averaged absorption can be estimated. Since the P-Cygni profile represents the absorption of radiation by a specific UV line, the relevant line opacity must be included in the calculation. In the 1D radial direction there is, of course, only an absorption component. The radiant intensity from the star, for a particular absorption line can be calculated from,

$$\tau(x) = \kappa_{\rm l}\eta(x, R_{\rm max}), \tag{3.9}$$

$$I(x) = I_\star(x)e^{-\tau(x)}, \tag{3.10}$$

where $\kappa_{\rm l}$ is the opacity coefficient of the particular ionic transition and $I_\star(x)$ is the incident intensity from the star. The calculation of a P-Cygni profile is deferred to Chapter 6, however it is still useful to consider the evolution of the wind structure in this regard and motivate the studies in further chapters.

A useful way of displaying the evolution of the continuum flux absorption, $\eta(x) = \tau(x)/\kappa_{\rm l}$, is in a trail plot. At first sight Fig. 3.16 appears unclear, however it contains much information about the dynamics of the wind. It indicates the path of optically thick shells in velocity space. Initially the shells do not feel much acceleration and the trails are steep. As the shells become optically thinner and more diffuse they accelerate and the corresponding trails develop shallower gradients. The detailed structure that is produced as shells accelerate and decelerate is dramatically shown as the trails follow a twisted path. It is clear that there is a minimum resolution for these optically thick blobs since all of the dark trails have similar width. This limiting size of the trails is the width of the line profile function, $\phi(x)$ (cf. equation (2.43)). The absorption of a blob with uniform constant density will be the same irrespective of its flow velocity due to the Doppler term

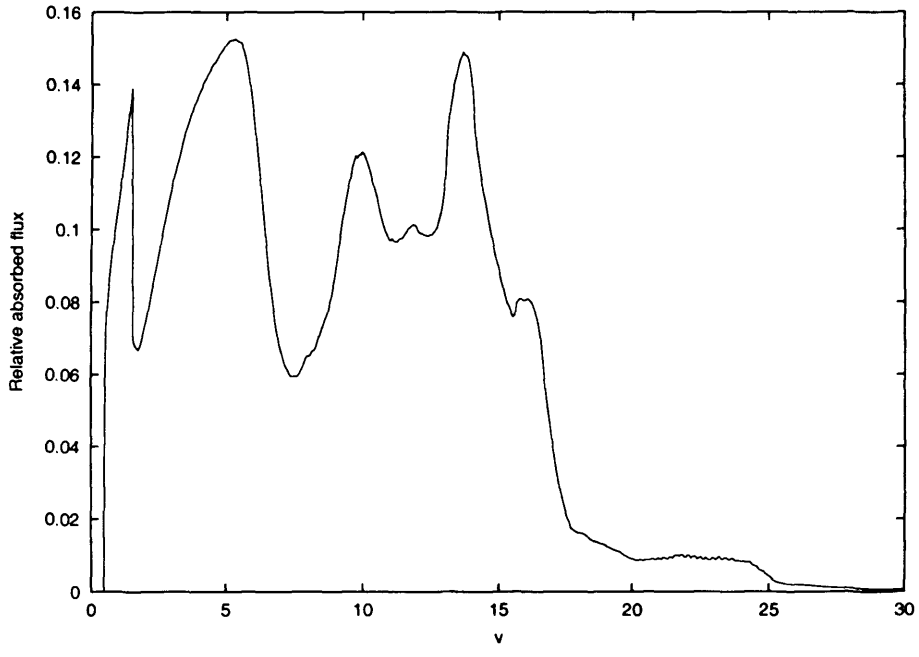

Figure 3.15: A time average of the absorbed flux from the model shown in § 3.6.2. This plot shows a strong absorption features at $v \approx 1$, 5 and 14. At the high velocity end the absorption becomes smaller as the gas is more rarefied. Due to the limited physical size of the computational domain the amount of gas at the high velocity end is less than in a real star.

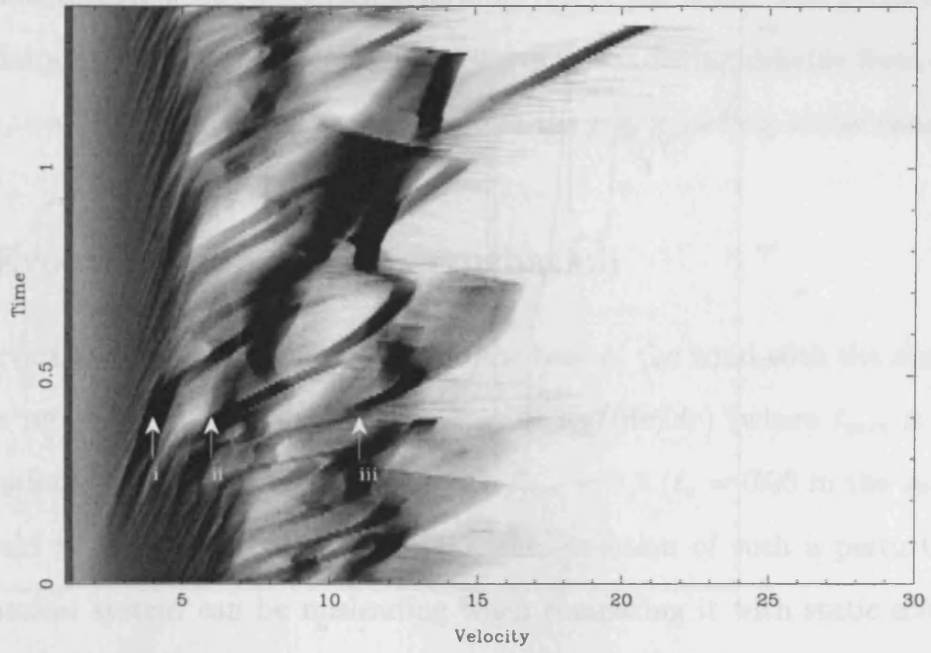

Figure 3.16: A trail diagram plotting values of $\eta(x)$ as mean averaged greyscale points at different times. The continuous, albeit diffuse, lines in the plot indicate the path of optically thick material. Between velocities $v = 0 - 3a_0$ the flow is smooth and not dominated by unstable shells. The points marked *i*, *ii* and *iii* are identified with discrete features in the flow, shown in Fig. 3.17.

in equation (2.43) (in a simple argument which neglects external dynamical influences on the blob). The absorption of the blob is smeared out over the width of the profile function. The top-hat nature of the profile function is reflected in the coarse structure of the trails. In Chapter 6 we address this issue further.

Care must be taken when interpreting information from such a trail plot, since flow structures with the same velocity can appear at different places in the wind. This can make the origin of each trail ambiguous. Nevertheless, a trail that remains well defined for a significant time is the result of a single optically thick feature, since the combination of differently spaced features would not have the same coherence.

The points marked i, ii, iii in Fig. 3.16 have been identified with dense shells on the density plot Fig. 3.17, which is taken at $t = 0.414$. In this case the three marked trails are the dense shells which stand out against the flow as being the most optically thick. It

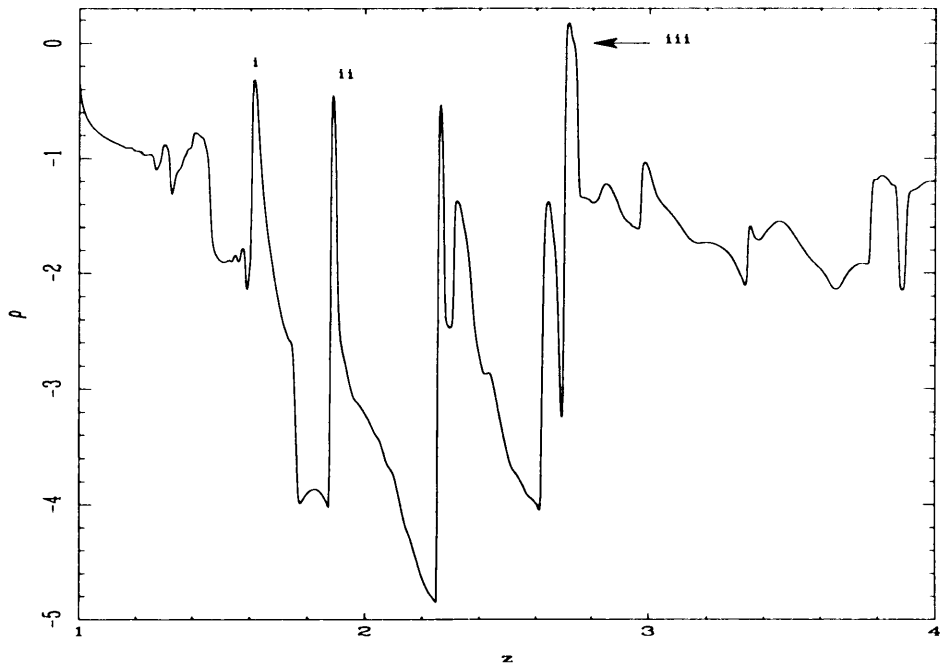

Figure 3.17: This plot of logρ against z is taken at $t = 0.414$. The dense shells labelled with i, ii, iii match those whose histories are shown in the absorption trail plot, Fig. 3.16.

is clear from Figs. 3.16 and 3.17 that, although the shell marked i is not the densest shell, it has the highest optical depth of the shells at this time. This is evident from its steep evolutionary path, indicating that the region accelerates slowly and therefore receives less driving.

The initial perturbation (described in §3.6.2) is marked iii in Figs. 3.16 and 3.17. The path marking the evolution of this lump is interesting. The point marked as iii in Fig.3.16 indicates where the evolution of this lump changes from optically thin evolution to optically thick. The difference in the evolution is obvious in two ways; the dark, steeper trail shows a marked difference to the earlier light, shallow trail of the optically thin evolution. This transition occurs because of minor shells colliding with the perturbation shell. As faster shells merge with the perturbation from upstream, so does the perturbation sweep up slower shells downstream of it. These interactions increase the density of the shell and make it optically thicker. As this behaviour continues the shell slows and at $t = 0.485$ it merges with another shell and its, once distinctive, optical depth becomes muddled with

that of a shell further upstream which is forming out of the noise. The perturbation shell does not disappear but from a spectral perspective it is indistinguishable from other parts of the flow, whilst remaining the densest shell in the region of flow under consideration.

3.6.5 Evolution of a large perturbation

A wide perturbation was introduced close to the base of the wind with the aim of investigating the properties of a structure with $\ell_{pert} > v_{\rm th}/(dv/dr)$ (where ℓ_{pert} is the length of perturbation). We add a perturbation with $\ell_{pert} = 0.2$ ($\ell_s = 0.05$ in the same region) which should be stable to the line driving. The evolution of such a perturbation in a hydrodynamical system can be misleading when comparing it with static solutions (i.e. those of OR84) since it will not behave as an unique block but as a patch of fluid. The perturbations used previously in this chapter (and in later chapters) have all been relatively narrow slabs of constant velocity or density. Contrary to the results of the previous section we use a smoothly oscillating form for the large slab, which will behave less like a pair of Sod shock tubes (cf. Appendix §A.4) and more like a smoothly varying sound wave. We use a cosine with a wavelength of $\lambda = \ell_{pert} = 0.2$.

The evolution of this perturbation is shown in Figs. 3.18 and 3.19. Initially the perturbation retains some of its sinusoidal nature and interestingly forms a weak forward-reverse shock pair either side of the thick swept up clump (cf. dashed curve in Fig. 3.18(b)).

Unlike the previous cases seen in this chapter the dense downstream clump does not continue becoming denser and spread over an increasingly narrow region but as shown in Fig. 3.19, at later times the clump becomes more extended and diffuser. Gradually the high density region steepens into a shock (cf. dashed line Fig 3.19(b)), but at this point in the flow we are no longer looking at a distinct object with a large wavelength but a more complicated feature containing rarefactions and compressions of gas. The analysis of the evolution of the perturbation cannot be further clarified since the shock structure which appears may be due entirely to a steepening of the high density shell as it ploughs

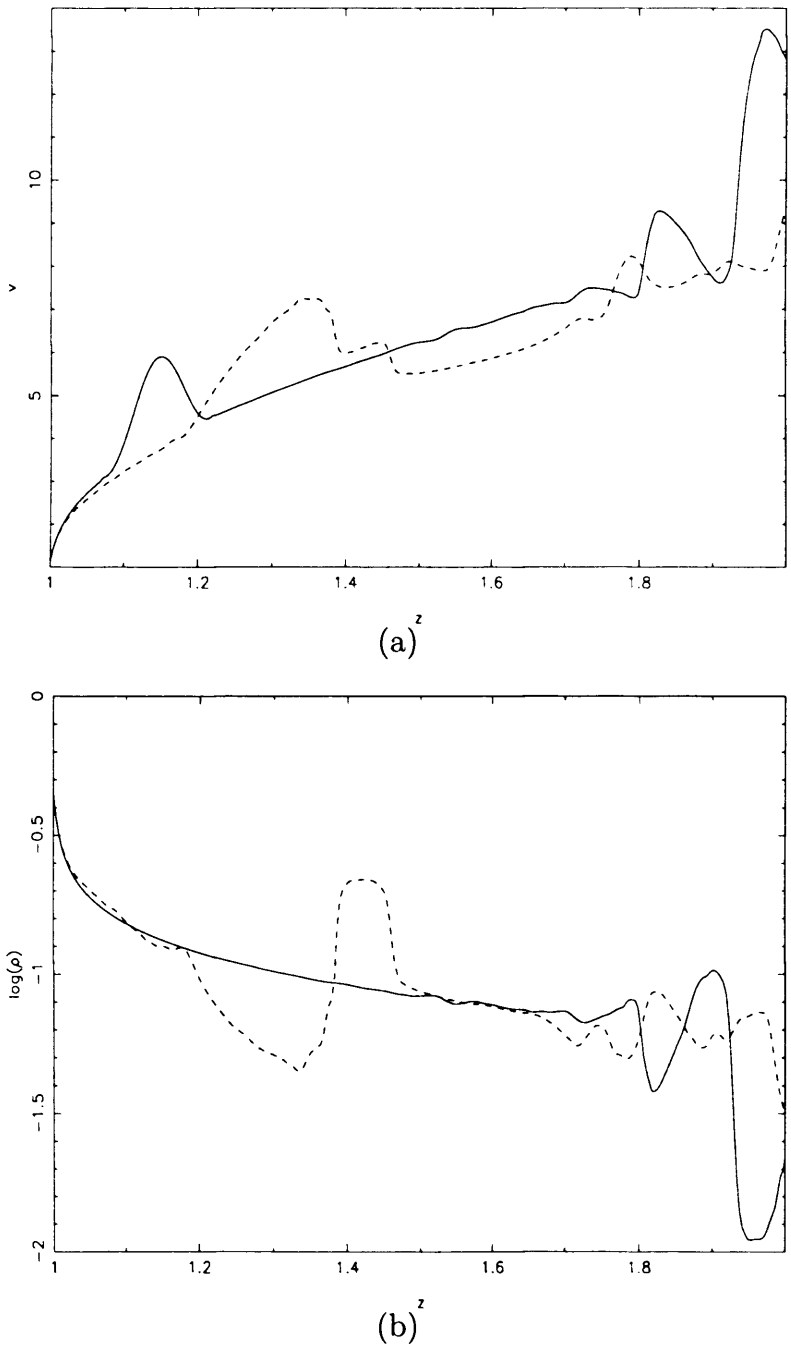

Figure 3.18: The initial evolution of a long perturbation applied just to the velocity field. Solid curve is the initial condition; dashed curve is at $t = 0.075$. a) velocity, b) density

into the downstream material.

The evolution of the perturbation is difficult to interpret in a rigorous way since its environment is highly structured. The amplitude of the perturbation is not rapidly amplified which suggests that it is stable, however the smooth feature develops structure which suggests that it is unstable. The prediction from OR84 shown in equations (2.54)-(2.55) is difficult to follow up because of the complications of the time dependency of the results (OR84 are idealised time independent results). The initial evolution of the perturbation appears to be stable and is dominated by smoothly varying structure, but as the line de-shadowing instabilities prevail, the dense clump begins to break up.

3.6.6 Physical model

The results in this section have thus far been calculated using the physical parameters of OCR (cf. Table 3.1), which does not accurately represent an OB star. By way of comparison we used our radiation driving code to simulate the wind from a star with parameters the same as ζ Puppis, given in Table 3.2. The velocity is given, not in multiples of the isothermal sound speed as was done with the OCR results but in km s^{-1}, so as not to cause confusion since the value of the sound speed in OCR is much higher than that of ζ Puppis. In these calculations, as with all of the previous calculations we use a supersonic inner boundary condition. We will relax this later but at present we keep it in place to allow the model to be compared with the toy model.

In this 'real' star model the wind velocity is much higher than the OCR toy model. From Fig. 3.20 we can see that the wind is still highly structured. An estimate of the terminal velocity and mass loss rate can be obtained from these results to be, $v_\infty \approx$ 1500km s^{-1} and $\dot{M} \approx 1 \times 10^{-6} M_\odot yr^{-1}$. These values are comparable to those published by Runacres & Owocki (2002), although they are a slightly lower. The value of the terminal velocity is much lower than the observed value, $v_\infty \approx$ 2400km s^{-1} (Howarth et al. 1997) but the reader must note that our models only extend out to $z = 4R_\star$, and

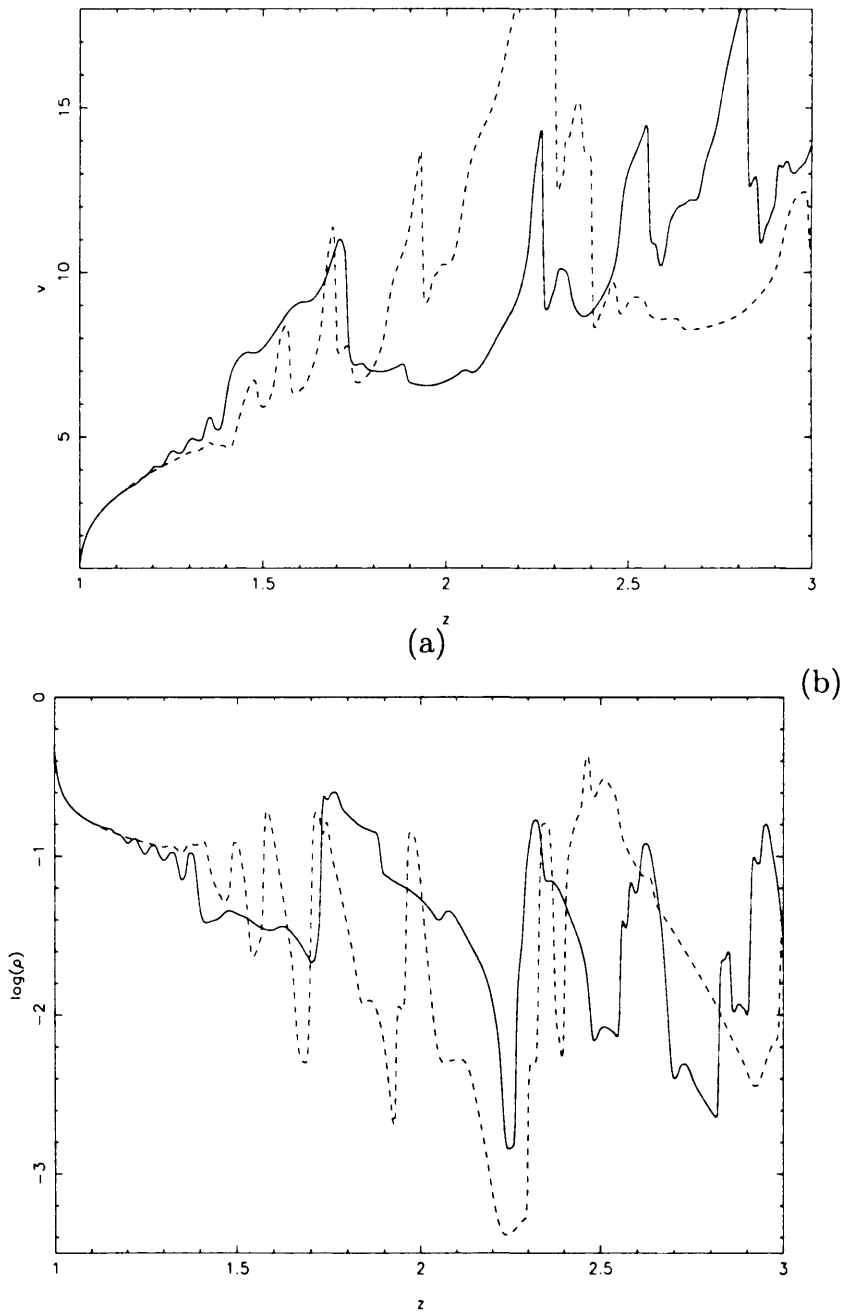

Figure 3.19: The evolution of the flow at $t = 0.135$ (solid) and $t = 0.210$ (dashed). In the dashed curve instabilities begin to appear at the trailing and leading edges of the perturbation as these become optically thin. a) velocity, b) density.

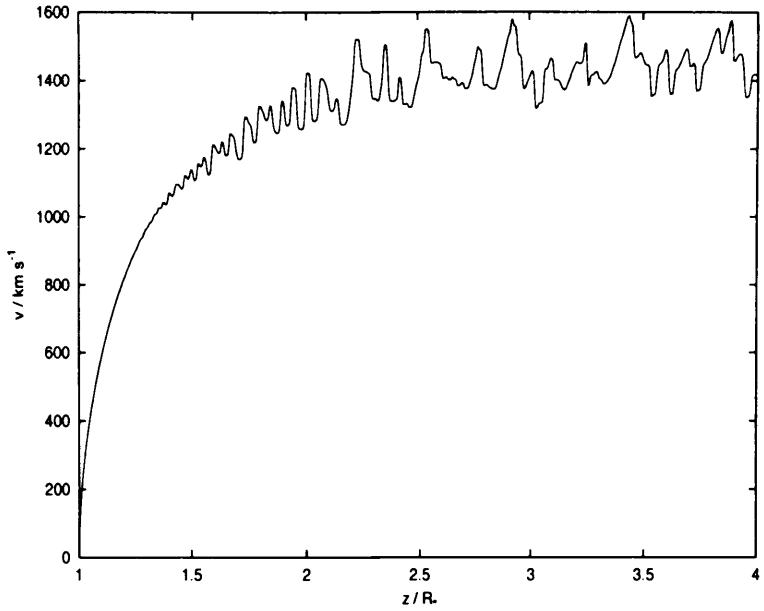

(a)

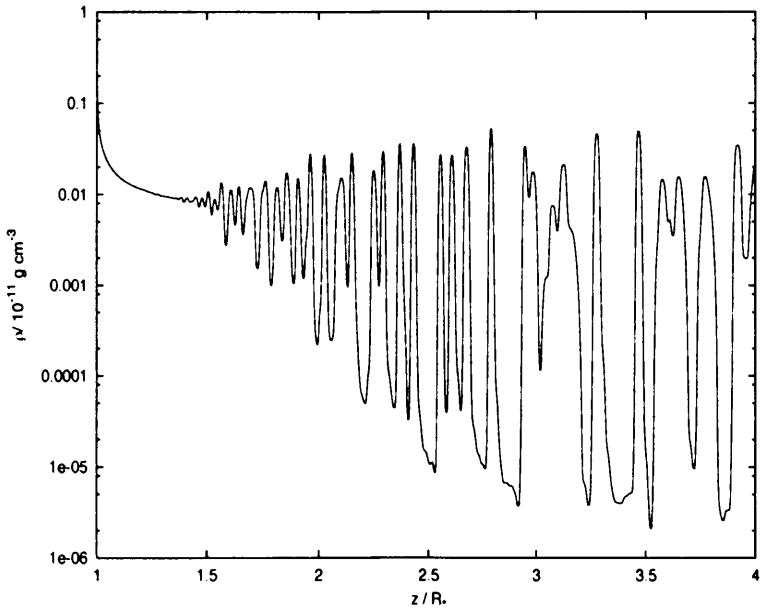

(b)

Figure 3.20: Results for ζ Puppis using the physical parameter data in Table 3.2. The flow contains much structure, comparable with the models in this chapter.

Physical Parameter	Value	
Stellar mass	$M_\star$	$40M_\odot$
Stellar radius	$R_\star$	$19R_\odot$
Isothermal sound speed	a_0	$22.7\mathrm{km\,s^{-1}}$
	v_{th}/a_0	0.3
CAK index	α	0.7
Wind temperature	T	3.78×10^4 K
Stellar Luminosity	$L_\star$	$6.8 \times 10^5 \mathrm{L}_\odot$
Opacity constant	$\kappa_0 v_{\mathrm{th}}/c$	$3500\ \mathrm{cm^2 g^{-1}}$
Optically thick line limit	κ_{max}	$10^{-3}\kappa_0$
Inner Boundary Condition	Parameter	Value
Density	ρ_0	$1.12 \times 10^{-11}\mathrm{g\,cm^{-3}}$
Velocity	d^2v/dz^2	0

Table 3.2: Code and physical parameter values for ζ Puppis

do not correspond to the same point in the flow that the observations are taken. In our results the wind is still accelerating so the term "terminal velocity" is not strictly true and "maximum velocity" would be more appropriate.

We will return to ζ Puppis in Chapter 5 where we will use our implementation of the radiative driving force to compare these results with those using a Gaussian profile function and a subsonic inner boundary condition.

Summary

During this chapter we have used the analytical models of Chapter 2, for continuum and line driven (in both the Sobolev and non-Sobolev cases) winds to:

- investigate the wind stability to perturbations in velocity and/or density.
- test the convolution method for the solution of non-Sobolev line driving. Our method and that of other authors are in good agreement in the structure which appears, the evolution of the structure into shocks and the statistical behaviour of the solutions.
- use our implementation of the line driving force to calculate the mass loss rate and

terminal velocity for a real star (in this case ζ Puppis). These results are comparable with those of Runacres & Owocki 2002, to a first approximation.

- investigate the stability of the wind solutions when the direction which the velocity gradient is calculated is changed.

An interesting result of this chapter is that the stability of the wind depends not only on the driving, as the stability analysis of Chapter 2 suggested, but in the line-driven case on numerical routine as well. Our results (published in Gomez & Williams 2003) show that the global relaxation of time dependent simulations to steady state depends on the direction which the velocity gradient is calculated. The behaviour can be understood in terms of inwards propagation of information, much as the CAK critical point can be understood in terms of Abbott waves. This is a difficult issue to resolve and we recognise that it requires further study.

In the following chapter we move the simulation of stellar winds into two dimensions, demonstrating the importance of including radial driving in two dimensional hydrodynamical simulations of these phenomena.

Chapter 4

2D time-dependence of wind models

4.1 Introduction

In this chapter we develop the study of unstable wind structure further by considering two dimensional flow. As in the previous chapter, we consider the same 'toy model' since at this stage we will not make any quantitative comparisons with observations. We re-iterate (with reference to the physical parameters in Table 3.1) the length scale is $1R_{\star}$, the velocity is measured in units of the sound speed and density is in units of$\times 10^{-11}$g cm^{-3} implying that the results are in a region of physical relevance and not just mathematical curiosity[1].

We will concentrate on the simplest two dimensional case, radial radiation transport through plane-parallel flow. This equates to studying a narrow slice of the wind at a reasonable distance from the photosphere. At such a distance from the central star we ignore finite disc effects and the incident continuum radiation is assumed to be radially streaming from the star (there are no non-radial photons).

This has the advantage that only a single ray calculation need be performed, parallel to one axis of the computational grid. It may be argued that this approach is little more than a series of one-dimensional simulations in separate but contiguous channels. However,

[1]Sections from this chapter have been published in Gomez & Williams (2003)

while there is no tangential component to the radiation driving, the hydrodynamics are calculated in both dimensions. We will see that flows which are driven only in the radial direction can have fully two-dimensional structures.

The flows are studied in a similar way to the one-dimensional cases presented above. Perturbations are made to the velocity and/or density field, close to the base of the wind. Dense shell structures appear in the flow once it has become less regular and more noise dominated. We will present a selection of results which highlight the effect of a perturbation to the initial conditions, on the flow structure.

4.2 Hydrodynamically unstable structures in 2D

There are 2 main classes of instability in 2D hydrodynamics, those associated with a shear at the interface between two fluids moving at different transverse velocities (i.e. Kelvin-Helmholtz) and those where low density fluid is accelerated through a high density fluid (i.e. Rayleigh-Taylor, Richtmyer-Meshkov). In the case of line driven winds the impetus is provided by absorption from the incident radiation field (while in the Parker wind the impetus is provided by the gravitational field although the acceleration is in the opposite direction).

In winds that have large tangential velocities (e.g. from stellar rotation), the shear instability is observed as different velocity 'streams' move past each other (e.g. Co-rotating Interaction Regions, cf. Cranmer & Owocki 1996). This phenomenon is also seen in colliding winds where post-interaction gas is pushed in a tangential direction from material behind (cf. Pittard 1999). In the solar wind there is a similar interaction where the colliding fast and slow winds can lead to the formation of spiral shocks, with shear flow along the internal contact surfaces.

Considering, as always, an incompressible, inviscid gas, the dispersion relation for a

perturbed two-fluid interface is given by Drazin & Reid (1981) in the following form,

$$s = \sigma + i\omega = -ik\frac{\rho_1 u_1 + \rho_2 u_2}{\rho_1 + \rho_2} \pm \left[\frac{k^2\rho_1\rho_2\Delta u^2}{(\rho_1+\rho_2)^2} - \tilde{k}g\left(\frac{\rho_1-\rho_2}{\rho_1+\rho_2}\right)\right]^{1/2}, \tag{4.1}$$

where $\tilde{k} = (k^2 + l^2)^{1/2}$ and k, l are the wavenumbers in the orthogonal directions, y and z. In the following analysis we assume that there is no z component to the wavenumber ($l = 0$). The acceleration across the interface between the two regions is represented by g, irrespective of whether it is due to gravity, gas pressure or another force (e.g. line driving) and is aligned with the z axis.

We identify modes varying as

$$\psi = A\exp(st + iky) \tag{4.2}$$

where the wave amplitude is given by A, the frequency s is complex (with real part σ and imaginary part ω), and the wavenumber k is real. This is the natural assumption when treating the development of free-boundary flows from an initial condition (rather than the spatial development of a flow from a time-varying source).

The interface between the two fluids is assumed initially to be at constant z and to have an infinitesimal width. The subscript '2' on variables refers to the fluid on top of (further from the star than) the ones with subscript '1'. The variable u refers to velocity of the gas in the y direction and $\Delta u = |u_1 - u_2|$.

Equation (4.1) produces unstable growth if the term in square brackets is real (i.e. $\sigma > 0$). This can be expressed in the criterion,

$$\Delta u^2 > \frac{g}{k}\frac{\rho_1^2 - \rho_2^2}{\rho_1\rho_2} \tag{4.3}$$

Below we look at two different scenarios where this can be satisfied.

4.2.1 Rayleigh-Taylor

This unstable phenomenon is named after Lord Rayleigh (1883) who investigated the stability of fluids in a medium whose density is stratified perpendicular to gravity. This work was taken further by Taylor (1950) who applied it to accelerating fluids in general and not just to those accelerated by a gravitational field.

Rayleigh-Taylor (R-T) instabilities occur at the interface between two regions of different density. The criterion, equation (4.3), is satisfied when $\rho_2 > \rho_1$, i.e. the heavier fluid is above the lighter. R-T instabilities affect a wide variety of astrophysical situations. These instabilities are often referred to as "fingers" when seen passing through dense gas.

We consider fluid motion in the radial direction alone and for $u_1 = u_2$ (and therefore that $\Delta u = 0$) equation (4.1) becomes,

$$\sigma = \left(gk \frac{\rho_1 - \rho_2}{\rho_1 + \rho_2} \right)^{1/2} . \tag{4.4}$$

When $\rho_2 > \rho_1$, s becomes real and equation (4.2) grows exponentially with the characteristic time, $\tau = 1/\sigma$.

4.2.2 Richtmyer-Meshkov

Another type of instability within this sharp density contrast class is the Richtmyer-Meshkov (R-M) instability. The distinction between this and the R-T instability is the presence of a shock crossing the interface between two fluids of different density. For such an impulsively accelerated interface, Richtmyer (1960) describes the velocity of the resulting perturbation as,

$$v = Ak\Delta v \frac{\rho - \rho'}{\rho + \rho'}, \tag{4.5}$$

where all of the variables have the meanings previously stated and Δv is the change in radial velocity of the interface from the passage of a shock. The passage of the shock amplifies the R-T structure which is present or forming at the interface.

4.2.3 Kelvin-Helmholtz

If at the interface between two fluids there is a difference in the tangential velocities of the fluids, Kelvin-Helmholtz (K-H) instability can develop. If we consider again equation (4.3), we can see that if $\rho_1 = \rho_2$ the criterion is always satisfied and the flow is always unstable. The criterion is also satisfied if $g = 0$ but in the applications we will be considering there is will always be an acceleration. This allows us to rewrite equation (4.1) as

$$\sigma = \frac{k}{\sqrt{2}}\rho_1 \Delta u \tag{4.6}$$

and when used in equation (4.2) shows the unstable growth of the perturbation.

K-H instabilities are found to exist in many astrophysical scenarios. The most prominent and widespread instance of these instabilities are astrophysical jets, which have a great variety of forms, from molecular gas jets from star forming regions (Lim 2003; Baty & Keppens 2002) to the vortical structure observed in the Cat's Eye nebula (Ryu et al. 2000). These instabilities often referred to as "Cat's eyes" (unrelated to the name of the nebula) because of their vortical structure.

These are simplistic and idealized formulations since they assume equilibrium large scale flow and that the fluids are in pressure equilibrium across the interface. This analysis does not allow for any time dependence, thus the state of two such fluids will locally change significantly in a hydrodynamical scenario. It does however illustrate the initial dependence that the state variables have on seeding the instability.

4.3 Two dimensional structure

With the above awareness of hydrodynamical instabilities we consider the two dimensional evolution of perturbations to the background flow in the continuum case. In two dimensions the structure is complicated by lateral expansion and the unstable structures detailed above.

In the following sections we will discuss perturbations with different characteristics in M, R_ρ space but having the same physical dimensions (20×40 cells $= 0.075 \times 0.15 R_\star$). We investigate how perturbations with different characteristics are affected by K-H and R-T instabilities as well as the instability associated with the driving mechanism. Some perturbations have higher velocity or density contrasts than could arise from noise in the lower wind. This is not too much of a problem because the conditions of the inner wind and effects from the photosphere are not observationally constrained.

All of the plots in the following sections have a greyscale density map which in the continuum driving case is overlaid with velocity contours. Although the greyscale corresponds to a fixed range of density it is not intended to be used to obtain detailed results, but rather to illustrate the structure in the flow. We choose the greyscale to best reflect the dynamical range of density, however we allow the higher densities to saturate. This causes very little information loss and improves the visibility of extended low-contrast features.

In all 2D simulations we insert a representative 1D flow solution dataset in each channel so that the gas is initially isotropic in the non-radial direction. For continuum and CAK winds the background is smooth whereas in the non-Sobolev case the inherent structure in 1D produces dense shells in 2D.

4.4 Continuum response to perturbations

4.4.1 High density contrast perturbation with mean flow velocity

This case is perhaps an extreme example of a perturbation that could arise out of noise in a wind flow, however a large scale mass ejection process could release a dense lump similar to this with $R_\rho = 10$ ($M = 1$). The evolution of the perturbation resembles that of an expanding bubble or what Smarr et al. (1984) refer to as a 'cocoon', as can be seen

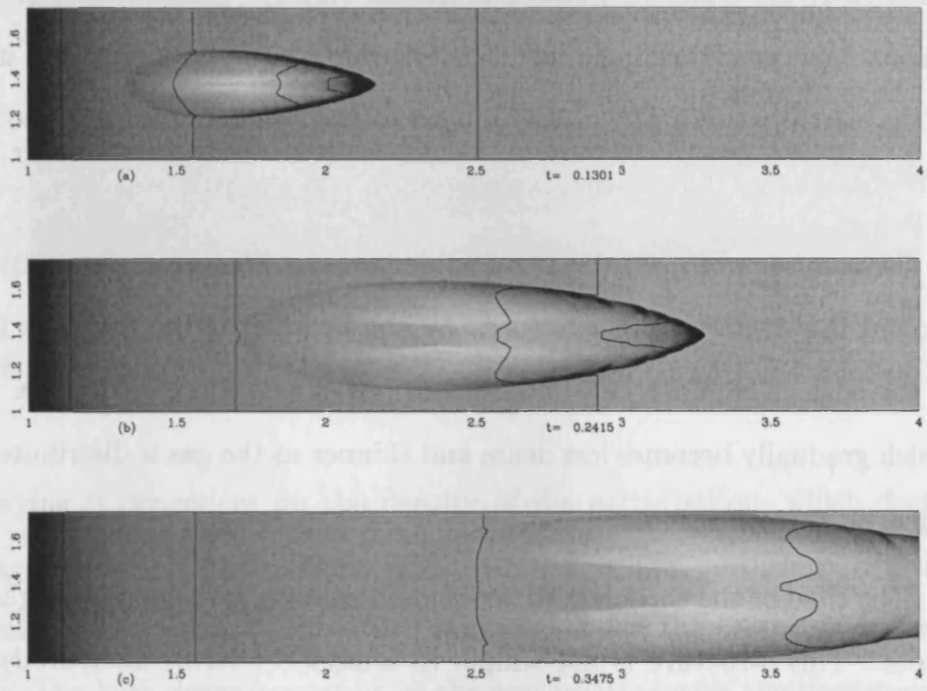

Figure 4.1: The evolution of a perturbation to a steady background flow with $R_\rho = 10$, $M = 1$. The contours are of constant velocity. These and subsequent plots are slightly compressed in the y-direction so that the complete set may be displayed together, for ease of viewing and comparison. The resolution of the grid is the same in each direction, however the aspect ratio is slightly different.

in Fig. 4.1. Although the structure is denser at the downstream end than the upstream end, it nevertheless is reminiscent of an expanding shell.

In this case there is no initial velocity gradient at the perturbation but as is expected, hydrodynamic expansion of the high density gas produces a velocity disturbance associated with the perturbation. The downstream edge becomes more compacted as it expands into the ambient gas. This edge has a higher velocity than its upstream counterpart since the driving increases with gas density; the rectangular perturbation evolves into a high density bow shock leading a low density reverse bow shock from the upstream expansion of the perturbation. The upstream component gradually blends into the background as it becomes more diffuse with expansion.

As can be seen from the velocity contours in Fig. 4.1 the velocity gradient steepens around this surface, as is evidenced by the bending of the contours to follow the shape of the edge. The, once flat, downstream bow-shock sharpens into an 'arrowhead' shape, which gradually becomes less dense and thinner as the gas is distributed over the expanding area.

The shell of the cocoon does not remain smooth, but develops higher density unstable knots. This structure is not simple to analyse in terms of hydrodynamic instabilities since the pressure field is not uniform, as required by our simple analysis of K-H and R-T instabilities. In Fig. 4.2(b), the velocity enhancement in the shell is small (a factor of $\approx$ 1.4) while the density is a factor of $\approx$ 5 times the background. This structure therefore is highly suggestive of R-T and not K-H instability despite the presence of shear velocities at the edge of the bubble. It seems likely that the structure formed is due to R-T instability which is then exacerbated by the radiation driving. The structure that this forms does not stay on the surface but propagates toward the centre of the disturbance, and although these unstable waves are initially small in amplitude they will break up the perturbation. The acceleration of the perturbation decreases as it expands, an effect of the driving instability.

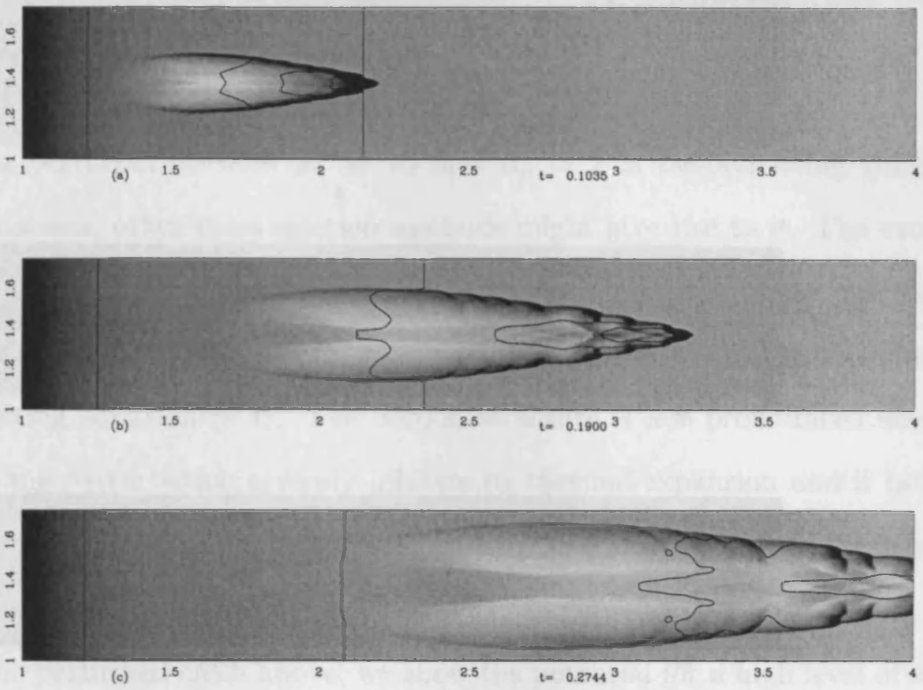

Figure 4.2: The evolution of a perturbation to a steady background flow with $R_\rho = 10$, $M = 2$.

The driving is dependent on the density of the perturbation, which decreases with thermal gas expansion. As Williams (1999) showed, a flow perturbation with $v_\mathrm{p} \leq 2a_0$ will be dominated by thermal expansion, thus in this case the perturbation expands as it propagates. The high density contrast of the perturbation with the background medium causes it to be driven downstream but as can be seen thermal expansion is still prominent.

4.4.2 Moderate Mach number, high density contrast perturbation

We repeat the model from the previous section but give the perturbation an initial velocity, $M = 2$, $R_\rho = 10$. The main difference between these is that the onset of the R-T instabilities is at an earlier time as shown in Fig. 4.2, also the 'fingers' are more pronounced and appear in the direction of the driving. The perturbation develops structure on a faster timescale than in he previous model. This is because of the increased initial

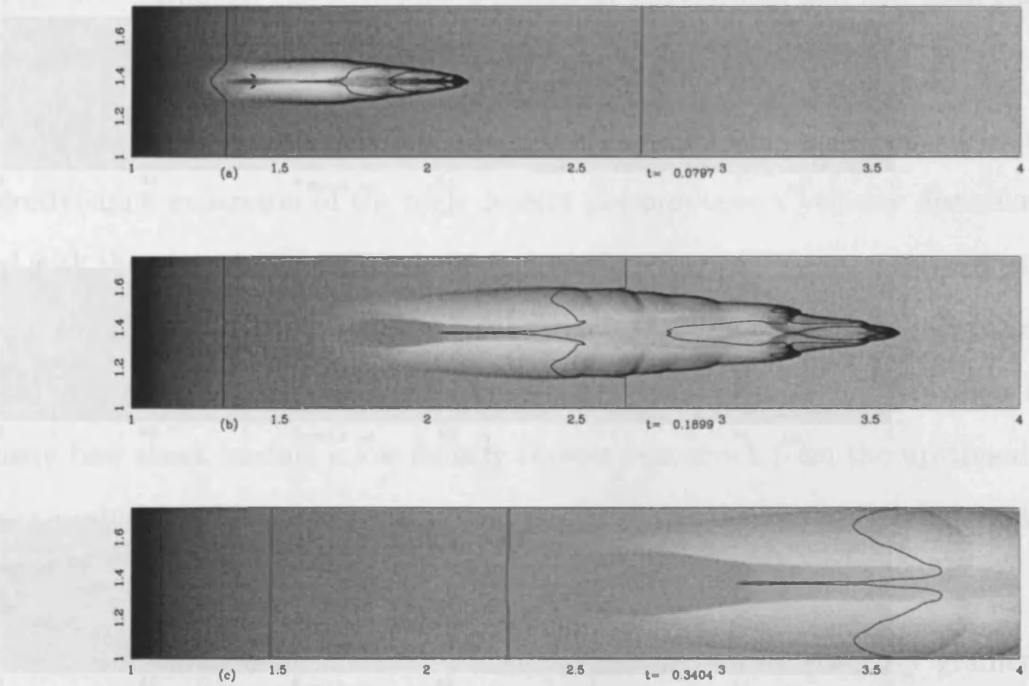

Figure 4.3: The evolution of a perturbation to a steady background flow with $R_\rho = 2$, $M = 10$.

velocity which pushed more gas into the expanding shell and increases the driving. In equation (4.4) $\rho_1 - \rho_2$ and g are larger than the previous perturbation, giving a smaller growth timescale.

At the downstream head of the cocoon the contours are tightly packed, showing that the high density region is strongly accelerated by the driving. With the addition of an initial velocity, the evolution of the perturbation is less similar to an expanding cocoon and more akin to a supersonic bullet. This is significant from a physical and an observational point of view, since any perturbation formed is likely to have both density and velocity components.

4.4.3 High Mach number, moderate density contrast perturbation

Although a perturbation with $M = 10$ and $R_\rho = 2$ is beyond being generated from noise fluctuations, other mass ejection methods might give rise to it. The evolution seen in Fig. 4.3 is strikingly similar to the structures seen in Fig. 4.2. This confirms that the unstable structure is directly dependent on ρ and indirectly on u which is counter intuitive after inspecting equation (4.4). The cocoon structure is less pronounced since the high initial v of the perturbation severely inhibits its thermal expansion and it behaves more like a supersonic bullet. This is similar to the sorts of objects seen in the studies of jets (e.g. Smarr et al. 1984, Downes & Ray 1998).

In all the perturbed cases above, we show the potential for a high level of structure in the wind, from small disturbances. In a real wind there is likely to be small scale structure which can seed such instabilities, thus making the wind highly structured.

4.5 Sobolev response to perturbations

The structure which develops in the flow due to externally added perturbations in the case of a line-driven wind model, although having similar general flow properties to the continuum driven case, is significantly different in specific circumstances. In this section we present a full hydrodynamical treatment of the wind for the OB star with characteristics given in Table 3.1, with a Sobolev form for the driving, in two dimensions. The method of calculating the velocity gradient (used in the calculation of the optical depth) is the stable, downstream method as discussed in §3.7. Close to the star the calculation of the optical depth at a point in the photosphere must include an average over the solid angle which the star subtends. In addition to this, the path length of the photons from the stellar limbs is different than those from the core, in this region. Lamers & Cassinelli (1999) show that beyond $R \approx 4R_\star$ the dependence of the path length on the point of

emanation of the photons can be neglected. As a first approximation we also ignore these effects.

We consider similar perturbation parameters to the continuum case above, to allow comparison between the results.

4.5.1 Moderate velocity and density contrast perturbation

A perturbation with $M = 2$ and $R_\rho = 2$ is placed in the supersonic region of the flow. The behaviour contrasts to that of the previous section in that the perturbation remains centrally condensed while the downstream end accelerates away from it. This downstream edge rapidly detaches from the main body and because it is optically thin is highly accelerated. This continues expanding until the optical depth of this edge is significantly increased as it ploughs further into background material. This effect is of very low amplitude and the perturbation appears to propagate in a quasi-static fashion (continuing to expand but interacting very little with the background gas).

The higher density upstream part of the initial perturbation expands under thermal pressure while it is optically thick. When it has become sufficiently optically thin, it too is driven by the radiation field. A point is reached where the evolved perturbation alters little in form as it continues to expand in the downstream flow, Fig. 4.4(b)-(c): the perturbation expands and becomes more diffuse but does not undergo any dynamical changes.

There is no appreciable change in the results of Fig. 4.4 if the model parameters are changed to $M = 1$, $R_\rho = 2$ (i.e. the same R_ρ as previously but with zero velocity perturbation). This supports the notion that the evolution of the perturbation is dominated by thermal pressure. Although the thermal pressure is important to this initially optically thick perturbation, that is not to say that the radiation driving is insignificant. Whilst the perturbation is optically thick gas pressure is dominant in the expansion of the perturbation. When the lump becomes optically thinner the effect of the radiation driving

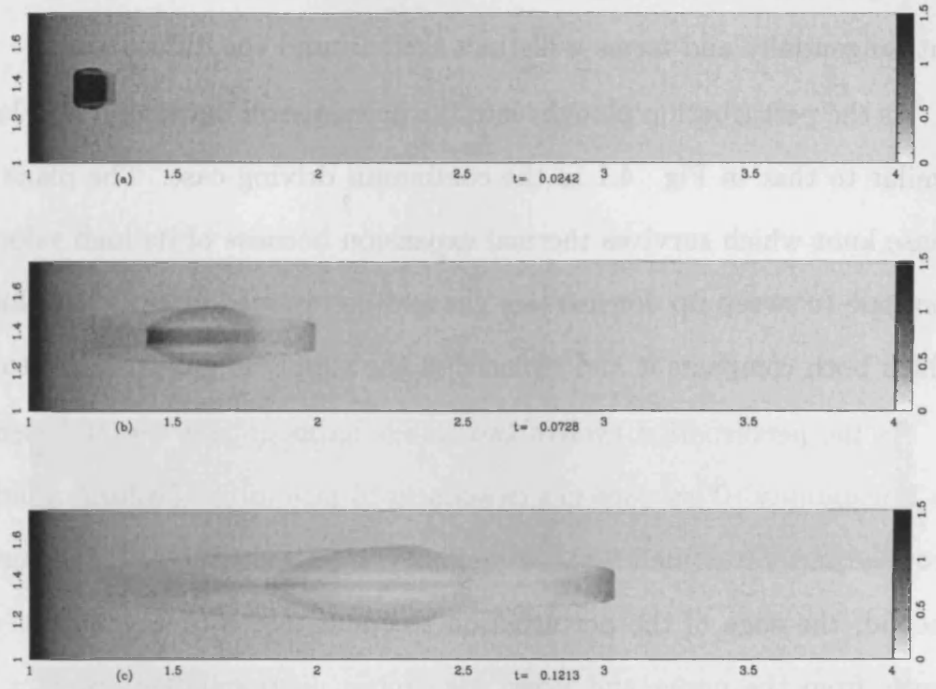

Figure 4.4: The evolution of an optically thick perturbation, $M = 2$ and $R_\rho = 2$, in a CAK force model. Due to the low velocity of the perturbation it initially expands predominantly from gas pressure expansion. Once the perturbation is optically thin enough to be driven by the radiation field the gas has formed a macroscopic structure which cannot be considered as one object, but distinct regions.

is felt by the gas and the subsequent expansion and evolution is reliant on this. The structure of the perturbation is set by the state which the thermal expansion leaves it in, at the time that radiation pressure dominates. The unstable nature of the radiation pressure appears as the accelerating gas becomes optically thin, further accelerating it and making it optically thinner.

4.5.2 High Mach number, mean flow density perturbation

As another example of perturbed behaviour we enhance the velocity over the perturbed region by $M = 4$ and leave the density of the wind undisturbed, $R_\rho = 1$. As Fig. 4.5 shows the enhanced velocity locally induces a density enhancement. As the faster moving gas sweeps up a dense shell, the shell continues to sweep up material as it propagates

leaving a wake of diffuse gas. As the shell accretes downstream gas some gas is pushed out tangentially and forms a distinct shell around the diffuse wake.

As the perturbation ploughs into the downstream material it develops a pointed shape similar to that in Fig. 4.1 in the continuum driving case. The plane front forms into a dense knot which survives thermal expansion because of its high velocity. This knot will continue to sweep up downstream gas and be rammed by optically thin gas from behind, which both compacts it and replenishes the supply of gas pushed into the cocoon.

As the perturbation evolves two things happen: first the high density shell develops R-T instability. This does not develop until late in the evolution and the characteristic growth time is too small for them to make an impact while the structure is inside the grid. Second, the edge of the perturbation steepens into a reverse shock. As the rarefaction waves from the upper and lower edge move upstream they interact forming a density enhancement in the middle of the diffuse gas, as seen in Fig. 4.5(c).

4.5.3 High Mach number, high density contrast perturbation

Although the perturbed flow of the previous section was useful for learning about the effect of velocity disturbances to the flow, there is little control over the initial form of the density perturbation induced. Therefore we return to a velocity and density perturbed flow introducing a perturbation which has twice the velocity and density amplitude of that in §4.5.1, $M = 4$ and $R_\rho = 4$. The reason for choosing such large amplitudes is to investigate whether the thermal or radiation pressure is more dominant in this initially high velocity and density perturbation.

The structure seen in Fig. 4.6 is reminiscent of that seen in Fig 4.5, with a thicker shell initially. The evolution of the perturbation departs from that seen in Fig. 4.5 gradually until the original slab perturbation becomes a focal lump. At this point optically thin gas from the perturbed region creeps around the lump and begins its own propagation into the undisturbed medium. This shows that the optically thin gas is inhibited by the

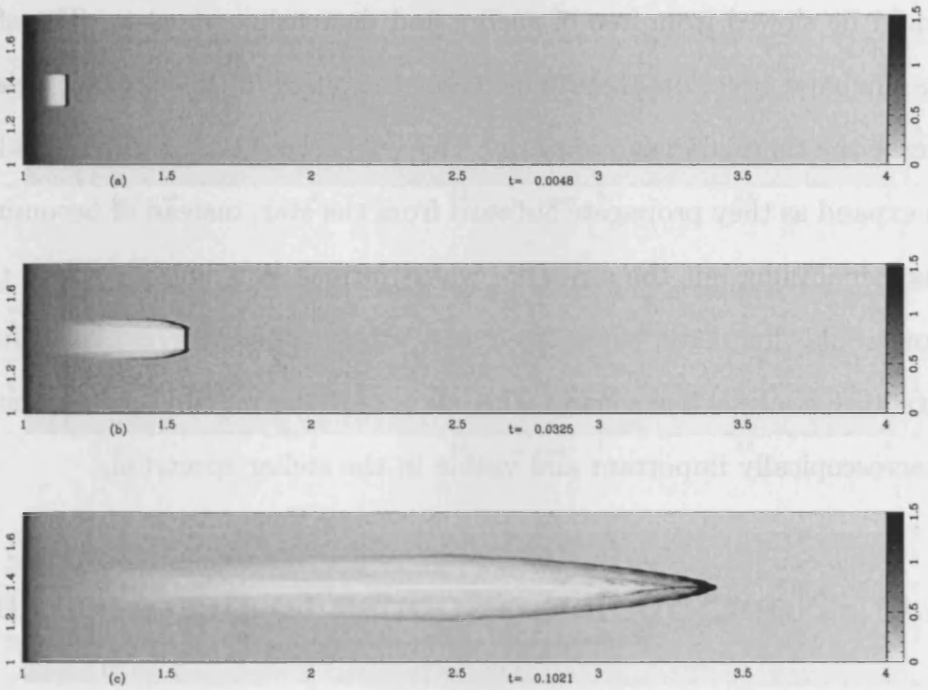

Figure 4.5: The evolution of a perturbation with $M = 4, R_\rho = 1$, in a CAK force model. This shows that a dense shell of swept up material is quickly formed from accelerated gas impacting on the high density perturbation. The perturbation forms a bow shock which subsequently suffers under RT instabilities.

downstream dense focal lump. Once past this obstacle the gas is accelerated freely by the radiation field.

This behaviour could be of importance to the wider structure of the wind. If this ejected optically thin region increases in density from interaction with the medium, subsequent dense knots could be formed along this path in the flow. However this treatment ignores the spherical divergence of the radiation field and any non-isothermal considerations about the state of the gas. We would expect that the propagation of the structure would be slowed from loss of energy and decreasing impetus. The effect of changing to an adiabatic equation of state increases the effect of the thermal pressure, and would increase the thermal expansion rate. This effect would make the dense knots more inclined to expand as they propagate outward from the star, instead of becoming more condensed. thus smoothing out the structure which forms. It is unclear where this thermal expansion would dominate, since the dynamics of the system are complicated, as the above structure analysis has shown. This allows for the possibility that the structures become macroscopically important and visible in the stellar spectrum.

4.6 Non-Sobolev response to perturbations

We now move to studying the 2D evolution of a non-Sobolev driven wind. The initial conditions and perturbation additions are performed in the same way as in previous sections. We continue to investigate perturbations with extreme characteristics, and also consider the evolution of small perturbations which can arise from background noise. Such small amplitude perturbations as these are likely to be common in a real wind so their evolution could assist the understanding of observations.

Running the model without further perturbation, its development is similar initially to one-dimensional runs. However, as the simulation progresses, the dense shell structures fragment in a direction perpendicular to the flow. We initially presumed that these instabilities are seeded by small rounding errors in the underlying hydrodynamical scheme

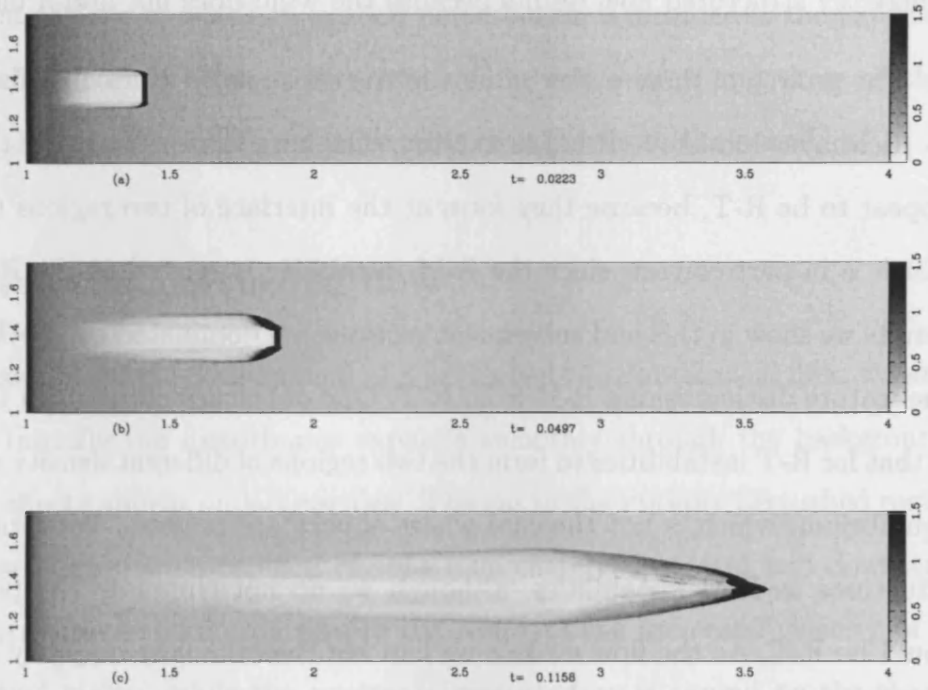

Figure 4.6: The evolution of a perturbation with $M = 4$ and $R_\rho = 4$, in a CAK force model. The perturbation behaves in a similar manner to that of Fig. 4.5. The higher dense makes the onset of -RT instability less prominent (cf. equation 4.4).

and variations in the CFL timestep (cf. OCR). The results of Poe, Owocki and Castor (1990) suggest that the variability in the wind appears because the solution is nodal, and therefore surrounded very closely by similar solutions. Each point in a numerical solution has an error with it associated with it, which can prevent the solution settling to a unique solution and continually generating structure. Numerical results with a constant timestep (smaller than the minimum value of the CFL timestep for the flow) do not indicate any reduction in the variability for our method of force calculation. This suggests that the inherently structured flow results because the wind does not find a unique solution.

The growth of these perturbations of the dense noise-excited shells may be attributed to Richtmyer-Meshkov (R-M) instability. On immediate inspection the structure might appear to be R-T, because they form at the interface of two regions of different density, which is in part correct, since the R-M instability is related to the R-T instability. The results we show in this and subsequent sections are dominated by shock structure which is the feature distinguishing R-M from R-T. One of the assumptions in the analysis of § 4.2 is that for R-T instabilities to form the two regions of different density must be in pressure equilibrium, which is not the case where shocks are present. We term all such unstable structures as R-M instabilities, although we do not eliminate the possibility that they could be R-T. As the flow evolves we can see that the vast majority of the motion is in the radial direction, thus discounting the possibility that such strong unstable structures could be K-H.

As structure evolves from these instabilities, it has a very definite effect on the downstream flow. When we allow the driving to act over a long time on a wind with no seeded perturbation, the result is a highly structured flow as can be seen in Fig. 4.7. Initially the instabilities appear to be regularly spaced and periodic but as the flow evolves the line de-shadowing instability (LDI) leads to an irregular and clumpy flow.

If the gas is diffuse the instabilities do not evolve to macroscopic structure, because the strong coupling with the driving 'washes out' the structure. Dense shells that have

become optically thick, expand from gas pressure alone. This provides mechanisms by which both dense and diffuse shells can expand. Shocks are formed where the edges of two such expanding shells collide, for example at (ii) in Fig. 4.8(b). Depending on the expansion velocities of the shells involved, hydrodynamical instabilities may develop at the interface. The development of instabilities in the flow can fragment the resulting shell into multiple bullets and diffuse bubbles.

To study the development of these structures in more detail, we will now investigate the development of flows in which an explicit perturbation is included in the initial conditions. The distinct difference between the results from this section and those of the previous sections is that the flow contains dense shell structure from the outset.

4.6.1 Velocity perturbed flow

As a first example of the development of a perturbed two dimensional flow, we set $M = 1.2$, $R_\rho = 1$. Initially the disturbance expands smoothly through the background, and no significant effects appear on large scales. The gas in the initially perturbed region collects into a dense clump, with rarefied regions immediately upstream and downstream of it. The downstream rarefaction is simply the result of the increased velocity of the gas in the perturbed region, while the upstream perturbation is caused by the shadow of the perturbation. In this shadow, the gas experiences a decreased radiation force, slows and is swept up by the clump.

As the perturbation increases in size, the changes of shadowing from gas shadowed by the perturbation (etc.) begin to have affects on the dense shells far downstream. The patch of the dense shell marked (i) in Fig. 4.8(b), falls in the shadow of the perturbation, decelerates and becomes more diffuse, causing the first break in the shell structure. At this time an instability develops in the unshadowed parts of the dense shell where the optically thin faster flowing gas meets an optically thick slower dense shock. The disruption of the shells is dependent on whether they continue to contract as they evolve, which is in

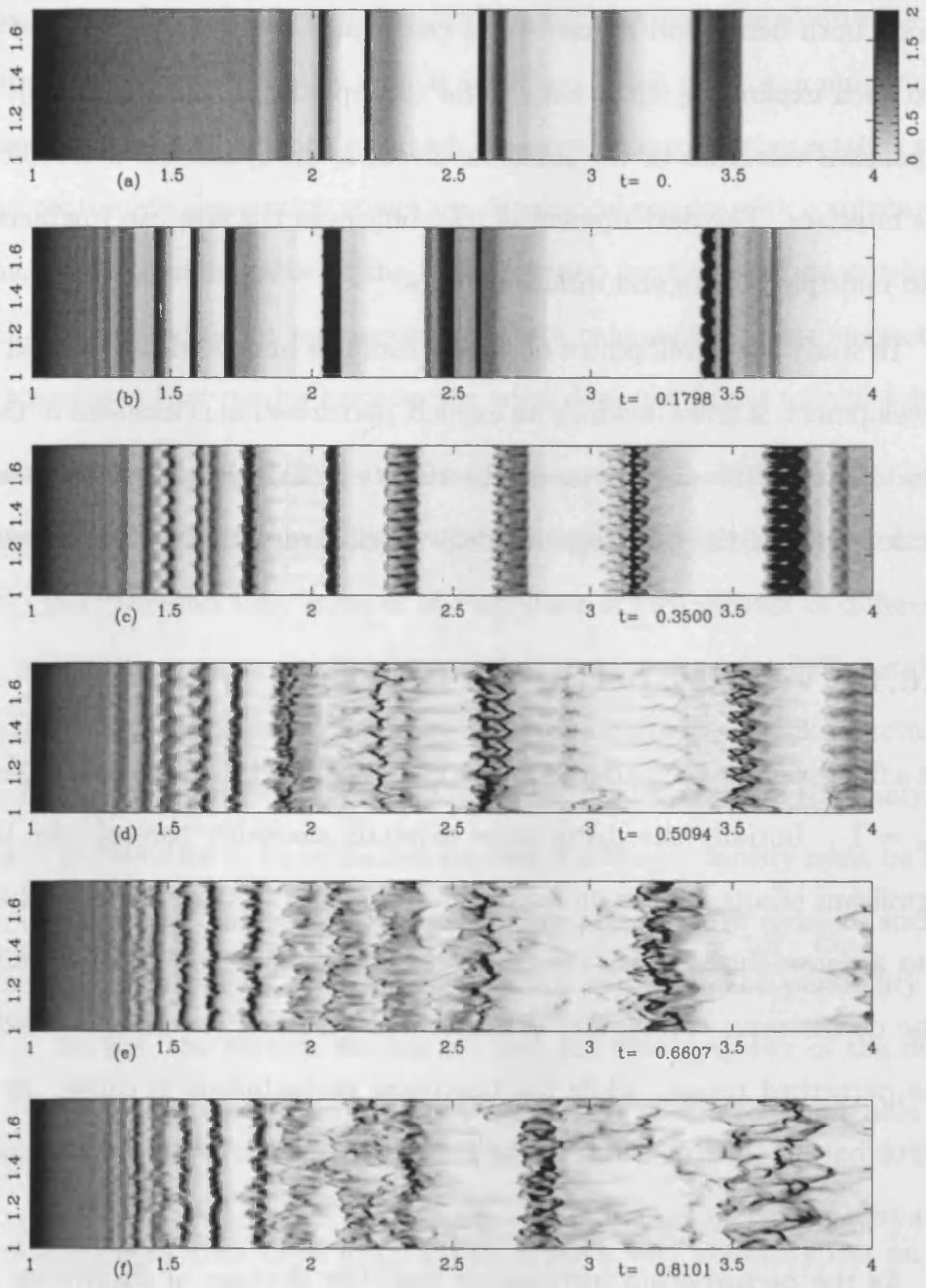

Figure 4.7: The evolution of the flow when no perturbation is added . The structure develops as R-T or R-M instabilities become a dominant feature in the flow. There is a complicated hydrodynamical interaction between shadowing, de-shadowing, and gas pressure expansion. The regular features result from the hydrodynamical instabilities, however edge effects begin to arise as well as a high level of unresolved structure which disturbs the flow in an amorphous fashion. The axes measure the same distance units as the one dimensional case (i.e. $R_\star$).

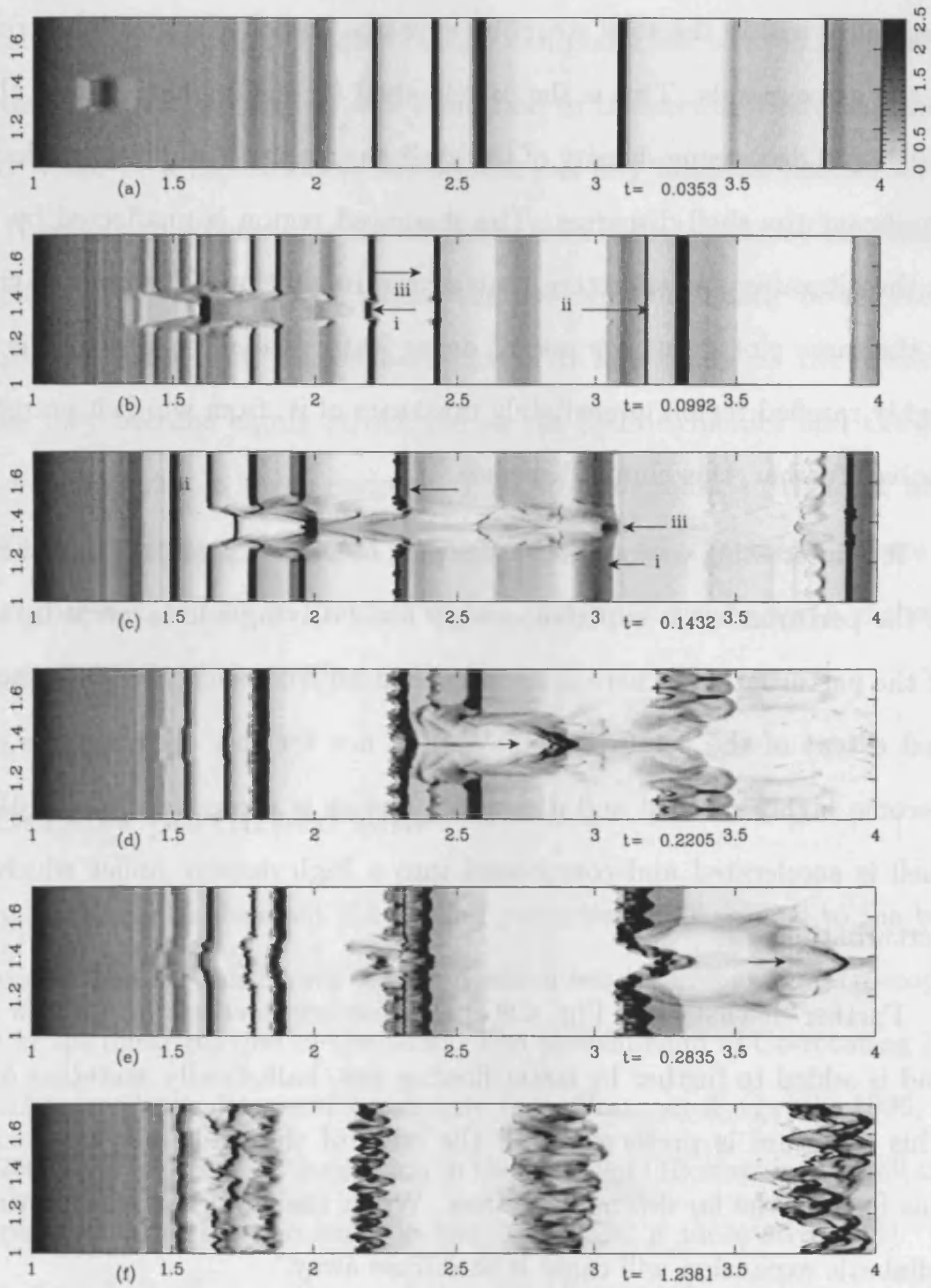

Figure 4.8: The evolution of a velocity perturbation of 20 per cent above the background level ($M = 1.2, R_\rho = 1$) is shown at variety of times, labeled beneath each plot. Many interesting features can be seen in this 2D model. As the perturbed gas moves through the background it appears to trigger Richtmyer-Meshkov instabilities in the dense shells and causes a disturbance to the upstream background.

turn dependent on whether they are compressed by a shock behind or retarded by a dense region ahead. If the shell expands slower than the perturbation evolves, the R-M instability within the shell structure develops. If not, the unstable structure diffuses away as the gas expands. This is the case in shell (i) of Fig. 4.8(c) where the increasing radial width and decreasing density of the shell damps the instability, so that before it becomes significant the shell disperses. The shadowed region is unaffected by this expansion due to the alterations in spectrum that govern its motion. The apex of the shadowed region in the same plot forms a transient dense feature labelled (ii) which is created by the fast highly rarefied region immediately upstream of it, from which it accretes gas. As the flow evolves further, this clump disperses.

It is interesting to note that when part of a dense shell falls into the rarefied slipstream of the perturbation it experiences very little driving and is swept up by the dense clump of the perturbation. There is steady accretion from such incidents, increasing the density and extent of the perturbation. Were it not for this accretion the perturbation would become highly rarefied and disappear, but as is shown in Fig. 4.8(d), part of the dense shell is accelerated and compressed into a high density bullet which rams through the perturbation.

Further downstream, Fig. 4.8(e) this feature develops into a bow shock/arrow shape and is added to further by faster flowing gas, ballistically accreting onto it from behind. This structure is preserved until the edge of the grid, but it is unlikely to remain in this form in the far downstream flow. When the wind has reached the terminal velocity, adiabatic expansion will cause it to diffuse away.

Persistent features appear in the inner wind at the position of the initial perturbation. Instabilities seeded by these disrupt the formation of dense shells in the downstream flow. This is eventually smoothed out as the features spread in the tangential direction, Fig. 4.8(f). However, as the flow is everywhere supersonic, the perturbations ought to have been advected downstream long before this affects the flow.

In an Eulerian hydrodynamical scheme, perturbations to smooth flow in a particular cell can only be removed exponentially with time (in essence by dilution). A sufficiently strong instability can decrease the exponential damping rate, or even force the perturbations to grow. This may be viewed as a limitation to the accuracy of these simulations – as indeed it would be a limitation to the accuracy of *any* Eulerian simulation with finite resolution (Lagrangian simulations would suffer from complementary problems as a result of sampling noise). However, in reality the flow will continually be affected by small scale perturbations from the photospheric flow. At late times, as the dense but noisy shells evolve they become highly structured as the hydrodynamics and the line-driving struggles for dominance in these regions. This flow is similar to that for unperturbed initial conditions, which suggests that it is not sensitive to the precise nature of the upstream perturbations, so long as they are small – the exponential growth of the instability erases the small details of its seeding.

4.6.2 Density perturbed flow

Contrasting behaviour is observed if a density perturbation is applied to the background flow. The motivation for this choice of perturbation was interest in a macroscopic persistent feature in the outer portion of the wind. The phenomenon of Co-rotating Interaction Regions (CIRs) has been discussed previously (e.g. Cranmer & Owocki 1996, Dessart & Chesneau 2002) but as yet their formation in the winds of OB stars is not well understood (although research into their presence in the Solar wind is more advanced). CIRs were proposed as a method of generating periodic optically thick features as seen in OB spectra. Work undertaken by Cranmer & Owocki (1996) suggest that CIR structure could be associated with velocity plateaus. Inspecting equation (2.33) and the accompanying definition of the optical depth reveals the importance of velocity plateaus, since like high density regions they make for a large optical depth. The subject is still controversial and we pursue an enhanced density perturbation method here.

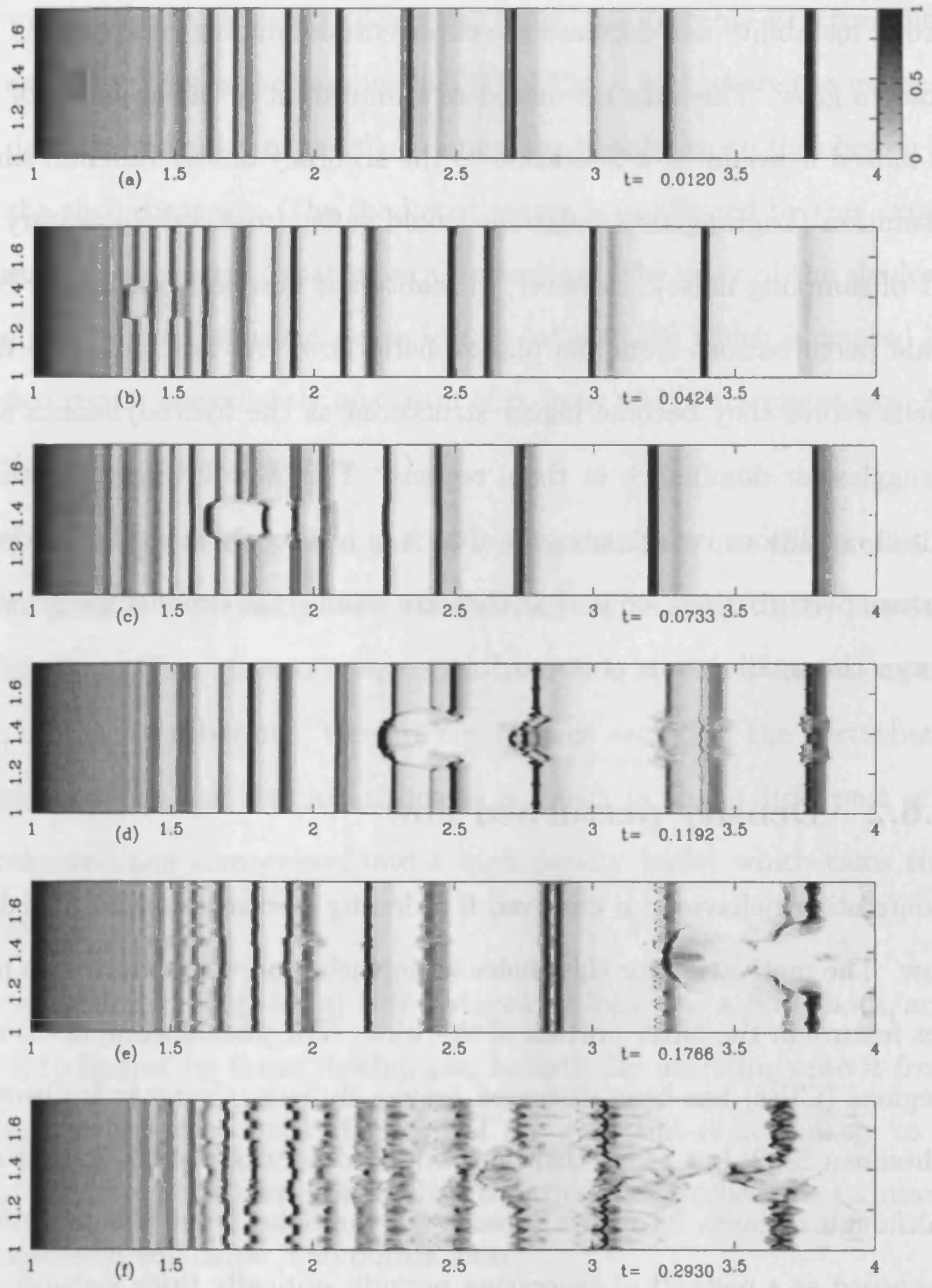

Figure 4.9: The evolution of a density perturbation of 20 per cent above the background level is shown at variety of times, labelled beneath each plot. These results contrast with those for a velocity perturbation shown earlier. Although the flow is similar the direction of the perturbation fronts is reversed.

Initially, the perturbation expands in the form expected for such an over-pressured region from pure hydrodynamics. A diffuse bubble appears, with dense shocked plates at its upstream and downstream edges. However, as the flow develops, these plates move apart and become more condensed, while the material between them is accelerated by line driving into the downstream clump, or is swept up by the approach of the upstream edge or clump. The direction which material will move and which clump it will be swept into is dependent on whether the gas falls in the shadow of the upstream clump or not (or any other structure for that matter).

The downstream flow still shows evidence of the spectral interference from the perturbation (i.e. LDI). The background dense shells are disturbed initially on the line of the edges of the perturbation, since at these positions a range of velocities are present while the body of the perturbation has a very narrow velocity dispersion; the downstream material is only disturbed if gas upstream of it blocks radiation in a relevant frequency range.

The subsequent evolution of the upstream and downstream components of the original perturbation is distinct from that found in the previous section, showing sensitive dependence of the details of the flow on the initial conditions. One obvious feature, shown in Fig. 4.9(b), is that both clumps of the perturbation appear to be blown away by the out-flowing wind whereas in Fig. 4.8(b) the perturbation forms bow shocks as it pushes through slower material ahead of it. These two graphs can be compared against the less structured flows in Fig. 4.4 and Fig. 4.5 suggesting that a massive perturbation ($R_\rho > 1$) results in a reverse bowshock while increasing the momentum ($M > 1$) results in a forward bowshock.

These results prompted an investigation of a higher density initial perturbation, so a density perturbation, with $R_\rho = 4$, $M = 1$ was applied to the same initial conditions as above. As one might expect the evolution of this perturbation, as seen in Fig. 4.10(a)-(f) is similar to that seen in Fig. 4.9(a)-(f). In this case the upstream edge of the expanding

bubble withstands disruption by the flow and eventually forms a 'v'-shaped front, which after further evolution develops highly detailed structure in Fig. 4.10(d) as a shock passes through it leaving R-M instabilities to develop.

The structure from the downstream edge of the bubble forms features in Fig. 4.10(c)-(d) that are reminiscent of the structure in Fig. 4.9(c)-(d). The perturbation has a great effect on the persistent features which remain in the upstream flow, leading to the beginning of highly clumped flow in Fig. 4.10(f).

Summary

Building on the one dimensional results of chapter 3 we extend the computational domain into two dimensions. The calculation of the line driven winds assumes that the incident radiation is entirely plane parallel. This is useful for the following reasons:

- It accurately describes the wind in the downstream flow where the radiation can be assumed to be approximately plane parallel.
- It provides us with a tractable method of obtaining two dimensional results without the analytical and numerical complications that a multiple ray approach would bring.

The results for continuum winds are useful in illustrating the behaviour of a simple driving mechanism, to perturbations and hydrodynamical instabilities. The results for line driven winds using our non-Sobolev method show significant structure:

- The self excited noise waves are seen to fragment from hydrodynamical instabilities (R-T and R-M), strongly affecting the flow. These are higher dimensional phenomena and thus their importance would not be observed in 1D.
- We have presented one of the first studies of line de-shadowing instability in two dimensions. While this dissertation was written a different approach to 2D LDI

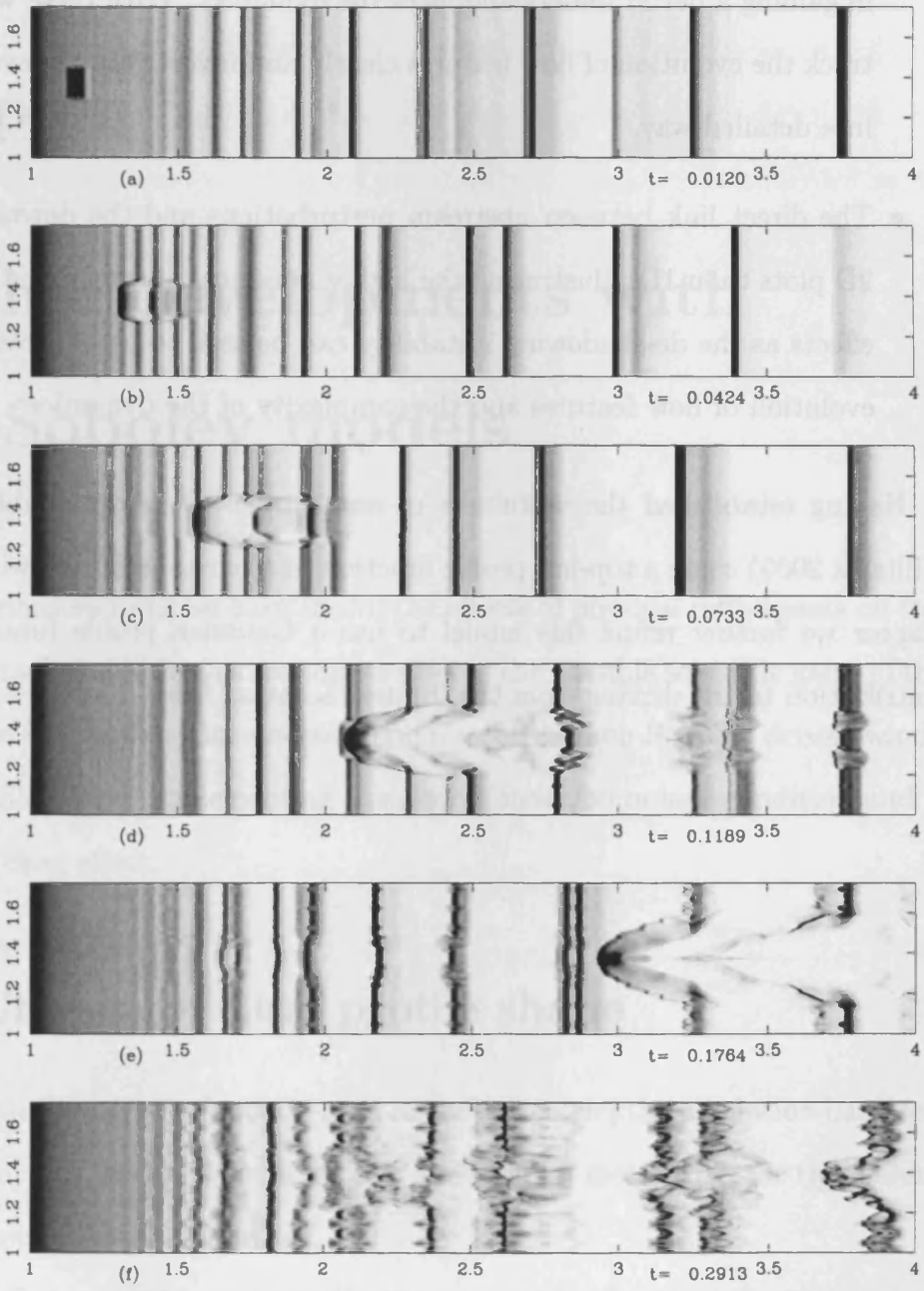

Figure 4.10: The evolution of a density perturbation a factor of 4 times the background level is shown at variety of times, labelled beneath each plot.

simulation has been proposed by Dessart & Owocki (2003).

- Effects of the driving become more evident in 2D. The 2D density plots are essential in gaining a better understanding of the dynamics. With these we have been able to track the evolution of flow features clearly and investigate the evolution of structure in a detailed way.

- The direct link between upstream perturbations and the downstream is clearer in 2D plots than 1D, illustrating the highly non-local nature of the driving force. Such effects as the de-shadowing instability can be seen to be of great importance to the evolution of flow features and the complexity of the dynamics.

Having established the usefulness of our simple 2D model (published in Gomez & Williams 2003) using a top-hat profile function in a pure absorption wind, in the following chapter we further refine this model to use a Gaussian profile function and include a contribution to the driving from the diffuse radiation field.

Chapter 5

Further developments with non-Sobolev models

In the previous sections we have shown the effects of physical refinements on the structure of the wind solutions. In this section we discuss the possible scientific gains of three further refinements on the two dimensional structure of the non-Sobolev driven wind: changing of line profile shape, implementing a subsonic inner boundary condition and calculation of the line drag effect.

5.1 Change of Line profile shape

Until now the line profile function used in the optical depth calculation has been a top-hat function. In this section we will explain the original motivation for this assumption and ways in which it can be improved.

As detailed in §2.3.3, we simplify the optical depth calculation by *updating* it from the local velocity and density of the gas at each grid point. Spectral information from gas interior to each point in the flow is also used in this calculation which distinguishes it from a local approach using the Sobolev approximation. This method is not wholly dependent on local conditions but requires knowledge of the absorption spectrum interior

to each calculation point on the grid.

We compute the non-Sobolev optical depth from the convolution of the line profile function with the column density in each grid cell in velocity space. If the density is assumed to be constant across the width of a cell the line profile function needs only to be convolved with a top-hat function with a width corresponding to the velocity difference across the cell and a height equal to the column density in the cell $\rho\Delta z$.

Initially we used another top-hat function for the profile function, as this was the easiest case to consider both analytically and conceptually (the convolution of two top-hat functions with different height and width). This has limitations which are discussed extensively by Owocki & Rybicki (1984). The essence of their argument against using a top-hat profile is that the growth rate of perturbations to a flow which is driven using such a profile, is larger than in reality. Also that it shortens the mean free path of photons absorbed at the blue edge of the line. In the top-hat case the blue (and red) edge of the profile function is infinitely steep, and all photons in the frequency range $\Delta\nu_D$ are absorbed equally. This overestimates the driving force from the absorption of these photons. For this reason we have used other functional forms of the profile function, specifically a triangular function and a Gaussian (Doppler) profile. The triangular function produces flow which contains much jagged structure because of the shape of this profile. The triangular profile is not useful in our analysis so we discuss the Gaussian form of the profile function only.

The Gaussian profile is a good match to a line profile which is broadened only by the thermal motion of the gas (Mihalas 1978). In this case we assume that other mechanisms of broadening are not so dominant. As was discussed in Chapter 2 the true form of the line profile function is more accurately described by a Voigt profile since this includes the effect of natural broadening (Mihalas 1978). However the Gaussian is a good approximation of this in the context of a numerical routine for the driving such as ours. The main difficulty when using a Gaussian profile in a numerical routine is that it has an infinite

extent, and consequently will contribute to the optical depth far from the line centre in frequency space, but this can be overcome by only including part of the function (3 standard deviations away from the mean of a Gaussian includes more than 99% of the area under the curve). In the beginning we assumed that using a top-hat function would simplify the analytical convolution calculation (the justification for this step has been given already in § 2.3.3) and it would be instructive to investigate the properties of the wind when using such a simplifying assumption, in comparison to results published by other authors.

In the asymptotic limit of a large velocity gradient $\Delta v/v_{\rm th} \gg 1$ the profile function (irrespective of its form) tends to a delta function, $\phi(x) \rightarrow \delta(x)$, which is a re-expression of the Sobolev approximation (if the flow is monotonic). In the opposite asymptotic limit, $\Delta v/v_{\rm th} \ll 1$ there is a numerical lower limit that inhibits the profile function being fully resolved (the Δ refers to differencing across one grid cell). The limiting size is the spacing of the spectral grid, Δx.

We give the functional form which is used in the numerical code in the equation (B.3) and more information about the form is given in §B. The results below are obtained by replacing the calculation of the radiative force using a top-hat profile function with that using a Gaussian profile function, in VH-1. To investigate the properties of the profile function we compare results in 3 limits (given below) for both the top-hat and Gaussian profile function.

5.1.1 Absorption profile of a single line

The effect of advancing the calculation of the driving from using a top hat to a Gaussian profile function is quite subtle. As indicated above, the form of the line profile tends to a delta function in the Sobolev limit, however in the optically thin limit the spectral grid resolution will have an effect on the optical depth calculation; the limitations of grid resolution can reduce the Gaussian to a function closer to the top hat function if it is

under-resolved.

To better characterize the nature of radiation pressure, we consider the absorption from one physical cell with velocity width Δv. We choose 3 values for $\Delta v/v_{\rm th}$ which represent: (a) $\Delta v/v_{\rm th} \gg \Delta x$, (b) $\Delta v/v_{\rm th} > \Delta x$, (c) $\Delta v/v_{\rm th} < \Delta x$. The differences between the two profiles are evident in the generally smoother shape seen in Fig. 5.1. generated from the Gaussian profile function. The figures display the convolution of the profile function with a top-hat with width Δv (from which the force is calculated). The curves are all normalized so that the area under all of them is equal to $1/\Delta x$. In the limit of large Δv the absorption profile produced by the two different methods becomes more similar, a flat topped structure with decreasing wings (Fig. 5.1(a)). This is close to the Sobolev limit and each profile function tends to a common shape, a delta function. The top-hat model always generates absorption structures which have flat tops, whereas the Gaussian model only generates flat top absorption features for $\Delta v > 4v_{\rm th}$, which can be thought of as the start of the Sobolev regime (there is always curvature in the Gaussian model, at all values of x).

The difference between the models is more obvious for smaller values of Δv as is shown in Fig 5.1(b),(c). The nature of the Gaussian having no definable edge, such as the top hat function has, means that wings are inclined to contribute to the absorption at frequencies/velocities beyond those defined by the physical grid cell of interest. We will address this issue below with reference to absorption calculations over an entire grid and not just the single cell discussed here.

Figs. 5.1 illustrate well what is meant by "the shortening of the mean free path of photons at the blue edge". The steep sides of the top hat function allow photons to be absorbed over a narrower range than the Gaussian function.

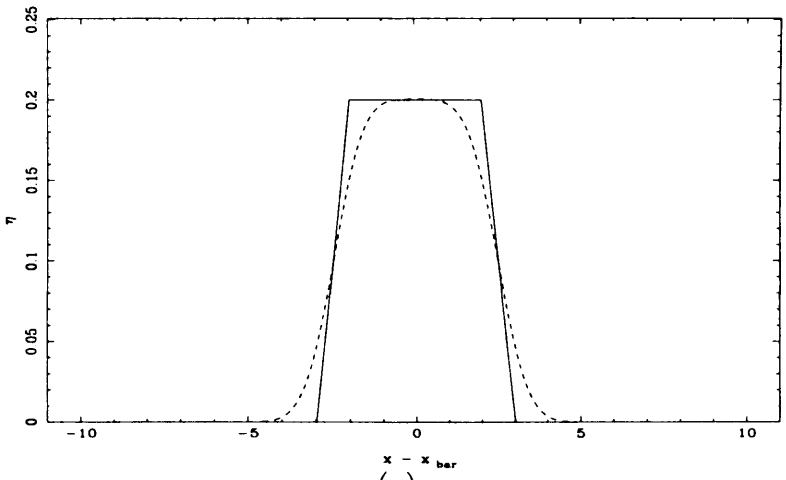

Figure 5.1: The spectral absorption due to one flow cell with different velocity ranges, (a)$\Delta v/v_{\rm th} = 5$, (b) $\Delta v/v_{\rm th} = 1$, (c) $\Delta v/v_{\rm th} = 0.01$, where $\Delta x = 0.05$ for each. The plots show the absorption with the top-hat profile function model (solid curve) and Gaussian profile function model (dashed curve). The area under the solid curves is the same as under the dashed curves. Remember that this shows the convolution of the profile and grid cell, so although (a) approaches the Sobolev limit it does not look like a delta function.

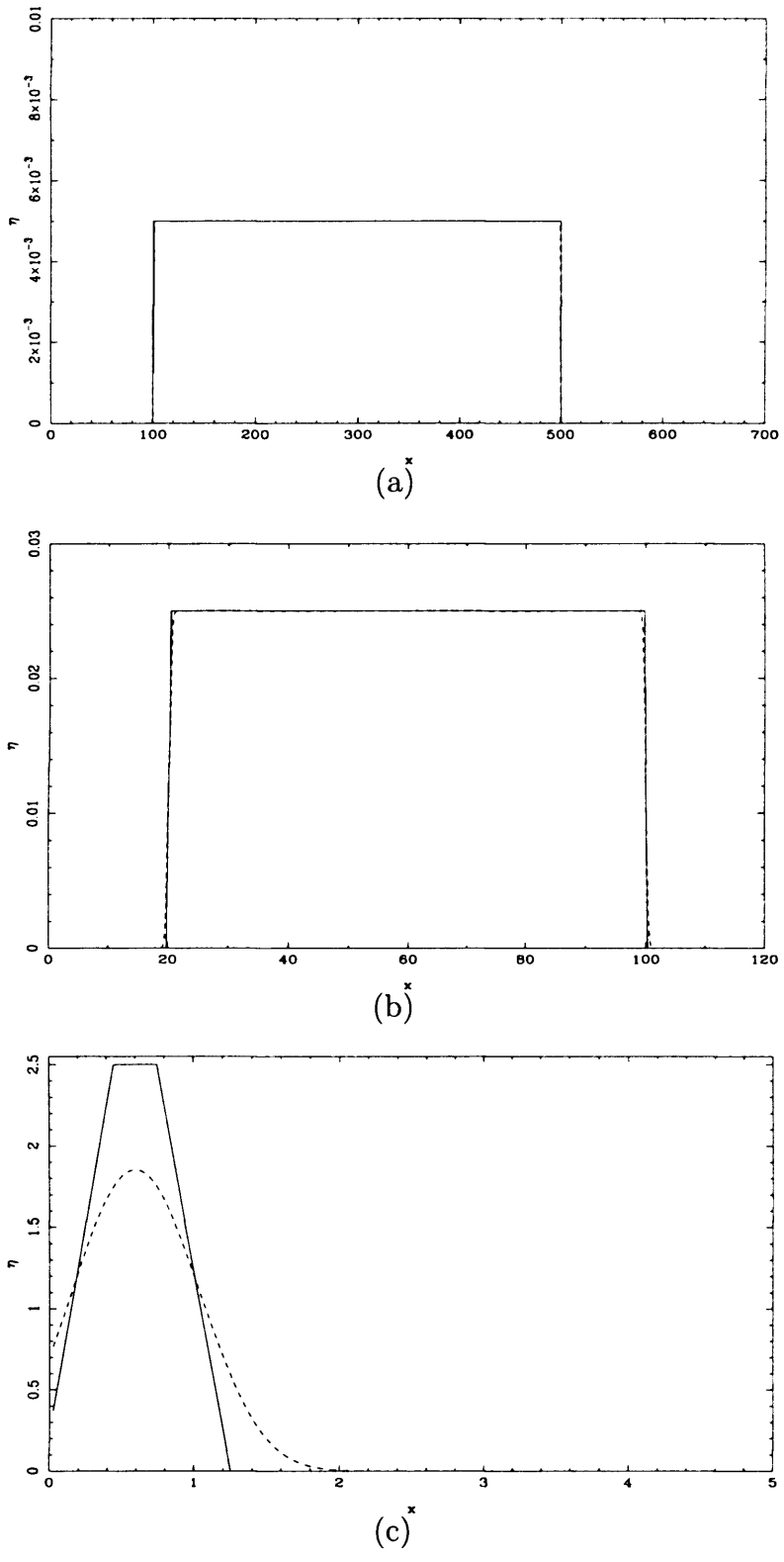

Figure 5.2: The spectral absorption from wind solutions with constant density, $\rho = 1$ and constant velocity gradient (a)$\Delta v/v_{\rm th} = 5$, (b)$\Delta v/v_{\rm th} = 1$, (c)$\Delta v/v_{\rm th} = 0.01$, with a spectral grid spacing of $\Delta x = 0.05$. The curves show a generally flat topped structure for both top-hat (solid) and Gaussian (dashed) models. As with the case of a single line, the area under each solid curve is the same as under the relevant dashed curve.

5.1.2 Absorption in wind solutions

We compare the optical depth calculation using the top hat and Gaussian profiles for the test cases discussed in the last section and Fig. 5.1 using a constant velocity gradient and constant density distribution over a physical range of $3R_\star$. It has the simple solution η = const and $g_{\rm rad}$ = const, for the range of velocities observed. Fig. 5.2 (a)-(c) are the absorption profiles for the full wind (in this approximate case) and show that both profile functions produce a flat topped spectrum for the applied range of velocity. The three graphs in Fig. 5.2 show the difference in the absorption profiles for (a) $\Delta v/v_{\rm th} \gg \Delta x$ (b)$\Delta v/v_{\rm th} > \Delta x$ and (c) $\Delta v/v_{\rm th} < \Delta x$ over $3R_\star$ in the wind. The only apparent change in the shape of the profile, in Fig. 5.2(a) and (b), is their width and height which scale with Δv. These figures show that there is little difference between the results using the two different profile shapes when $\Delta v/v_{\rm th} > \Delta x$. Fig. 5.2(c) shows that in the small velocity gradient limit $\Delta v/v_{\rm th} < \Delta x$ there is an appreciable difference in the absorption. Once again these results are normalized as in the previous section, which is the reason for the variable height of the profiles.

The values of $\Delta v/v_{\rm th}$ used differ from those shown in Fig. 5.1. It was convenient to show the difference in the absorption profile of a single line for velocity gradients which vary widely from the spectral grid resolution (cf. Fig. 5.1). In the case of a large physical domain ($\approx 3R_\star$) we show only two calculations of the absorption from constant density and velocity gradient models. These models emphasize the significant discrepancy between the top-hat and Gaussian models in the low velocity gradient case, e.g. Fig. 5.2(c), and the convergence of the models in the high velocity gradient case, Fig. 5.2(a). As the velocity gradient increases, so the curved shape of the Gaussian model steepens into a shape that more closely resembles the top-hat model. We do not include further results as their high velocity nature moves them out of the spectral domain shown. An expansion of the spectral domain obscures the low velocity gradient results.

As can be seen from Fig. 5.3(a) and (b) there is only a slight difference between

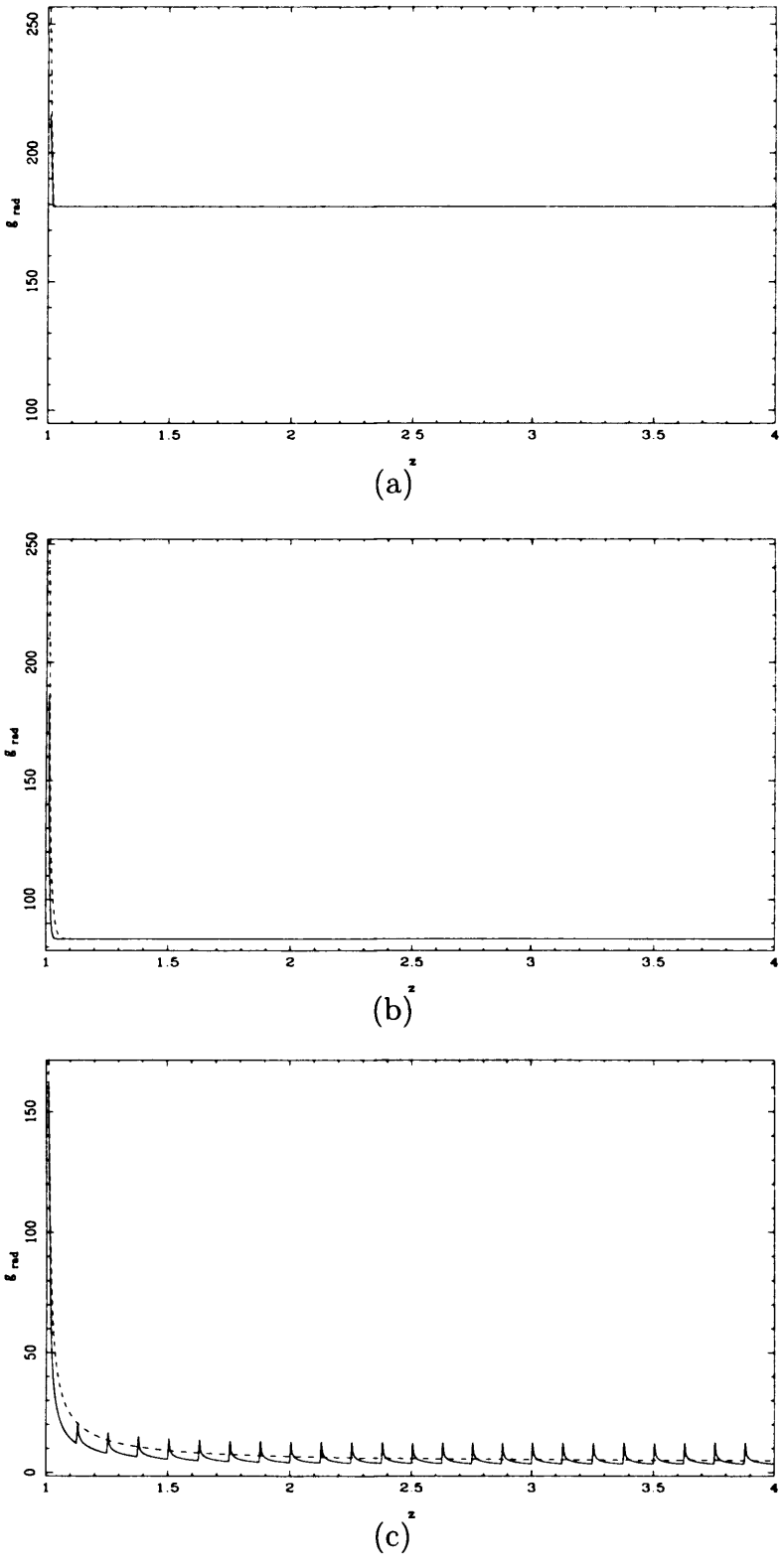

Figure 5.3: The acceleration due to radiation absorbed, as shown in Fig. 5.2. As in that case these are wind solutions with constant density, $\rho = 1$ and constant velocity gradient (a)$\Delta v/v_{\rm th} = 5$, (b)$\Delta v/v_{\rm th} = 1$, (c)$\Delta v/v_{\rm th} = 0.01$, with a spectral grid spacing of $\Delta x = 0.05$. The Gaussian model curve (dashed) is overlaid onto the top-hat model curve (solid). The 'saw-tooth' structure in (c) is due to aliasing in the force calculation using the top-hat method. More evidence for this effect is shown in Fig. 5.4(c).

the acceleration derived from the two models, while in Fig 5.3(c) there is a noticeable difference in the structure. This noisy structure in the results for the top-hat case is due to the velocity width not being resolved by the spectral grid in the top-hat case. In this region the Gaussian tails are important to the smooth transition between the absorption in neighbouring spatial grid cells. The acceleration has a significant contribution from the overlapping of the convolution profile tails instead of from the flat region in the centre of the convolved function (as is the case in Fig. 5.3(a)-(b)). These results once again are for the contrived case of a wind with constant density $\rho = 1$,and velocity which varies according to $\Delta v/v_{\rm th} = \text{const}$ (defined in the caption of Fig. 5.3.

We test these models further by applying a non-idealized 1D velocity and density data set to the two different driving models; we pass the dataset through the force calculation subroutine for both the top-hat and gaussian driving methods for one timestep only. The data set contains shocks and detailed structure, and is from a typical 1D run of the non-Sobolev model from § 3.6. In Fig. 5.4 we show the supplied velocity condition and driving results for this data set. There is good agreement once again between the Gaussian and top-hat models. The noise content of the acceleration and absorption is still present in the top-hat results of Fig. 5.4(b) and (c) while the Gaussian shows smooth structure especially obvious in the absorption results (cf. Fig. 5.4(c)). The noise in Fig. 5.4(c), 5.3(c) (top-hat results, solid curves) can be reduced by decreasing the size of the grid Δx, but it cannot be eliminated because in practice there will always exist regions where $\Delta v < \Delta x$.

5.1.3 Gaussian line profile: 2D results

Using this reformulated model of the radiation driving, we run simulations which are similar to those of § 3.6 using the parameters is Table 3.1 so that the results can be compared with that of the top-hat line profile. We compare two of the models: (A)$R_\rho = 1$, $M = 1.2$ and (B)$R_\rho = 4$, $M = 1$. The grey-scale results of these simulations are shown in Figs. 5.5 and 5.6 respectively, and can be compared directly with Figs. 4.9 and 4.10

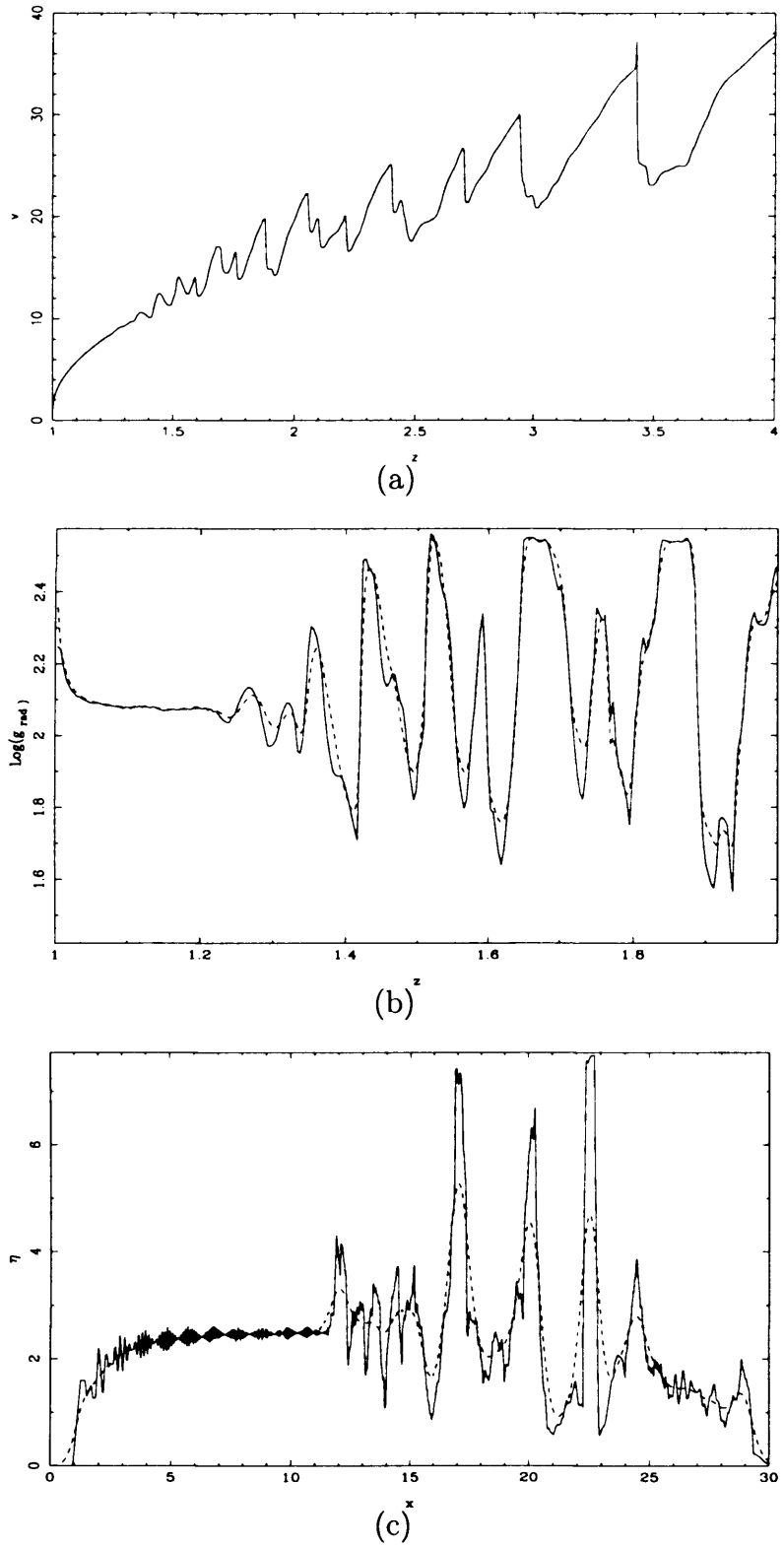

Figure 5.4: Absorption and acceleration profiles for a non-idealized velocity and density data set. As before top-hat model results (solid) are overlaid with Gaussian model results (dashed). The values are given in code units and the plots are shown for comparison purposes, the amplitude of the radiation acceleration in (b) can be compared to the 1D results of chapter 3. The physical range of the acceleration is zoomed so as to best view the difference between the 2 models. The Gaussian model smooths out the features which

(the variable CFL timestep makes the times of these plots are slightly different from the corresponding plots in Chapter 4).

There are various differences between the flow structures in these models and the top-hat models. The initial state of the flow is noticeably less structured since it uses 1D relaxed data from the Gaussian model and not those of the top-hat model as a seed. The decreased structure in the Gaussian model is a result of the 'softening' of the driving force. This is well illustrated by Figs. 5.4, where the top-hat model has much sharper features derived from a profile function which has sharp edges; the continuous form of the Gaussian yields a smooth overlap of line interaction regions.

The question of the level of structure which is generated by the driving is of great importance, since in it lies the power to either cause or disrupt flow features. As is illustrated by Fig. 5.4(b) the top-hat case over-estimates the driving, albeit by a very small amount. It is not this effect that causes the structure, but rather the noise which appears as a result of the sharp edges of the top-hat, as appears in Fig. 5.4(c). The lessening of the structure in Figs. 5.5 and 5.6 is a result of the decrease in seeding from the radiation absorption in the smoother Gaussian case.

The response of the perturbation to the driving is largely unchanged by the changed profile function. As was indicated in the 1D results (cf. Fig. 5.2) there is no substantial difference between the two profile models when $\Delta v/v_{\rm th} > \Delta x$ which is largely satisfied in such a wind and with a sufficiently low choice of $\Delta x (= 0.05 v_{\rm th})$. The nature of the driving is not generally affected by this change of profile function only the level of noise (or structure from LDI in the early wind) it produces.

The perturbation in model (A) remains as a coherent lump in the flow and because of the decreased structure in this model is not disrupted whilst it remains within the grid. Model (B), expands rapidly by gas pressure expansion which is not inhibited by the large amounts of flow structure seen in Fig. 4.10. Consequently, although the presence of the perturbation is strongly felt by the flow in the structure that it creates, it does

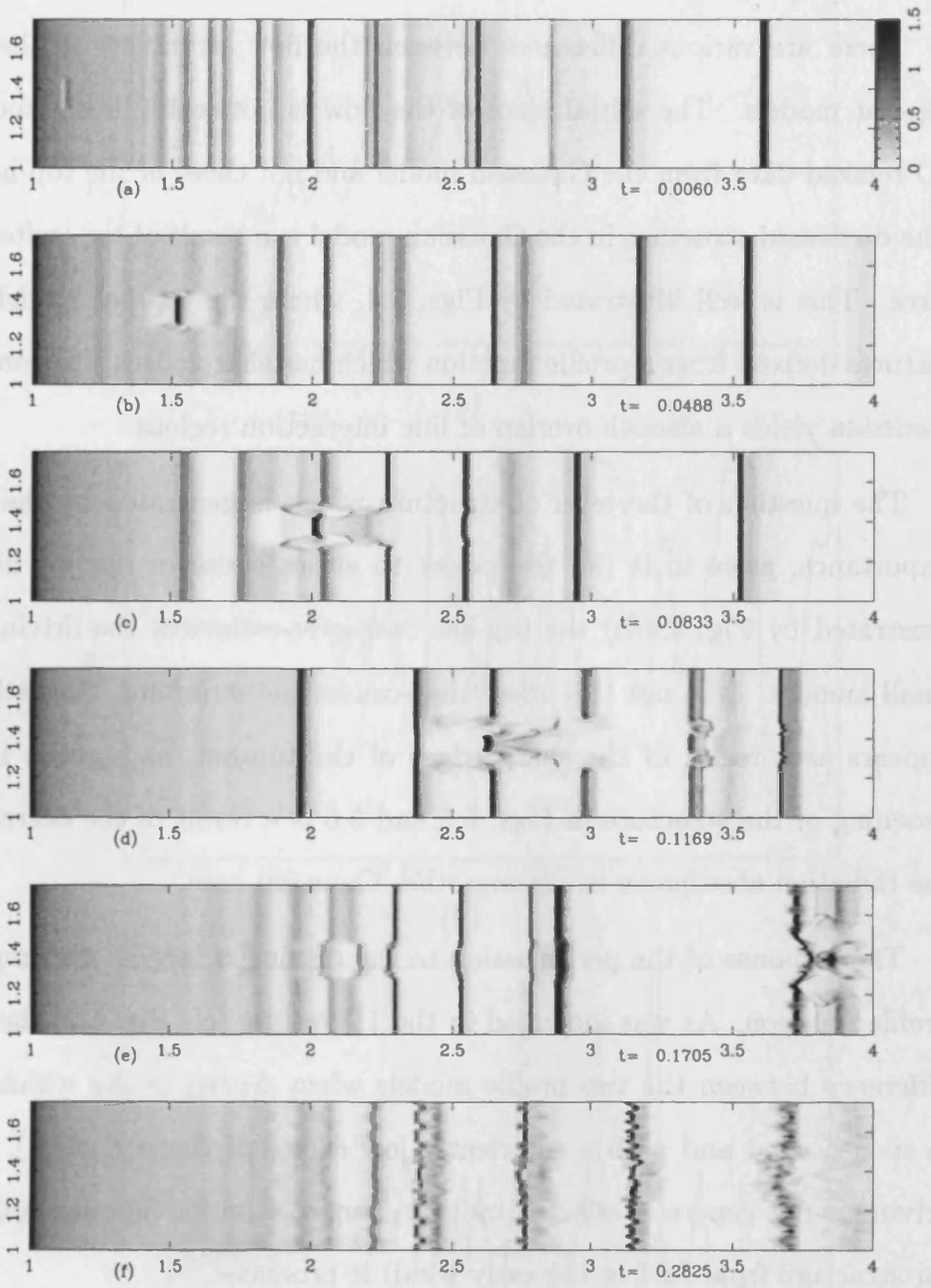

Figure 5.5: Two dimensional velocity perturbed ($M = 1$, $R_\rho = 1.2$) flow using a Gaussian profile function. The flow is less structured than its top-hat model counterpart shown in Fig. 4.9, while the response of the perturbation to the driving force is very similar to the top-hat case.

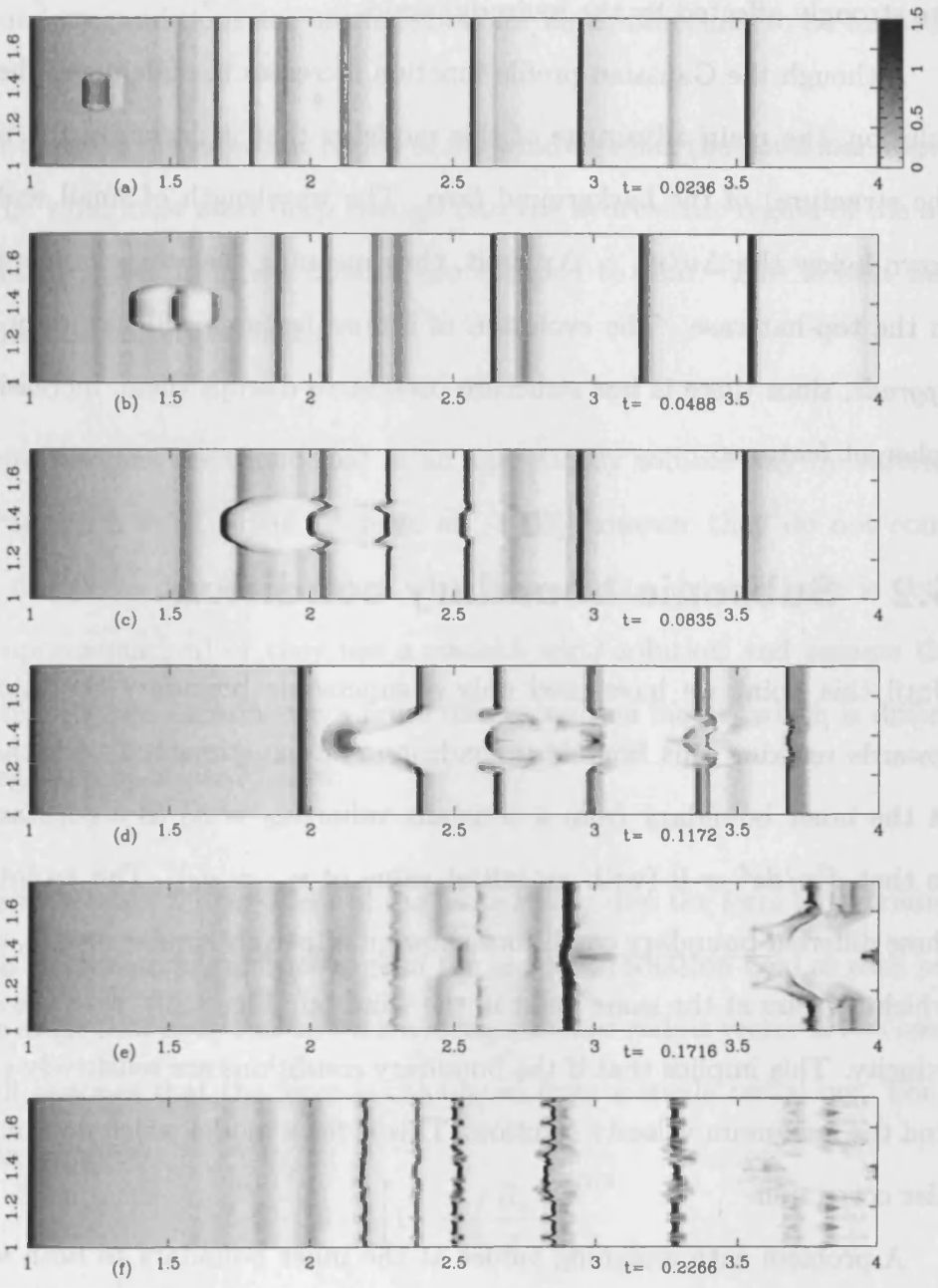

Figure 5.6: Two dimensional velocity perturbed ($M = 1$, $R_\rho = 4$) flow using a Gaussian profile function. The flow is less structured than its top-hat model counterpart shown in Fig. 4.10, while the response of the perturbation to the driving force is very similar to the top-hat case

not condense into a high density structure such as is seen in the top-hat case. This is further evidence that the flow properties, whilst dependent on the radiation driving, also are strongly affected by the hydrodynamics.

Although the Gaussian profile function increases the fidelity to the real physical wind solution, the main advantage of this model is that it decreases the noise (and therefore the structure) of the background flow. The wavelength of small scale noise can extend down below the $\Delta v/v_{\rm th} > \Delta x$ limit, thus meaning that there is more inherent structure in the top-hat case. The evolution of diffuse features will naturally be affected by this *upgrade*, since there is less structure present to disrupt them, increasing their lifetime as coherent features.

5.2 Subsonic boundary condition

Until this point we have used only a supersonic boundary condition. As a first step towards relaxing this boundary condition, we experimented with changing the velocity at the inner boundary from a constant value $v_{\rm BC} = a_0$ to a constant velocity gradient so that $d^2v/dz^2 = 0$ (with an initial value of $v_{\rm BC} = a_0$). The evolution of models with these different boundary conditions show qualitatively similar results, containing structure which appears at the same point in the wind (cf. Fig. 3.20), with the same time-averaged velocity. This implies that if the boundary conditions are sensitively chosen the wind will find the maximum velocity solution. This is for a model which does not include any finite disc correction.

A problem with assigning values at the inner boundary to both velocity and density is that the solution can become over specified. If the chosen values are completely incompatible it can trap a shock at the inner boundary. Flows with a similar form were investigated by e.g. Williams, Hartquist & Dyson (1995), as models for the structure of planetary nebulae (where a supersonic stellar wind can be stagnated by mass loading). In Fig. 5.7 we show the behaviour of the wind, while it tries to establish a steady solu-

tion, with $\rho_{\rm BC} = 10^{-11}{\rm gcm}^{-3}$ and $v_{\rm BC} = a_0$. This behaviour persists because the density boundary condition is fixed at a value to high for the solution to relax; the velocity and density boundary conditions are incompatible for an equillibrium to be formed.

In order to probe the sub-sonic region of the wind we relax the point star approximation of OCR. The wind must start deep enough into the hydrostatic region of the atmosphere that any disturbances from the outside are damped to zero. This is best modelled by using a finite-disc correction factor.

The finite disc has been modelled in an analytically soluble way by various different authors (Pauldrach et al. 1986, Puls et al. 1993) however they do not consider time dependent models so detailed feedback with the radiation driving force is not necessary (as a first approximation) or they use a smooth wind solution and assume the Sobolev approximation. These authors use a finite disc correction factor, which is different to the angle average approach used below.

In order to account for the effect of the finite stellar disc the form of the radiation force is altered to include an angular average of the incident radiation field at each point in the flow z. The angle that a ray makes with a local, outward radius vector is $\theta = \cos^{-1}\mu$. This method still assumes that the force is calculated from a single radial ray. The definition of μ is given by,

$$\mu = \left[1 - y\left(\frac{R_\star}{z}\right)^2\right]^{1/2} \tag{5.1}$$

where we introduce another term $y = (z\tan\theta/R_\star)^2$ the ray parameter. Following Owocki & Puls (1996) we re-express equation (2.42) to account for finite disc effects as,

$$\rho g_{\rm rad} = \int_0^1 dy \frac{dP_{\rm rad}(z,\mu)}{dz} \tag{5.2}$$

$$P_{\rm rad} = \frac{g_{\rm thin}}{\kappa_0^\alpha}\frac{\Gamma(\alpha)}{1-\alpha}\int_{-\infty}^{\infty} dx\phi(x - v(r)/v_{\rm th})\left[\eta(x,z,\mu) + 1/\kappa_{\rm max} + \phi(x)/\sigma_{\rm c}\right]^{1-\alpha}, \tag{5.3}$$

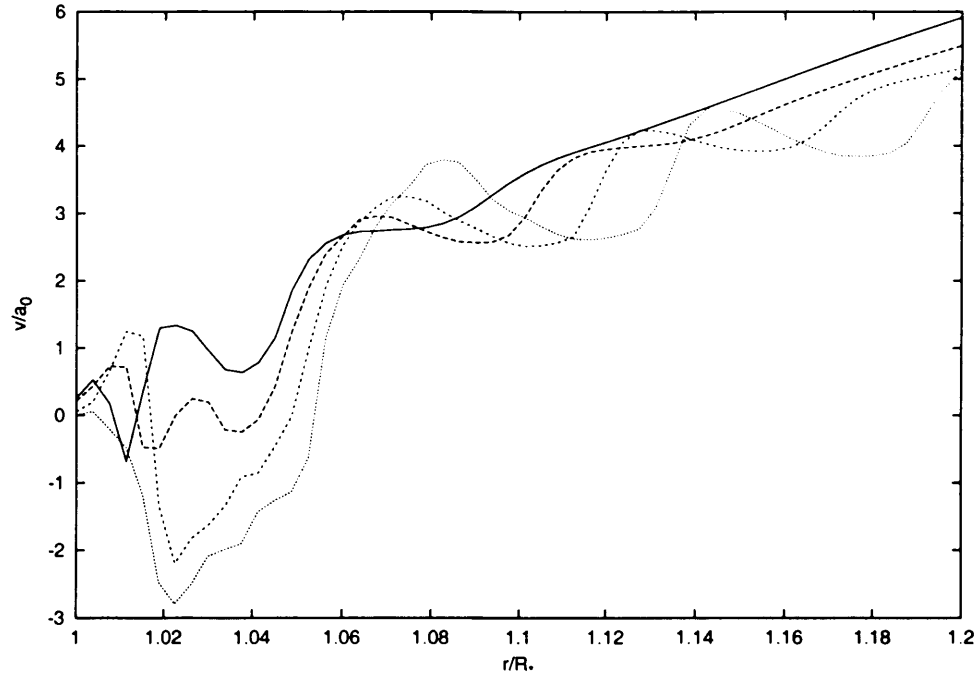

(a)

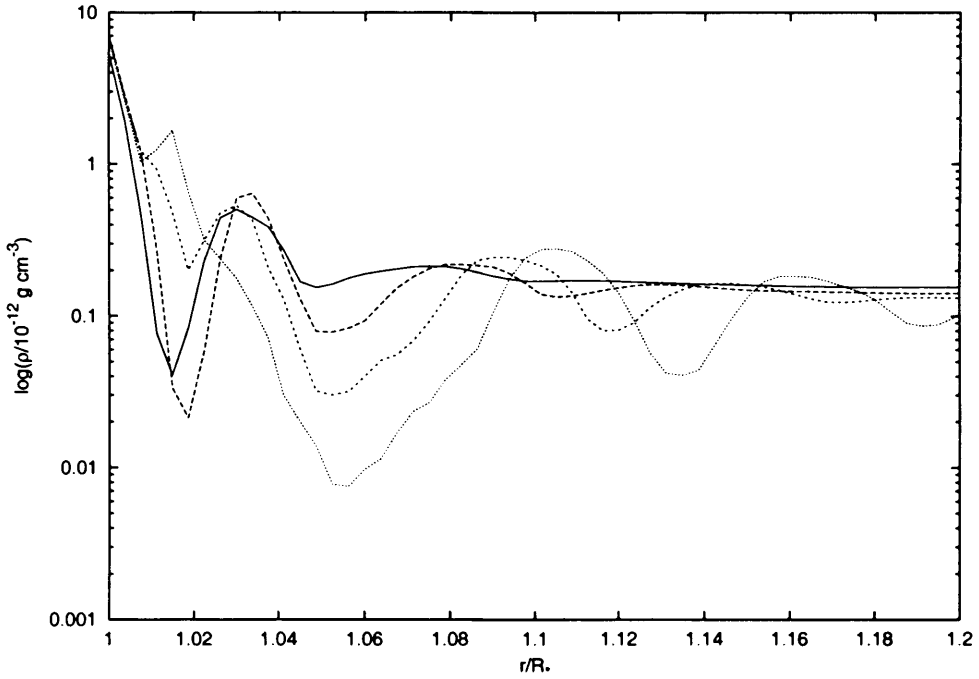

(b)

Figure 5.7: The result of having a shock trapped at the inner boundary is shown by the curves in this figure. The behaviour is cyclic as the wind continually tries to establish an equilibrium solution. The gas rushes in towards the inner boundary trying to match the high density boundary condition. The wind cannot sustain the steep velocity gradient and the equilibrium is destroyed as a high density shell is ejected from the inner boundary. The sequence of the curves runs from solid, dash, smaller dash to dot in time intervals of $\approx$ 4ks

where we modify the definition of $\eta(x,z)$ to,

$$\eta(x,z,\mu) = \int_{R_*}^{z} \rho(r)\phi(x-\mu v(r)/v_{\rm th})\frac{dr}{\mu}. \tag{5.4}$$

The integral over y has a range [0,1] which reflects only rays that impact on the stellar core are considered.

The above form of the driving was incorporated into the numerical method shown in § 2.3.6 using a gaussian form of the profile function. The angular integral was discretised using an impact parameter step-size of $\Delta y = 0.01$, which gives sufficient angular resolution without causing the force calculation to be slowed down drastically.

Fig. 5.8 shows a representative dataset for the above model using the parameters for ζ Pup as given in Table 3.2. There is a substantial amount of structure in both the velocity and density plots, much more than is seen in Fig. 3.20. The reason for this is the subsonic boundary condition. In this case the velocity at the inner boundary condition can vary. The density at the inner boundary in this case is much higher than in Fig. 3.20 possibly giving rise to large amounts of structure also. The high level of noise can be attributed to the spatial resolution of the grid and is reduced on a finer grid. We keep the resolution the same as in all previous models.

The time averaged value of the terminal velocity is $1520\mathrm{km\,s^{-1}}$ and the mass loss rate is $2.43 \times 10^{-6}\mathrm{M_{\odot}yr^{-1}}$. These values are in good agreement with observed values (cf. Howarth et al. 1997).

5.3 Line Drag

The treatment of line driving thus far has only been to implement a pure absorption approach, whereas in reality the driving is provided by scattering. It is however computationally demanding to perform a complete scattering calculation since the trajectory of each photon incident on a gas particle of interest and the re-emitted photon trajectory

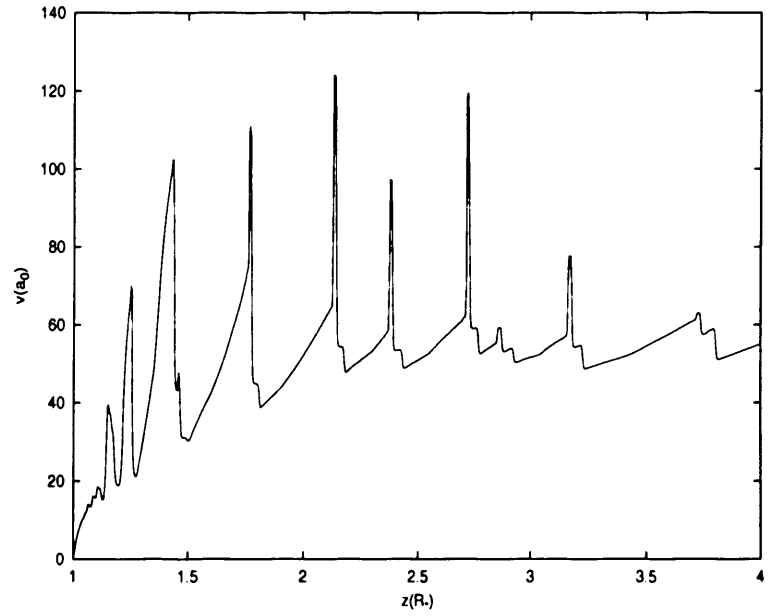

(a)

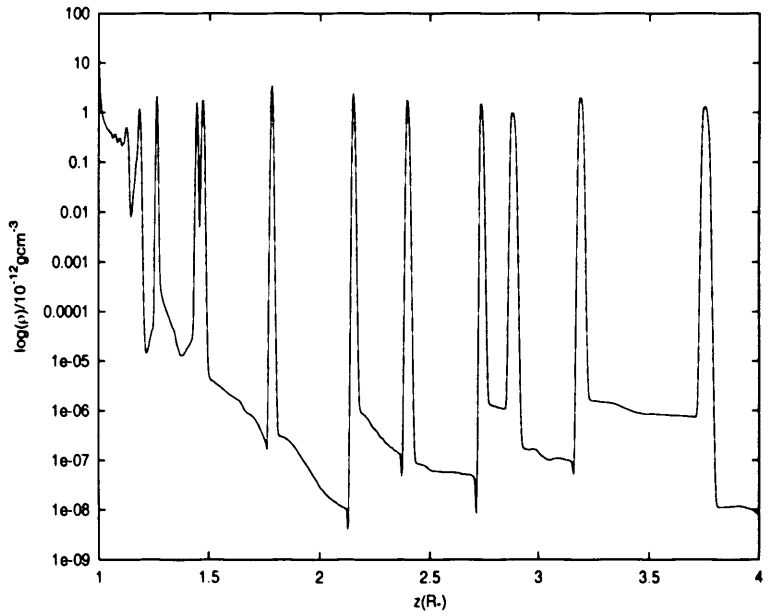

(b)

Figure 5.8: Model results for ζ Puppis using the physical parameter data in Table 3.2. The flow contains much structure. The very sharp structure is due to the isothermal assumption being stretched where the gas shocks.

must be calculated. Interesting work has been done by Stamatellos & Whitworth (2003) which tracks $\sim 10^8$ photons incident on a molecular cloud and after performing detailed radiative transfer calculations on the gas and using a Monte Carlo method to predict the re-emission trajectories, updates the cloud temperature. Because of the computationally intensive nature of this model, it is at present neither time-dependent nor hydrodynamical.

In a diffuse radiation field, at each point in the flow photons are scattered by ions. If the flow is smooth and monotonic the scattering of photons is symmetrical and the amount scattered downstream balances the amount scattered upstream. The force from this scattered radiation also balances in the upstream and downstream directions, resulting in no net force on the flow from this diffuse radiation field.

This idea is further developed by Owocki & Puls (1996) in the context of a non-Sobolev approach to the calculation of the optical depth. Following their formulation of the problem we write the intensity of the radiation field as,

$$I(z,\mu) \equiv \int_{-\infty}^{\infty} dx \phi(x - v(z)/v_{\rm th})[I_{\rm dir}(x,z,\mu) + I_{\rm diff}(x,z,\mu)], \tag{5.5}$$

where $I_{\rm dir}$ is the frequency integrated intensity of the radiation field *direct*-ly from the star and $I_{\rm diff}$ is the frequency integrated intensity of the *diffuse* radiation field.

Owocki & Puls (1996) show how the diffuse force can be calculated using a Smooth Source Function (SSF) approach. This assumes that the radiation field is a smoothly varying function of radial distance which is insensitive to changes in the state variables (e.g. velocity, density). This allows $I_{\rm diff}$ to be calculated without prior knowledge of the form of the Source function, which we can now write as,

$$I_{\rm diff}(x,p,r) = S(r)[1 - e^{-t(x,p,z,z_b)}], \tag{5.6}$$

which uses the optical depth variable $t(x,p,z,z_b)$, the frequency dependent line-optical depth along a ray path p from z to z_b where again x is the dimensionless frequency

variable.

Owocki & Puls (1996) write the acceleration (or retardation) from the diffuse field in the following form,

$$g_{\rm diff} \approx g_{\rm thin}\frac{\Gamma(\alpha)}{2(1+\mu_\star)}\frac{S^{int}(r)}{S^{int}_{\rm thin}(r)} \times \int_0^1 dy \int_{-\infty}^{\infty} dx \phi(x-\mu v(r)/v_{\rm th})[t_-^{-\alpha}(-x,r,\mu) - t_+^{-\alpha}(x,r,\mu)], \tag{5.7}$$

A commonly used source function is the optically thin form (or weak line limit) of the Sobolev function, allowing the above equation to be written as,

$$g_{\rm diff} \approx g_{\rm thin}\frac{\Gamma(\alpha)}{2(1+\mu_\star)} \times \int_0^1 dy \int_{-\infty}^{\infty} dx \phi(x-\mu v(r)/v_{\rm th})[t_-^{-\alpha}(-x,r,\mu) - t_+^{-\alpha}(x,r,\mu)], \tag{5.8}$$

where

$$\mu_\star = \left(1-\left(\frac{r}{R_\star}\right)^2\right)^{1/2}. \tag{5.9}$$

We adopt the optical depth notation of Owocki & Puls (1996),

$$t_+(x,r,\mu) = \kappa_0\left(\frac{1}{\kappa_{\rm max}} + \frac{\phi(x)}{\sigma_c} + \int_{R_\star}^{r}\frac{dr'}{\mu}\rho(r')\phi(x-\mu v(r')/v_{\rm th})\right) \tag{5.10}$$

$$t_-(-x,r,\mu) = \kappa_0\left(\frac{1}{\kappa_{\rm max}} + \int_{r}^{\infty}\frac{dr'}{\mu}\rho(r')\phi(x-\mu v(r')/v_{\rm th})\right). \tag{5.11}$$

The '+' and '−' signs refer to the direction which the optical depth is derived from, compared to the flow direction. The positive optical depth extends from the stellar surface to a point in the flow r and so includes the atmospheric reversing layer term (second term on RHS) in addition to the optically thick line limit (first term on RHS). The negative optical depth term integrates the profile weighted column density (previously called $\eta(x,r)$) from r to ∞. The negative optical depth can be obtained from the following

relation,

$$t_-(-x, r, \mu) - t_-(-x, R_{\max}, \mu) = t_+(x, R_{\max}, \mu) - t_+(x, r, \mu) \tag{5.12}$$

which expresses that the negative optical depth is equal to its positive counterpart over a large range $(r, R_{\max})$, reinforcing that the diffuse force is a local effect and that globally this diffuse field is isotropic. From this we can see that if $t_-(-x, R_{\max})$ is defined as a boundary condition, $t_-(-x, r)$ can be calculated from the positive optical depth alone, thus saving much computational effort. It can be written as a reflection boundary condition,

$$t_-(-x, R_{\max}) = t_+(2u(R_{\max}) - x, R_{\max}). \tag{5.13}$$

The diffuse radiation field requires information about the wind beyond $R_{\max}$ (and out to ∞). It is this problem that the reflection boundary condition solves.

5.3.1 Numerical SSF formulation

We can re-write the fundamental equations for the calculation of the line drag force in the notation that we introduced in §2.3.6 using our method for the calculation of the optical depth. In terms of a sum over frequency in each spatial grid cell this can be written as,

$$g_{\rm rad}|_i \propto \sum_{n=x_1}^{x_2} \left[\eta_{-,n,i}^{-\alpha} - (\eta_{+,n,i}^{-\alpha}\right] \Delta x \tag{5.14}$$

$$\propto \sum_{n=x_1}^{x_2} \left[(\eta_n^* - \eta_{+,n,i})^{-\alpha} - \eta_{+,n,i}^{-\alpha}\right] \Delta x, \tag{5.15}$$

using the notation we introduced in §2.3.6. The relation in equation (5.12) allows us to re-write $\eta_{-,i} = \eta^* - \eta_{+,i}$ using $\eta^* = \eta_{+,imax} + \eta_{-,imax}$. This requires knowledge of $\eta_{-,imax}$ at each step of the calculation and therefore this is calculated outside of the main force calculation loop. This is only the diffuse force and must be added to the direct force for the complete treatment.

5.3.2 Numerical results of SSF

Using the characteristics for ζ Pup, given in Table 3.2, we created a model using the above SSF formulation. The inclusion of the line drag force should be to increase the stability of the wind producing a less structured flow. In Fig. 5.9 we show results which include the diffuse force in the calculation of the dynamics. The solid curves are those calculated with the above SSF approach while the dashed curves are for a model which is exactly the same but does not include the diffuse force. Both models employ a finite disc correction and have a sub-sonic boundary condition at the surface of the star and a Gaussian line profile function.

The presence of the line drag force increases the stability of the wind as can be seen in Fig. 5.9. There is much less structure in the wind solutions. The line drag damps the LDI throughout the flow but especially in the early wind. This directly affects the structure present in the outer wind which is seeded by the structure in the early wind and develops because of the instability.

From these results we can obtain a mass loss rate of $\dot{M} = 1.2 \times 10^{-6} \mathrm{M}_{\odot}\,\mathrm{yr}^{-1}$ and a terminal velocity of $v_{\infty} = 1520 \mathrm{km\,s}^{-1}$. These values are in agreement with other published results for ζ Pup (e.g. Runacres & Owocki 2002) out to a radial distance of $4R_{\star}$.

As was done in § 3.6.3 we have calculated the statistical variables f_{cl} (clumping factor), v_{disp} and $C_{v\rho}$ (velocity-density correlation function) for both the subsonic pure absorption model and the SSF model. These averages were calculated over the time range $1.25 - 2.5 \times 10^{6}$s (i.e. data which is free from any effects of the starting conditions and can be thought of as representative). The distribution of the statistical variables for each model are shown as functions of radial distance in Fig. 5.10.

The dashed curves in Fig. 5.10 are for the pure absorption model and the solid curves are for the SSF model. Fig. 5.10(a) shows that the clumping factor for the SSF model is always at a lower value than that of the pure absorption model. This illustrates that there is less high density structure in the SSF model. Both models initially have $f_{\mathrm{cl}} = 1$

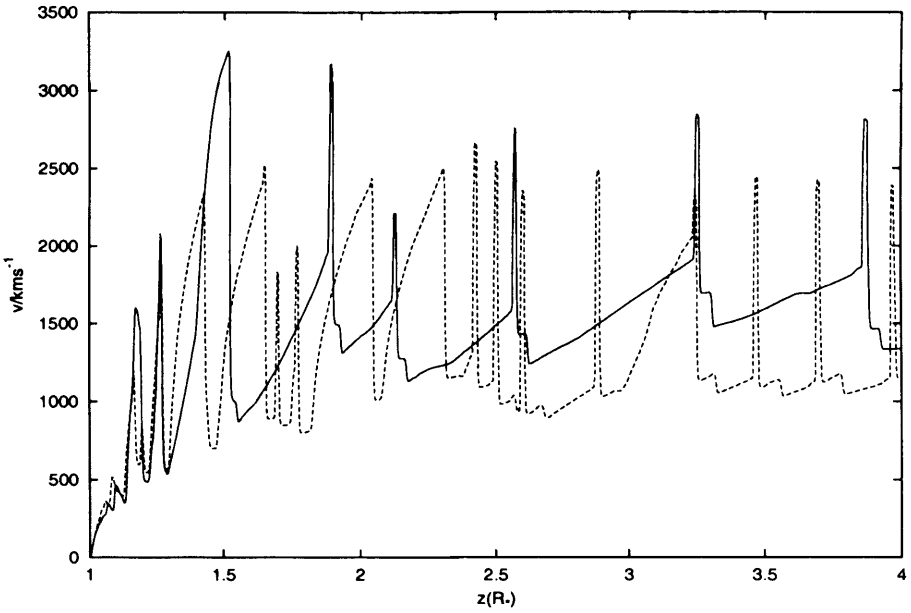

(a)

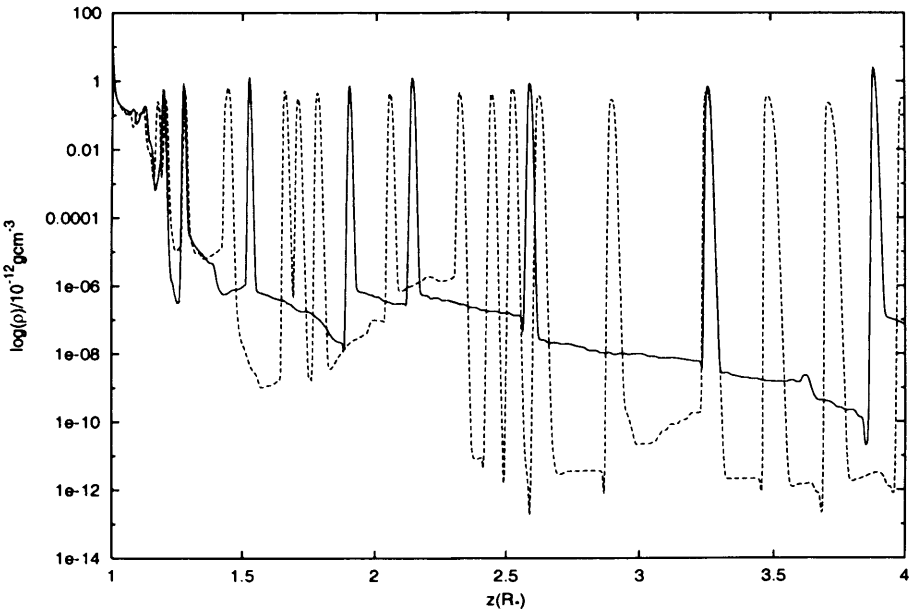

(b)

Figure 5.9: Representative results for models of ζ Pup. SSF approach (solid) and pure absorption approach (curve). The graphs show plots of a) Velocity, b) density in the cases. This demonstrates that the inclusion of the line drag force reduces the amount of structure present in the outer wind by reducing the perturbations which seed it in the inner wind.

where the flow is smooth. The clumping factor rises earlier in the pure absorption model than the SSF model, showing that the structure appears at an earlier point in that model.

The velocity dispersion, shown in Fig. 5.10(b), shows that the dashed curved is higher than the solid curve at each z. This indicates that there is more velocity variability in the pure absorption model than in the SSF model. A consequence of introducing the diffuse force in the calculation of the radiation driving on the wind is a reduction in the amount of structure present in the wind. This is borne out by the results of Figs. 5.10(a) and (b) where both the velocity dispersion and the clumping factor are higher in the case of the pure absorption model indicating a more structured wind.

The correlation function measures the correlation between velocity and density at each point in the wind. For both models there is a strong anti-correlation ($C \approx -0.8$) in the early wind which is similar to the findings of Runacres & Owocki (2002). Both models then increase at $z \approx 1.3R_\star$ to show approximately zero correlation. At this point the value of C for each model diverges but neither show any significant positive or negative correlation. The SSF model rises to show a slight bias towards a positive correlation (indicating that forward shocks become more important) while the pure absorption model shows a slight negative bias (indicating a region where reverse shocks are more important). The function then increases up to a slight positive correlation at $z \approx 3.5R_\star$.

5.3.3 Velocity gradient approach to line drag

From the premise that the diffuse radiation field is a local phenomena we explore an alternative solution to the calculation of the line drag force. Line drag occurs when there is a small local difference in the optical depth calculated in the up and downstream directions. With their Sobolev treatment, Owocki & Puls (1996) show that there is no difference between the up and downstream optical depths when viewed from a distance, i.e. the Sobolev length, showing that the effect is indeed highly localized. The reason for this is that the Sobolev approximation calculates the optical depth at a point in flow

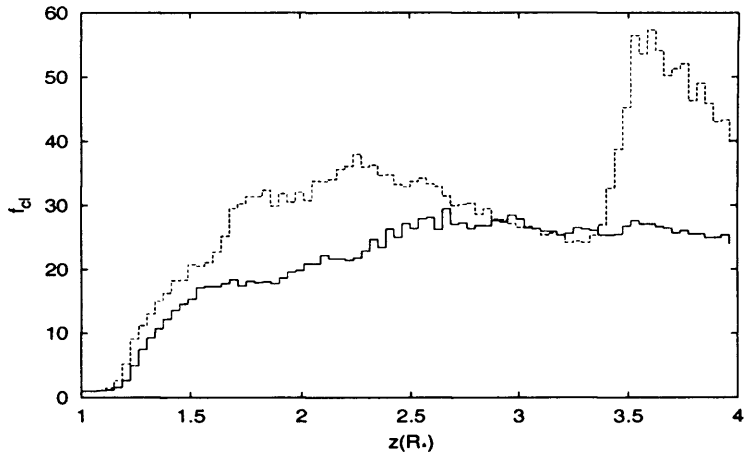

(a)

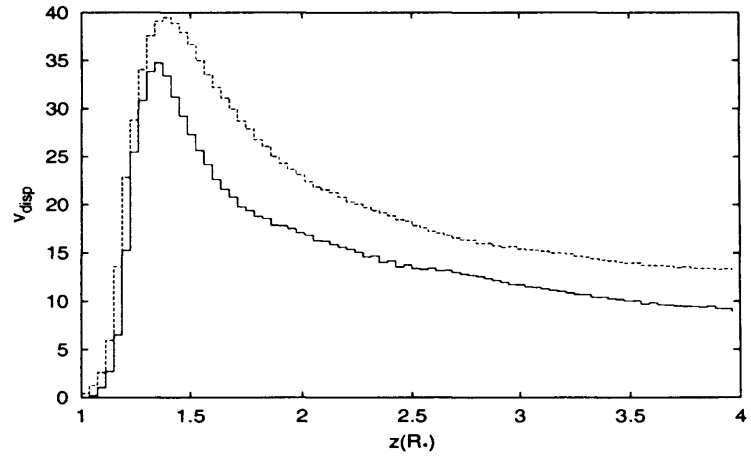

(b)

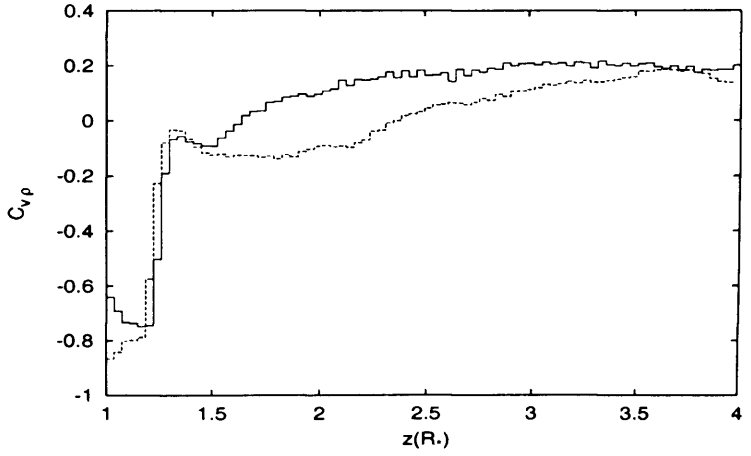

(c)

Figure 5.10: The above graphs show the variation of each of the statistical descriptors from equation (3.1) with radial distance. The data has been binned from 800 grid cells to 80 bins of equal size, to reduce the scatter at each z. This scatter does not represent noise in the data but that the flow features move quickly across the grid and are under resolved in the time average.

from the conditions (velocity gradient and density) at this point, and therefore the diffuse force calculated by this method is zero, since there is no fore-aft asymmetry.

As we showed in §3.5.1, in the Sobolev case the optical depth is different depending on which direction the velocity gradient is calculated in. This is shown by the fact that the velocity gradient calculated in the downstream direction (i.e. $v' = (v_{i+1} - v_i)/\Delta z$) produces stable flow whereas when it is calculated in the upstream direction (i.e. $v' = (v_i - v_{i-1})/\Delta z$) the flow is highly unstable (cf. Fig. 3.7).

The difference in the up and downstream optical depth is a type of fore-aft asymmetry, similar to that discussed above which causes the line drag effect. This difference does not remain constant but is large where the flow is locally asymmetric, i.e. in the presence of structure, and tends to zero when the gradient is constant, i.e. mean flow regions, thus behaving in a similar manner to the physical approach of Owocki & Puls (1996). We express the line drag acceleration as,

$$g_{\rm diff}(z) = g_{\rm thin}\Gamma(\alpha)e^{-t'(z)}\left(t_u^{-\alpha} - t_d^{-\alpha}\right) \tag{5.16}$$

where we define t_u and t_d as the Sobolev optical depths calculated using $t = v_{\rm th}\rho\kappa_0/v'$ from velocity gradients in *up* and *down*-stream directions respectively. In this notation t_u replaces t_+ from the SSF formulation, and t_d replaces t_- . In this analysis $t_u \neq t_d$ and therefore differs from the analysis of Owocki & Puls (1996), which uses the Sobolev optical depth calculated in one direction only.

We express the source function in the form,

$$S(z) = I_\star = I_\star^0 e^{-t'(z)}, \tag{5.17}$$

so that in regions where there is likely to be a high level of noise (where the wind is structured the velocity differencing will have large errors) the source function will be small. The variable $t'(z)$ represents the optical depth interior to point z as calculated

from the function η in the direct force calculation, over all contributing frequencies,

$$t'(z) = \int_{-\infty}^{\infty} \kappa_0 \eta_+(x,z)dx. \tag{5.18}$$

In our numerical scheme this can be approximated to $t(z) = \int_{x_{min}}^{x_{max}} \kappa_0 \eta_+(x,z)dx$ and $x_{min/max}$ refers to the minimum and maximum values of the dimensionless frequency within the area interior to the point z.

The effect that this method will have on the evolution of wind structure and mean flow conditions will be to increase stability, since the form of the source function makes the effect of this driving largest in the early part of the wind. Nevertheless, it will evoke the same response in downstream features but with decreasing affect until only the largest features are affected.

5.3.4 Numerical simulation of line drag

We use this velocity gradient approach to the calculation of the diffuse force in conjunction with the non-Sobolev calculation of the direct force from §2.3.6. The results will be compared with those of the previous section gained using the SSF method. In order to calculate the diffuse force using our convolution approach to the optical depth calculation requires an extra 3 lines of code to be performed to be performed at each frequency at each grid cell, plus the initialization of the spectrum at the beginning of each timestep. The velocity gradient method calculates the diffuse radiation force in about 1/3 of the time that SSF uses. This saving may become significant for a long integration over many timesteps, however the price for this saving is that the velocity gradient approach has higher noise component than SSF and an unphysical degree of freedom in the definition of $t'(z)$, as we will see below.

We employ the same toy model that has been consistently used to investigate the dynamics of the line drag phenomenon, with a top-hat profile function. We choose the value

$\kappa_0 = 1.3 \times 10^4 \mathrm{cm}^2\mathrm{g}^{-1}$ which shows a significant line drag effect (much larger values damp the diffuse field to an insignificant level and much smaller values yield an unfeasibly dominant contribution). This value is smaller than the value used in the full SSF treatment of the previous section, $\kappa_0 = 1.7 \times 10^7 \mathrm{cm}^2\mathrm{g}^{-1}$. Artificially adjusting this to a lower value in this velocity gradient method introduces an unphysical degree of freedom. A value of κ_0 which is too high exerts a perturbing influence on the early wind, and far from causing stability is responsible for making the wind unstable by accelerating it inward interior to a certain radius.

Line drag acceleration

We now construct the acceleration associated with the line drag by the means discussed above and embodied in equation (5.16). Fig. 5.11 shows the acceleration of the wind from the direct radiation force (upper curve) and the diffuse radiation force (lower curve). This figure suggests that the direct force is at least an order of magnitude larger than the diffuse force for most of the domain, however there are places where the diffuse component is comparable to the direct component. These are well aligned with shock structure, where the change in acceleration and optical depth is severe.

Compared with the curve for g_{dir}, g_{diff} contains much noise. This can be attributed to the differencing nature of its calculation and can be little improved upon by employing a more sophisticated differencing technique, without losing some of the uniqueness of this approach. We recognize this as a limitation of the method.

Velocity and density with line drag

The effect of including line drag in the calculation of the driving force is shown in Fig. 5.12. The source function has strong coupling with the line acceleration (Fig. 5.11) in the early part of the wind. On comparing the structure of the wind in Fig. 5.12 we observe that the net effect of the line drag is that it appears to damp the unstable structure; the unstable

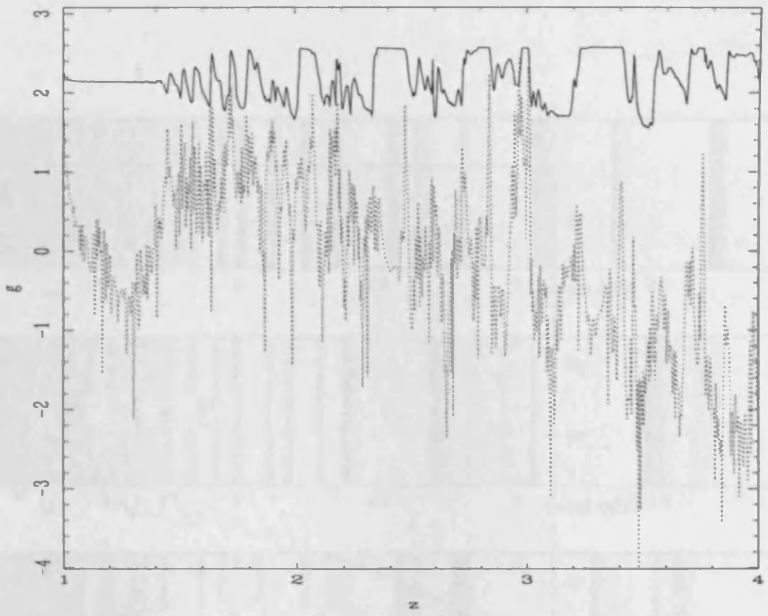

Figure 5.11: In this logarithmic plot, the line acceleration from the direct component of the acceleration is shown as the solid top curve, whereas the dotted lower curve shows the diffuse component of the acceleration

structure appears further downstream in the model which includes line drag. Line drag effectively reduces the amplitude of the structure which does form, however this effect only occurs where the source function does not vanish.

Having seen the effect of line drag on the background flow in 1D we now move to the 2D domain. In order to explore the line drag effect we perturb a steady flow background with 2 perturbations, similar to those of § 4.6. A major feature of all of the results until this point is that they contain a noticeable wake which appears upstream of the perturbed region as it propagates in the flow (e.g. Fig. 4.10(c)). Two models were considered, with characteristics, (A)$R_\rho = 1.2$, $M = 1$ and (B) $R_\rho = 10$, $M = 1$. The evolution of the perturbation in model (B), shown in Fig. 5.14 has an evolutionary pattern similar to that shown in Fig. 4.10, although the initial perturbation size is 2.5 times the density amplitude of the pure absorption model (Fig. 4.10). The motivation for using extreme perturbations is firstly to investigate the effect this has on the upstream wake and secondly to test stability of the model.

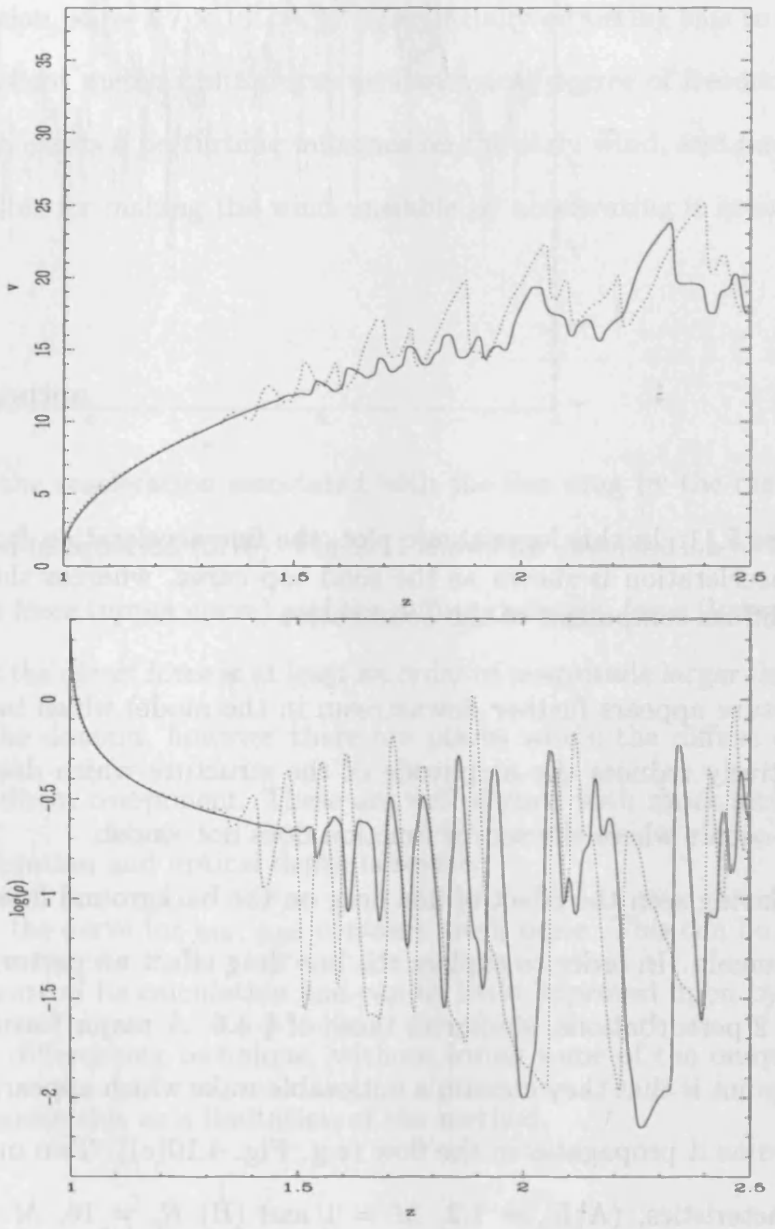

(a)

(b)

Figure 5.12: A comparison of the (a) velocity and (b) density structure in the pure absorption case (dotted) and the case including line drag (solid).

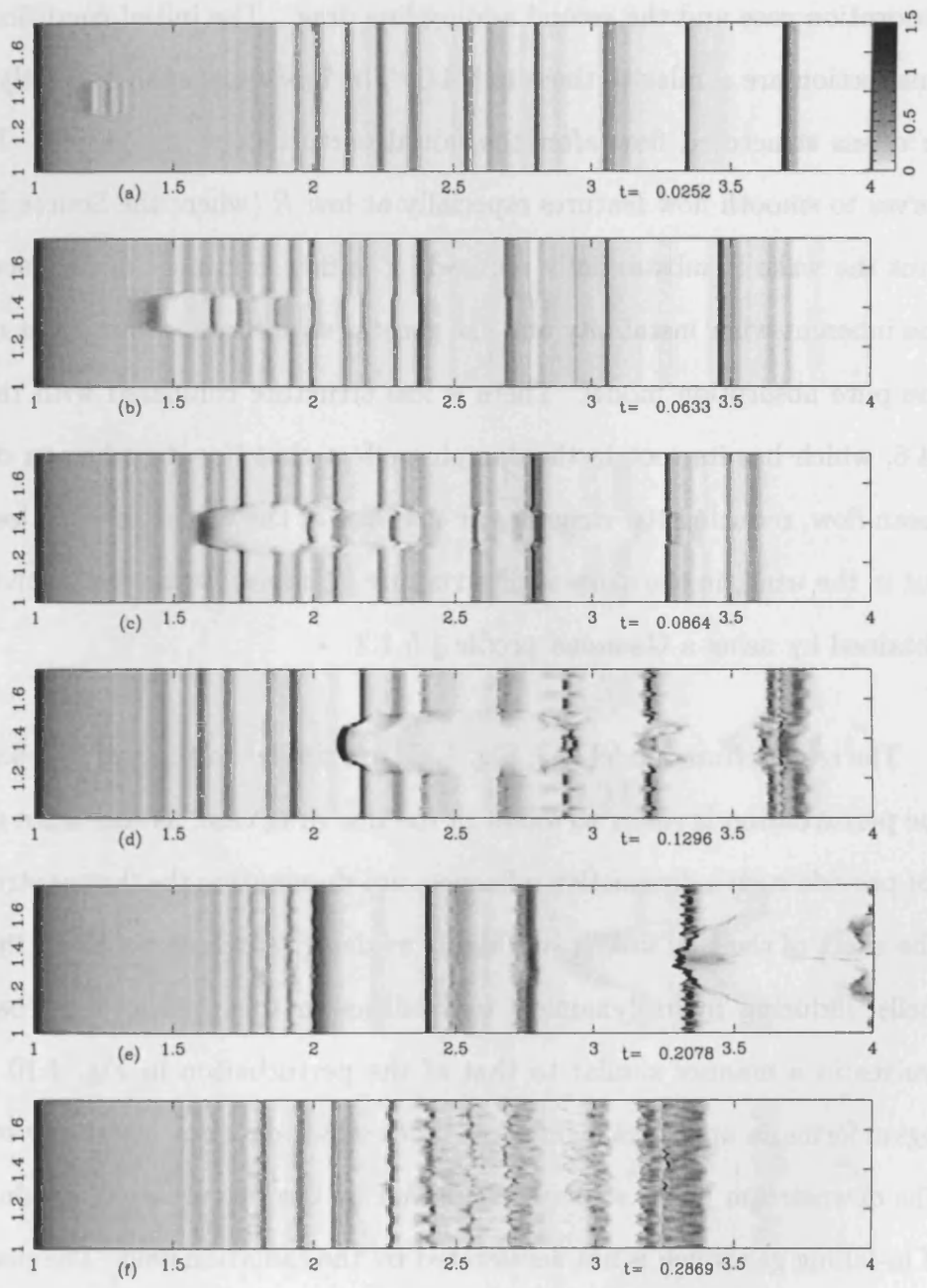

Figure 5.13: Pure absorption and line drag effect expressed as a two dimensional grey-scale plot. The steady flow was supplied with a perturbation 20% larger than the background density. The structure of the flow is less noisy than the equivalent pure absorption results of Fig. 4.9. This implies that the modelling of the line drag does serve to pacify the flow.

In two dimensions the effect of line drag is immediately noticeable when comparing Fig. 4.9 with Fig. 5.13, both with perturbations of $R_\rho = 1.2$, $M = 1$ the first in the pure absorption case and the second adding line drag . The initial conditions of the models of this section are similar to those in § 4.6. The upstream wake is greatly reduced, resulting in a less structured flow after the initial perturbation has passed. The line drag force serves to smooth flow features especially at low R (where the Source function is largest), thus the wake is substantially reduced. The flow continues to produce dense shells from the inherent wind instability and the general structure is reminiscent of that produced in the pure absorption model. There is less structure compared with the results shown in §4.6, which has its root in the damping effect that line drag has on deviations from the mean flow, reducing the structure at the base of the wind and (to a lesser extent) further out in the wind, in the dense shell structure. The results are qualitatively similar to those obtained by using a Gaussian profile § 5.1.3.

The results from model (A), Fig. 5.13, are similar to those of Fig. 4.9. The evolution of the perturbation is easier to follow in the line drag case, as the dense shell structure does not provide such a destructive influence, not dominating the flow as strongly as in Fig. 4.9. The effect of the LDI flow is still highly evident, as well as the effect this has on the dense shells, inducing hydrodynamical instabilities in them. The perturbation in model (B) evolves in a manner similar to that of the perturbation in Fig. 4.10. The high density region forms an upstream facing bow shock which develops instability structure on its face. The downstream gas is strongly shadowed by the perturbation, producing a large region of in-falling gas which is not accelerated by the radiation field. The perturbation expands as it propagates and also is bloated by swept up material, as has been shown to happen throughout this chapter. There is a visible, but faint, wake upstream of the perturbation in Fig. 5.14(b) and (c). It is well defined and has little effect on its surroundings; the life of the wake is strongly dependent on the perturbation, it does not linger to a great extent in the post-perturbation flow, leaving a more ordered flow.

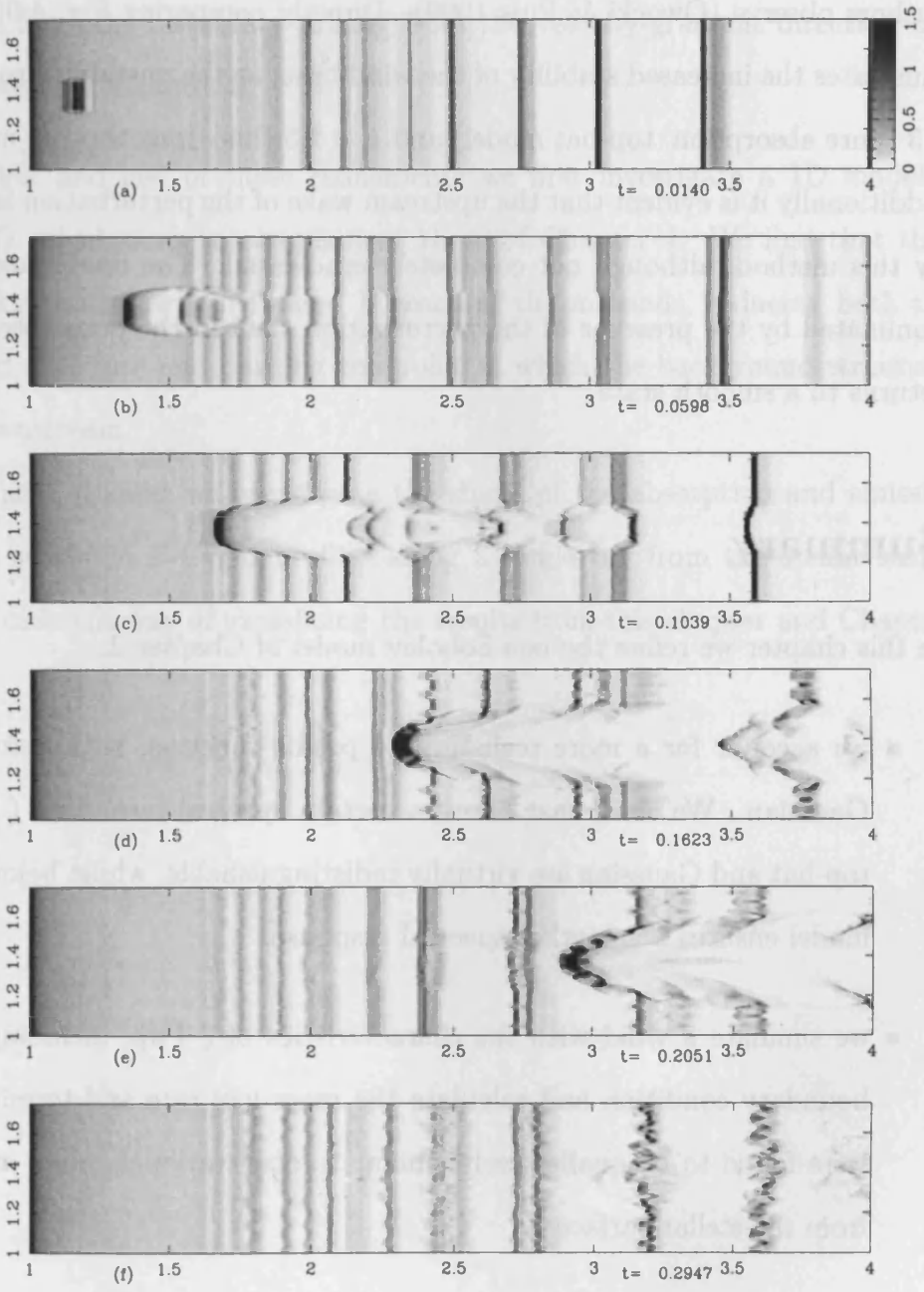

Figure 5.14: Pure absorption with line drag force. The steady flow is perturbed with a region of $R_\rho = 10$, $M = 1$. The line drag solution is numerically stable and the flow solution appears to be similar to published results. The behaviour of the perturbation is similar to that of Fig. 4.10, which has a 2.5 times smaller density amplitude.

This formulation provides a qualitative model describing the line drag force which, far from containing any numerical pathologies, appears similar to the results that previous authors observe (Owocki & Puls 1999). Directly comparing Fig. 4.9(f) and Fig. 5.13(f) illustrates the increased stability of the wind base, as the unstable structure begins at $z = 1.3$ (pure absorption, top-hat model) and $z \approx 1.5$ (line drag, top-hat model), respectively. Additionally it is evident that the upstream wake of the perturbation is constrained better by this method, although not completely eradicated. The final state of the flow is less dominated by the presence of the perturbation than in the pure absorption model, as it returns to a smooth state.

Summary

In this chapter we refine the non-Sobolev model of Chapter 2.

- we account for a more realistic line profile function, with a functional form of a Gaussian. We show that above a certain spectral resolution ($\Delta v/v_{\rm th} > \Delta x$) the top-hat and Gaussian are virtually indistinguishable, whilst below this the Gaussian model ensures a smoother spectral response.

- we simulate a wind with the characteristics of ζ Pup, including a sub-sonic inner boundary condition and calculate the mass loss rate and terminal velocity. These were found to be qualitatively similar to observational values at a distance of $4R_*$ from the stellar surface.

- we build on our model of ζ Pup and move to an approach which includes line drag in a smooth source function approach, similar to that of Owocki & Puls (1999). We obtain results which are in agreement with the structure that they observe in velocity and density, and also we obtain a mass loss rate and terminal velocity which agrees well.

- we include the contribution of the diffuse force to the original top-hat form of the pure absorption case. We approximate the diffuse radiation field using the knowledge from the instability arising from the velocity-gradient direction calculation, expressed in Chapter 3.

With first and last of these refinements we first investigate a 1D model and then perform 2D calculations to complement those of Chapter 4. We find that the stability of the background flow is increased by each of the methods, reducing both the level of background structure and pushing the point at which the background structure appears further downstream.

In the next chapter we investigate the shape of the absorption and emission contributions to synthetic P-Cygni profiles along a single ray from the stellar surface. This explores a different way of visualizing the results from this chapter and Chapter 4.

Chapter 6

Spectral details

This chapter is concerned with processing the density and velocity data from the simulations of the previous two chapters into observable quantities, specifically synthetic UV spectra. Although the simulation of these winds provides us with insight into the physics of such flows, it does not reveal how such features would appear in the spectrum of a star. Current observational techniques cannot resolve small surface and nearby wind features such as unstable shells.

The models that we use to construct spectra are: (i) pure absorption using a top-hat profile, (ii) pure absorption using a Gaussian profile, (iii) pure absorption (top-hat) with velocity gradient line drag. We have seen in the previous chapter that these 3 methods produce results which are quantitatively different and this is our motivation to study the previous models in a way which could be distinguished observationally. In this chapter we investigate the differences which exist between the models, in the observational domain.

6.1 Synthesizing spectra

During the calculation of the radiation driving force (which is computed alongside the hydrodynamics) it is necessary to calculate the absorption of the radiation field by the gas in the wind, which is achieved by the method described in §4.6. We show below that

the absorption which is calculated in this fashion can be used to generate synthetic UV spectra. The data from the 3 models is converted into spectral information using the formulation of Lucy (1983) which was further developed by Puls, Owocki & Fullerton (1993; hereafter POF) for a resonance emission line singlet.

We will not re-derive the formulation here since we use this method as a tool rather than being concerned with it as a detailed physical argument. We will explain the more important assumptions that POF use in addition to the ones that we make in our approach.

6.1.1 Calculation of spectra

Calculating the source function for a pure-scattering line involves an angle average of the escape and core-penetration probabilities, which are in turn calculated from the optical depth at each point in the flow. The approach of POF employs the Sobolev approximation to simplify the calculation of the source function. The Sobolev approach although not suitable for a hydrodynamical non-monotonic flow, where fine-scale structure is rife (and therefore important), can be used here because in the calculation of the emission component of a spectral line the averaging over angle serves to smooth out fine-scale spectral features. The coupling between distinct resonance points in a non-monotonic flow is an issue which POF treat more specifically, whilst still using the Sobolev optical depth. For our analysis the Sobolev approach adequately models the escape probability. The escape probability is the probability of a photon arriving at a point r will escape to an observer at infinity. The coupling between different points along each ray is implicit in each data set, since a non-local approach was used in its calculation (as part of the driving force calculation).

The calculation of the source function is written in the form provided by Sobolev (1960) as follows,

$$S(r) = \frac{\beta_c(r) I_c}{\beta(r)}, \tag{6.1}$$

where the angle-averaged escape probability is

$$\beta(r) = \frac{1}{2}\int_{-1}^{1} \frac{1-e^{-\tau}}{\tau} d\mu, \tag{6.2}$$

and the angle-averaged core-penetration probability is

$$\beta_c(r) = \frac{1}{2}\int_{\mu_\star}^{1} \frac{1-e^{-\tau}}{\tau} d\mu, \tag{6.3}$$

where $\mu_\star \equiv \sqrt{1-R_\star^2/r^2}$ and μ is the cosine of the angle between the normal to the photosphere and the chosen ray path ($\mu = 1$, radially outwards; $\mu = -1$, towards the star). The optical depth is calculated using the Sobolev approximation along μ (Lucy 1983) as follows,

$$\tau(\mu, r) \equiv \frac{\rho\kappa_l v_{\rm th}}{\left|(1-\mu^2)\frac{v}{r} + \mu^2\frac{dv}{dr})\right|}. \tag{6.4}$$

The equations for the emission and absorption components to the spectrum are given as follows,

$$\Re_\nu^{em} = \int_0^{R_{\rm max}} \frac{2pdp}{R_\star^2} \int_0^{t(\nu,p,z_{\rm min})} \frac{S(r)}{I_c} e^{-t} dt \tag{6.5}$$

$$\Re_\nu^{abs} = \int_0^{R_\star} \frac{2pdp}{R_\star^2} e^{-t}, \tag{6.6}$$

where the distance along the path in the radial direction $z \equiv \mu r$ and the tangential direction $p \equiv r\sqrt{1-\mu^2}$ and the stellar intensity, I_c, is assumed to be constant.

We re-express the absorption component as,

$$\Re_\nu^{abs} = e^{-t(z)}, \tag{6.7}$$

but we perform the angular integration for the emission component, equation (6.5). We make this compromise since in our simulations all the photon rays are parallel and therefore there is no angular absorption over which to integrate. This absorbed radiation is

scattered in all directions, hence the calculation of the emission component must include the integral over μ.

6.1.2 Resonance line formation

The potency of the line driving in winds is due to the presence of metal ions. The effective cross-section of a metal ion is larger than that of H^+ and He^+ ions, and increases with the resonant frequency of the ion. Metal ions have more electronic line transitions at lower frequencies than HI . From atomic theory the line profile integrated form of the line strength is given by

$$\alpha_{\rm l} = \frac{\pi e^2}{m_{\rm e} c} \frac{1}{\Delta\nu_{\rm D}} f_{mn} N_n \left[1 - \exp\left(\frac{-h\nu}{kT}\right)\right], \tag{6.8}$$

where e and $m_{\rm e}$ are the charge and mass of an electron, $\Delta\nu_{\rm D}$ is the line width, Doppler broadened by thermal motions, c is the speed of light. The parameter f_{mn} is the oscillator strength, which is a function of the line centre wavelength and the Einstein B coefficient (excitement probability). N_n is the population of the ions in the lower state, n and assumed to be proportional to the mass density at a particular radius. A further assumption is that the exponential term in equation (6.8) can be neglected, implying that this is a high frequency or low temperature limit. With these assumptions in mind we re-express equation (6.8),

$$\alpha_{\rm l}(r) = \kappa_{\rm l}\rho(r) \tag{6.9}$$

with $\kappa_{\rm l}$ as the mass absorption co-efficient or line opacity, and is taken to be constant. It is useful to introduce the dimensionless line opacity parameter, defined by Hamann (1980),

$$k_{\rm l} = \frac{\dot{M}}{4\pi R_\star v_\infty^2} v_{\rm th} \kappa_{\rm l} \tag{6.10}$$

where both $\dot{M}$ and v_∞ are taken from published stationary models. If we take values of the stellar characteristics of ζ Pup from Table 1.1 with a thermal velocity of $v_{\rm th} = 7.5\,{\rm km\,s^{-1}}$. We can calculate a value of $k_{\rm l} = 1.6 \times 10^{-4}\,{\rm g\,cm^{-2}}\kappa_l$. The maximum value of $k_{\rm l}$ can be found by replacing $\kappa_{\rm l}$ with κ_0, where $k_{\rm l} \approx 10^3$.

6.1.3 Spectral structure

We consider two lines with different strengths, a moderate strength line with $k_{\rm l} = 1$ and a strong line with $k_{\rm l} = 100$. The moderate line shows much detail which reflects the structure in the wind whereas the strong line saturates, thus swamping the wind structure and exposing the blue absorption edge structure.

Once the wind approaches the terminal velocity, the bulk of the mass should be traveling at this velocity (according to the mean flow solution). However in reality the structure present in the wind will persist, causing rarefactions and high density patches. In the mean flow solution (monotonic and unstructured) the blue absorption edge is sharply defined (Lucy 1983), since the wind cannot travel faster than the terminal velocity. In such a stationary solution there is strong absorption at the blue edge, since there is a large amount of mass in this spectral region. However the gas is much more diffuse in this region than at the inner wind, making it optically thinner, and thus the absorption due to individual flow elements is insubstantial, while the total absorption from all of such flow elements is considerable due to the large spatial area they cover.

Of course this is only applicable for a stationary and unstructured wind. In the more realistic case of a wind with time-varying non-monotonic structure, the blue absorption edge will not be well defined. Structure present in the wind, traveling faster (and slower) than the terminal velocity, notably alters the shape and definition of the blue edge. High velocity clumps cause the sharp cut off of the edge to be smoothed into a curve by the strong absorption. The amount of variation or smoothing in the blue edge is dependent on how widely populated the outer wind is with structure. This is something which we

will return to in the context of processing the results of the downstream approach to structure evolution.

The P-Cygni profiles which we generate are not complete, nor are they intended to be definitive. Our intention is to compare structure in the physical domain with their spectral manifestations and thus learn more about the observational relevance of such hydrodynamical models. As has been discussed we employ a supersonic condition at the inner boundary. The subsonic region of the wind does not make a substantial contribution to the low velocity part of the absorption profile.

Since we are missing the subsonic part of the spectrum in both absorption and emission our P-Cygni profiles are truncated in a region about zero velocity (at the line rest frequency). This not only affects the subsonic region, but also the region out to $\approx 3a_0$ where the rapid acceleration of this wind solution makes the gas optically thin (but increasing in optical thickness rapidly). A solution which passes through the critical point corresponds to gas which has a large optical depth initially and decreases further out in the wind. Our model does not establish such an optically thick region and spatially the optical depth of the early wind increases rapidly (as the velocity gradient is initially large). However in the spectral domain this appears as a gap where the wind is optically thin, which is an effect of the early supersonic wind not being able to establish an optically thick region in such a spatially small area of the wind (contains only a few spatial grid cells).

6.2 Synthetic P-Cygni profiles

We first compare the results from a β-law (power law of radial distance) wind solution with those of a representative mean flow, individually showing the absorption and emission components to the spectrum. We do not include the radiation which is scattered back to the core. This radiation is reflected back towards the star and is therefore seen in absorption at the red wing of the line. It only affects the positive velocity part since

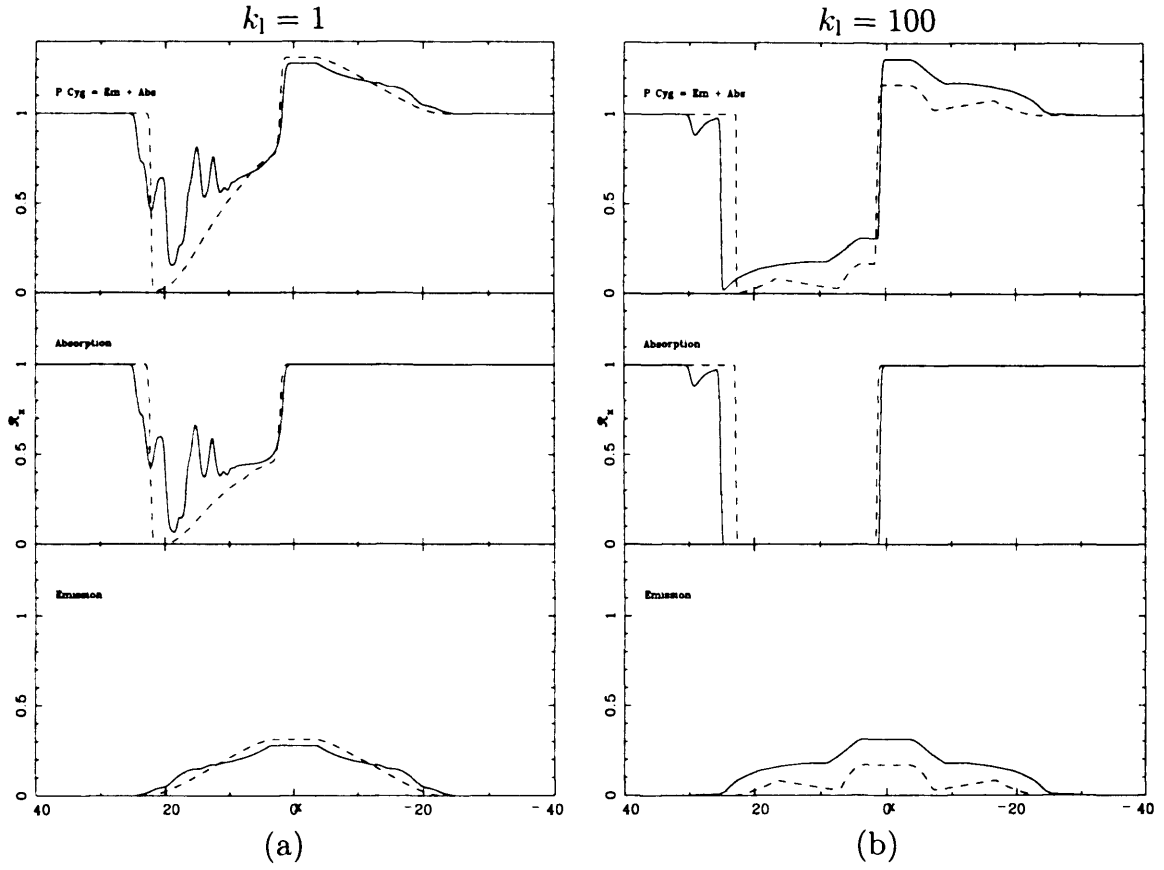

Figure 6.1: The comparison of two methods of P-Cygni profile calculation for (a) a moderate strength line, $k_1 = 1$, (b) a strong line, $k_1 = 100$. The solid curve is formed from a structured wind solution shown in Fig. 5.4(a), and the dashed line is formed from the β-law description given in equation 6.11. It is seen that the strong line (b) saturates the spectral features exposing the blue absorption edge, whereas the moderate strength line (a) displays the wind structure well.

the negative region of the emission contribution is by definition from velocities directed towards the observer.

We use the results from the top-hat and Gaussian pure absorption models and the line drag model to generate synthetic P-Cygni profiles.

6.2.1 Absorption and Emission components

In the calculation of the P-Cygni profiles shown in Fig. 6.1 we choose two different line opacities reflecting (a) moderate strength line opacity, $k_1 = 1$, and (b) strongly

absorbed line, $k_1 = 100$. In the case of the high opacity line, Fig. 6.1(b), the absorption component is highly saturated, whereas the emission component sharply steepens towards zero velocity. This effect cannot be directly seen in Fig. 6.1(b) since there is information missing concerning the velocity structure of the inner wind, but the steepening is visible. The higher opacity line, by saturating the lower velocity spectral features, allows the low amplitude features which exist in the wind (in this case at high velocity) to be exposed. This is especially important for investigating the variability of the blue edge of the absorption spectrum, which arises from gas propagating at the terminal velocity.

The contrast between the smooth β-law (Lamer & Cassinelli 1999) solution (dashed) with form,

$$v(r) \approx v_0 + v_\infty \sqrt{1 - \frac{R_\star}{R}} \tag{6.11}$$

and the pure absorption model data emphasizes the importance of a structured wind, not only on spectral absorption features but also on blue edge variability. Comparison of Fig. 6.1 with the results of POF and the stationary wind result of Lucy (1983), shows that although the low velocity region is ignored the results of our approach bear a strong resemblance.

6.2.2 Pure Absorption spectra

We generate P-Cygni profiles from the 2D results shown in §4.6. In order to gain an accurate impression of the profile shape the results from an entire star should be averaged over the stellar disc solid angle. The spectra that we calculate here are only relevant for a narrow slice through the wind. When calculating the spectra we use only the data along a central ray and do not average over the width of the 2D slice in the physical domain. Averaging the optical depth would dilute the extreme characteristics of the perturbed flow and also confuse the analysis since the spatial resolution would be further complicated by absorption components in non-central rays. The structure in the rest of the wind (i.e. $z > 4R_\star$) is unknown so we do not perform this averaging since it would involve making

assumptions about the state of the outer wind.

In the physical domain it is clear what is meant by 'perturbation', since a region of high density or velocity gas remains at or close to its position from the previous timestep and the evolution of the condensation is clear. In the spectral domain, at any velocity there is an absorption contribution from across the flow which obscures the evolution of any particular physical flow feature. This makes the spectra more difficult to interpret as the amount of structure increases. In a simple monotonic background flow any perturbation is obvious as a non-uniform spectral feature. That luxury is not afforded by a real, highly structured wind, however it does not mean that the evolution of a perturbation is unobservable.

For the purpose of spectral analysis we must consider the perturbation as an object which has two velocity components, corresponding to the high density part (low velocity) and its accompanying downstream rarefaction (high velocity). Physically these two parts are adjacent, however the distinction between the two sections in the spectrum is evident after consideration of, for example, Fig. 6.2.

These model spectra are highly idealized since they are calculated from the absorption along a single ray only. Observations are the sum of all rays directed towards an observer therefore small local features will be smeared out, further removing the association of a particular spectral feature with a particular spatial feature.

Top hat line profile model

In the spatial domain the top-hat models have a large amount of structure from the LDI, is largely due to the shape of the profile function (cf. Fig. 5.3). We take the results from one of the models discussed in §4.6, with contrasting perturbation characteristics. The synthetic spectra shown in Fig. 6.2 match those shown in Fig. 4.8; the spectra are calculated from the data along the central ray at each of the times shown in the physical plots.

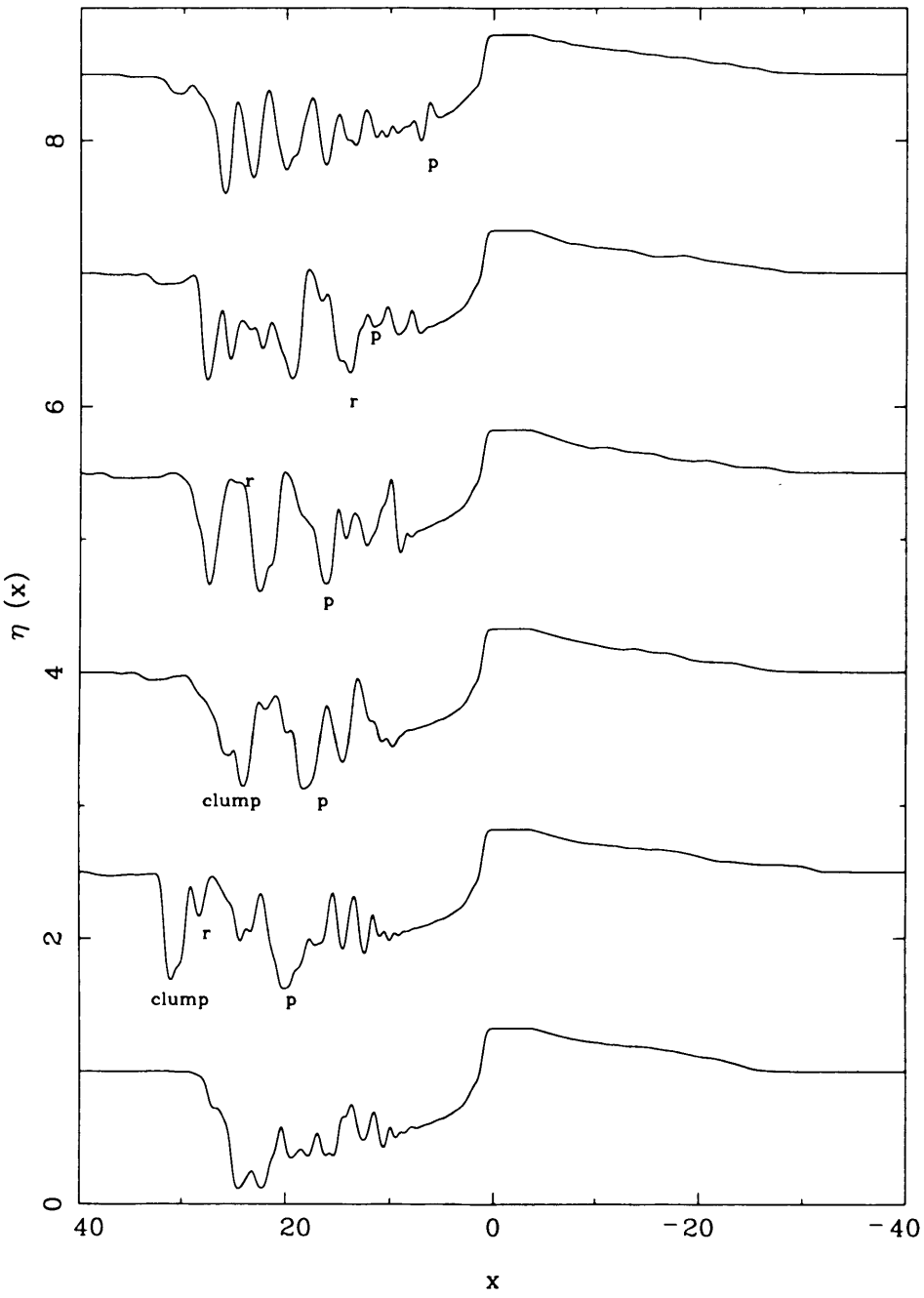

Figure 6.2: The set of P-Cygni profiles generated from the wind data shown in Fig. 4.8. $R_\rho = 1$, $M = 1.2$. From the markers the evolution of the two components of the perturbation can be observed. In all subsequent P-Cygni profiles the dense part of the perturbation is labelled 'p', while the rarefied part is labelled 'r'. There is strong absorption from a feature not correlated with the perturbation (labelled 'clump') which interferes with the spectral evolution of the perturbation. The 'clump' is not physically linked to the perturbation.

There are various strong absorption features visible in the spectra of Fig. 6.2. It is clear from the spectra at different times that the structure is not constant and we infer from this that the wind is indeed highly structured (as was demonstrated in the 2D results of §4.6). From these results we can trace the evolution of the perturbation as it accelerates into the outer wind.

We have traced the evolution of the perturbation across the stellar spectrum from its inception to its disappearance from the grid. In Fig. 6.2(a) we can see that initially the dense and rarefied parts of the perturbation have not yet spread apart in velocity. As time progresses, the spectral positions of the two components spread apart. The dense part is quite visible as a discrete absorption region. Although there is some contamination of this feature from the non-monotonic flow, the majority of the absorption in this feature is from the high density region which the perturbation has evolved into.

The rarefied region is optically thin and, although this assists its propagation through the flow, it hinders its ability to be observed in the spectrum. In Fig 6.2(c) this is particularly obvious, where the rarefactions velocity is marked showing that there is very little absorption. At the next time shot, Fig. 6.2(d), this optically thin part is superposed with an optically thick downstream clump of gas, and thus completely obscured, illustrating a disadvantage of the lack of spatial resolution in this domain.

Gaussian line profile model

Moving from the top-hat line profile function to the Gaussian line profile function does not generate significantly different spectra. This is not unusual since the wind remains non-monotonic and contains structure at all velocity scales. In the physical domain (cf. Fig. 5.6) the effect of the change in profile shape is shown by the increased stability of the inner wind. This phenomenon is not easily conveyed to the spectral domain as when structure does appear in the wind, it is present at similar scales to the top-hat model.

The P-Cygni spectra generated from the Gaussian models, the results of which are

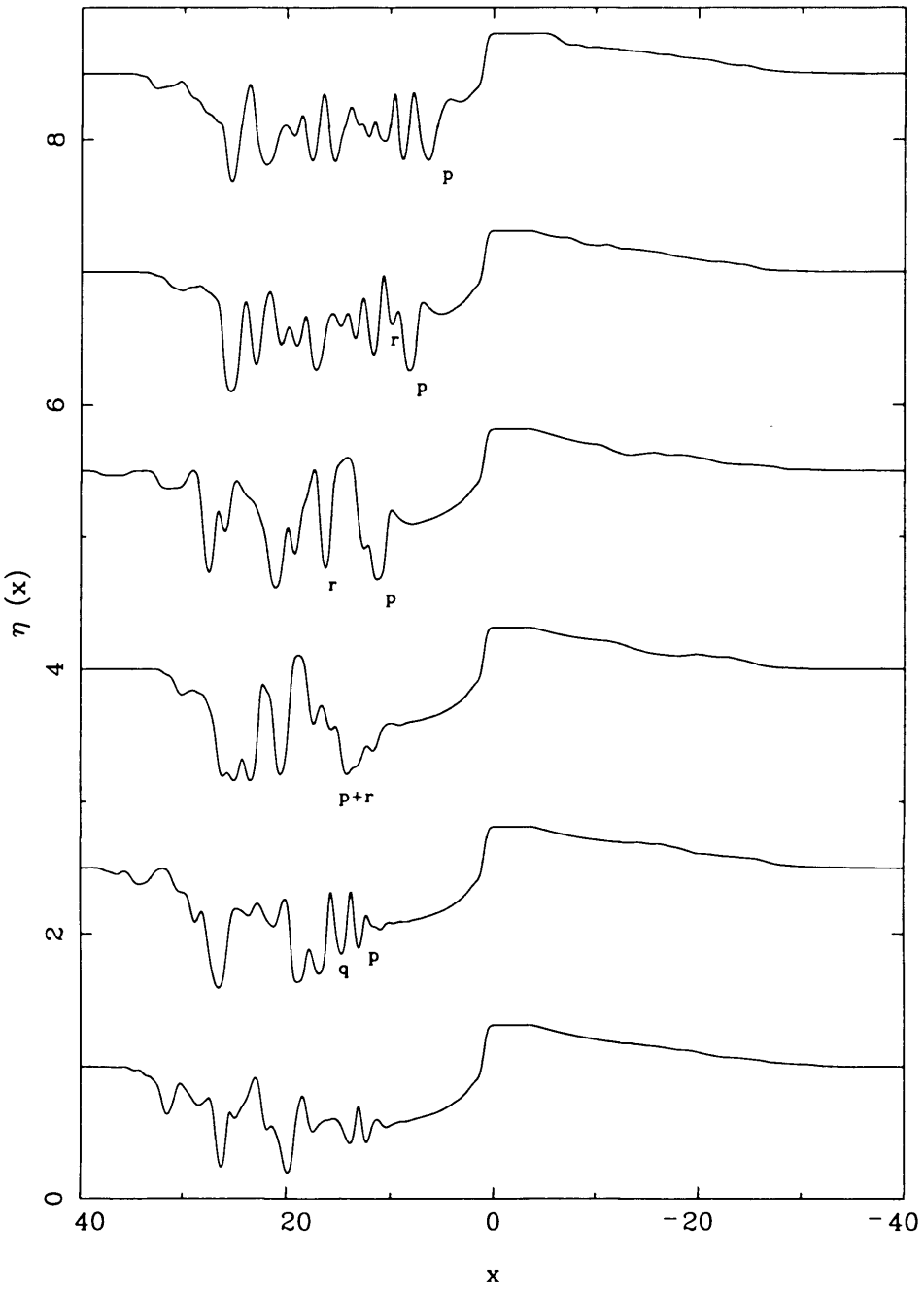

Figure 6.3: The set of P-Cygni profiles generated from the wind data shown in Fig. 5.6, $R_\rho = 4$, $M = 1$, generated from the Gaussian line profile function. The labels 'r' and 'p' refer to rarefied gas and the densest part of the perturbation, repspectively.

shown in Fig. 5.6, are shown in Fig. 6.3. Similar analysis of the spectra, to that of the previous section, shows that the change of driving does not significantly affect the evolution of perturbations. The specifics of the spectra are different to those of the top-hat model.

In Fig. 6.3(c) the strong absorption feature r, does not represent a contribution entirely from the rarefied part of the perturbation, but the superposition of this with a dense shell further out in the flow. At a subsequent time, Fig. 6.3(d), the observation of the perturbation becomes less clear. Inspection of the physical domain at that time, Fig. 5.6(d), shows that the high density region begins to thermally expand spreading the perturbation out and blurring the physical distinction between the rarefied and dense regions. This feature continues to expand and propagate with the flow until a dense shell from the background impacts into its upstream end, causing the shell to bow and become unstable. This can be observed in Fig. 6.3(e) where an optically thin clump q, which is unrelated to the initial perturbation p (and has a higher velocity) appears. We will see in § 6.3 how this feature spectrally interacts with the perturbation in more detail.

The flow in this Gaussian model evolves back to a structured spectrum similar to the initial condition, (cf. Fig. 6.3(f)). The low velocity spectrum is initially dominated by the strong absorption of the perturbations, in both cases. As the perturbations accelerate to higher velocities, the low velocity region ($0 < v < -10a_0$) becomes more exposed and its smooth structure more easily observable.

6.2.3 Line drag

As with the spatial results we consider the effect of introducing the line drag effect to the pure absorption model. We have included a diffuse radiation field term in the top-hat model only.

The perturbation model that we consider here was introduced in §5.3.4, Fig. 5.14. The resulting spectrum is seen in Fig. 6.4. A notable difference between these spectra

and the pure absorption spectra is the amount of small amplitude velocity structure. The line drag spectra contain a lesser amount of low velocity absorption structure than the pure absorption models. This is to be expected since the diffuse radiation field stabilizes the flow against small wavelength structure, meaning that there is less variation in the velocity field and that the spectra will tend to contain larger absorption features. As discussed in §5.3, the line drag force is most potent in the early part of the wind where the source function is large, which specifically will affect lower velocities. This can be seen in the flow once the effect of the perturbation abates, the inner wind is more uniform than the equivalent pure absorption case (top-hat model). In the spectral domain this is manifest in the smooth absorption feature from $-10 < x < 0$, seen in for example Fig. 6.4(f).

The perturbation shown in Fig. 6.4 matches that shown in Fig. 5.14 and has a rather extreme initial density. Fig. 6.4 shows the upstream (p) and downstream (a) parts of the initial perturbation as it expands. Initially we see that the absorption characteristics of the two parts are very similar, implying that initially the shell expands isotropically, which can be confirmed in the density plot (Fig. 5.14), the perturbation initially expands with fore-aft symmetry. As the perturbation continues to expand, a becomes disrupted by hydrodynamical instability, so we now indicate the evolution of the dense upstream part and the rarefaction associated with the perturbation p since it remains distinct in the flow for the majority of its life on the grid. The dense part of the upstream edge continues to grow optically thicker as it moves across the spectrum and its rarefied counterpart grows optically thinner. In Fig. 6.4(e) there is another example of the superposition of this optically thin region with other flow features, emphasizing that the lack of spatial resolution can confuse the spectral analysis.

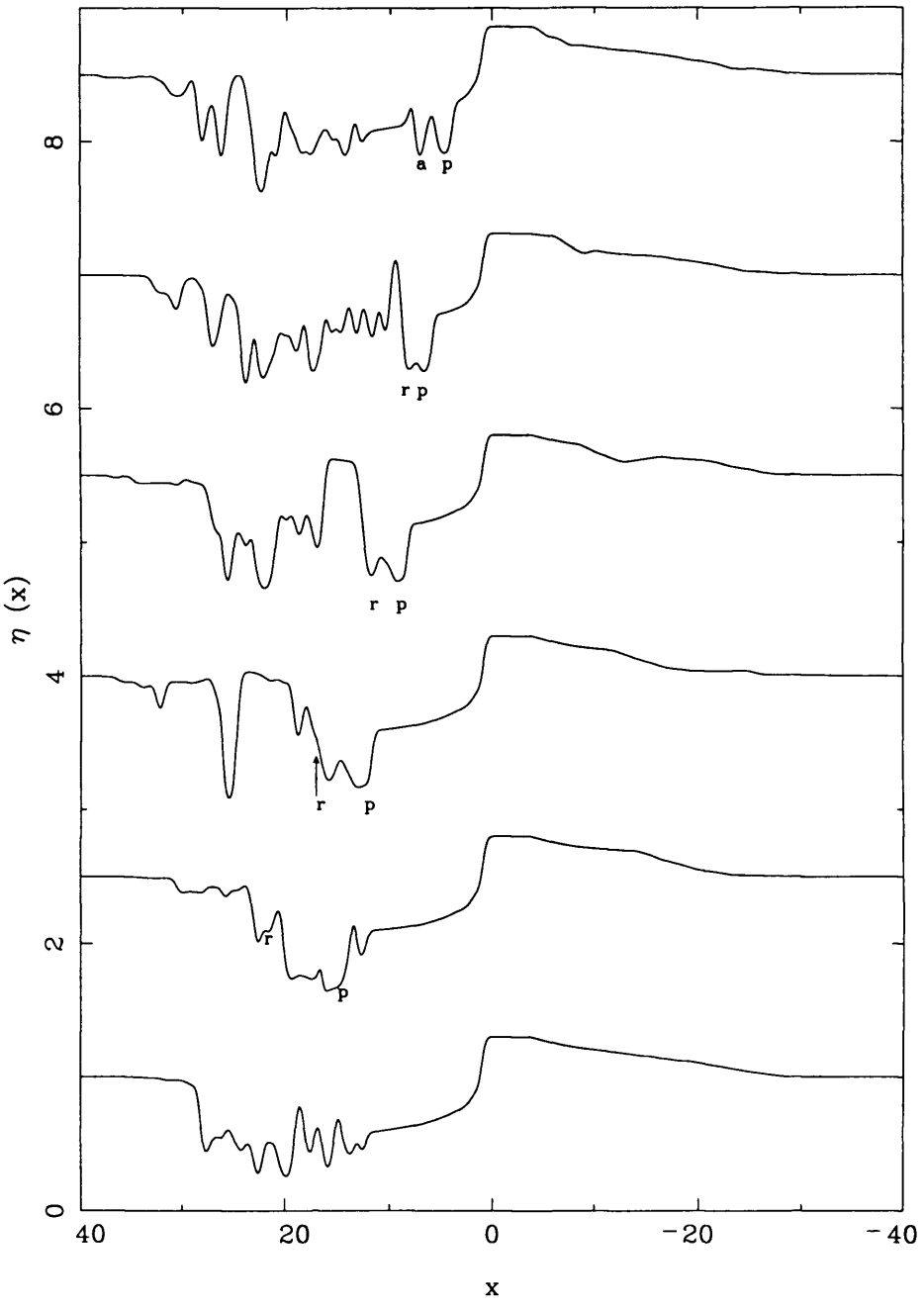

Figure 6.4: The set of P-Cygni profiles generated from the wind data shown in Fig. 5.14, $R_\rho = 10$, $M = 1$, using the top-hat pure absorption model in conjunction with the approximate line drag model. The label 'a' refers to the downstream part of the perturbation and 'p' the upstream denser part. 'r' refers to the region of rarefied gas which accompanies the dense perturbation.

6.3 Trail diagrams

Much information can be gained from a quantitative analysis of the spectra, such as has been done above, since discrete velocity structure can be identified and correlated with physical components to the flow. However since this data is isolated in time the continuous evolution of the flow features can be difficult to visualize. In order to further explore the spectral evolution we plot the P-Cygni profile generated at each time step as a linear greyscale. Each greyscale strip is laid contiguously onto that of the previous time step, forming an absorption trail diagram.

In this section we show trail diagrams which accompany each of the models shown in § 6.2.2 and 6.2.3; pure absorption using a top-hat line profile ($R_\rho = 1.2$), pure absorption using a Gaussian line profile ($R_\rho = 4$) and the top-hat profile model with line drag effect ($R_\rho = 10$) the velocity is unperturbed for all of them ($M = 1$).

There are many interesting effects which can be observed in this trail diagram, revealing information about the character of the flow and the perturbations. The acceleration history of features is clearly demonstrated by looking at an optically thick (dark) trail. A steep trail indicates slow acceleration, and a shallow trail likewise shows fast acceleration. Typically the slope of any trail will change as the wind evolves and generally a dark trail will be steep and a light trail will be shallower. This is not always the case, for two main reasons. Firstly the acceleration of a region of gas is not entirely governed by the radiation field coupling (in non-monotonic structured flow the dynamics are also constrained by the motion of the surrounding gas), so optical depth is not a reliable indication of radiative acceleration. Secondly, since the flow is non-monotonic there is no spatial resolution in the spectra and therefore features from different physical positions in the flow can be superimposed contributing to an absorption feature at a particular velocity. These will often quickly broaden as the two separate physical features evolve differently in the flow. There are also numerous incidents of colliding trails which does not necessarily indicate a physical collision of gas clumps and may just reflect a superposition (although it does

imply an interaction between the shells by line de-shadowing).

The trails end suddenly as the features disappear from the edge of the grid. This lends support for having a larger grid size but any grid must have a finite size which would be reflected in a similar manner. The majority of the trails exist out until $x \approx 30a_0$ which gives an estimation of the terminal velocity. There is only small scale, optically thin structure which exists beyond $v = 30a_0$, from small amounts of structure which exist with a velocity greater than v_∞ (e.g. Runacres & Owocki 2002). In a real wind the trails would disappear gradually as the flow diverges.

6.3.1 Top-hat line profile: $R_\rho = 1.2$

Fig. 6.5 shows the evolution of the smallest of the density perturbations in the top-hat line profile model. The dense part of perturbation is indicated by p and the rarefaction by r as before. Its evolution is quite indistinct from the evolution of other flow features; the dark trail of the optically thick p component blends into the flow amongst a myriad of similar features and whilst being among the strongest is by no means unique.

At various places in the flow, optically thin regions appear to be bounded by optically thick lanes (one example is marked a, Fig. 6.5). This structure is a chance alignment of two regions with similar optical depth (the optically thick lanes) which evolve in a similar manner (which are not directly physically connected). The example a shows that the optical depth of both the lanes and the rarefied region remains segregated and roughly constant. They have similar optical depth which makes their propagation similar.

This structure is reminiscent of the segregated optical depth structure seen in Discrete Absorption Components (DACs) of UV spectra (e.g. Prinja & Howarth 1988), which contain optically thick features which move across the spectrum. These results look similar to the features of Fig. 6.8. This is observational data for an emission line doublet and which is the reason for the apparent duplication in the figure.

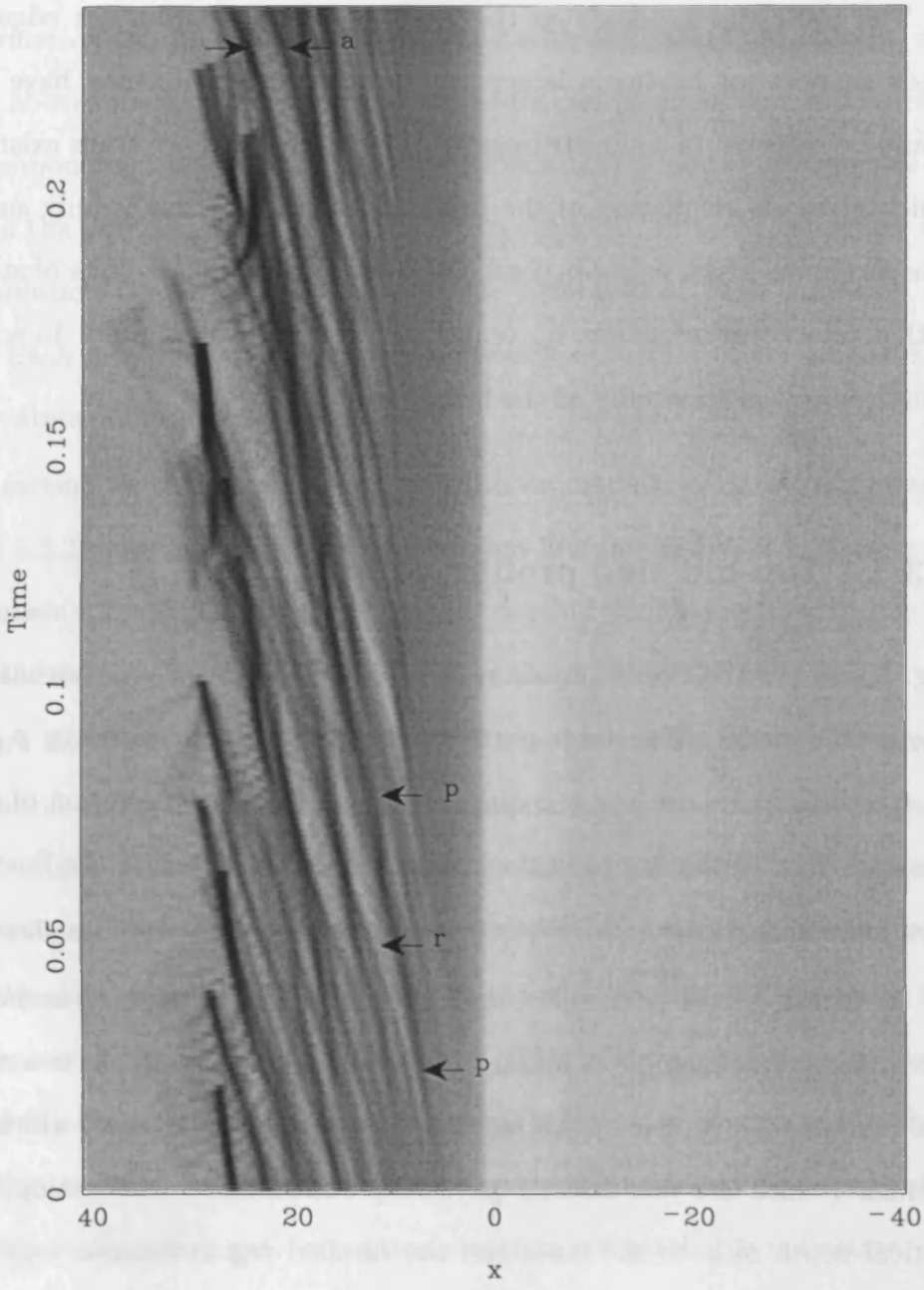

Figure 6.5: A trail diagram, graphically displaying the evolution of the optical depth for the model shown in Fig. 4.8 (pure absorption, top-hat line profile). Emission is light, strong absorption is dark. We observe the evolution of many optically thick clumps in the flow, some arising out of clump collisions and others with a more hydrodynamical origin. The perturbation is shown at the points labelled 'p' at two different times. Label 'a' shows two features which evolve in a similar way but at different velocities.

6.3.2 Gaussian line profile: $R_\rho = 4$

The spectra are not substantially altered by changing to a Gaussian line profile function as Fig. 6.6 shows. Generally there is a subtle difference in the amount of optically thick structure. Fig. 6.6 shows that there is a relatively small number of optically thick features. In the top-hat method the shape of the profile function generates much small scale dense noise. The Gaussian line profile does not generate this and so there is less peripheral optically thin structure, leaving only the more constrained (optically thicker) features to evolve in the flow.

The perturbation in this case is more dense ($R_\rho = 4$) than that shown in Fig. 6.5 and thus the evolution trail is more substantial. The dense part, shown in Fig. 6.6, initially displays a near to constant velocity evolution, since at first it is very optically thick and is pushed outward by upstream gas. As it evolves it becomes optically thinner, while still remaining optically thick enough to be accelerated effectively by the incident radiation. At *a* this compact, optically thick area begins to thermally expand becoming optically thinner and accelerates more quickly. At *b* the initial perturbation appears to split into two dense parts, but this is a superposition effect, and not a physically accurate description of the state of the gas. The perturbation is accompanied by a rarefied region as shown in §6.2.2 and 6.2.3. The rarefied region is well defined and increases in extent, spreading over a larger range of velocity with time. The leading edge of the diffuse region accelerates faster than the dense part of the perturbation, because it is optically thin.

The optically thick structure at *d* in Fig. 6.6 apparently ends disappearing into optically thinner gas, and later a similar optically thick feature appears. This is in fact the same feature which at *d* becomes narrow and lower density therefore the velocity width decreases as does the optical depth. The effect seen is a result of the thermal expansion of the clump making it optically thinner (the break in the dark line at *d*) which allows the clump to coast along until part of it moves out of the shadow of upstream material and is accelerated by the LDI. This part sweeps up the rest of the clump reforming the

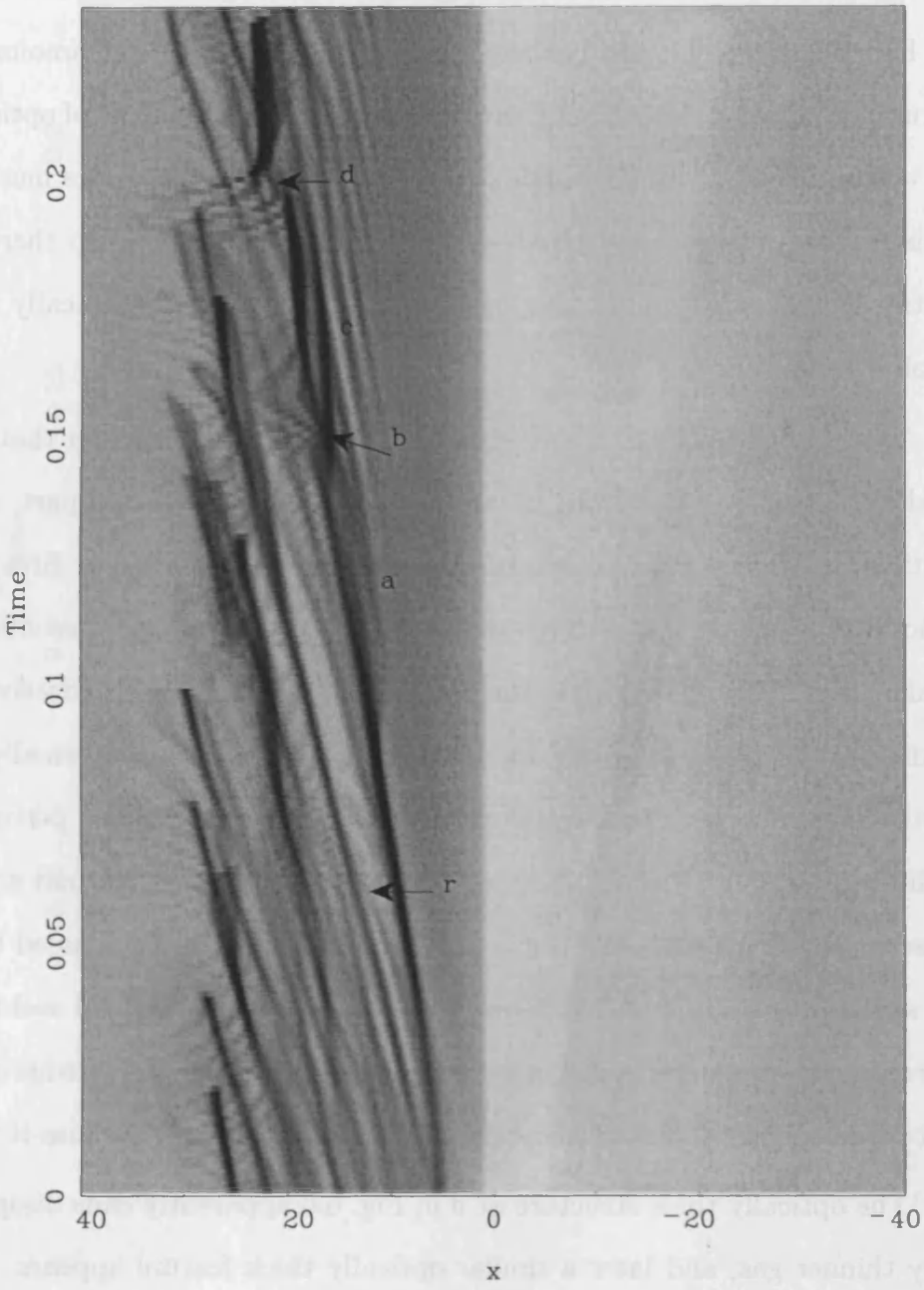

Figure 6.6: A trail diagram, graphically displaying the evolution of the optical depth for the model shown in Fig. 5.6 (pure absorption, Gaussian line profile). 'r' marks a rarefied region while 'a', 'b', 'c' and 'd' are time markers in the evolution of the main perturbation.

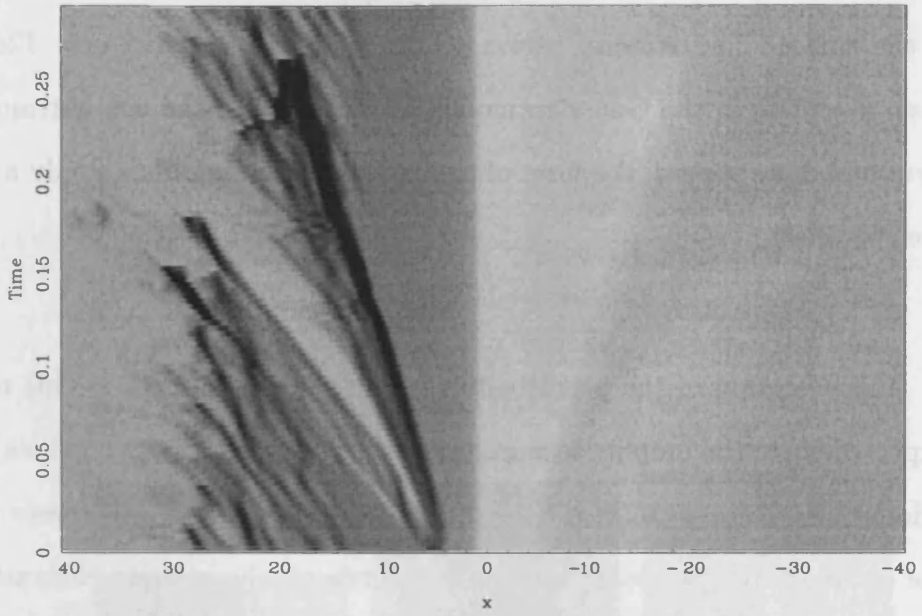

Figure 6.7: A trail diagram, graphically displaying the evolution of the optical depth for the model shown in Fig. 5.14 (pure absorption, top-hat line profile augmented by the line drag effect). This plot is more squat than the previous two trail plots even though the time span is roughly comparable, due to a larger timestep.

optically thick feature.

There are some very small features which are not fully resolved in Fig. 6.6, and also in 6.5, that appear to decelerate in the flow. An example of this phenomenon is shown at *d* in Fig. 6.6. This is again due in part to a superposition effect of clumps with different dynamics but mostly it is caused by dense shell expansion. While a dense shell is narrow we can assume that the shell as a whole has a particular velocity. Once it begins to expand the chief contribution to the optical depth is from the highest density part of the dense shell (also the area with the smallest velocity gradient) and as the shell expands this part decreases in velocity even though the shell as a whole is not decelerating.

6.3.3 Line drag model: $R_\rho = 10$

The evolution of the largest perturbation ($R_\rho = 10$) is described in Fig. 6.7 using the line drag method shown in §5.3. Once again there are only slight differences between

the spectra from this model and the previous models. The most notable spectral feature is the smooth low velocity region. This region extends to $v = 12a_0$ in the line drag case, $v = 10a_0$ in the Gaussian model and $v = 8a_0$ in the top-hat model. However once structure does appear, the form of the radiation driving makes only a slight difference to the spectra.

The evolution of the perturbation is particularly distinct in this case, which is to be expected since the amplitude is in excess of twice that of the previous perturbations considered in this section. The dense edge of the perturbation increases in optical depth as the evolution progresses.As the density increases, the velocity contrast across it becomes smaller and it appears to spread out in velocity space. The companion diffuse region is not contiguous with it in spectral space. This again is due to the superposition of structure elsewhere in the flow onto the velocity region occupied by the diffuse region. At the end of the evolution of the perturbation the dark trail begins to bend more towards the vertical, propagating outwards with a velocity near to terminal. The trail ends abruptly where the optically thick region propagates off the edge of the grid. This structure is similar to the DACs shown in Fig. 6.8 (Howarth, Prinja & Massa 1995) but these are periodic and associated with rotation. Brown et al. (2004) show recent support that the formation of DACs is closely associated with the rotational velocity of the star. Cranmer & Owocki (1996) strongly implicate velocity plateaus in CIRs as being responsible for DAC structure and not high density regions.

Although the models we have shown here indicate how the results of perturbed physical models would appear in a stellar spectrum, we can draw no conclusions about the global effect of such perturbations to the general shape of such spectra.

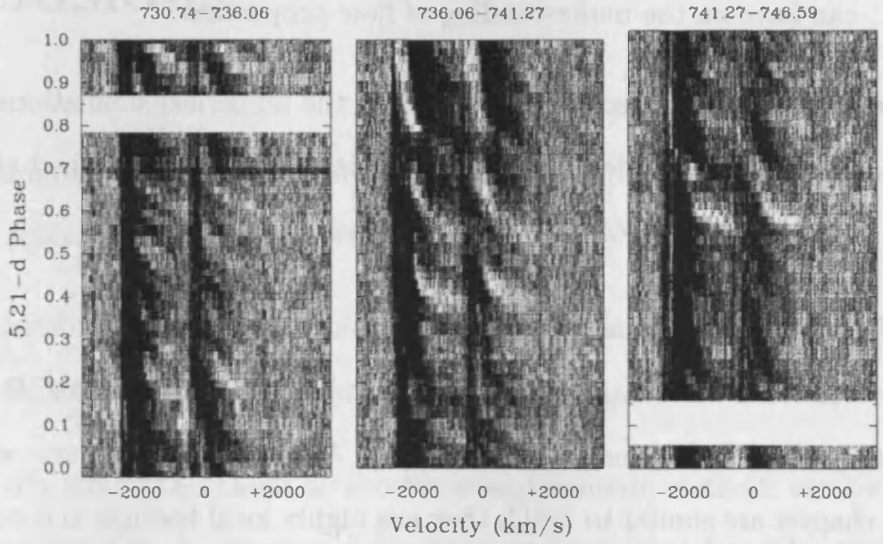

Figure 6.8: The DACs observed by Howarth, Prinja & Massa (1995) in the wind of ζ Pup. There is some similarity between these DACs and the strong absorption features in the trail diagrams, Figs. 6.5, 6.6 and 6.7, in the way that a strong absorption feature can propagate across the spectrum without being lost in the noise of the system. However the periodic nature of these observational features makes it unlikely that they have the same cause as the features shown in our models.

Summary

In this chapter we study the spectral signatures from the 2D non-Sobolev line-driven results of Chapters 4 and 5. These plots allow us to:

- identify physical structure in the wind with structure seen in the spectra of a wind solution.
- further illustrate how structure appears and what effect the lack of spatial resolution can have on the understanding of flow properties.
- show that the effect of refinements to the numerical simulations (e.g. using a Gaussian profile function, including line drag) have a diminished effect in the observational domain because the spatial resolution is reduced.

However what is usually seen in observations is large-scale, ordered, localized structure. The rotational modulation of DAC structure has been shown to be to connected to the photosphere (cf. Cranmer & Owocki 1996). Although the structures which we have seen in this chapter are similar to DACs they are highly local features and could not produce the macroscopic structures seen in observations. This analysis has been useful in visualizing the results of Chapters 4 and 5 and to put in context variations in P-Cygni profiles.

Chapter 7

Conclusions

In this concluding chapter, we summarise the content of each of the chapters and draw conclusions from the work undertaken.

7.1 General remarks

It has been our aim in this thesis to show how approximate methods can be employed to simulate the winds from hot stars and structure similar to that found by previous authors is generated. In our perturbation models we have shown that the flow is seriously affected by the presence of an obstacle in the flow. The main thrust of previous research has been to add a periodic signal (Owocki 1991 and subsequent authors) to the base of the wind with the aim of investigating the driving and flow response to noise. We adopt a different approach and concentrate on the behaviour of macroscopic additions to the flow.

Our approach was one of the first investigations of line driving in two dimensions adopting a single ray approach for a region in the downstream flow (where the spherical divergence of the photons is not important), to simplify the calculation of the driving force.

Another important discovery of this work has been to show that the stability of flows driven using the Sobolev approximation is affected by the direction which the velocity

gradient is calculated. The more stable gradient direction is the one which is opposite to the direction of information propagation (i.e. the downstream direction). This is thought to be because information is artificially transmitted upstream by the gradient calculation which acts to stabilise the flow.

Recognition of the fact that the state of the flow and the interaction of flow features is primarily responsible for the observed structure seen in the spectra of hot star winds, was important in directing our line of research. The study of interactions between flow features often occurs on a scale which is independent of the form of the driving, dominated by isothermal gas pressure. Thus the driving force is important for the background flow and formation of structure, while the equation of state is important for interactions within the flow.

7.1.1 Driving force calculation

In Chapter 2 we presented three different driving mechanisms: perfect gas pressure driving (Parker wind), radiation driving proportional to density (Continuum driving), radiation driving proportional to a power law of the optical depth (CAK and non-Sobolev driving). We propose a convolution method for calculating the driving force in a non-Sobolev driven wind. The essential point of this method is that the non-local calculation can be reduced to a local calculation at each grid point. The algorithm convolves the shape of the line profile function with a top-hat function (representing a constant density gradient across a spectral grid cell). This method records the absorption in each frequency bin at each spatial grid cell location.

We have shown in Chapter 5 that using a more realistic Gaussian profile function yields results which although qualitatively similar to those of the top-hat function, produce less noise in all of the state variables. In essence, this noise reduction is a result of the smooth shape of the profile function thus making the spectral absorption features smooth. The top-hat model, having a sharp edged profile function, causes the spectrum to not only

have features which are also sharp edged but also to contain much noise due to the aliasing of overlapping profile functions.

Undoubtedly the Gaussian model is more faithful to the physical response of the photospheric gas to the incident radiation than the top-hat model. The difference in the profile will cease to have a significant effect on the growth of perturbations once their velocity amplitude is a few times greater than the thermal profile, i.e. comparable to the sound speed in the flow. In reality, it is likely that photospheric structure and oscillations will seed the wind with fluctuations at this level.

7.1.2 One and two dimensional models

From the one dimensional results in Chapter 3 we show that low amplitude perturbations are highly accelerated by the driving. In the non-Sobolev models the effect of the inherent instability is present in the high velocity low density regions. Dense shells are formed immediately downstream of high velocity regions causing shocking at their interface. This behaviour is seen often throughout the flow especially in the non-Sobolev models where the instabilities in the wind grow to form macroscopic structure. It is thought that from such strong shock fronts comes thermal radio and x-ray emission (as discussed in Chapter 1).

There is much hydrodynamical information which lies hidden if we are confined to calculations in one dimension, and for that reason we make a tentative investigation in two dimensions. We consider, as a tractable first attempt, a single ray approach which only requires the radiation force to be calculated from absorption along a single photon ray in the x direction. We assume that the physical domain of calculation is located in the downstream flow where all the photons can be considered to be parallel.

These two-dimensional calculations show that the flow features are strongly affected by the hydrodynamics as well as the line-driving. It is clear that the line-driving causes unstable dense structure in the flow, while the hydrodynamics enhances some effects and

damps others. The initial perturbations, through the line de-shadowing instability, cause a downstream disturbance which triggers the onset of hydrodynamically unstable structure. The growth of this structure is not important if the gas is expanding on a timescale faster than the instability growth timescale.

The combination of hydrodynamics and radiation driving gives important insight into further understanding the dynamics of macroscopic clumps in the flow. We have shown that depending on the density contrast and initial velocity of such a clump, it will have a severe effect on the whole downstream flow before it is in direct physical contact with that region (because of the nature of the line driving). The clumps survive to a greater or lesser extent into the downstream flow suggesting that directly observable features could derive from them. This is possible but unlikely since the downstream flow, with its noise structure, will tend to break up a feature which is growing more diffuse.

7.1.3 Supersonic boundary condition and SSF

The simulation of the wind from the star ζ Puppis was modelled including both a finite disc correction factor and the diffuse force (using a Smooth Source Function approach (Owocki & Puls 1996)). Changing from a supersonic to a subsonic inner boundary condition produces a flow with a larger noise component to the flow but average values for the mass loss rate and terminal velocity which is in agreement with observed values.

The inclusion of the diffuse force in the model of the wind from ζ Pup, decreases the amount of structure present and increases the size of the smooth flow region at the base of the wind (although only marginally). The increase in calculation time is not significant making this method practicable for the simulation of more detailed winds or the winds of different OB stars.

7.1.4 Spectral results

It is important both to investigate the effect of explicit flow perturbations on the spatial dynamics and the spectral dynamics. The region of hot star winds, close to the central star, can only be examined quantitatively through spectroscopy. The different models for the line-driving are not too dissimilar once we have moved into the spectral domain. The models where there is less structure in the physical domain show less structure in the spectral domain. With increased structure there is the possibility of increased superposition of features with the same velocity in the ensuing spectra.

7.2 Future refinements

The main thrust of this research has been to develop an approximate model for the solution of the line-driving force calculation, although we have used other driving forces to illustrate the nature of winds in general. We have not considered the possibility of extending the research of these other types of driving, and while we do consider it a worthy topic of work it does not naturally follow on from the work in this thesis. There are many other modifications which can be made to the line-driving models we have presented here.

Building on this work and these results there are a number of directions that the modifications can progress. The isothermal equation of state while we feel is justified within the boundaries of this work, is a limitation and should be replaced with a thermal equation of state which can represent the temperature behaviour of the wind more accurately. The most important observational support for this is to investigate both the thermal radio and x-ray emission.

Moving to a larger physical domain is clearly advantageous as it would allow the evolution of flow features to be traced for longer as they retreat further from the central star. This has the main advantage of giving additional information about the asymptotic

nature of the flow. The flow predominantly travels at the terminal velocity and therefore the structure present will have a strong effect on the blue absorption edge. Observers are undecided as to the exact effect of DACs on the blue edge, but there appears to be evidence that DAC structure is accompanied by blue edge variability. We feel it important to further study this in the light of our perturbation models.

It would be interesting to vary the luminosity at the photosphere to see what effects this would have on the wind in 2D. The temperature and luminosity of the star is not constant (the grainy structure of the Sun is well observed, as are Sun-spots although these involve magnetic field effects), and could have an impact on the stability of the flow, specific spectral features and mass loss rate. Also to simulate large mass loss events or a moving photosphere, would give further insight into observed spectral variations.

The last major refinement that we consider to be important is a two dimensional multiple ray approach. The radiation emanating from the star cannot be thought of as purely radial, especially in the inner wind. The inclusion of non-radial rays could give more insight into the structure observed in the winds of OB stellar spectra. The inclusion of these has been attempted by previous authors but was limited in its development. Unfortunately it is a hugely computationally intensive process to trace rays across grid cells which do not have a direct sight line to the stellar surface. Any non-radial rays would have to follow a locally crooked path back to their origin. This however is not holding back the simulation of winds in two dimensions, as we have demonstrated in this work.

7.3 And finally..

Research into line-driven winds has developed steadily over the last 3 decades to the stage where computational models can predict the structure found in observations. The physics has gone from being reactive to proactive as more refinements are made to the theory and faster algorithms assist the representation of real winds by computational wind models. There is hope in the next 30 years that all the observations will be clearly explainable by

hydrodynamical models of stellar winds, but as the discovery of quantum mechanics has told us, nature is always stranger than mankind expects.

Appendix A

Hydrodynamics

A.1 Introduction

The aim of this appendix is to introduce the equations of hydrodynamics in differential form and to discuss numerical methods for solving them. The basic equations of hydrodynamics are derived from the conservation equations of mass, momentum and energy. From the differential form of these conservation equations a Finite Difference method can be used to numerically determine the values of the flow variables at discrete points. More details of these numerical methods will be given below

A.2 Hydrodynamical conservation equations

The differential form of the Eulerian conservation equations, for a single inviscid, non-magnetic fluid, are as follows:

Conservation of mass

$$\frac{\partial \rho}{\partial t} + \nabla \cdot (\rho \vec{v}) = 0 \tag{A.1}$$

Conservation of momentum

$$\frac{\partial \rho \vec{v}}{\partial t} + \nabla \cdot (\rho \vec{v} \cdot \vec{v}) = -\nabla P + \rho \vec{f} \tag{A.2}$$

Conservation of energy

$$\frac{\partial}{\partial t}\left[\rho\left(e + \frac{v^2}{2}\right)\right] + \nabla \cdot \left[\rho\left(e + \frac{v^2}{2}\right)\vec{v}\right] = \rho\dot{q} - \nabla \cdot (\vec{v}P) + \rho\vec{f} \cdot \vec{v} \tag{A.3}$$

where ρ is density, $\vec{v}$ is the Cartesian velocity vector $(= u\vec{i} + v\vec{j} + w\vec{k})$, p is the pressure $\vec{f}$ is the Cartesian force vector$(= f_x\vec{i} + f_y\vec{j} + f_z\vec{k})$, e is the internal energy of the fluid, $\dot{q}$ is the volumetric heating rate per unit mass and t is time.

This system of coupled partial differential equations form the basis for all of the hydrodynamical calculations in this thesis. The Eulerian form uses distance as the independent variable which is conceptually simpler to consider than the Lagrangian form where the conservation equations are re-expressed with mass as the independent variable. The above equations are complicated to solve analytically due to their coupled nature. They are of course highly valuable in perturbation analysis. Here a Taylor expansion of the state variables about a fixed point can be solve. There is no closed-form solution to the above hydrodynamical equations.

In their current form there are 6 unknown flow variables (ρ,p,e and $\vec{v}$) with only 5 equations with which to solve them. In order to eliminate this redundancy we can impose an equation of state which marries the density and pressure in the system allowing each variable to be uniquely solved for, $P = RT\rho$, where R is the molar gas constant and T is the temperature. It is sufficient for most astrophysical applications to only consider a *Perfect* gas because of the near asymptotic nature of the environment, since the extreme conditions allow us to assume that the intermolecular forces are zero. This equation of state is often called the *Thermal* equation of state and it only partly ameliorates the redundancy problem. In this research we have assumed that the gas is isothermal, which

removes this final redundancy, but we could have allowed the temperature to vary by imposing further conditions on the temperature. A *caloric* equation of state, $e = c_v T$, where c_v (ratio of specific heats) remains constant, is a possible alternative.

It is not entirely necessary to attempt to solve the partial differential equations (equations(A.1)-(A.3)) to examine shock structure. The Rankine-Hugoniot jump conditions can be used to examine individual shock cases. These jump conditions do not resolve shocks but they can be used to predict the values of the flow parameters downstream of a shock, and in this regard they can be used for *Shock fitting.* This is not practical for a hydrodynamical simulation since it requires advance knowledge of the location of each shock front. The only way which this can be achieved satisfactorily is in a *Shock capture* scheme. For this scheme the conservation equations (A.1)-(A.3) are numerically solved using a finite differences method[1].

A.3 Finite difference methods

Since the partial differential equations are difficult to solve for simple boundary conditions, their solution is further complicated as more complicated structure appears in the flow. Further levels of complexity which appear with more structure make analytical solutions decreasingly practicable. Ultimately an analytical approach requires the hydrodynamic equations to be in closed-form where each flow variable can be written as a continuous function of an independent variable (e.g. distance), which is not possible except in a simplified form. The vast majority of hydrodynamical calculations are performed with the assistance of numerical routines where the values of flow variables are defined at discrete points in the flow.

[1]While other methods are used this is the most common.

A.3.1 General methods

By replacing the partial differential equations with finite difference quotients we can obtain approximations to the conservation equations. The continuous functions are sampled at intervals which can be regular or variable (regular in our implementation); the continuous function can be thought of as being superimposed onto a grid (in two dimensions) where the indices i and j represent the location of a particular grid-cell.

The simplest (and most common) method of solution of the flow variables from the conservation equations is by using the Taylor approximation. If we define the discretized flow variable in a cell with co-ordinates (i, j) as $u_{i,j}$ we can represent the value of the flow variable in the next cell in the x direction as follows:

$$u_{i+1,j} = u_{i,j} + \left(\frac{\partial u}{\partial x}\right)_{i,j} \Delta x + \left(\frac{\partial^2 u}{\partial x^2}\right)_{i,j} \frac{(\Delta x)^2}{2} + \left(\frac{\partial^3 u}{\partial x^3}\right)_{i,j} \frac{(\Delta x)^3}{6} + \ldots \tag{A.4}$$

This representation is mathematically exact provided that there is an infinite number of terms in the sequence on the RHS and that the series converges. The expression will also be exact when the spacing of the grid tends to zero, which is strictly the definition of an derivative. The definition of the partial derivative in the finite difference method is obtained from re-arranging equation (A.4),

$$\left(\frac{\partial u}{\partial x}\right)_{i,j} \approx \frac{u_{i+1,j} - u_{i,j}}{\Delta x}, \tag{A.5}$$

while the remainder of equation (A.4) gives us the truncation error in the result

$$E(u) = \left(\frac{\partial^2 u}{\partial x^2}\right)_{i,j} \frac{(\Delta x)^2}{2} + \left(\frac{\partial^3 u}{\partial x^3}\right)_{i,j} \frac{(\Delta x)^3}{6}. \tag{A.6}$$

This scheme is called *forward* difference since it looks ahead of the current grid cell, taking no account of cells to the left of i. This method of replacing the partial differential equations with finite difference quotients is a highly versatile technique and forms the

basis of many hydrodynamical grid codes (e.g. VH-1 (Blondin 1991), ZEUS (Stone & Norman 1992), AQUALUNG (Williams 1999)), each flow variable being represented by an algebraic difference equation.

There are other variations on this method, backward and central difference and also higher order difference methods. Throughout all of this analysis we assume that the grid spacing Δx is constant, irrespective of the difference method used. The method of difference calculation also determines the numerical direction of information propagation. One might imagine that it would be most consistent to follow the direction which the hydrodynamic flow is in. However the flow direction can locally change mid-flow so a direct tracking of this may be neither desirable nor practical. A numerical calculation that includes cells which are not in the domain of interest can cause spurious results. However if the majority of the flow is smooth with continuous variation, there is no significant effect to the choice of direction.[2] When a shock wave passes through the flow the differencing direction can be critically important. The response of the central difference method is to produce oscillations, often severe, around the disturbance which are spurious numerical artifacts and do not represent the physics of the scenario.

A.3.2 Upwind methods

Because of such spurious effects as these, so called *Upwind* methods have been developed. The philosophy of these is to only include cells which are in causal contact with the current cell in the differencing. Therefore along an outward directed characteristic the cell i is immediately effected by cell $i-1$. For higher order approaches this backward differencing method can include further cells interior to i, and to increase the accuracy of the results, higher order algorithms should be used. The upwind techniques are stable and therefore an advantage over the central and forward difference methods, which has lead to many different implementations of this philosophy, such as Reimann solvers and

[2]From an entirely hydrodynamical point of view this is correct. We discuss the effect of difference direction on the stability of a driven wind in more detail in §3.5.1 and §3.6.1.

Godunov schemes.

Godunov scheme

Until this point we have discussed approximate solutions to the partial differential conservation equations. Godunov (1959) suggested an alternative which involved an exact solution of the conservation equations for a small local region. Many such regions are created to span the entire physical region and *pieced* together to simulate the flow. This assumes that the flow is *piecewise constant*, in that the flow variables from one cell can be bolted on to those of the next. This can produce microscopic effects in rapidly changing flows since there is a step between the variables in each cell. A second order method was proposed by van Leer (1979) where from the cell average values of the flow variables, a linear interpolation can be used to piece the cells together (*piecewise linear*). However there are still problems with small oscillations in flow associated with shock fronts. This leads to the development of the *piecewise parabolic* method.

Piecewise Parabolic method and VH-1

Throughout this thesis we use a hydrodynamical code called VH-1 which uses the piecewise parabolic method (PPM) and was written by John Blondin (1994). This is a third-order extension of the Godunov scheme as detailed by Collela & Woodward (1984). The difference between this and a piecewise linear method is that the flow variables are calculated from the cell average values and then the distribution of each fluid variable is calculated by using a parabolic interpolation between each grid cell. This algorithm has been compared with many other schemes and has out performed them all.

VH-1 is freely available code which can make 1, 2 and 3 dimensional calculations constructed on Cartesian, cylindrical or spherical co-ordinate systems. All of the code is open source and can be tailored to the needs of any scenario. We used the code in 1 and 2 dimensions adding extra subroutines to calculate the line driving force along side

the hydrodynamical calculation, minimising the number of interations required. VH-1 simplifies the exact calculation of the flow variables within each cell (called the Riemann problem) by mapping the Eulerian grid onto a Lagrangian grid solving the Riemann problem and then remapping to an Eulerian grid. The code also resolves shocks to within two cells with good stability and no oscillatory features. This code has been extensively tested with over a decade of use and has been updated as necessary, it is currently being used by many people for a wide range of astrophysical applications.

A.4 Hydrodynamical response to shocks

A good example of the evolution of a shock in a purely hydrodynamical scenario (i.e. without any external forces, only the force from ideal gas pressure) is the Sod shock tube (Sod 1978). The model describes a tube of constant velocity which has a two regions with different density and pressure separated by a diaphragm. When the diaphragm is removed a disturbance forms and shock propagates into the low density gas. This is followed by a contact disconinuity and a rarefaction which propagates in the opposite direction to the shock. Thus the tube is split into four regions as shown in Fig. A.1 (Pittard 1999); 1) undisturbed flow at pressure p_1, 2) shocked, accelerated gas at a higher pressure p_2, 3) a rarefaction where $p_2 = p_3$ since the gas cannot support a pressure discontinuity, 4) the undisturbed higher pressure region at pressure p_4. In regions 2 and 3 the pressure and velocity are constant (and have no discontinuities) until the gas becomes rarefied.

During this work we have shown how perturbations of different amplitude behave when added to a driven flow. In the majority of cases the perturbation has been a rectangular slab, with fixed height. This approximates to a pair of shock tubes, placed back to back. In the above model the velocity, pressure and density is initially constant in the two regions, but in our models (cf. Chapters 3, 4 and 5) this is not the case. To directly compare our models with the results obtained for a model with only ideal gas pressure we use a typical starting condition for the models in Chapter 3, for a line driven wind,

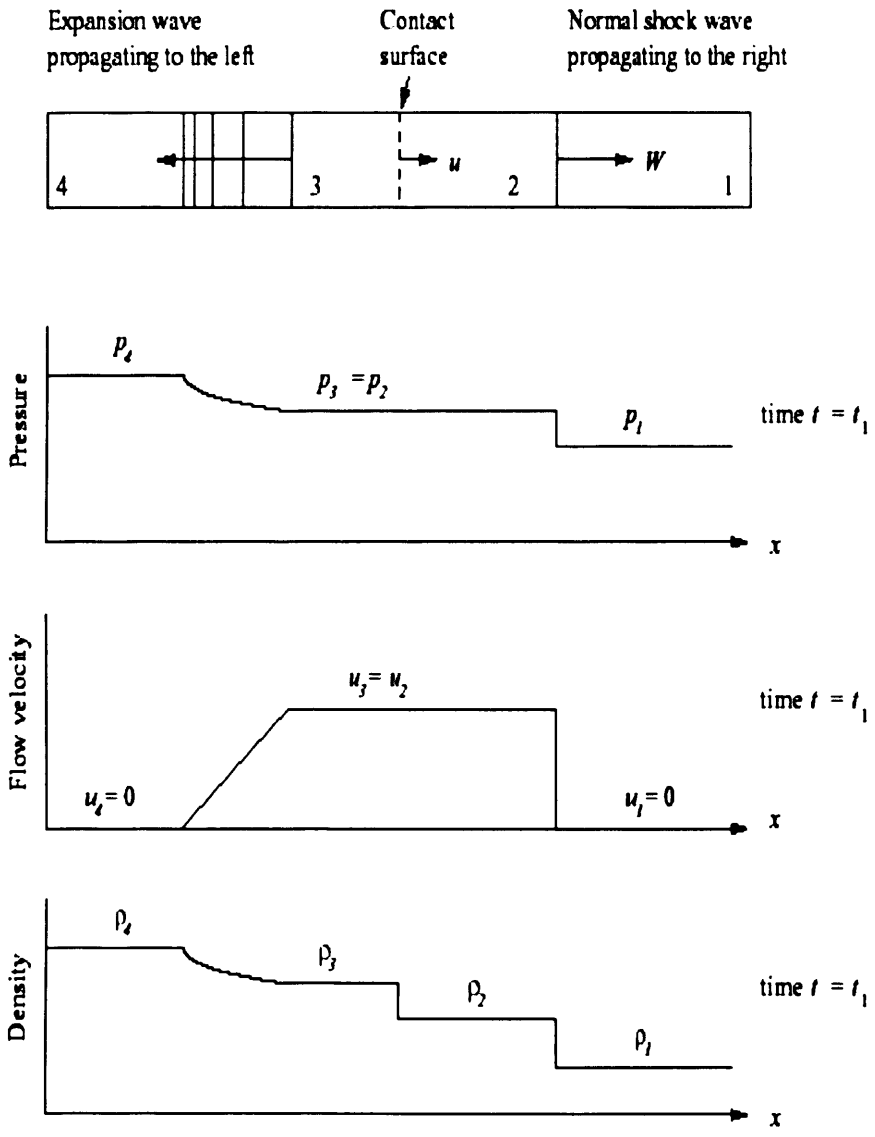

Figure A.1: Schematic of flow in a shock tube. Conditions at $t > 0$.

and perturb it with a rectangular slab of amplitude $R_\rho = 2$. The model was run in the abscence of all forces except ideal gas pressure, and the results are shown in Figs. A.2 and A.3.

The initial conditions used (cf. Fig. A.2) are a representative soltuion in the line driven flow. When line drivin is switched off and the wind is driven by gas pressure alone, so the flow undergoes global changes as it tries to relax into its own equilibrium solution. For comparison we superimpose the evolution of the background flow (dashed) onto that of the perturbed flow (solid), to distinguish the structure associated with the perturbation with that associated with the flow.

The perturbation evolves in a very similar manner to the schematic diagram shown in Fig. A.1. The velocity of the perturbation is antisymmetric about the centre line of the perturbation because the pair of shocks accelerate away from each other. The density plot is not exactly the same as the schematic diagram since there is no contact discontinuity. This is because we have used an isothermal model, as we have used in the simulations for Chapters 3, 4 and 5. Aside from this the density plot is also highly similar to the schematic, as it includes a shock and rarefaction matching the velocity evolution.

Comparison of these results and those of Chapters 3, 4 and 5 shows that when extra forces are present the analogue of a shock tube can no longer be applied to the evolution of a slab perturbation.

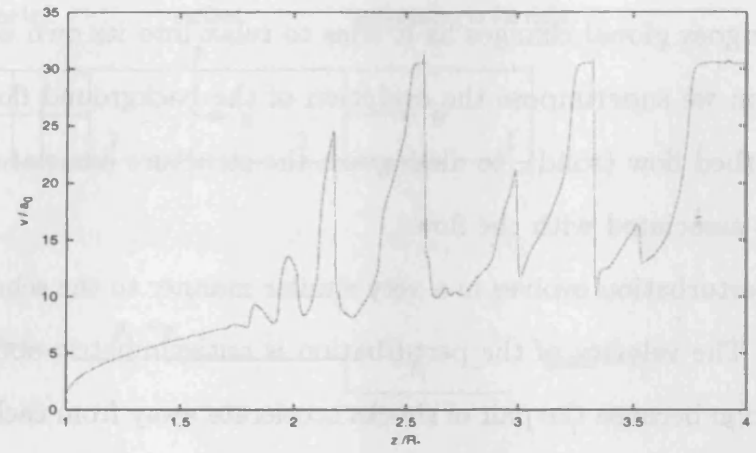

(a)

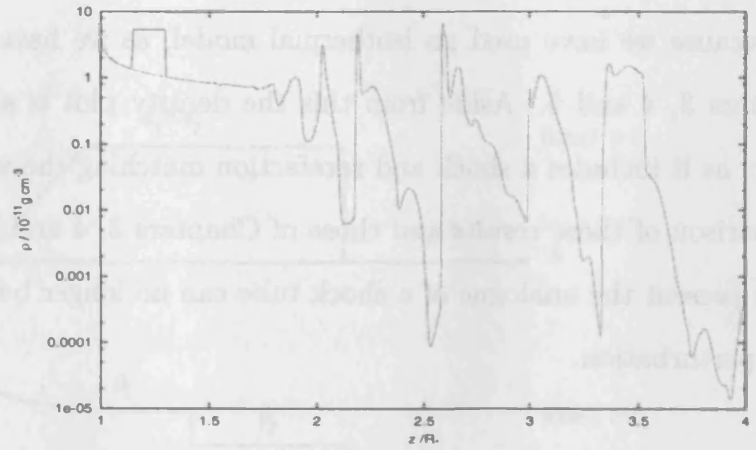

(b)

Figure A.2: Initial conditions of an example flow with only gas pressure. a) Velocity, b) density

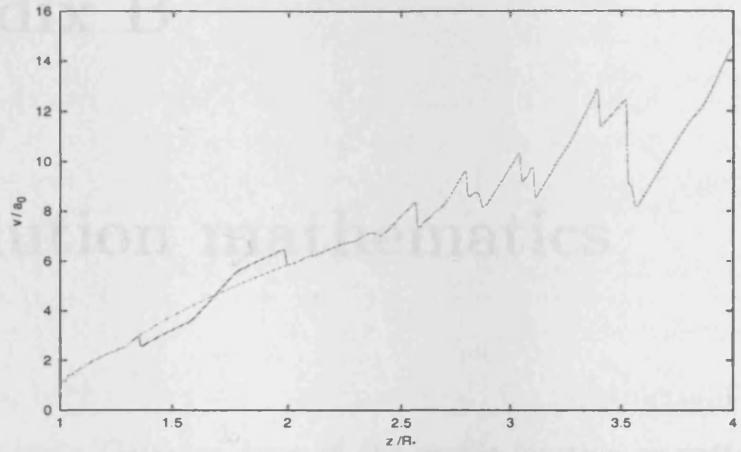

(a)

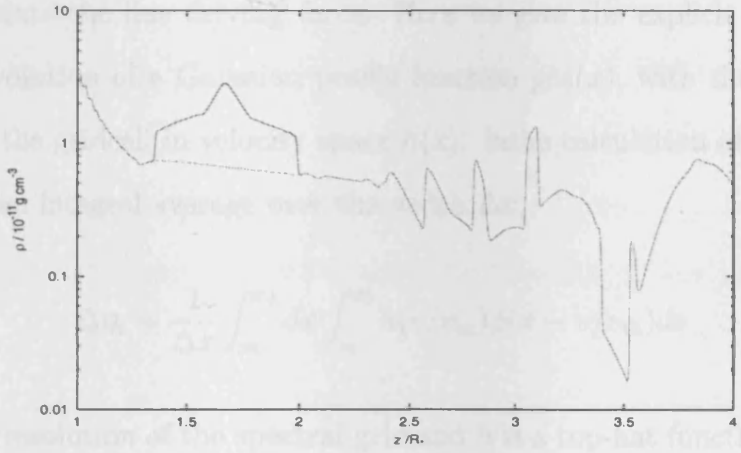

(b)

Figure A.3: The state of the flow shown in Fig A.2 after a short time. The evolution of the flow is reminiscent of that shown in Fig. A.1. The dashed curves indicate flow evolution without the rectangular perturbation.

Appendix B

Convolution mathematics

In Chaper 5 we use a Gaussian form of the profile function as part of our covolution method to calculate the line driving force. Here we give the explicit calcaultation and form of the convolution of a Gaussian profile function $phi(x)$, with the top-hat function for hte shape of the gridcell in velocity space $h(x)$. Inthe calculation of the optical depth we now include an integral average over the width Δx,

$$\Delta\eta_i = \frac{1}{\Delta x}\int_{x_1}^{x_2} dx \int_{v_1}^{v_2} h(v/v_{\rm th})\phi(x - v/v_{\rm th})dv \tag{B.1}$$

where Δx is the resolution of the spectral grid and h is a top-hat function with a a width Δv and a height of $\rho\Delta z$, which varies between spatial grid cells (cf. analysis in § 2.3.6).

In the case of a top hat we do not include this averaging, partly to reduce the complexity of the calculation and partly because for large velocity differences the averaging wings are vanishingly small. The above expression can be re-expressed in terms of a triple convolution in velocity space. In order to do this we must consider the frequency variable, x, in terms of a velocity. If we consider a line with a stationary frequency, x', at a point r in the flow it will be Doppler shifted to a frequency $x = (v(r)/c - 1)x'$, and we have x

as a function of v. The above expression becomes,

$$\Delta\eta_i = \Delta x \otimes [h_i \otimes \phi_i]$$

$$\Delta\eta_i = [\Delta x \otimes h_i] \otimes \phi_i$$

thus simplifying the mathematics, since Δx_i is a top-hat function (the shape of each spectral grid cell) and we take $h_i(v/v_{\rm th})$ to be a top-hat function also.

The form of the two top-hat functions $A = \Delta x \otimes h_i$ is given by the expression,

$$\begin{aligned}
-\frac{\Delta v - \Delta x}{2} < \quad x \quad < \frac{\Delta x - \Delta v}{2} A &= (1 + x/\Delta x)h_i \\
\frac{\Delta x - \Delta v}{2} < \quad x \quad < \frac{\Delta v - \Delta x}{2} A &= h_i \\
\frac{\Delta v - \Delta x}{2} < \quad x \quad < \frac{\Delta v + \Delta x}{2} A &= (1 - x/\Delta x)h_i
\end{aligned} \tag{B.2}$$

where once again $h_i = \rho_i \Delta x/\Delta v$ for grid cell i. This is the shape of the spatial grid cell i on the spectral grid.

This we can convolve with the profile function, as was done in § 2.3.6 for a top-hat profile function. Below we give the resulting functional form of $g(x)$, which we define such that,

$$\Delta\eta(x) = \frac{\rho_i \Delta z_i}{\Delta x \Delta v_i} g(x).$$

which must be summed over the contributing range of x to give the absorption in each spatial grid cell,

$$\Delta\eta_i = \sum_{x_1}^{x_2} \eta(x)\Delta x.$$

We define the function $g(x)$, the scaled convolution of the function A with a Gaussian profile function, as,

$$|x - \bar{x}| < w, \quad g(x) \quad = \frac{1}{2(\Delta v - \Delta x)}(\mathrm{erf}(x + w) - \mathrm{erf}(x - w));$$

$$= g_{\mathrm{n}}(x);$$

$$\frac{\Delta v + \Delta x}{2} > |x - \bar{x}| > w, \quad g(x) = g_{\mathrm{n}}(x) + \frac{1}{2\Delta x(\Delta v - \Delta x)} \times \left[\left(x + \frac{1}{2(\Delta v - \Delta x)}\right)\mathrm{erf}(y) - \frac{\sqrt{\pi}}{2}e^{-y^2}\right]_{w}^{w-\Delta x} \quad ;(B.3)$$

where $w = (\Delta v - \Delta x)/2$, $\bar{x} = (x_2 + x_1)/2$ is the centre of the x range for each spatial grid cell, and $\mathrm{erf}(t) = 2/\sqrt{\pi}\int_0^y \exp(-t^2)dt$ is the Error Function. The infinite extent of the Gaussian is the reason for the inclusion of $g_{\mathrm{n}}(x)$ in equation B.3(c). These three expressions show the normalised value of the convolution in the two discrete domains of its existence. The first expression, equation B.3(a), shows the convolution for the range $|x-\bar{x}| < w$ or where the Gaussian centre passes along the maximum of $\Delta x_i \otimes h_i$. The value of the resulting convolution is therefore the difference between error functions separated by the spectral width the region.

The second expression, equation B.3(b), is the convolution of the Gaussian profile with the wings of $\Delta x_i \otimes h_i$. This is region is small since generally the velocity difference is much larger than the resolution of the spectral grid $\Delta x \gg \Delta v$.

The above form is implemented and used in the Gaussian profile function calculation in Chapter 5.

References

[1] Abbott, D. C., 1980, ApJ, 242,1183

[2] Abbott, D. C., 1982, ApJ, 263,723

[3] Baty, H., Keppens, R., 2002 ApJ, 580, 800

[4] Biermann, L, 1951, Zeitschrift für Astrophysik, 29 274

[5] Blondin, J., 1994, VH-1: Users guide, *unpublished*, `http://wonka.physics.ncsu.edu/pub/VH-1/`

[6] Blomme, R., van de Steene, G.C., Prinja, R.K., Runacres, M.C., 2003, A & A, 408, 715

[7] Böhm-Vitense, E., 1992, 'Introduction to Stellar Astrophysics, Vol. 3: Stellar Structure and Evolution', Cambridge University Press

[8] Brown, J. C., 1994, Ap&SS, 221, 357

[9] Brown, J. C., Barrett, R. K., Oskinova, L. M., Owocki, S. P., Hamann, W.-R., de Jong, J. A., Kaper, L., Henrichs, H. F., 2004, A&A, 413, 959

[10] Burgers, J.M., 1948, Advances in Applied Mathematics, vol. 1, eds. R. von Mises & T. von Karman, New York: Academic Press

[11] Carlberg R. G., 1980, ApJ, 241, 1131

[12] Cassinelli, J. P., Olson, G. L., 1979, ApJ, 229, 304

[13] Cassinelli, J. P., Castor, J. I., & Lamers, H. J. G. L. M., 1978, PASP, 90,496

[14] Cassinelli, J.P., Swank, J.H., 1983, ApJ, 271, 681

[15] Cassinelli, J. P., Lamers, H. J. G. L. M., 1987, Exploring the Universe with IUE satellite, ed. Kondo, Y., D. Reidel Publ. Co., p139

[16] Cassinelli, J. P., Miller, N. A., Waldron, W. L., MacFarlane, J. J., Cohen, D. H., 2001, ApJ, 554, 55

[17] Castor J. I., Abbott D. C., Klein R. I., 1975, ApJ, 195, 157 [CAK]

[18] Chamberlain, J. W., 1965, ApJ, 141, 320

[19] Chen, W., White, R. L., 1991, ApJ, 381, 63

[20] Cherchenff, I., Le Teuff, Y. H., Williams, P. M., Tielens, A. G. G. M., 2000, A&A, 357, 572

[21] Cohen, D. H., 2001, ApJ, 554, 55

[22] Colella, P., Woodward, P. R. 1984, J. Comp. Phys., 54, 174.

[23] Courant, R., Friedriachs, K. O., Lewy, H., 1928, Math Ann, 100, 32

[24] Cranmer, S. R., Owocki, S. P., 1996, ApJ, 462, 469

[25] Dessart, L., Chesneau, O., 2002, A & A, 395, 209

[26] Dessart., L., Owocki, S., 2003, A & A, 406, L1

[27] Downes, T. P., Ray, T. P., 1998, A & A, 331, 1130

[28] Dougherty, S. M., Williams P. M., 2000, MNRAS, 319, 1005

[29] Drazin, P. G., Reid, W. H., 1981, 'Hydrodynamic Stability', Cambridge University Press

[30] Eversberg, T., Lépine, S., Moffat, A. F. J., 1998, ApJ, 494, 799

[31] Falle, S. A. E. G., Perry, J. J., Dyson, J. E., 1981, MNRAS, 195, 397

[32] Feldmeier, A., 1995, A & A, 299, 523

[33] Feldmeier, A., Puls J., Pauldrach, A. W. A., 1997, A & A, 322, 878

[34] Feldmeier, A., Oskinova, L., Hamann, W-R., 2003, A & A, 403, 217

[35] Feuchtinger, M. U., Dorfi, E. A., Hofner, S., 1993, A & A, 273, 513

[36] Foltz, C. B., Weymann, R. J., Morris, S. L., Turnshek, D. A., 1987, ApJ, 317, 450

[37] Fullerton, A. W. 1997, PEADN, Predoctoral school IX, Heidelberg, 'Stellar atmospheres: Theory and observations', ed J.-P. de Greve, Springer

[38] Fullerton, A. W., Massa, D. L., Prinja, R. K. *et al.*, 1997, A & A, 327, 699

[39] Gail, H.-P., Keller, R., Sedlmayr, E., 1984, A&A, 133, 320

[40] Gayley, K. G., 1995, ApJ, 454, 410

[41] Godunov, S. K., 1959, Math Sb., 47, 271, *translated* 1969, JPRS, 7226

[42] Gomez, E.L., & Williams, R.J.R., 2003, MNRAS, 344, 725

[43] Habbal, S. R., Woo, R., Fineschi, S., O'Neal, R., Kohl, J., Noci, G., Korendyke, C., 1997, ApJ, 489, 103

[44] Hamann, W. R., 1980, A & A, 84, 342

[45] Hearn, A. G., 1975, A & A, 40, 277

[46] Howarth, I. D., Prinja, R.K., 1989, ApJS, 69, 527

[47] Howarth, I. D., Prinja, R.K., Massa, D. 1995, ApJ, 452, 65

[48] Howarth, I. D., Siebert, K. W., Hussain, G. A. J., Prinja, R. K. 1997, MNRAS, 284,265

[49] Hundhausen, A. J., Gosling, J. T., 1976, JGR, 81, 1436

[50] Kaper, L., Henrichs, H.F., Nichols, J.S., Snoek, L.C., Volten, H., Zwarthoed, G.A.A., 1996, A & A Supp., 116, 257

[51] Krticka, J., Kubát, J., 2000, A & A, 359,983

[52] Lamers, H. J. G. L. M., 1986, A & A, 159, 90

[53] Lamers, H. J. G. L. M., Morton, D. C., 1976, ApJ Supp., 32, 715

[54] Lamers, H. J. G. L. M., Cassinelli, J. P., 1999, 'Introduction to Stellar Winds', Cambridge University Press

[55] Lépine, S., Moffat, A. F. J., St-Louis, N., Marchenko, S., Dalton, M., Crowther, P. A., Smith, Linda J., Willis, A. J.; Antokhin, I. I., Tovmassian, G. 2000, AJ, 120, 3201

[56] Lépine, S., Moffat, A. F. J., 1999, ApJ, 514, 909

[57] Lim, A. J., 2003, Rev. Mex. AA., 15,131

[58] Lucy, L.B., White, R.L., 1980, ApJ, 241, 300

[59] Lucy, L. B., 1983, ApJ, 274, 372

[60] Lucy, L. B., 1984, ApJ, 284, 351

[61] Lucy, L. B., Solomon, P. M., 1970, ApJ, 159, 879

[62] Marchenko, S.V., Moffat, A.F.J., Vacca, W.D., Côté, S., Doyon, R., 2001, ApJ, 565, L59

[63] Marchenko, S. V., 2003, IAU Colloquium No. 212, 'A massive star odyssey, from main sequence to supernova'

[64] Mihalas, D., 1978, 'Stellar atmospheres', W. H. Freeman and Co.

[65] Milne, E. A., 1926, MNRAS, 87, 43

[66] Monnier, J. D., Tuthill, P. G., Danchi, W. C., 1999, ApJ, 525, 97

[67] Owocki, S. P., 1991, 'Stellar atmospheres: Beyond classical models', 235

[68] Owocki, S. P., 1998, IAU Colloquium No.169, 'Variable and Non-Spherical Stellar Winds in Luminous Hot Stars'

[69] Owocki,S. P., Castor, J. I., Rybicki, G. B., 1988, ApJ, 335, 914 [OCR]

[70] Owocki, S. P., Puls, J., 1996, ApJ, 462, 8940

[71] Owocki, S. P., Puls, J., 1999, ApJ, 510, 3550

[72] Owocki, S. P., Puls, J., 2002, ApJ, 568, 965

[73] Owocki, S. P., Rybicki, G. B., 1984, ApJ, 284, 337 [OR84]

[74] Owocki, S. P., Rybicki, G. B., 1985, ApJ, 299, 265

[75] Owocki, S. P., Rybicki, G. B., 1986, ApJ, 309, 127

[76] Parker, E. N., 1958, ApJ, 128, 664

[77] Pauldrach, A., Puls, J., Kudritzki, R. P., 1986, A & A, 164, 86

[78] Pauldrach, A., Kudritzki, R. P., Puls, J., Butler, K., Hussinger, J., 1994, A & A, 283,525

[79] Pittard, J. 1999, Ph.D. Thesis, University of Birmingham

[80] Poe, C.H., Owocki, S.P., & Castor, J.I., 1990, ApJ, 358, 199

[81] Prinja, R. K., Howarth, I. D, 1986, ApJS, 61, 357

[82] Prinja, R. K., Howarth, I. D. 1988, MNRAS, 233, 123

[83] Prinja, R. K., Smith, L. J., 1992, A & A, 266, 377

[84] Puls, J., Owocki, S. P., Fullerton, A. W., 1993, A & A, 279, 457 [POF]

[85] Robert, C., Moffat, A. F. J., Bastien, P., *et al.*, 1989, ApJ, 347, 1034

[86] Rayleigh, 1883, Proc. Lond. Math. Soc., 14, 170

[87] Richtmyer, R. D., 1960, Commun. Pure Appl. Math. 23, 297

[88] Röser, H.-J., 1979, A & A, 80, 179

[89] Runacres, M. C., Owocki, S. P., 2002, A & A, 381, 1015

[90] Runacres, M., Blomme, R., 1996, A & A, 309, 544

[91] Ryu, D., Jones, T. W., Frank, A., 2000, ApJ, 545, 475

[92] Sayle, K. A., Simnett, G. M., 1998, A & A, 331, 405

[93] Setia Gunawan, D. Y. A., de Bruyn, A. G., van der Hucht, K. A., Williams, P. M., 2000, A&A, 356, 676

[94] Sobolev, V. V., 1960, 'The moving envelopes of stars', Cambridge: Harvard University Press

[95] Sod, G. A., 1978, J. Comp. Phys., 27, 1

[96] Smarr, L.L., Norman, M.L., Winkler, K-H. A., 1984, Physica, 12D, 83

[97] Smith, E. J., Wolfe, J. H., 1976, GeoRL, 3, 137

[98] Stamatellos, D., Whitworth, A. P., 2003, A & A, 407, 941

[99] Taylor, G. I., 1950, Proc. Roy. Soc. A, 201, 192

[100] Turnshek, D. A., Grillmair, C. J., Foltz, C. B., Weymann, R. J., 1988 ApJ, 325, 651

[101] Williams, P. M., van der Hucht, K. A., Thé, P. S., 1987, A & A, 182, 91

[102] Williams, P. M., van der Hucht, K. A., Spoelstra, T. A. Th., 1994, A & A, 291, 805

[103] Williams, R.J.R., Hartquist, T.W., Dyson, J.E., 1995, ApJ, 446, 759

[104] Williams, R.J.R., 1999, MNRAS, 310, 789

[105] Williams, R. J. R., 2000, MNRAS, 316, 803

[106] Woodward, P. R., 1982, NATO ASI series C, 188, 245, 'Workshop on astrophysical radiation hydrodynamics'